Characterization of Microstructure, Texture and Oxidation Behaviour of Low Temperature Processed Nb-1Zr-0.1C (wt.%) Alloy

by

B. Vishwanadh
(Enrolment Number: ENGG01200904021)
BHABHA ATOMIC RESEARCH CENTRE

A thesis submitted to the
Board of Studies in Engineering Sciences Discipline

In partial fulfillment of requirements
For the Degree of

DOCTOR OF PHILOSOPHY
of
HOMI BHABHA NATIONAL INSTITUTE

March, 2015

Homi Bhabha National Institute

Recommendation of the Viva Voce Board

As members of the Viva Voce Board, we certify that we have read the dissertation prepared by Sri. B. Vishwanadh entitled "Characterization of Microstructure, Texture and Oxidation Behaviour of Low Temperature Processed Nb-1Zr-0.1C (wt. %) Alloy" and recommended that it may be accepted as fulfilling the dissertation requirement for the Degree of Doctor of Philosophy,

Date: 24/03/2015

Chairman- Prof. V. Kain

Date: 16/03/2015

Guide-Prof. R. Tewari

RNSingh Date: 16. 3. 2015

Co-Guide-Prof. R. N. Singh

Gautam Kumar Dey Date: 16/03/2015

Technical Adviser: Prof. G. K. Dey

Date: 26/3/15

External Examiner-Prof. B. S. Murty

Date: 16/3/15

Member: Prof. J. B. Singh

Alok Awasthi Date: 23.3.2015

Member: Prof. A. Awasthi

Date: 23/03/2015

Member: Prof. A. Arya

Final approval and acceptance of this dissertation is contingent upon the candidate's submission of the final copies of the dissertation to HBNI.

We hereby certify that we have read this dissertation prepared under our direction and recommend that it may be accepted as fulfilling the dissertation requirement.

Date: 16th March, 2015
Place: Mumbai

RNSingh
Co-guide

Guide

STATEMENT BY AUTHOR

This dissertation has been submitted in partial fulfillment of requirements for an advanced degree at Homi Bhabha National Institute (HBNI) and is deposited in the Library to be made available to borrowers under rules of the HBNI.

Brief quotations from this dissertation are allowable without special permission, provided that accurate acknowledgement of source is made. Requests for permission for extended quotation from or reproduction of this manuscript in whole or in part may be granted by the Competent Authority of HBNI when in his or her judgment the proposed use of the material is in the interests of scholarship. In all other instances, however, permission must be obtained from the author.

B. VISHWANADH

Declaration

I, hereby declare that the investigation presented in the thesis has been carried out by me. The work is original and has not been submitted earlier as a whole or in part for a degree / diploma at this or any other Institution / University.

B. VISHWANADH

Publications in International Journals

1. Development of Nb-1%Zr-0.1%C alloy as structural components for high temperature reactors, **B. Vishwanadh**, K. Vaibhav, S. K. Jha, K. V. Mirji, I. Samajdar, D. Srivastava and R.Tewari, journal of nuclear materials, 2012, 427, 350-358.

2. Study on recrystallization behaviour of Nb-1Zr-0.1C alloy, **B. Vishwanadh**, K. V. Mirji, K. Vaibhav, S. K. Jha, R. Ajay Kumar, I. Samajdar, D. Srivastava, G. K. Dey and R. Tewari, Materials Science Forum, 2012, 702-703, 631-634.

3. Textural and microstructural evolutions during deformation and annealing of Nb-1Zr-0.1C (wt%) alloy, **B. Vishwanadh**, K. V. ManiKrishna, A. K. Revelly, I. Samjdar, R. Tewari and G. K. Dey, Materials Science and engineering A, 2013, 585, 343-355.

4. A study on the oxidation behaviour of Nb alloy (Nb-1%Zr-0.1%C) and silicide coated Nb alloys, **B. Vishwanadh**, Naina R H, S. Majumdar, R. Tewari, G. K. Dey, Metallurgical and materials transactions A, 2013, 44, 2258-2269.

5. Characterization of silicide phases formed during pack siliconizing coating on the Nb-1Zr-0.1C alloy, **B. Vishwanadh**, S. Majumdar, J. Orsborn, R. Banerjee, R. Tewari, H. Fraser and G. K. Dey, Intermetallics, In Press.

6. Formation of the Nb_2C Phase in the Nb-1Zr-0.1C (wt.%) Alloy, **B. Vishwanadh**, K.V. Mani Krishna, A.K. Arya, R. Tewari and G.K. Dey, Acta materialia, under review.

(B. VISHWANADH)

Dedicated to

my dear parents and spouse

Acknowledgments

First and foremost, I would like to express my gratitude to Dr. Raghvendra Tewari, my thesis supervisor for his supervision, constructive criticisms and constant encouragement. I enjoyed all the discussion which I had with Dr. R. Tewari because of his friendly in nature. I am also indebted to Dr. R. N. Singh for his inspiring guidance and invaluable suggestions. I am also equally thankful to Dr. G. K. Dey for his helpful advice, continuous support and guidance. I would like to thank doctoral committee for their valuable suggestions and support through out the duration of work.

I would like to express my sincere thanks to all of my colleagues in Physical Metallurgy Section, Bhabha Atomic Research Centre, especially Mr. R. D. Hankare and Mr. Sanjay Kumar Verma of for their help and support received in carrying out experiments. It would have been impossible to bring this work into this form without their effort. I am also thankful to Dr. Dinesh Srivastava, Mr. K. V. Mani Krishna and Mr. Suman Neogy for their valuable suggestion and help in analyzing the results.

I am grateful to Dr. I. Samjdar, IITBombay for allowing me to use his Orientation Imaging Microscopy and X-ray diffraction facility. I express my sincere thanks to Dr. S. Majumdar, Materials Processing Division, BARC for his help in carrying out pack cementation coating experiments. I would like to thank my friend Mr. Amit Verma, Mechanical Metallurgy Division, BARC for the help in carrying out dilatometry and heat treatment experiments. I am also thankful to Dr. B. C. Maji for his help in carrying out tensile testing experiments. I am also thankful to Dr. Purandere, Mrs. Shilpa and Mr. R. Bapat, TIFR, mumbai for allowing me to use their TEM facilities.

It is a great pleasure to acknowledge my friends Dr. Naveen Kumar, Mr. R. Ajay Kumar, Dr. Kiran Kumar and Dr. Amit Srivastava for their encouragement. I would specially thank to Dr. A. Laik for helping in writing my thesis in latex.

I would like to express my deep sense of gratitude to my beloved wife Soujanya, for her patience, encouragement and love. Finally, I thank my cute little baby Aashna for allowing me to work at home.

(B. VISHWANADH)

Contents

Synopsis

Nb-Zr-C alloys show a good combination of high temperature properties. As a result, Nb alloys have found many structural component applications especially in high temperature reactors [1-4]. Delgrosso *et al.* [3] have studied the effect of Zr and C on the mechanical properties of Nb alloys at different temperatures and developed high strength Nb alloys. In Nb-Zr-C based ternary alloy system, Nb-1Zr-0.1C (wt.%) alloy show optimum high temperature properties [3, 4]. Alloying with 1% Zr greatly improves the resistance to oxygen absorption as well as provides solid solution strengthening to the alloy [3]. Addition of C, on the other hand, increases the strength of the material by forming various carbide precipitates [3]. Solubility of C in Nb is limited at low temperatures [5]. Therefore, excess C precipitate out in the form of C-rich Nb-C phases during cooling from high temperatures. In Nb-Zr-C alloys, formation of various kinds of carbide phases, like Nb_2C, Nb_3C_2, Nb_4C_3, NbC and Nb_6C_5 phases take place depending on the processing condition of the samples [6-8]. According to the equilibrium Nb-C binary phase diagram, at low C concentration (<5 wt.%), formation of the Nb_2C carbide phase occurs. This phase exists at least in three polymorphic forms; γ-Nb_2C phase (with disordered hexagonal structure), β-Nb_2C (with ordered tetragonal structure) and α-Nb_2C (with orthorhombic structure) [9]. The other two carbide phases Nb_3C_2 and Nb_4C_3 are metastable. They exist in Nb-C alloys only when the alloy is quenched from high temperatures [10]. Addition of Zr in the Nb alloy makes the Nb_2C phase unstable which dissolves during thermomechanical processing and the excess C re-precipitates in the form of stable (Nb,Zr)C carbide [6, 10]. In general, mechanical properties of the Nb alloys can be improved by optimizing the microstructure including grain size, type of carbide phase, size and its morphology. However, there are a few points which need to be addressed before using these materials as structural material for high temperature applications. These are:

1. Existing literature on Nb alloys shows that deformation temperatures for these alloys should be higher than 1600 °C and recrystallization temperatures should be in the range of 1450 - 1500 °C. It is also a known fact that Nb alloys are susceptible to oxidation and decarburization above 1400 °C [3]. As a result, any thermomechanical treatment above 1400 °C needs special arrangements to keep oxygen concentration extremely low to avoid oxidation. Therefore, by reducing the processing temperatures, oxidation and decarburization problems can be addressed. In addition, Nb alloys have high toughness and adequate ductility at temperatures as low as 0.3 T_m. Therefore, two fold benefits could be attained by working the material at low temperatures. Deforming the Nb alloys at low temperatures would store sufficient energy which will bring down the recrystallization temperatures. Therefore, a detailed study to explore the possibility of low temperature deformation should be carried out.

2. High temperature strength of the Nb alloys is mainly attributed to the presence of carbides in the alloy. In order to improve the mechanical properties of the alloy, a stable carbide phase with sufficient volume fraction, size and desirable morphology in the Nb matrix needs to be produced. In order to produce this, information about microstructure, crystallography and formation mechanisms of each carbide is necessary. Though the formation of multiple carbides, Nb_2C, Nb_3C_2, Nb_4C_3, NbC and Nb_6C_5 have been reported in the literature, crystallographic details on these carbides are not well documented. Therefore, systematic studies on the identification and formation mechanism of each carbide phase at every processing stage is required.

3. Development of texture during deformation and annealing decides properties of the material [11]. Therefore, by inducing suitable texture in the material, desired properties can be obtained. In order to tailor the texture of the materials, it is important to know the type of texture development in the material during various thermomechanical processing treatments. However, such texture studies on Nb alloys are virtually non-existent. Hence, analysis on the texture development in Nb alloys during deformation and annealing are to be carried out.

4. One of the main concerns in using Nb based alloys for high temperature applications is their poor oxidation resistance. Pure Nb undergoes oxidation at extremely low temperatures ($\sim$ 0.3 T$_m$). Oxidation resistance of Nb alloy can be improved either by alloying addition or by providing an oxidation barrier coating. As nuclear applications restrict addition of alloying elements because of their often unfavourable nuclear properties. Therefore, special attention needs to be given on the development of oxidation barrier coatings on Nb alloy.

In the present study, above issues have been addressed by carrying out microstructural characterization and structure property correlation studies of Nb-1%Zr-0.1%C alloy. Initially, deformation and annealing experiments were carried out on the Nb alloy at various temperatures. Based on these studies, parameters for deformation and annealing at low temperatures were optimized. Further, using these data, a flow sheet for the fabrication of Nb alloy at low temperatures was developed. Subsequently, carbide phases present in all the samples were characterized and their transformation mechanisms were studied. These data were used in preparing the alloy having similar mechanical properties as that of the material fabricated by thermomechanical processing at higher temperatures. In addition, a detailed study on the development of crystallographic texture during deformation and annealing treatments was carried out. In this study, additional emphasis was given to identifying the type of slip systems getting activated during deformation of the alloy. Finally, in order to reduce oxidation of the Nb alloy at higher temperatures, silicide coating was produced and its oxidation behaviour was studied and compared with the bare Nb alloy.

This thesis is divided into eight chapters. A brief introduction about Nb-Zr-C alloys, phase diagrams and their applications are given in the chapter 1. Chapter 2 deals with the literature review on the development of Nb-1Zr-0.1C alloys and formation of various carbides in the Nb alloy system. It also includes development of textures during deformation and annealing in various bcc materials. Literature on the oxidation behaviour of Nb alloys and pack cementation coatings have also been described in this chapter. The details of the alloy preparation, fabrication and the experimental methods employed in the present study are given in Chapter 3. Chapters 4, 5, 6 and 7 present the detailed description of the obtained experimental results and their discussions. A Summary of each chapter pertaining to experimental results have been given in the following sections:

Chapter.4: Thermomechanical processing of the alloy

This chapter is focused on exploring the possibility of deformation and recrystallization of the Nb alloy at relatively low temperatures. For this, the effect of thermomechanical treatments on the microstructure and mechanical properties of Nb-1%Zr-0.1%C alloy have been studied. It includes studies on the deformation behavior of as-solidified Nb alloy at different temperatures and strain rates, recrystallization behavior at different temperatures and time, and evolution of microstructures at different processing conditions (as-solidified, deformed and recrystallized).

The Nb-1%Zr-0.1%C alloy was produced by electron beam melting technique. The as-solidified microstructure of Nb alloy (Fig.1(a)) showed presence of the needle morphology carbide precipitates in the large grain size of the Nb matrix. Mechanical properties of the as-solidified sample showed low ductility ($\sim$ 2%). Hence, to break the as-solidified structure at low temperatures, compression testings were carried out in a dilatometry in the temperature range of 600 - 1300 °C. It showed two regions of low flow stress: one at 800 °C and the other at temperatures higher than 1000 °C. In order to reduce the effect of oxidation, deformation temperature for breaking of as-solidified structure was selected as 800 °C. The ingots of the alloy were extruded successfully at 800 °C. The deformed microstructure showed the presence of two types of carbides: one was having needle morphology and other showed the cuboidal morphology. Detailed recrystallization study of the deformed samples showed that annealing treatment at 1300 °C for 3 hrs produces a nearly full recrystallized microstructure (Fig.1(b)).

Mechanical properties of the annealed samples were determined at room temperature. It showed similar mechanical properties as that of the material developed using high temperature deformation route [4]. Based on these experiments, a flow sheet for the fabrication of Nb alloy at low temperature has been developed.

Chapter.5: Formation of different carbide phases in the Nb alloy

In this chapter detailed microstructural characterization of the second phase precipitates present in the as-solidified, deformed and annealed samples of Nb alloy was carried out using Synchrotron X-ray diffraction (XRD), transmission electron microscopy (TEM) and high resolution transmission electron microscopy (HRTEM) techniques.

Detailed analysis of synchrotron XRD and SAED (selected area electron diffraction) patterns obtained from the second phase precipitates of needle morphology (Fig.2(a)) present in the as-solidified samples showed that precipitates are of γ-Nb_2C carbide phase. Orientation

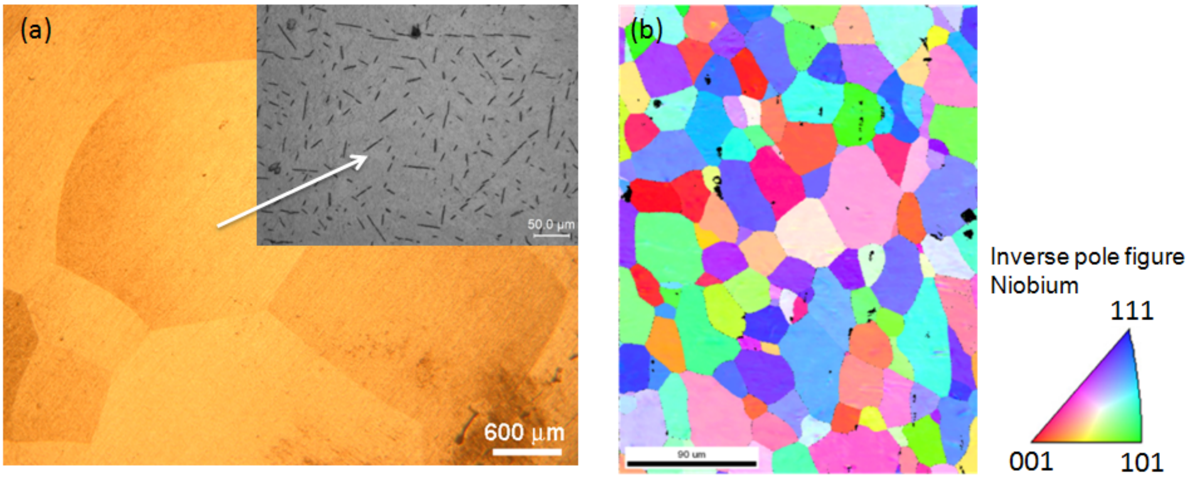

Figure 1: (a) Optical micrograph of as-solidified Nb alloy showing the presence of large grain size (∼ 1 mm) and needle morphology precipitates within the grain (shown in inset figure) and (b) EBSD image of the heat treated sample at 1300 °C for 3 hrs showing the presence of recrystallized microstructure.

relationship between the matrix and carbide phase has also been determined as:

$$[1\bar{1}\bar{1}]_{Nb} // [\bar{1}\bar{1}23]_{Nb_2C}, (0\bar{1}1)_{Nb} // (01\bar{1}1)_{Nb_2C} \text{ and } (12\bar{1})_{Nb} // (1\bar{2}1\bar{1})_{Nb_2C} \quad (1)$$

High resolution images of the carbide phase were obtained and compared with the simulated HRTEM images. The simulated HRTEM image matched well with the experimental image of the Nb_2C phase. When carbide needles were viewed along $[\bar{1}\bar{1}23]$ direction, HRTEM analysis showed presence of the coherent interface between Nb and Nb_2C carbide phase. Based on these structural relationships and crystallographic analysis, transformation mechanism for the Nb_2C phase has been proposed. It was shown that the transformation of Nb to Nb_2C requires very small movement of Nb atoms and interstitial C atoms play a key role in the formation of the Nb_2C phase.

Similarly, other carbide phase precipitates (needle and cuboidal morphology) present in the deformed samples were characterized by XRD and TEM techniques (Fig.2(b)). Crystallographic analysis showed that the needle morphology and cuboidal morphology precipitates corresponds to α-$(Nb,Zr)_2C$ and $(Nb,Zr)_3C_2$ carbide precipitates, respectively. The crystal structure of the $(Nb,Zr)_2C$ was determined as orthorhombic structure with lattice parameters as a = 10.89, b = 12.36 and c = 4.956 A° and the crystal structure of the $(Nb,Zr)_3C_2$ was determined as hexagonal crystal structure with lattice parameters as a = 11.46 A° and c = 18.30 A°. The HREM and crystallographic analyses showed that the Nb_2C carbide precipitates present in the

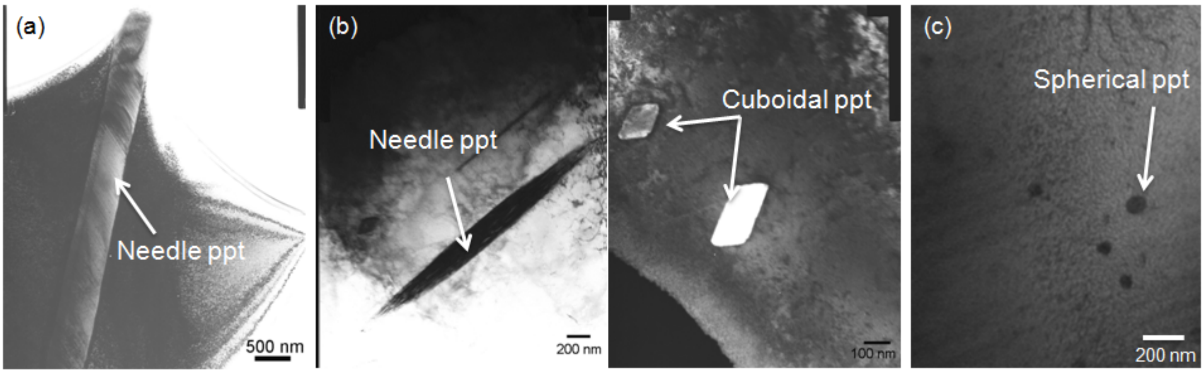

Figure 2: TEM micrographs of the (a) as-solidified (b) deformed and (c) annealed samples showing the presence of needle morphology, cuboidal and needle morphology, and spherical morphology carbide precipitates, respectively.

as-solidified sample dissolved during deformation and re-precipitated in the form of $(Nb,Zr)_2C$ and $(Nb,Zr)_3C_2$.

Microstructure of the annealed Nb alloy samples (Fig.2(c)) showed the presence of very fine spherical morphology carbide precipitates ($\sim$ 100 nm) in the Nb matrix. Synchrotron XRD and SAED patterns analysis showed that the precipitate phase has the fcc structure with a lattice parameter as 0.475 nm. EDS (energy dispersive spectroscopy) analysis showed that chemical composition of the precipitate matches well with the (Nb,Zr)C carbide phase. HRTEM images of the carbide phase showed the presence of $(Nb,Zr)_3C_2$ at the interface between Nb and (Nb,Zr)C phases. Based on HRTEM analysis it was found that (Nb,Zr)C carbides get precipitated in the vicinity of the $(Nb,Zr)_3C_2$ carbide phases. It indicates that the decomposed C of the dissolved $(Nb,Zr)_3C_2$ aids in forming the (Nb,Zr)C phase. Due to this, the (Nb,Zr)C precipitates have nucleated in the vicinity of the $(Nb,Zr)_3C_2$ carbide phases.

This chapter showed that formation of different type of carbide phase depends on the processing condition of the alloy and it has been shown that the phase transformation sequence for the formation of stable (Nb,Zr)C carbide phase can be expressed as: γ-$Nb_2C \rightarrow \alpha$-$(Nb,Zr)_2C$ + $(Nb,Zr)_3C_2 \rightarrow (Nb,Zr)C$.

Chapter.6: Textural and microstructural evolutions during deformation and annealing

The chapter deals with the development of macro and micro texture during deformation and annealing of the Nb alloy. The bulk texture analysis showed that up to 40% deformation, texture remains nearly random and beyond 60% deformation predominant development of α and γ-fiber textures was observed. Among these two fibers, strength of the γ-fiber was higher than that of the α-fiber. Intensities of individual orientations present in the α and γ-fibers were analyzed (Fig.3(a)). In the case of 60% deformed sample, evolution of three texture components in the α-fiber was observed. After 80% deformation, the maximum intensity shifted to the $\{111\}\langle110\rangle$ texture component. In the case of γ-fiber, for the sample deformed beyond 40% reduction, all the orientations present in the γ-fiber have increased and a weak preference for $\{111\}\langle110\rangle$ texture component was observed.

The rolling textures were simulated using Taylor type full constraint (FC) and relaxed constraint (RC) models using combination of various slip systems. Comparing experimental ϕ_2 sections of ODFs 80% deformed samples with simulation carried out using the pancake RC model involving $\{110\}\langle111\rangle$ slip system close resemblance was observed. Intensity of individual texture components in α and γ- fibers were estimated from the simulation results ((Fig.3(b))) and it matched with the experimentally observed texture. This study shows that deformation in Nb alloy takes place by activation of $\{110\}\langle111\rangle$ type of slip systems. The simulation results obtained using RC Taylor type model matching with the experimental results indicates that in Nb alloy, during deformation grain boundaries plays a vital role in the development of rolling texture.

Similarly, texture analysis was carried out on the annealed samples which are heat treated at 1300 °C for different soaking time periods. When intensities of individual texture components was compared, it showed two major changes in the annealed texture with respect to deformed texture. Firstly, enhancement of the $\{001\}\langle110\rangle$ component in the α-fiber and decrease in the other two components $\{111\}\langle110\rangle$ and $\{112\}\langle110\rangle$. Secondly, decrease in the intensity of the γ-fiber. These changes lead to the development of a relatively random texture in the annealed samples with a weak $\{001\}\langle110\rangle$ texture.

These annealed samples were also examined under TEM. It showed the presence of similar (Nb,Zr)C carbide precipitates as present in the recrystallized sample. Detailed EDS analysis of these carbides showed that with increasing annealing time, Nb/Zr ratio in the precipitates has decreased. It indicates that Zr present in the Nb alloy partitioned preferentially into precipitates. Due to this, Zr content in the matrix region has decreased and it lead to decrease in hardness of the annealed samples.

Chapter.7: Oxidation behaviour and silicide coating of Nb alloy

This chapter deals with the oxidation behaviour of bare Nb alloy and silicide coated Nb alloy samples from room temperature to higher temperatures in air environment.

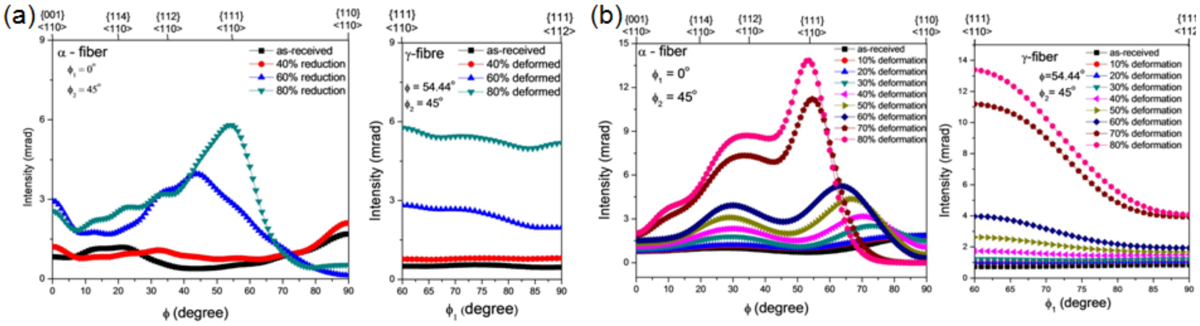

Figure 3: ODF intensities of individual orientations present in the α and γ-fibers in the deformed samples of Nb alloy (a) experimental and (b) simulated using Taylor type relaxed constraint model using $\{110\}\ \langle 111 \rangle$ slip system.

Silicide coatings on the Nb alloy samples were produced by pack cementation technique at different temperatures for different time periods. Cross-sectional views of silicide coatings showed that coatings produced at 1200 °C have a single phase, whereas, coatings produced at higher temperatures (1300-1500 °C) have two phases in the coating layer. EDS analysis showed that the stoichiometry of the coating layer in the samples coated at 1200 °C matched with the $NbSi_2$ phase. In the case of sample coated at 1300 °C, an intermediate layer between outer layer and substrate (Nb alloy) formed which was identified as Nb_5Si_3. The crystal structure and grain morphology of the $NbSi_2$ and Nb_5Si_3 were determined by TEM using SAED patterns. The crystal structure of the Nb_5Si_3 was determined as tetragonal structure with lattice parameters as a = 0.65 nm, c = 1.19 nm and the crystal structure of $NbSi_2$ was determined as hexagonal crystal structure with lattice parameters as a = 0.48 nm, c = 0.66 nm. Fig.4(a) shows the EBSD image of the silicide coated sample produced at 1300 °C for 6 hrs. In the input data for EBSD analysis, the crystallographic information obtained from the TEM has been provided. EBSD could index all the three phases very clearly with the crystallographic data provided from the TEM analysis. The EBSD and TEM micrographs revealed that Nb_5Si_3 had formed with equiaxed grain morphology, whereas, $NbSi_2$ had two types of morphologies: one columnar morphology which has formed near to the Nb_5Si_3 phase and second bigger equiaxed grain morphology near the surface of the sample.

Oxidation behavior of the silicide coated samples was studied and compared with the bare Nb alloy. The weight gain data in air environment (Fig.4(b)) showed that up to 1200 °C there was no substantial change in the weight of the silicide coated sample, whereas the bare Nb alloy had undergone heavy oxidation at 500 °C. This shows that silicide coating has effectively

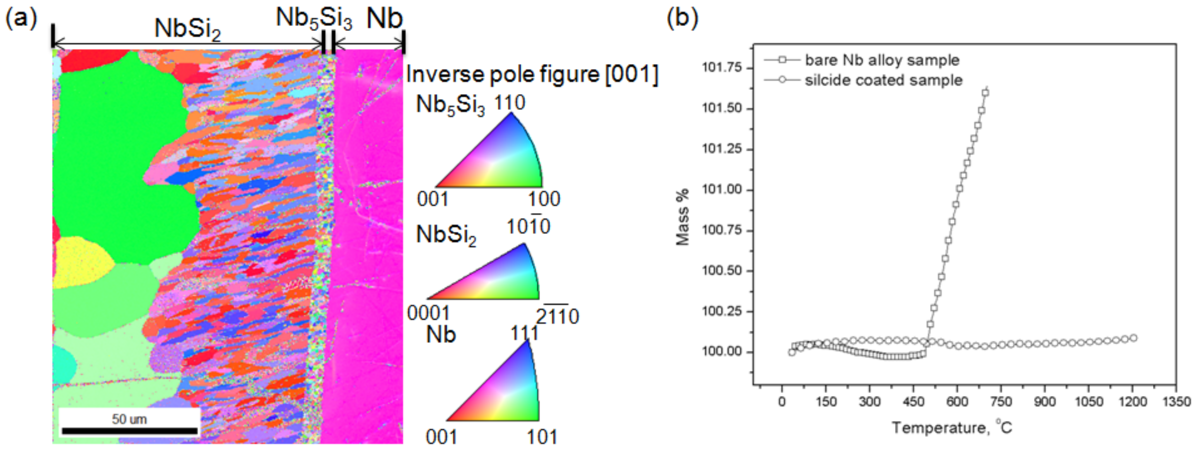

Figure 4: EBSD image of the cross-section of silicide coated sample showing the presence of $NbSi_2$, Nb_5Si_3 and Nb phases and (b) TGA analysis of silicide coated and bare Nb alloy heated in air atmosphere showing silicide coated sample has better oxidation resistance than bare Nb alloy.

provided the resistance against oxidation. Isothermal oxidation experiments carried out on the silicide coated samples at 1000 °C up to 64 hrs. It showed initial weight gain of the sample (0.020 kg/m^2) up to 8 hrs, which reduced considerably at later stage. Initial weight gain was essentially due to the formation of protective oxide phase on the surface of the sample, which has protected further oxidation of the sample. When the oxidized samples were characterized by EDS and XRD showed that oxide layer contained a mixture of Nb_2O_5 and SiO_2 phases. Microstructural analysis of these samples showed that the formation of SiO_2 phase was the main reason for the improved oxidation resistance of the silicide coated Nb alloy samples.

Conclusions

The important conclusions that have been drawn from the results of the present investigation are as follows:

- Based on the thermomechanical processing studies low temperature processing flow sheet for the fabrication of Nb alloy tubes was established. It was shown that extruding the Nb alloy at 800 °C followed by annealing at 1300 °C for 3 hrs can produce well recrystallized microstructure.

- Detailed carbide phase formation study has shown that phase formation sequence for the formation of stable (Nb,Zr)C carbide phase as:
  γ-$Nb_2C \rightarrow \alpha$-$(Nb,Zr)_2C + (Nb,Zr)_3C_2 \rightarrow (Nb,Zr)C$.

- The macro and micro-texture studies of deformed samples showed that at and beyond 60% deformation, Nb alloy undergoes predominant development of α and γ-fiber texture. Among α and γ-fiber texture, γ-fiber texture was dominant. Upon annealing, the deformed samples texture got randomized and weak $\{001\}\langle 110\rangle$ type of texture developed.

- The silicide coated samples produced by pack cementation technique provided high temperature oxidation resistance for the Nb alloy by the formation of thin SiO_2 oxide layer.

References

1. I. V. Dulera and R. K. Sinha, ”High temperature reactors”, *J Nucl Mater*, vol. 383, no. 1-2, pp. 183-188, 2008.

2. D. C. Goldberg, G. Dicker, and S. A. Worcester, ”Niobium and niobium alloys in nuclear power”, *Nucl Eng Des*, vol. 22, no. 1, pp. 124-137, 1972.

3. E. J. Delgrosso, C. E. Carlson, and J. J. Kaminsky, ”Development of niobium-zirconium-carbon alloys”, *J Less Common Met*, vol. 12, no. 3, pp. 173-201, 1967.

4. R. H. Titran and M. Uz, ”Effect of themomechanical processing on the microstructure and mechanical properties of Nb-Zr-C alloys”, NASA, vol. TM-107207, 1996.

5. R. K. Viswanadham and C. A. Wert, ”Electron microscopic study of precipitation in the niobium-carbon system”, *J Less Common Met*, vol. 48, no. 1, pp. 135-150, 1976.

6. J. F. Smith, O. N. Carlson, and R. R. D. Avillez, ”The niobium carbon system”, *J Nucl Mater*, vol. 148, no. 1, pp. 1-16, 1987.

7. E. Parthe and K. Yvon, ”On the crystal chemistry of the close packed transition metal carbides II A proposal for the notation of the different crystal structures”, *Acta Crystallogra B*, vol. 26, pp. 153- 163, 1970.

8. R. L. Crane and F. Ostermann, ”An X-ray diffraction analysis of the ϵ phase in dilute Nb-C alloys”, *Metall Trans*, vol. 2, pp. 3487-3488, 1971.

9. E. Rudy and C. E. Brukl, ”Lower temperature modifications of Nb_2C and V_2C” *J Am Ceram Soc*, vol. 50, pp. 265-268, 1967.

10. F. Ostermann, ”Controlling carbide dispersions in niobium base alloys”, *J Less Common Met*, vol. 25, no. 3, pp. 243-256, 1971.

11. H. Jiang, T. R. Bieler, C. Compton, and T. L. Grimm, ”Cold rolling evolution in high purity niobium using a tapered wedge specimen”, *Physica C*, vol. 441, pp. 118-121, 2006.

List of Figures

List of Tables

List of Abbreviations

BF	Bright field image
DF	Dark field image
EBSD	Electron back scattered diffraction
EB	Electron beam melting
EDS	Energy dispersive spectrometer
FC	Full constraint Taylor model
GOS	Grain orientation spread
HRTEM	High resolution transmission electron microscope
ID	Inner diameter
IPF	Inverse pole figure
ND	Normal direction
OD	Outer diameter
ODF	Orientation distribution function
OIM	Orientation imaging microscope
OR	Orientation relationship
RC	Relaxed constraint Taylor model
RD	Rolling direction
SAED	Selected area electron diffraction
SEM	Scanning electron microscope
STEM	Scanning transmission electron microscope
TEM	Transmission electron microscope
TGA	Thermogravimetric analyzer
TD	Transverse direction
VHN	Vickers hardness number
WT	Wall thickness
XRD	X-ray diffraction

CHAPTER 1

Introduction

1.1. Background

Niobium is one of the most useful element among refractory metals because of its superconducting and nuclear properties. In fact, niobium is nearly always found together with tantalum, and was named after Niobe, the daughter of the mythical Greek king Tantalus for whom tantalum was named [1]. Niobium has many uses, some of which it shares with other refractory metals. Nb is the least dense of the refractory metals. It can be worked by adopting suitable thermo-mechanical treatments [2] and a wide range of strength and elasticity of materials could be produced. Because of such properties it is used in electrolytic capacitors [3], in the most practical superconducting alloys [4] and in aircraft gas turbines [5]. In addition, Nb alloys have shown good resistant to liquid metal corrosion [6, 7], low thermal neutron capture cross-section [8] and very high temperature strength [2, 9], hence these have been considered as potential candidate material for cladding, tubing and other structural material in high temperature reactors [9–11]. Niobium is the only element which finds application from a temperature as low as -269 °C to as high as 1127 °C. Applications of niobium could be broadly divided into two groups: structural and precision. The former application could be attributed to the structural applications and the later application to the superconducting and biomedical [12, 13] applications.

In 1960s, the attentions of material experts were drawn towards the refractory metal base structural materials for aerospace applications [14]. These applications demand apart from ability to perform at high temperature conditions should also have low density, high melting point and adequate strength at the operating temperatures to bring down the launch weight. High ductility at low temperatures and high solubility for interstitial were additional requirements added from the workability view point. In this regard, niobium with melting point ($\sim$ 2468 °C) and lowest density among refractory metals ($\sim$ 8.4 g/cc) exhibits highest low temperature ductility ($\sim$ 20% at -173 °C) and highest solubility of interstitial elements; and least sensitivity

Table 1.1: High temperature niobium alloys [6].

	Alloy composition	**Strength (MPa)**		
		1100 °C	1200 °C	1300 °C
Low strength	Nb-5V Nb-5V-12.5Zr Nb-10Hf-1.0Ti-0.7Zr Nb-1Zr-0.1C	160-260		
Medium strength	Nb-5Mo-5V-1Zr Nb-27Ta-10W-0.7Zr Nb-4.6Mo-1.4Zr-0.12C Nb-5W-2Mo-1Zr-0.05-0.07C Nb-10W-2.5Zr	260-450	190-280	70
High strength	Nb-15W-5Mo-1Zr-0.1C Nb-15W-5Mo-5Ti-1.0Zr Nb-10Mo-1.5Zr-0.3C-0.03Ce,La Nb-5W-2Mo-1Zr-0.05-0.07C Nb-(22-28)W-2Hf-(0.067-0.13)C Nb-30Hf-9W	350-450	190-350	100

in ductility with interstitial content. In view of such attractive properties it is not surprising that niobium was the first refractory metal selected for prospective basis for the structural material for high temperature applications.

Initial efforts for the development of the material were directed towards obtaining high temperature strength without compromising its ductility and protection against oxidation at elevated temperatures exceeding 1000 °C. As a result, first few alloys of niobium developed could be divided into three broad groups [6]; low, medium and high alloy groups. Most of these alloys find applications in the temperature range from 1000-1200 °C for a long term operations whereas for short time working temperature range was 1200-1700 °C. Table.1.1 enlists some of these alloys and their possible range of temperatures.

The initial developments were taken a brief pause because;

(i) these developments could not solve issues related with achieving of high workability with high strength of an alloy,

(ii) any adequate environmental coating could not be developed which was economically viable and

(iii) most importantly, the development of new series of superalloys which could sustain high temperatures, advances made in Ti intermetallics which offered superior strength to weight ratios.

During this period, though the research on the development of Nb based alloys as structural materials was reduced, its application as an alloying element in metallic superconductors raised several fold. In addition, Nb was profusely used in steel industry and its use in Ti industry increased with the discovery of the fact that ductilization of Ti_3Al intermetallics with the addition of Nb was possible. By the middle of decade of 1980, research on niobium alloys gained momentum as it was soon realized that superalloys have reached to their maximum temperature ($\sim$ 0.95 Tm) of utilization and creep properties of TiAl were not as good as initially thought of; particularly as the proposed operating temperatures exceeded 1100 °C [15]. In the temperature range 1100 to 1500 °C where Ni and Ti alloys are not possible to work, structural ceramics do not provide adequate fracture toughness and thermal shock resistance, refractory metal based (particularly Nb based) provide the necessary solution.

The second renewed interest on the niobium related research brought several new concepts and the problem of high temperature softening was addressed through strengthening mechanisms. The common Nb alloys listed in Table.1.1 are hardened primarily by solid solution strengthening and precipitation hardening strengthening mechanisms.

Among various Nb alloys, the Nb-1Zr based alloys have been proposed for various high temperature applications as these alloys exhibit high resistance to liquid alkali metal corrosion and also remain as a single phase from room temperature to the melting point in addition to aforementioned properties. Carbon addition in the Nb-1Zr alloy improves its high temperature strength and increases creep-resistance to provide additional design and safety margins through the formation of the primary carbide phase. An earlier studies on Nb-Zr-C alloy [16] shows that the Nb-1%Zr-0.06%C alloy has excellent microstructural stability at temperatures of interest with or without applied load. The total creep strain in the sample of this alloy was less than 0.1% after 4 years (35,000 hours) at 1077 °C under a stress of 10 MPa. With further addition of carbon the strength in the material was gained at the cost of reduction in ductility and poor fracture strength and the composition of the alloy system was optimized to Nb-1%Zr-0.1%C.

One of the potential applications of Nb-1%Zr-0.1%C is the structural material for compact high temperature nuclear reactor [10]. It is pertinent to take an account of advantages of Nb and Nb-1Zr-0.1C alloy over other alloys.

Table 1.2: Reactions in Nb-C phase diagram (Fig.1.2)

Reaction type)	**Reaction**	**Composition (C at.%)**			**Temperature °C**
Melting	L $\longleftrightarrow$ Nb		0		2469
Eutectic	L $\longleftrightarrow$ Nb + Nb_2C	10.5	5.7	28	2340
Peritectic	L + NbC $\longleftrightarrow$ Nb_2C	31	38	33.3	3080
Congruent	L $\longleftrightarrow$ NbC		45		3600
Eutectic	L $\longleftrightarrow$ NbC + C	60	49	98	330

1.2. Physical metallurgy of Nb-Zr-C system

Fig.1.1 & 1.2 shows the equilibrium binary alloy phase diagrams of Nb-Zr and Nb-C systems, respectively [17, 18].

1.2.1. Nb-Zr binary phase diagram

The binary Nb-Zr equilibrium phase diagram (Fig.1.1) shows the existence of three equilibrium solid solution phases: α-Zr, β-Zr and β-Nb. β-Zr, β-Nb have bcc structures and the α-Zr has hcp structure. Pure Zr and pure Nb melts at 1855 °C and 2469 °C, respectively. The phase diagram shows that pure Nb consists of single phase β-Nb and it exists up to the melting point. In contrast, pure Zr shows allotropy transformation, the liquid phase transforms to β-Zr at 1855 °C and it exists in the temperature range of 1855 to 863 °C. At 863 °C, β-Zr transforms to α-Zr. At 620 °C, monotectoid reaction take place. The β-Zr transforms to α-Zr and β-Nb. The solid solubility of Nb in α-Zr is 0.6 wt.% at monotectoid reaction temperature.

Considering the alloy composition in the present study i.e., Nb-1%Zr in the Nb-Zr binary equilibrium phase diagram, it shows that the alloy will have a single phase β-Nb phase from room temperature to melting temperature.

1.2.2. Nb-C binary phase diagram

Fig.1.2 shows the equilibrium Nb-C binary phase diagram. It shows the existence of Nb_2C, NbC and Nb_6C_5 carbide phases. The reactions which takes place at different temperatures in the Nb-C alloys are listed in the table.1.2.

Nb_2C exists as a disorder hexagonal phase γ-Nb_2C at higher temperatures (>2500 °C) and transforms to an ordered hexagonal phase, β-Nb_2C, at about 2500 °C. The Nb_2C phase field exists from 28 to 33 at.% C at the eutectic temperature of 2340 °C. Beyond 37 at.% C, NbC

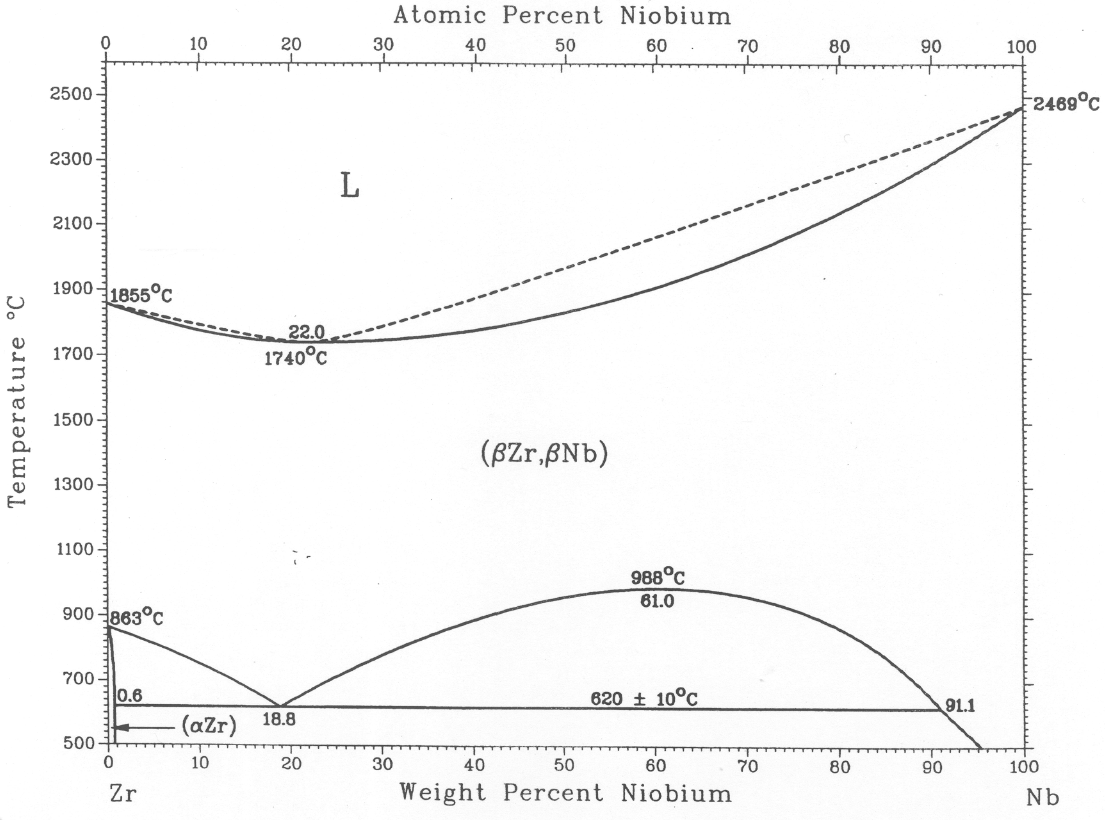

Figure 1.1: Nb-Zr binary alloy equilibrium phase diagram [17].

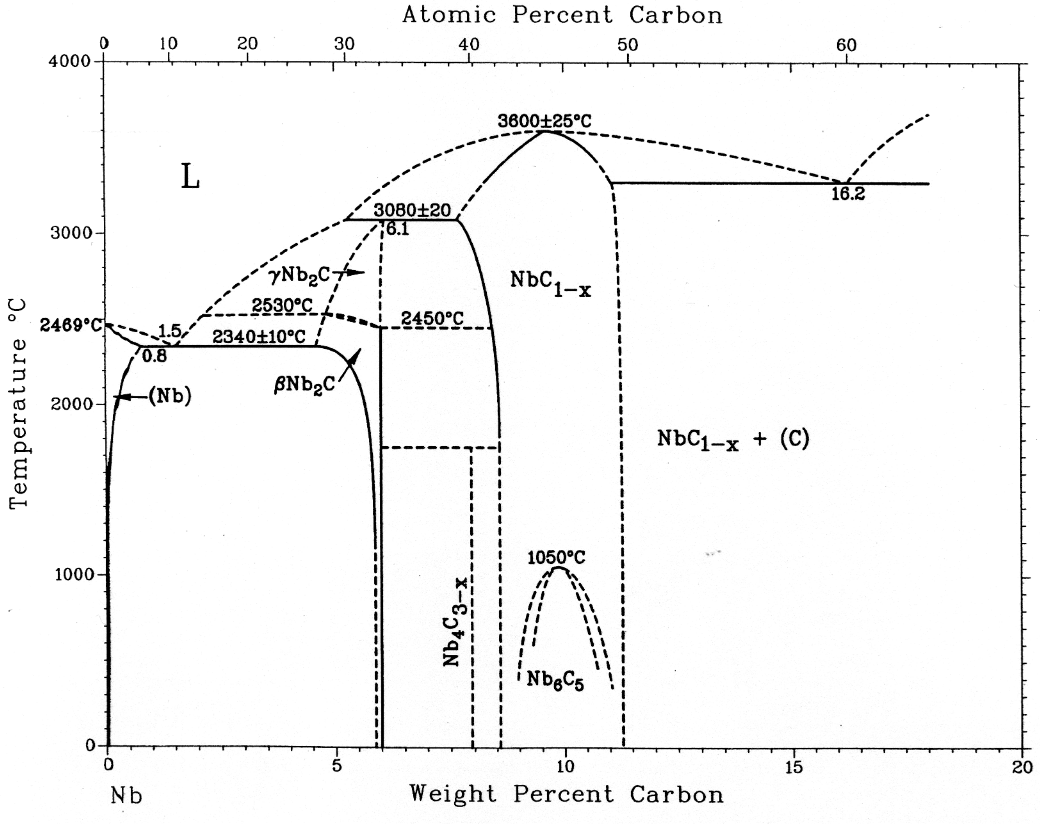

Figure 1.2: Nb-C binary alloy equilibrium phase diagram [18].

cubic phase exists in the binary alloys. The NbC phase has 41 at.% C and has fcc structure. In alloys Nb-10 wt.% C, at lower temperature C atoms tend to develop long range ordering. The ordering temperature depends upon composition and it has a range of 1025 °C to 1082 °C. The ideal stoichiometry for ordered array is generally accepted as Nb_6C_5. The Nb_6C_5 has 45.5 at.% C.

According to equilibrium Nb-C binary phase diagram, the Nb-0.1 wt.%C alloy will have β-Nb and disordered hexagonal Nb_2C phases below melting temperature to 2500 °C. Below 2500 °C to 1200 °C temperature, the alloy will have β-Nb and ordered hexagonal Nb_2C phases [19]. Below 1200 °to room temperature, the alloy will have β-Nb and orthorhombic Nb_2C phases.

Considering both Nb-Zr, Nb-C binary alloy phase diagram, at room temperature the alloy Nb-1%Zr-0.1%C should have Nb_2C carbide precipitates in the β-Nb matrix.

1.3. Objectives of the study

In spite of having high applicability of the Nb-Zr-C alloys, studies on this alloy are very limited. There are few points need to be addressed before using these materials as structural materials for high temperature applications. These are:

1. Existing literature on Nb alloys shows that deformation temperatures for these alloys should be higher than 1600 °C and recrystallization temperatures should be in the range of 1450 - 1500 °C. It is also a known fact that Nb alloys are susceptible to oxidation and decarburization above 1400 °C [2, 11]. Therefore, any thermomechanical treatment above 1400 °C needs special arrangements to keep oxygen concentration extremely low to avoid oxidation. Therefore by reducing processing temperatures, oxidation and decarburization problems can be addressed. In addition, Nb alloys have high toughness and adequate ductility at temperatures as low as 0.3 T_m. Therefore, two fold benefits could be achieved by working the material at low temperatures, thereby storing sufficient energy which will bring down the recrystallization temperatures. Hence, a detailed study to explore the possibility of low temperature deformation should be carried out.

2. High temperature strength of the Nb alloys is mainly attributed to the presence of carbides in the alloy. In order to improve the mechanical properties of the alloy, a stable carbide phase with sufficient volume fraction, size and desirable morphology in the Nb matrix

needs to be produced. In order to produce this microstructure, crystallographic information and formation mechanisms of each carbide is necessary. Though the formation of multiple carbides, Nb_2C, Nb_3C_2, Nb_4C_3, NbC and Nb_6C_5 have been reported in literature [19–23], crystallographic information and formation mechanisms of these carbides are not well documented. Therefore, systematic studies on the identification and formation mechanism of each carbide phase at every processing stage is required.

3. Development of texture during deformation and annealing decides properties of the material [24]. Therefore, by inducing suitable texture in the material, desired properties can be obtained. In order to tailor the texture of the materials, it is important to know type of texture development in the material during various thermomechanical processing treatments. Specially, literature is devoid of such texture studies on Nb alloys. Hence, complete understanding on the texture development during deformation and annealing are to be carried out.

4. One of the main concerns of using Nb based alloys for high temperature applications is their poor oxidation resistance. Pure Nb undergoes oxidation at extremely low temperatures ($\sim 0.3\ T_m$) [25]. Oxidation resistance of Nb alloy can be improved either by alloying addition or by providing an oxidation barrier coating [26, 27]. As nuclear applications restrict the addition of alloying elements due to nuclear properties of many elements are not favourable, therefore, special attention needs to be focused on the development of oxidation barrier coatings on Nb alloy.

In the present study, these issues have been addressed by carrying out microstructural characterization and structure property correlation studies of Nb-1%Zr-0.1%C alloy. Initially, deformation and annealing experiments were carried out on the Nb alloy at various temperatures. Based on these studies, parameters for deformation and annealing at low temperatures were optimized. Further, using this data, flow sheet for the fabrication of Nb alloy was developed. Subsequently, the carbide phases present in all the sample were characterized and their transformation mechanisms were understood. This data was used in preparing the alloy having similar mechanical properties as that of the material developed at higher temperatures. In addition, detailed study on the development of crystallographic texture during deformation and annealing treatments were carried out. In this study, emphasis was given to find the type of slip systems getting activated during deformation of the alloy. Finally, in order to decrease oxidation of the Nb alloy at higher temperatures, silicide coating was produced and its oxidation behaviour was studied and compared with the bare Nb alloy.

1.4. Structure of the thesis

The outline of the thesis is as follows: Chapter 2 deals with the brief literature review on the topics directly pertinent to the present study. Details of the alloy preparation, fabrication and the experimental methods employed in the present study are given in Chapter 3. Chapter 4 deals with the effect of thermomechanical processing on the microstructure and mechanical properties. It also includes development of processing flow sheet for the fabrication of structural material of Nb alloy at low temperatures. Chapter 5 gives the detailed microstructural characterization of as-solidified, deformed and annealed samples. It involves identification of the various carbides, their stabilities, morphologies and understanding the phase formation mechanisms. Chapter 6 deals with the development of macro and microtexture during deformation and annealing. It also discusses the effect of annealing soaking time on the carbide phase stability and mechanical properties. Chapter 7 deals with the understanding the oxidation behaviour of Nb alloy and study on the silicide coating and its oxidation behaviour at higher temperatures. Finally, the main conclusions drawn are summarized in Chapter 8.

CHAPTER 2

Literature Review

This chapter deals with the literature on the four aspects of Nb alloys. The first aspect deals with the effect of thermomechanical processing on the microstructure and properties of Nb alloys as well as provides detailed account of the development of Nb-1%Zr-0.1%C alloy. Second aspect includes crystallographic, chemical composition and other details for various carbide phases observed in the Nb-Zr-C systems. The third aspect deals with the development of texture in the bcc materials during deformation and annealing treatments. Finally literature on oxidation behaviour and oxidation barrier coatings on the Nb alloy have been reviewed.

2.1. Development of Nb based alloy

Interatomic metallic bonding in niobium is extremely strong, accounting for high melting temperature, high elastic modulus, high strength and considerable hardness of Nb based materials. The strength of Nb, however, decreases substantially at temperatures above 927 °C. As a result, various approaches have been used to improve the strength of Nb at elevated temperatures. Increase in the strength to Nb based alloys by alloying addition is achieved by solid solution strengthening as well as by precipitation hardening. Alloying additions should be carefully done so that in addition to the high temperature strength, the material should also have the following properties useful from nuclear and other applications view points.

1. Adequate fabricability to form general mill products, such as sheets and tubes.

2. Good weldability.

3. High liquid metal corrosion resistance at service temperatures.

4. Low thermal neutron capture cross-section.

2.1.1. Solid solution strengthening

With moderate atomic size (r = 0.146 nm) niobium shows wide solubility range when alloyed with other elements [28, 29]. The approach in selecting the element for solid solution strengthening stems on two facts. Firstly, alloying with those elements which have larger size differences to distort the parent lattice impeding the dislocation movement. Examples of these elements are Cr, Zr, Hf, V, Os, Ir to name a few. Secondly, alloying with elements like Cr, Si, Al, which help in forming smooth oxide layer at the surface of the material. W, Mo, Ta and Re were added to improve the high temperature strength (>0.5 T_m) whereas Cr, V, Hf and Zr were added for low temperature strength. High density elements like Ir (22.65 g/cc), Os (22.6 g/cc), Re (21.03 g/cc) could not be used in structural application because of sharp increase in the density of the alloy and also because of high cost involve with these elements.

Addition of interstitial elements like C, N , B or O could not show very promising results as high diffusivity at elevated temperatures did not allow them to contribute on the solid solution strengthening whereas any small additions of interstitials degrade low temperature ductility considerably.

2.1.2. Strengthening by precipitation/dispersoids

Initial work on precipitation based strengthening by Al, Fe or Cr addition was by introducing an intermetallic phase in a controlled manner by suitably selecting a proper combination of thermo-mechanical treatment [30, 31]. These attempts met serious challenges, as their concentration if exceeds beyond a certain value introduced profuse grain boundary precipitation of Nb_3Al and $NbCr_2$ phases which caused substantial reduction in the ductility of the alloy. In addition, most of these elements brought down the liquidus temperature rather sharply making the niobium alloy system softer at higher temperatures (0.4-0.5 T_m). In addition, high solubility and diffusivity of these elements at high temperatures made microstructure of the alloy unstable. In short, these initial attempts of strengthening by precipitation were effective only up to 1000 °C and failed to improve mechanical properties of niobium based alloys beyond this temperature.

Later efforts were drawn towards obtaining strengthening by dispersoids separately or in combinations with intermetallics. Basic idea behind this approach was to select a suitable size which is large enough to make the second phase non-shearable by dislocations, the volume fraction sufficient enough to diminish Orowan loops and, in addition, particle size should remain stable at operating temperatures. In order to achieve these goals high temperature thermodynamic characteristics of various phases were explored. Diffusivity of the elements involved in the process of precipitation or dispersoids was estimated (low solubility as well as low diffusivity was the desirable property). Low surface energy with the matrix was another criterion to stabilize second phase particles at elevated temperatures. In this regard, the phase diagrams showing sufficient solubility at elevated temperatures and an intermetallic phase with Nb were studied in detail and elements which form stable borides, nitrides, carbides or oxides were also explored [32–34].

The most stable oxides, carbides and nitrides formers belong to group IVA elements (Ti, Zr, Hf and Th) and oxides of Group IIIA (Al, Y, La, Ce and Lu) and Group IIA(Ba, Sr, Mg and Ca). As oxides of Group IIIA do not dissolve in liquid or solid state of Nb based alloys, alloys containing these oxides were synthesized through powder metallurgy routes. The oxides, nitrides, borides or carbides of Group IVA have strong tendency of dissolving into the melt. These phases provide strength either by reprecipitation or by solid solution strengthening upon solidification or any heat treatment thereafter [32–35].

Detail thermodynamic analysis was carried out to study isothermal section of the ternary Nb-M_{IV} (group IV)-X (X = O, N, C, B) system which showed at least two types of possible phase diagrams [36–38]. One of those show a tendency for pseudo binary phase diagram and another mostly carbides where the formation of a pseudo binary diagram is interrupted by the formation of the Nb_2C phase. Under the later condition, two-phase equilibria occur; one between Nb and (Nb, M_{IV})C and second between NbC and M_{IV}C. For latter condition, Nb-M_{IV}C section is considered as a pseudo binary with limited solute concentration.

One of the first series of Nb alloys was strengthened by the formation of oxide phase which formed in the alloy system due to contamination during fabrication as well as during testing. Later deliberate attempts were made to add oxide particles during powder metallurgy route of fabrication. In oxygen containing alloys, an intermediate step of aging was necessary to realize the full potential of oxide dispersoids. Aging between 900-1100 °C appears to provide fine size distribution of the oxide phase which are uniformly distributed in the matrix. For example, Nb-Ti-O alloys showed $\sim$ 6 nm size of TiO_2 particles aligned along the elastically soft $\langle 100 \rangle$ directions with average separation of 35 nm among them when aged at 1000 °C. Similarly, internally oxidized Nb-1%Zr alloy showed 4-6 nm particles when aged around 1100 °C [39]. Adding zirconium to niobium greatly improves its oxygen absorption resistance by removing oxygen from the niobium solution through the formation of zirconium oxide (ZrO_2). Alloys containing such oxide precipitates with volume as high as 2% exhibited ultimate tensile strength of nearly 1 GPa. However, higher concentration of Zr leads to the rapid growth of these oxide particles resulting in substantial reduction in the strength as well as room temperature ductility. Detailed experimental results showed that the volume content of oxide particles should not exceed beyond 1% to retain the aforementioned properties of the material.

Nitride containing alloys were produced by melting in nitrogen containing plasma or by arc melting with nitride containing charges [34]. Long aging of nitride alloys showed the decomposition of the large nitride phase and redistribution of the ZrN precipitates. These nitride precipitates were coherent with matrix. Such precipitates remain highly dispersed up to 1500 °C. One of the major problems associated with these nitride precipitates was their contribution in slowing down the recrystallization process which could not be completed even after raising temperatures beyond 1500 °C [26]. Another problem associated with nitrides is that most of nitride phase equilibria appear to have eutectic or eutectoid phase reactions because of which formation of long fibers of ZrN occurs which appears to lower the rupture strength.

Among all precipitates (oxides, nitrides, borides or carbides), carbides were considered the only suitable interstitial compounds capable of not only providing precipitation strengthening but also of satisfying the above mentioned alloy properties criteria; in particular, minimal susceptibility to liquid-metal corrosion. The thermodynamic stability of various carbides in niobium was reviewed and it was concluded that NbC, ZrC, HfC, ThC_2, TaC, Ta_2C and TiC should be relatively stable in a niobium matrix up to a temperature of 1315 °C [2]. Out of these carbides HfC has high thermal neutron absorption cross-section, hence it is not desirable. Thorium carbide was also eliminated on the basis of its nuclear properties. Titanium and tantalum carbides were excluded because the addition of either titanium or tantalum to Nb-C or more complex alloys produced negligible improvement in the high temperature strength. Of this group, therefore, niobium and zirconium carbide are the most suitable precipitates. The zirconium carbide particles also enhance strength, creep strength and brittle failure resistance of the alloy by creating distortions in the crystal lattice, and therefore, making it difficult for dislocations to propagate through the lattice [40].

Delgrosso et al. [2] have studied the effect of alloying elements (Zr and C) on the mechanical properties of Nb alloys at different temperatures and developed high strength niobium alloys. They have found that in Nb-C alloys, matrix regions are relatively soft (82-93 DPH), but the carbides are extremely hard (1000-1700 DPH). Due to this the fabricability of the Nb-C alloy is poor. Addition of zirconium to the Nb-C alloy increased the hardness of matrix from 20 to 70 DPH, but significantly reduced the hardness of the carbide phase by a factor of two to three. Thus addition of Zr to Nb-C alloy, reduces difference in hardness between matrix and carbide phases as well as changes morphology of the carbide phases. This way Zr could improve the fabricability of the Nb-Zr-C alloy. At 3-4 wt.% zirconium concentration the carbide phase in Nb-Zr-C alloys did not show any significant increase in the hardness until the carbon concentration had risen to above 11,000 ppm. Hence, an alloy containing Zr less than 4 at% and C less than 4 at% appears to meet all the property requirements as mentioned above.

There are several other approaches reported in the literature to increase the strength of the Nb at elevated temperatures by solid solution strengthening and precipitation hardening mechanisms. Solid solution strengthening of Nb-based alloys with the addition of some refractory elements such as V, Ta, Mo or W has been reported [28, 29]. The results showed that Nb-Mo/W alloys have excellent strength even at temperature above 1500 °C. However, these alloys suffer from poor ductility at room temperature. To improve both high temperature strength and room temperature ductility of Nb based alloys, several two-phase alloys containing solid solution and intermetallics, for example Nb/Nb_3Al, Nb/Nb_3Ir and Nb/Nb_5Si_3 [30, 41–44] were investigated. Recently, the effect of carbon addition on the mechanical properties of Nb-/Mo-W ternary alloys was also investigated [45]. It was found that with small amount of carbon addition to the Nb-Mo-W ternary alloys both the 0.2% yield stress and the ductility increased. This was attributed to the presence of carbides, which increased the grain boundary strength and led to change the fracture mode from inter- to transgranular, thus improving the ductility of the Nb-Mo-W alloys. More recently, Nomura *et al.* [46] also investigated mechanical properties and creep behavior of Nb-Ti-C ternary alloys containing 40 at.% TiC. Their results showed that Nb-40 at.% TiC alloy exhibited a very high strength at high temperatures. Similar results have been reported for the Mo-40 at.% ZrC alloy [47]. The mechanical behavior of Nb-based alloy containing ZrC phase has also been investigated by Y.Tan *et al.* [48]. Their results indicate that the 0.2% flow stress of the Nb/ZrC alloys increases with increasing ZrC content from room to elevated temperature. However, the compressive ductility and fracture toughness decreased with increasing ZrC content. In this study they have suggested alloying Nb with Mo appears to be a promising approach to further increase the yield strength of the Nb alloy. Further they extended their work and studied high temperature behavior of Nb-Mo-ZrC. They found strength of Nb alloys increases by Mo by solid solution strengthening. Maximum solid solution strengthening effects can be achieved when the Nb/Mo ratio is around 1.

2.2. Mechanical properties of various Nb alloys

Delgrosso *et al.* [2] have prepared different Nb-Zr-C alloys and estimated their mechanical properties under different processing conditions. Table.2.1 shows the chemical composition of the alloys and their commercial names. Nomenclature of the alloys can be divided into two categories, one for binary alloys which was based on the concentration of C alloy and another for ternary which is based on the concentration of C and Zr.

Table 2.1: Chemical compositions of Nb alloys.

Alloy	Designation	Code	Composition				
			Zr (wt.%)	C (p.p.m)	O (p.p.m)	N (p.p.m)	Nb
NbC	PWC-03		nil	3000	72	91	remainder
	PWC-05		nil	5000	57	165	remainder
	PWC-09		nil	9000	170	215	remainder
Nb-Zr-C	PWC-11	Alloy A	0.87	840	240	210	remainder
		Alloy B	0.76	1050	270	135	remainder
	PWC-22		1.71	2000	110	125	remainder
	PWC-33		3.19	3600	260	230	remainder

2.2.1. Binary alloys

(i) Nb-C alloys

Table.2.2 shows mechanical properties of three binary Nb-C alloys in extruded and re-extruded conditions. It shows that the alloy containing 3000 p.p.m carbon exhibited greatest yield strength at 1315 °C in single and double extruded conditions. However, the alloy containing 9000 p.p.m carbon exhibited highest rupture strength at 1315 °C for the single extruded condition. Microstructures of all the binary alloys in single extruded condition had coarse Nb_2C carbide precipitates at the grain boundaries. When single extruded samples were re-extruded, carbides in all the alloys got refined. The Nb-0.3C exhibited the greatest carbide refinement and showed consistent improvement in the yield strength despite of the fact that it contained the smallest volume fraction of carbide precipitates. The main disadvantage of Nb-0.9C alloy is poor ductility and fabricability.

Table 2.2: Mechanical properties of Nb-C alloys in different processing conditions [2].

Tensile mechanical properties						Rupture mechanical properties				
Sample	**Condition**	**Test temperature (°C)**	**Yield strength (MPa)**	**Ultimate strength (MPa)**	**Elongation (%)**	**Stress (MPa)**	**Time to failure (hrs)**	**Elongation (%)**	**Min. creep rate (in./in./hr**	**100 hrs rupture stress (MPa)**
PWC-03	Extruded at 1760 °C (4/1)	1315	14.47	23.44	45.3	13.79	48.1	40.4	$3.4X10^{-3}$	14.47
	Re-extruded at 1760 °C (6/1)	1315	35.85	37.23	22.1	Not available				
PWC-05	Extruded at 1760 °C (4/1)	1315	19.30	23.44	32.3	13.79	360	18.3	$4.0X10^{-4}$	15.85
	Re-extruded at 1760 °C (6/1)	1315	21.37	26.89	31.8	Not available				
PWC-09	Extruded at 1760 °C (4/1)	1315	22.06	29.64	28.7	13.79	491	4.4	$7.2X10^{-5}$	20
	Re-extruded at 1760 °C (6/1)	1315	20.68	28.95	32.9	Not available				

(ii) Nb-1Zr alloy

Table. 2.3 shows mechanical properties of the Nb-1Zr alloy at different temperatures. From this table it could be observed that the solid solution strengthening provided by Zr remain effective only up to 1095 °C. Reduction in the yield strength and ultimate tensile strength beyond this temperature is due to extreme softening shown by Nb matrix, which is shown in form of large reduction in area or in high ductility. The data at 1315 °C shows that the addition of 1% Zr to Nb, the alloy strengthened to the same degree by the addition of 3000 p.p.m carbon.

Table 2.3: Mechanical properties of Nb-1Zr alloy at different temperatures [2].

Test temperature (°C)	**Yield strength (MPa)**	**Ultimate strength (MPa)**	**Elongation, %**	**Reduction in area**
Room temperature	222.7	330.94	31	88
205	106.18	200.63	29	95
425	108.24	221.32	23	92
650	124.79	248.90	18	88
870	106.18	186.15	15	82
980	103.42	255.79	23	86
1095	128.24	230.97	14	76
1205	77.91	91.70	39	99
1315	41.36	48.26	27	—

2.2.2. Ternary alloys

Mechanical properties of different Nb-Zr-C alloys (mentioned in Table.2.1) at different conditions are tabulated in Table.2.4. Mechanical properties of PWC-11, PWC-22 and PWC-33 are reviewed separately.

Table 2.4: Mechanical properties of Nb-Zr-C alloys in different processing conditions [2].

Tensile mechanical properties						**Rupture mechanical properties**				
Sample	**Condition**	**Test temperature (°C)**	**Yield strength (MPa)**	**Ultimate strength (MPa)**	**Elongation (%)**	**Stress (MPa)**	**Time to failure (hrs)**	**Elongation (%)**	**Min. creep rate (in./in./hr**	**100 hrs rupture stress (MPa)**
PWC-11 (Alloy A)	Extruded at 1593 °C (8/1)	1315	115.14	119.96	23	62.05	49.4	26.3	$4.5X10^{-4}$	51.71
	Re-extruded at 1650 °C (8/1)	Not available				62.05	23.5	39.4	$1.6X10^{-3}$	43.43
	Extruded+H.T at 1427 °C for 1 hrs	1315	108.24	113.07	28.0	Not available				
	Extruded+H.T at 1205 °C for 1 hrs	1315	125.48	128.24	30.0	62.05	133.4	21.7	$2.0X10^{-4}$	66.19
PWC-11 (Alloy B)	Extruded at 1593 °C (4/1) + Re-extruded at 1593 °C (4/1)	1315	126.17	135.82	22.0	62.05	133.4	21.7	$2.0X10^{-4}$	66.19
	Extruded+H.T at 1205 °C for 2 hrs	1315	164.78	171.67	16.3	Not available				
PWC-22	Extruded at 1650 °C (4/1)	1315	163.40	172.36	18.7	62.05	10.7	33.2	$9.3X10^{-3}$	37.92
	Extruded at 1760 °C (4/1)	1315	107.55	113.07	15.3	62.05	39.4	28.2	$1.2X10^{-3}$	51.02

…continued

Tensile mechanical properties						Rupture mechanical properties				
Sample	**Condition**	**Test temperature (°C)**	**Yield strength (MPa)**	**Ultimate strength (MPa)**	**Elongation (%)**	**Stress (MPa)**	**Time to failure (hrs)**	**Elongation (%)**	**Min. creep rate (in./in./hr**	**100 hrs rupture stress (MPa)**
PWC-33	Extruded at 1760 °C+H.T at 1205 °C for 2 hrs	1315	Not available			62.05	5.6	31.9	$1.9\text{X}10^{-2}$	32.40
	Extruded at 1760 °C (4/1)	1315	189.60	193.74	28.9	Not available				
	Re-extruded at 1700 °C (4/1	1315	158.57	179.95	17.5	62.05	409.1	27.5	$9.8\text{X}10^{-5}$	89.63
	Extruded at 1760 °C+H.T at 1205 °C for 2 hrs	1315	117.90	157.20	36.0	Not available				
	Extruded at 1760 °C+H.T at 1815 °C for 3/4 hrs	1315	224.07	238.55	25.0	Not available				

(i) PWC-11 alloy

Delgrosso *et al.* [2] have prepared two PWC-11 alloys (A and B) having little difference in composition (Table.2.1). These alloys were prepared and processed at different processing conditions. Mechanical properties of these materials were estimated at 1315 °C (shown in Table.2.4). These results show that after re-extrusion of the alloy A at 1650 °C reduced the 100 hrs rupture strength by 30%. However, double extrusion of alloy B showed good mechanical properties. PWC-11 was strongest in the latter condition.

Detailed microstructural examination of all the samples showed that the single extruded alloy A material slightly recrystallized with a polygonized substructure containing relatively fine carbide precipitation within grains as well as at subgrain boundaries. After re-extrusion, the material contained large acicular carbides which re-precipitated in a Widmanstatten pattern; an unfavorable precipitate configuration for strengthening. In addition, the structure was recrystallized for about 25%. The re-extruded alloy B did not contain acicular precipitates, but instead exhibited evidence of refinement of carbide precipitates. Little or no recrystallization had occurred in the alloy B. This provides a clue for obtaining a good elevated temperature strength. In order to fully realized the strength of the PWC-11 alloy it must be warm worked under conditions which do not cause pronounced recrystallization or, even more importantly it should induce reprecipitation of large carbide particles in the matrix phase.

When both the alloys in single extruded condition were annealed at 1427 - 1650 °C, they underwent a strength reduction at high temperatures (1315 °C). However, annealing at 1205 °C resulted in strengthening for both the alloys in both the conditions. The microstructure analysis of annealed samples showed that annealing at higher temperature $>$1427 °C resulted in the formation of acicular carbides and excessive grain growth, both of them are unfavorable for strengthening of the material. The sample heat treated at 1205 °C showed the formation fine carbides precipitates on dislocation lines and tangles. This observation has suggested that for strengthening of the alloy heat treatment should be carried out at 1205 °C.

(ii) PWC-22 alloy

The PWC-22 alloy has higher amount of Zr and C as compare to PWC-11 but the ratio Zr/C was maintained at 1.2 to facilitate its comparison with PWC-11 alloy. The main aim of the preparation of this alloy was to evaluate the influence of precipitate concentration on mechanical properties. PWC-22 alloy was extruded at 1760 °C and 1650 °C. The material extruded at 1760

°C showed lower yield strength but higher rupture strength than the material extruded at 1650 °C. Microstructural analysis provided the evidence for this change in mechanical properties. The material extruded at 1760 °C showed higher concentration of acicular carbides as compare to the material extruded material at 1650 °C. In contrast to PWC-11 the strength of PWC-22 did not increase upon annealing at 1205 °C.

(iii) PWC-33 alloy

PWC-33 alloy was prepared to produce materials having three times as many carbides particles as in the PWC-11 alloy. The Zr/C atomic ratio was maintained at 1.2, the same ratio as in the PWC-11 and PWC-22 alloy. The mechanical properties of PWC-33 at different conditions are shown in Table.2.4. The re-extruded sample at 1700 °C showed low yield strength, but exhibited a 100-hrs rupture strength at 1315 °C of 89.63 MPa. The re-extruded sample got slightly recrystallized because of which its yield strength decreased marginally. Annealing of as-extruded sample for 3-4 hrs at 1815 °C showed increase in the yield strength to 224.07 MPa. In Nb-Zr-C alloys, in this condition the sample obtained good mechanical properties. The microstructural analysis of this sample showed that it got completely recrystallized and the initial carbides were dissolved and re-precipitated as fine particles at grain boundaries as well as within the grains. In contrast, the yield strength of the as extruded sample dropped to 117 MPa after annealing at 1205 °C for 2 hrs. The annealed sample has similar microstructure as that of as-extruded sample.

The above discussion on mechanical properties of Nb-Zr-C alloys shows that when both zirconium and carbon are added to niobium, the yield strength and 100 hrs rupture strength at 1315 °C could be improved three to five fold compared to Nb-1Zr alloy. The resultant alloys are easy fabricable and have good ductility.

2.3. Formation of various carbides in different Nb alloys

Mechanical properties of Nb alloys have shown that the formation of fine, stable dispersion of carbides in the alloy can improve the high temperature properties of Nb alloys [2]. Therefore, in this section nucleation kinetics aspects of various carbides in Nb alloys are reviewed. The phase diagram of Nb-C shows that the solid solubility of carbon in niobium (Fig.1.2) decreases with decreasing temperature. It provides suitable conditions for carbide precipitation from solid solution. The carbide phases observed in binary and multi-component Nb-C alloys are listed in Table.2.5. Essentially, four types carbides are important in binary Nb-C alloys and these are Nb_2C, NbC, Nb_6C_5 and Nb_3C_2. The ϵ- phase, Nb_3C_2, is a metastable phase and found in quenched samples from high temperatures [49]. The ϵ- phase sometimes in the literature has been referred as ζ phase because its x-ray diffraction matches with the ζ phase in the Ta-C system and it was first reported by Lesser *et al.* [50].

Smith *et al.* [20] have reviewed the available data on the formation of various carbides in the Nb-C system. Table.2.5 enlists the presence of various carbides in the Nb-C system. Description of each carbide has been mentioned below:

Table 2.5: Crystal structure and lattice parameters of stable and metastable intermediate niobium carbide phases in Nb-Zr-C alloys.

Phase	**Composition (at.% C)**	**Pearson symbol)**	**Space group**	**Prototype**	**Lattice structure**	**Lattice parameters (nm)**			**Atom Positions**	**References**
						a	b	c		
Nb	0	cI2	Im3m	W	bcc	0.3307				[20, 51]
β-Nb$_2$C	$\sim$ 28 - 33.3	hP9	P-31m	ϵ-Fe$_2$N ϵ-W$_2$C	Trigonal	0.5407	0.5407	0.4968	6Nb in 6(k) with x$\sim$1/3, z$\sim$1/4 2C in 2(d) 1C in 1(a)	[20, 22]
γ-Nb$_2$C	$\sim$ 32 - 33.3	hP3	P6$_3$/mmc	β-W$_2$C β-Mo$_2$C	Hexagonal	0.3120	0.3120	0.4950	2Nb in 2(c) 1C in 2(a) randomly distributed	[20, 22]
α-Nb$_2$C										
(1)	$\sim$ 32 - 33.3		Pbcn		Orthorhombic	0.4966	0.624	0.540	8Nb in 8d with x$\sim$1/4, y$\sim$1/8, z$\sim$1/12 4C in 4c with y$\sim$3/8 Vacancies in 4c with y$\sim$7/8	[22]
(2)	$\sim$ 32 - 33.3		Pnma (D$_2h^1$6)		Orthorhombic	1.0900	0.4974	0.3090	4Nb in 4(c) with x$\sim$ 1/24, z$\sim$3/4 4T in 4(c) with x$\sim$5/24, z$\sim$1/4 4C in 4(c) with x$\sim$3/8, z$\sim$0	[20, 22]
(3)	$\sim$ 32 - 33.3		Pbcn		Orthorhombic	1.0890	1.2360	0.4966		[20]
(4)	$\sim$ 32 - 33.3	oP12	Pmc2$_1$		Orthorhombic	1.0920	0.4974	0.3090		[51]
(5)	$\sim$ 32 - 33.3		Pbcn		Orthorhombic	0.5382	0.3135	0.4966		[20]
Nb$_4$C$_3$	$\sim$ 40	hR20	R-3m	V$_4$C$_3$	Hexagonal	0.3140	0.3140	3.010	6Nb in 6(c) with z$\sim$3/24 6Nb in 6(c) with z$\sim$7/24 6C in 6(c) with z$\sim$10/24 3C in 3(a) 3C in 3(b)	[20–22]
Nb$_6$C$_5$	$\sim$ 45.5		C2/m	V$_6$C$_5$	Monoclinic	0.5460 β-109.471°	0.9458	0.5460		[20]
		hP32	P31	V$_6$C$_5$	Trigonal	0.5464	0.564	1.5422	see ref.[52]	[52]

…continued

Phase	**Composition (at.% C)**	**Pearson symbol)**	**Space group**	**Prototype**	**Lattice structure**	**Lattice parameters (nm)**			**Atom Positions**	**References**
						a	b	c		
Nb_3C_2					Hexagonal	1.1460		1.8300		[20, 23, 51]
NbC	~ 50	cF8	Fm-3m	NaCl	fcc	0.4471			4Nb in 4(a) 4C in 4(b)	[20, 22, 51]
C	100	hp4	$P6_3/mmc$	C (Graphite)		0.2461		0.6707		[20]

Nb_2C:

The Nb_2C phase can form directly from the liquid phase as well as through a solid state reaction in the Nb-C system. The Nb_2C phase was first reported by Brauer *et al.* [53]. It exists at least in three polymorphic forms [54]: γ-Nb_2C with disordered hexagonal structure forms above 2500 °C, β-Nb_2C with ordered hexagonal structure presents in the temperature range of 1200 - 2500 °C and α-Nb_2C with orthorhombic structure at temperature 1200 °C and below. Crystallographic details of these phases are provided in Table.2.5.

Vishwanadham *et al.* [55] have studied the formation of Nb_2C carbide phase during the aging of supersaturated Nb-0.3 at.% C alloy at 400 to 800 °C. They have found that precipitation in the Nb-C system is a multi-stage process. The initial precipitate has bcc structure with lattice parameters very near to those of the niobium matrix. It was coherent with the matrix, with 310 habit plane. With increasing aging time precipitates transformed to hexagonal Nb_2C carbide. This carbide is incoherent with the matrix. These carbides had specific orientation relationship with the matrix: $(0001)_{Nb_2C} // (011)\,,\, [11\bar{2}0]_{Nb_2C} // [11\bar{1}]_{Nb}$.

Nb_4C_3 and Nb_3C_2:

Brauer *et al.* [53] have found the presence of weak reflections in x-ray diffraction patterns (XRD) persisting through the composition range 34.8 - 40.0 at.% C. This reflection was extraneous to both the Nb_2C and NbC patterns. On the basis of this observation they postulated the existence of a ζ phase intermediate between Nb_2C and NbC analogous to the ζ phase in the Ta-C and V-C systems. Yvon *et al.* [21] have reported that the Nb_4C_3 phase is isostructural with Ta_4C_3 and V_4C_3, which have actual stoichiometry near to Ta_3C_2 and V_3C_2. Crane *et al.* [23] have studied microstructure evolutions in Nb-3.1 at.%C system. The Nb alloy was prepared by electron beam melting and homogenized for 0.5 hrs at 2100 °C and quenched in liquid tin. The carbide phase which has been formed in the alloy was extracted by phase extraction technique. Composition analysis has shown that the carbide phase has 40 at.% C. X-ray diffraction pattern from this separated precipitate showed that many XRD peaks were matching with the Nb_4C_3 phase proposed by Yvon *et al.* [21]. However, there were additional lines present in the X-ray diffraction pattern, which remain unindexed indicating that the structure determination was incomplete. Crane *et al.* [23] have reanalyzed the x-ray diffraction pattern and showed that the XRD pattern matched better with the Nb_3C_2 with hexagonal phase having lattice parameter a = 1.146, c = 1.830 nm.

NbC and Nb_6C_5:

According to the Nb-C phase diagram, monocarbide (NbC) exists in the composition range of 41 - 51 at.% C. It has the fcc - NaCl-type structure. It was first prepared by Freiderich *et al.* [56] who observed melting point of NbC as 3375 °C. The high purity material showed the congruent melting point at 3600 ± 20 °C at a composition near 45 at.% C.

At lower temperatures C atoms tend to develop long range order. The ordering temperature depend upon composition changes and maximum in the range of 1025 °C to 1082 °C. The ideal stoichiometry of ordered phase is Nb_6C_5. It has monoclinic structure with a = c = 0.54605 nm, b = 0.94579 nm, $\alpha = \gamma = 90\,^\circ$ and $\beta = 109.471^\circ$.

2.3.1. Effect of thermomechanical processing on carbide phase stability

Ostermann has carried out detailed study on the carbide phase transformations in Nb-10W-1Zr-0.1C alloy [19]. The commercial name of this alloy is D-43. Table.2.6 shows the heat treatments of the sample and the carbide phases present in the samples. It shows that the rapidly cooled samples (quenched in tin) contain Nb_3C_2 carbide phase and the furnace cooled samples have a mixture of Nb_3C_2 and β-Nb_2C phases. Quenched samples were further heat treated at different temperatures and their microstructure characterization revealed that Nb_3C_2 remained stable up to 800 °C but transformed to Nb_2C at higher temperatures. Continued annealing of the rapidly cooled samples at 1200 °C for 41 hrs eventually produced MC carbide phase. Metallographic evidences seem to suggest that subsequently the driving force for NbC precipitation is too small to permit general nucleation throughout the alloy matrix, at least at low aging temperatures (around 1200 °C). The equilibrium monocarbide tends to precipitate instead in the volume surrounding the metastable Nb_3C_2 platelets or needles. This precipitation behaviour has been interpreted as being due to the availability of carbon from the decomposing metastable phases [57]. A second mechanism for the formation of NbC phase is in-situ transformation of the metastable phases as indicated by the apparent fragmentation of the long, thin M_3C_2 particles [57, 58]. This apparent fragmentation may, however, simply be the result of preferred nucleation of MC at the metastable carbide/matrix interface. Spectroscopic analysis of the sample containing Nb-W-Zr-C showed that the MC has equal amounts Nb and Zr and no tungsten was found in the carbide phase [19]. The preferred nucleation of MC phases on dislocations have led to the development of thermomechanical treatments to achieve optimum strengthening at intermediate and high temperatures. Keeping this in view Ostermann [19, 49] has studied the

Table 2.6: Precipitation reactions in D-43 (Nb-10W-1Zr-0.1C) alloy [19].

Heat treatment		Phases
Solution anneal		M(ss)
Cooling to room temperature		
	$\sim$ 0.334 °C/hrs	M(SS) $\longrightarrow$ M' + M_2C
	$\sim$ 6.667 °C/hrs	M(SS) $\longrightarrow$ M' + M_3C_2 + M_2C
	$\sim$ 66.667 °C/hrs	M(SS) $\longrightarrow$ M' + M_3C_2
Precipitation anneal (aging)	at 1100 - 1400 °C	M' + M_3C_2 + M_2C $\longrightarrow$ M + MC

M(ss) = homogeneous solid solution
M' = solid solution in metastable equilibrium with M_2C and M_3C_2
M = solid solution in equilibrium with stable monocarbide, MC

effect of thermomechanical treatment on the carbide distribution in D-43 alloy. The alloy was solution annealed at 1900 °C furnace cooled to room temperature, cold rolled to a reduction in thickness of 25%, and aged at 1200 °C for 41 hrs. This alloy showed uniform distribution of NbC carbide precipitates except at the vicinity needles or platelets of Nb_3C_2, which have fragmented in the process of transformation to equilibrium MC phase.

2.3.2. Effect of alloying elements on carbide phase stability

Thermomechanical treatments may not always be practical methods for achieving optimum carbide dispersions in niobium-base alloys, and it is therefore necessary to consider alloy development as an alternate possibility. It has been reported that for the formation of the NbC cubic carbide phase addition of a reactive metal like Ti,Zr or Hf is required. Therefore majority of the research remained focused on alloying effects of these elements, which remained the principal metallic constituents of niobium alloys. Fig.2.1 shows the ternary phase diagram of Nb-Zr-C system at 1300 °C. Fig.2.1 shows that most of the niobium-base alloy compositions lie in the two-phase field (M(ss) + MC), close to the niobium-rich corner. It has been pointed out that excessive solid solution addition of the Group IVa elements has adverse effect on the creep-rupture properties of niobium. Thus, limiting the concentration of those necessary for achieving the M(ss) + MC equilibrium. Lower concentrations on the other hand will permit the presence of coarse M_2C particles, which have deleterious effect on ductility and are of little use for strength. The Fig.2.1 shows that the lines in the phase diagram emanating from the Nb-rich corner show that addition of a few at.% of Hf, Zr or Ti can change the composition of the MC phase considerably in the direction of increased IVa-metal content, which should give higher MC-phase stability and lower carbon solubility in the matrix phase.

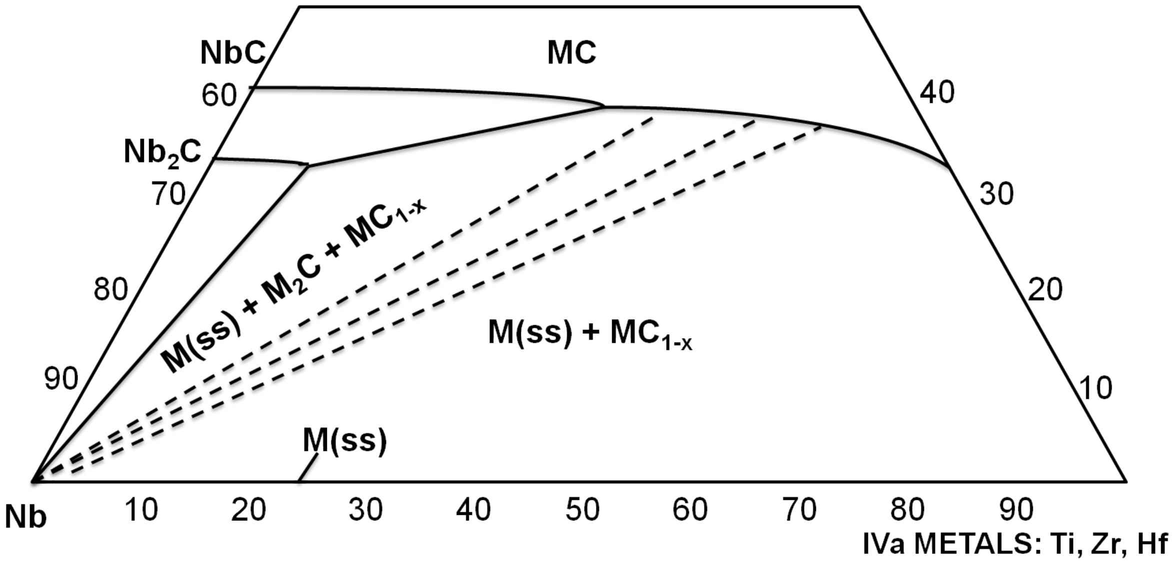

Figure 2.1: Schematic illustration of the ternary phase diagram of Nb-(Ti,Zr,Hf)-C system at around 1300 °C temperature [19].

To determine whether this additional driving force for MC formation and the increased precipitation kinetics due to higher Zr content would lead to a more general MC phase precipitation. Ostermann [19] has prepared several compositions of Nb-10W-0.1C with zirconium additions ranging from 5 to 15 at.%. The samples were heat treated and their microstructures were evaluated metallographically. The main conclusion from these experiments is that MC precipitation is still largely controlled by the metastable carbide phases and probably depends on the supply of carbon during their decomposition. The work of Williams *et al.* [58] on Nb-Hf-C alloys have also shown that adjustment of the content of Group IVa metals does not by itself improve the uniformity of carbide dispersions.

Y. Tan *et al.* [48] have studied the effect of alloying elements on the microstructure of Nb-Zr-C ternary alloys. The microstructure of the Nb-Zr-C alloy after annealing at 1800 °C for 24 hrs consists of Nb solid solution and MC type of carbide phase. The carbide was identified as (Zr,Nb)C. Two distinct morphologies of the carbide (MC) have been reported in the stoichiometric Nb/ZrC alloys: (i) For alloys containing less than 30 at.% ZrC, the microstructure consists of mixed Nb solid solution as the matrix phase and uniformly distributed (Zr, Nb)C and (ii) in the case of ZrC higher than 40 at.%, the microstructure consists of carbide dendrites as the matrix phase and Nb solid solution.

Nb based alloys are generally prepared by electron beam melting. The microstructure of the as-solidified samples have structural inhomogeneity, lamellar form of the carbides and thermal stresses (stresses resulting from the decomposition of the solid solution in the process of cooling of the ingot). Such microstructures having lamellar carbides, chemical inhomogeneities and stresses, are not good for mechanical properties of the alloys. Due to these unfavourable microstructures, under as-solidified condition, Nb alloys show low ductility. If the alloys are deformed at lower temperatures, they undergo brittle fracture. Hence as-solidified samples have to be deformed at higher temperatures (1500-1700 °C). After deformation also the products may have several defects. In order to avoid this, Filipleva *et al.* [59] have found the best heat treatment to decrease the strength of the as-solidified material so that they can be easily deformed. They heat treated VN3-(4.7-5.2% Mo, 1.3-1.6% Zr, 0.1-0.16% C) and VN4-(9-10.2%Mo, 1.5%Zr, 0.25-0.3%C, and 0.01% Ce) from 1000 - 2000 °C. In these alloys two types of carbides have been found, one with lamellar carbide-Nb_2C (a = 0.31 nm,, c= 0.49 nm) (size 0.006-0.020 mm long and 2-3.5.10-4 mm thick) and second with spherical morphology carbides - NbC (a=0.448 nm) (size- 4-7.10-4 mm). Annealing between 1300-1400 °C resulted in the uniform precipitation of second phase throughout the grains, except in few cases, where preferential precipitation was observed in a narrow region as well at grains boundaries. The carbides precipitated as a result of annealing showed spherical morphology, with size in the range of 300-400 nm. The lamellar carbide which was not stable at this temperature dissolved back into solution. The annealing ensured precipitation of all the excess carbon from the solid solution in the form of spherical carbides, relaxation of thermal stresses resulting in an increase in the ductility and softening of the alloy.

2.4. Studies on Nb-Zr-C alloys

T.L. Grobstein *et al.* [60]. have carried out microstructural characterization of precipitates in a Nb-1%Zr-0.063%C alloy in different conditions (as-rolled, annealed condition and after high temperature exposure at 1077 - 1127 °C for 5000 hrs with and without an applied stress). Material in the as-rolled condition showed mostly Nb_2C and a very minor phase with NbC which was nearly free from Zr. The rolled sample was annealed for 1 hr at 1482 °C and then 2 hrs at 1202 °C. The annealed sample showed the presence of both Nb_2C and NbC phases in the Nb matrix. These annealed samples were subsequently exposed up to a duration longer than 100 hrs with and without applied load at 1102 °C. Microstructure analysis of these samples showed that it has single (Nb,Zr)C phase with Zr/Nb ratio close to 2.3. The carbide precipitates were coarsening slightly after 5000 hrs exposure without applied stress whereas the same material exposed for 5000 hrs with applied stress showed decrease in the size and in the inter particle spacing between particles. Lyuti *et al.* [61] have carried out similar experiments and they found increase in the average size of the particles from 86 to 133 nm upon aging for 5000 hr at 1102 °C. The inter particle spacing also increased from 390 to 450 nm. Exposure at this temperature for 10000 hrs resulted in a particles size of 150 nm and an inter particle spacing of 450 nm. Lyuti *et al.* [61] have reported virtually no difference when a stress of 15 MPa was applied. These studies showed that high temperature exposure with and without load introduce marginal changes in the precipitates size but the composition and morphology of the (Nb,Zr)C precipitates remained nearly unaltered. It indicates that the (Nb,Zr)C particles are stable at high temperatures.

Mehmet Uz *et al.* [62] have carried out the effect of thermomechanical processing on the microstructure of the Nb-1%Zr-0.1%C alloy. They have worked mainly on as-solidified, extruded (at 1627 - 1277 °C) and annealed samples. The as-solidified microstructures have coarse grain (up to 500 microns) size with coarse (>1 μm) intra and intergranular Nb_2C (orthorhombic) precipitates. After extrusion the resulted microstructure showed that it had predominant presence of the Nb_2C phase and a small amount of (Zr,Nb)C phase and all the precipitates were aligned along the extrusion direction. The extruded samples at 1627 °C and 1277 °C had Vicker's hardness of 131 ± 5 and 108 ± 5, respectively. The high temperature extruded samples showed higher hardness than those extruded at low temperatures. The high temperature extruded samples had higher volume fraction of finer precipitates of (Nb,Zr)C than low temperature extruded sample. It was attributed to higher solid solubility of C at 1627 °C than at 1277 °C. This would lead to dissolution and subsequent re-precipitation of carbides during the high temperature processing. The extruded samples were double annealed at 1482 °C for 1 hrs and then 1202 °C for 2 hrs. Microstructure of double annealed samples had equiaxed grains (size $\sim$ 25 to 30 μm) and finely distributed precipitates which were mostly 1 μm in size with a few about 5 μm. Again, the precipitates were identified as Nb_2C and (Zr,Nb)C in all the samples with no significant change in the Zr/Nb ratio upon double annealing. Vicker's hardness of the annealed sample was 90 ± 5 VHN. These results are similar to the results of Uz *et al.* [62]. They have fabricated Nb-1Zr-0.1C sheet by cold rolling a sheet bar following triple 4:1 extrusion at 1627 °C. This sheet had a VHN of about 158 ± 7 in the as-rolled condition with about 60% cold work, and 104 ± 5 after double annealing heat treatment. In the double annealed condition, its grain had an average diameter of 32 ± 3 μm. Mehmet Uz *et al.* [63] have also studied the effect of number of extrusion steps following with varying annealing temperature on the microstructure of Nb-1%Zr-0.1%C alloy. It has been found that with increasing the number extrusion steps the Zr/Nb ratio increased. Similarly, with increasing first and second step annealing temperature in the the double annealing treatment, Zr/Nb ratio increased but reduction in grain size was observed. It is due to the increase in the volume fraction (Nb,Zr)C phase.

Mehmet *et al.* [16] have shown that Nb-0.9 wt.%Zr - 0.06 wt.%C in the rolled, double annealed and aged condition, predominantly consists of relatively coarse (>1 μm) orthorhombic carbides of Nb_2C. Upon prolonged exposure of the material to high temperature with or without applied stress gives rise to the conversion of Nb_2C particles to fine fcc carbides of Nb and Zr. It was noticed that the precipitates were distributed throughout its matrix as well as along the grain boundaries. The lattice parameters of the cubic carbides were determined to vary from 0.458 to 0.465 nm as the Zr/Nb ratio varied from 38/62 to 75/25.

Changes in the phase composition and morphology of the carbide precipitates when the alloy is maintained under stress for long periods at high temperatures may lead to changes in its mechanical properties. Therefore, several researchers have investigated the possible structural and morphological changes in the precipitates in Nb alloy during prolonged stressing at high temperatures. Maksimovich *et al.* [61, 64–66] have carried out these experiments on recrystallized sample with load (49 MPa) and without load at 900 °C and 1100 °C in a high vacuum atmosphere for a period of 10,000 hrs. After recrystallization at 1400 °C for 2 hrs, the alloy contained primarily Nb_2C with an orthorhombic lattice and a small quantity of NbC carbides with an fcc lattice. After prolonged holding at 900 and 1100 °C, the volume fraction of NbC carbides is increased. It also showed that with increasing temperature and time, the size of the carbide particles increased. it is attributed to the acceleration of the dissolution of fine particles and the growth of carbides due to diffusion of atoms of alloying elements into the matrix. These results also showed that maximum growth was in the first 100 hrs of aging time. The possible reasons for such behaviour are; (1) high dispersity of the precipitates in the original condition leads to high solubility of the finer particles; (2) particles growth occurs at a higher rate by diffusional transfer of carbon and zirconium atoms from the dissolving fine particles to the larger particles; (3) with increasing holding time (up to 1000 hrs or more) at 900 °C the consumption of fine particles by large particles practically ceases. It was noticed that the rate of increase in the particles size under loading condition is lower than without loading condition. The reason for this could be due to the generation of dislocations under loading condition. Dislocations acts as a favorable sites for the accumulation of dispersed precipitates. These retard the movement of alloying element atoms, particularly finely dispersed particles, so that the growth of coarse particles is impeded. These studies showed that under load after 100 hrs of exposure at high temperatures the NbC particles scarcely undergo any change in size, morphology and composition. From this data it can be concluded that the Nb-1Zr-0.1C alloy is thermally stable, and so this material can be used up to 1100 °C.

2.5. Development of texture during deformation and annealing

Crystallographic texture (a non uniform distribution of crystal orientations in the aggregate) in a material plays a vital role in improving the formability and mechanical properties of a material [24]. The generated crystallographic texture mainly depends on the crystal structure, starting texture, microstructural constituents like grain size, type of precipitates, phases and their sizes and most importantly on prior deformation texture of the material [67, 68]. Therefore, it is necessary to study texture developments during deformation and annealing of a material. In order to understand the deformation and annealing texture, it is necessary to understand the terminology and the presentation methods of texture. This section therefore, provides a brief account of the methods to understand the texture.

For any material, crystal orientation is expressed with the help of Miller indices, which is written as: (hkl) $[uvw]$. This means that a plane (hkl) is parallel with the rolling plane and the direction $[uvw]$ is parallel with the rolling direction (RD). Fig.2.2 shows an example of cubic crystal orientation (001) $[1\bar{1}0]$. In general, orientations of grains in a sample are represented in pole figures and inverse pole figures. In pole figure, the crystallographic directions of each grain are plotted on the stereogram with respect to sample direction (Fig. 2.3(a)) . Fig.2.3(b & C) shows the construction of (100) pole figure. Pole figures are suitable for representing the texture data for the rolled samples. For wires or other samples with axial symmetry, inverse pole figures are more appropriate for representing texture. In inverse pole figure, orientation distribution of a sample axis is plotted on a stereogram with respect to crystallographic orientation. Fig.2.4 shows IPF for cubic system where distribution of sample direction [001] or ND axis on the unit triangle of the standard stereographic projection is shown. A detailed review on the texture representation including pole figures, inverse pole figures and Euler angles can be found in the reference [68]. It is possible to describe the complete texture information of the sample by defining orientation distribution function (ODF). ODF is the volume fraction of grains with

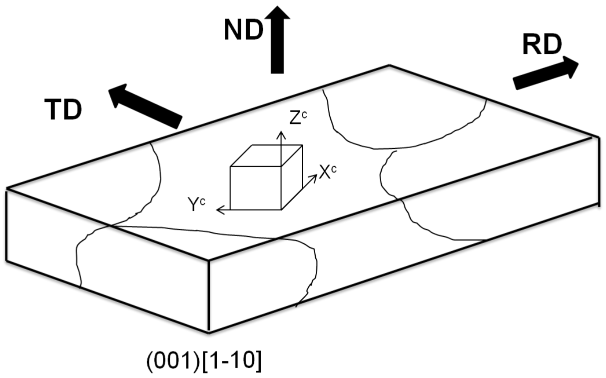

Figure 2.2: Representation of a cubic crystal orientation $(001)\,[1\bar{1}0]$ in a sample [68].

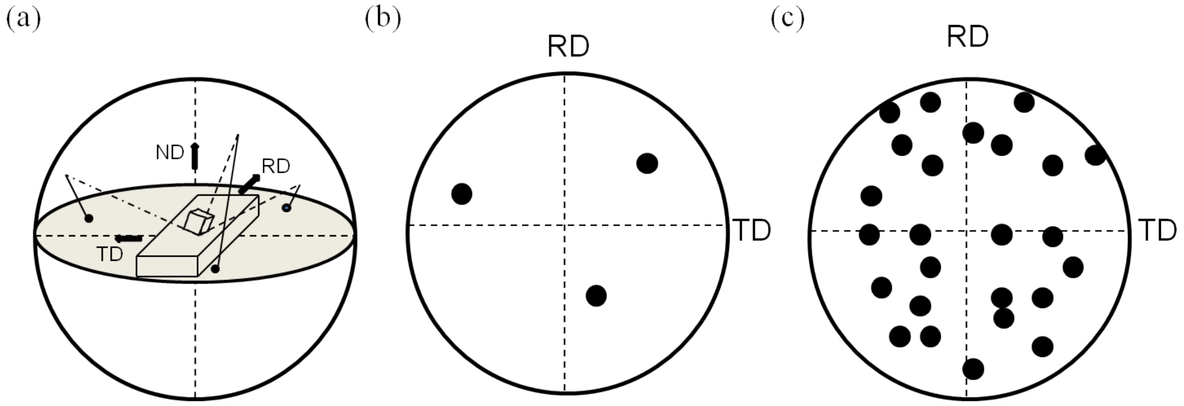

Figure 2.3: Construction of a (100) pole figure (a) Stereographic projection of the (100) poles, (b) projection of the (100) poles of one grain on the equatorial plane and (c) projection of the (100) poles of a polycrystal [68].

certain orientation (g) and it can also be defined as a probability density function of orientations (f(g)). If dV is a volume of a crystal element i.e. crystallites, which possess orientations in the range dg and V is the total volume of a sample consisting of all crystallites then the orientation distribution function f(g) is defined as:

$$\frac{dV}{V} = f\,(g)\,dg \tag{2.1}$$

The integral of the ODF over all possible orientations should be equal to 1. The ODF of a sample without texture is a constant. If the sample has a texture, the ODF would show maxima and minima. In order to give a graphical representation of an ODF, Euler angles (ϕ_1, ϕ, ϕ_2) [68] are used to define the orientation ’g’ of a grain. The Euler angles describe the transition from the sample’s reference frame into the crystallographic reference frame of each individual grain of the polycrystal. When the three Euler angles are plotted in Cartesian coordinates, it is called Euler space. Euler space is shown in Fig.2.5(a). This space is limited for ϕ_1 and ϕ_2 between

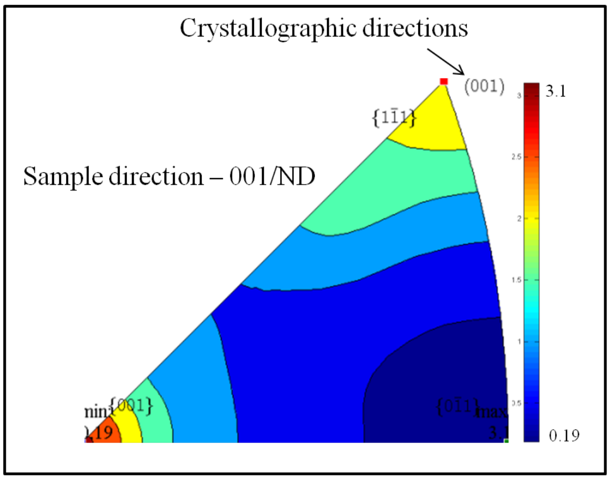

Figure 2.4: Example of the inverse pole figure for cubic system (distribution of (001)/ND sample axis on the unit triangle of the standard stereographic projection).

0° and 360°, and for ϕ between 0° and 180°. Each crystal orientation can be represented in this Euler space. In general, for easy understanding, ODF's are not represented in the 3D Euler space, they are represented in the 2D sections of the euler space (Fig.2.5(b)). For bcc materials, ϕ_2-45° section (Fig.2.5(b)) is important in the 3D euler space, as in this section, the presence of two important α and γ-fibres are shown in Fig.2.5(b).

Typical texture of a bcc material consists of two fibers: α and γ-fibers. The α-fiber consists of those grains which have one of $\langle 110 \rangle$ axes lying in Euler space parallel to the RD. The most important components of α-fiber are traditionally indicated with the letters A, B, C and D as indicated in Fig. 2.5(b). The γ-fiber contains orientations with a $\{111\}$ plane parallel to the rolling plane (or a $\langle 111 \rangle$ direction parallel with the rolling plane normal). The most important components of the γ-fiber are indicated with D, E, F and G (indicated in Fig.2.5). D is thus the cross point of both the fibers.

Among bcc materials, majority of literature pertains to the texture evolutions in steels. The complete ODF of low-carbon steel is shown in Fig.2.6, with constant ϕ_1 sections and ϕ_2-45° section. It shows the presence of α and γ-fiber texture in the cold rolled steel samples. Cold-drawn bcc materials have in general a simple $\langle 110 \rangle$ fiber texture. This texture is, for example, found in cold-drawn pearlitic wire or in drawn W-wire (Fig.2.7).

When a cold deformed material is annealed, the fresh nucleated grains show preferential arrangement along certain directions which lead to the development of annealing texture. During annealing, in deformed samples, if each deformed grain acts as nucleus for recrystallization, then the recrystallized material will show the same texture as shown by deformed samples.

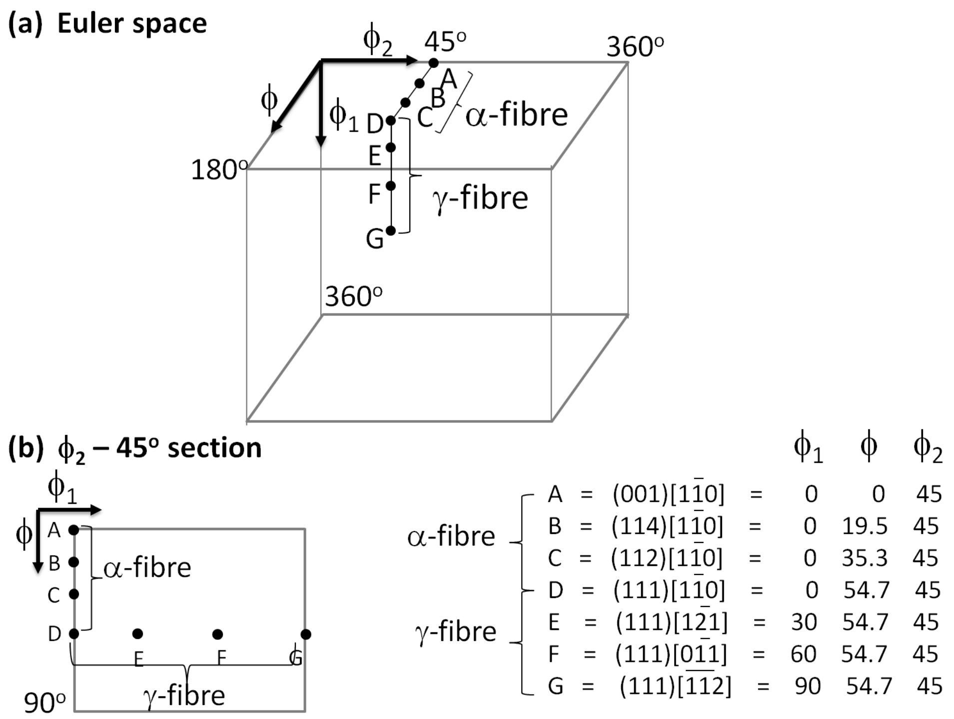

			ϕ_1	ϕ	ϕ_2
α-fibre	A	$(001)[1\bar{1}0]$	0	0	45
	B	$(114)[1\bar{1}0]$	0	19.5	45
	C	$(112)[1\bar{1}0]$	0	35.3	45
	D	$(111)[1\bar{1}0]$	0	54.7	45
γ-fibre	E	$(111)[1\bar{2}1]$	30	54.7	45
	F	$(111)[0\bar{1}1]$	60	54.7	45
	G	$(111)[\overline{11}2]$	90	54.7	45

Figure 2.5: (a) Euler space showing representation of crystallographic orientations (A, B, C, D, E, F, G) present in the α and γ-fibers with Euler angles and (b) ϕ_2 45° section showing the orientations present in the α and γ-fibers.

However, in general, texture evolved during recrystallization is different from the deformed texture. The reason for generating different annealing textures is the preference for some deformed grains to act as recrystallization nuclei. This is called oriented nucleation. In addition, in some cases, few of the grains grow faster than the other grains and it develops texture in the material. This is called oriented growth. The growth of a grain depends strongly on the type of boundaries surrounding it. The grains which have high angle grain boundaries, will have higher growth in comparison to the grains which have low angle grain boundaries. Due to oriented nucleation and oriented growth, material will have a recrystallization texture different from the deformation texture.

Fig.2.8 shows statistical distribution of various texture components in deformed and annealed steel samples. During deformation, the volume fraction of the α-fiber is higher than the γ-fiber. However, after recrystallization, texture got reversed, i.e., volume fraction γ-fiber is higher than the α-fiber. The recrystallized grains are having mainly of E and D orientations. This type of orientation are the consequences of oriented nucleation in generating recrystallization texture. Because of high stored energy, the deformed grains belonging to the γ-fiber

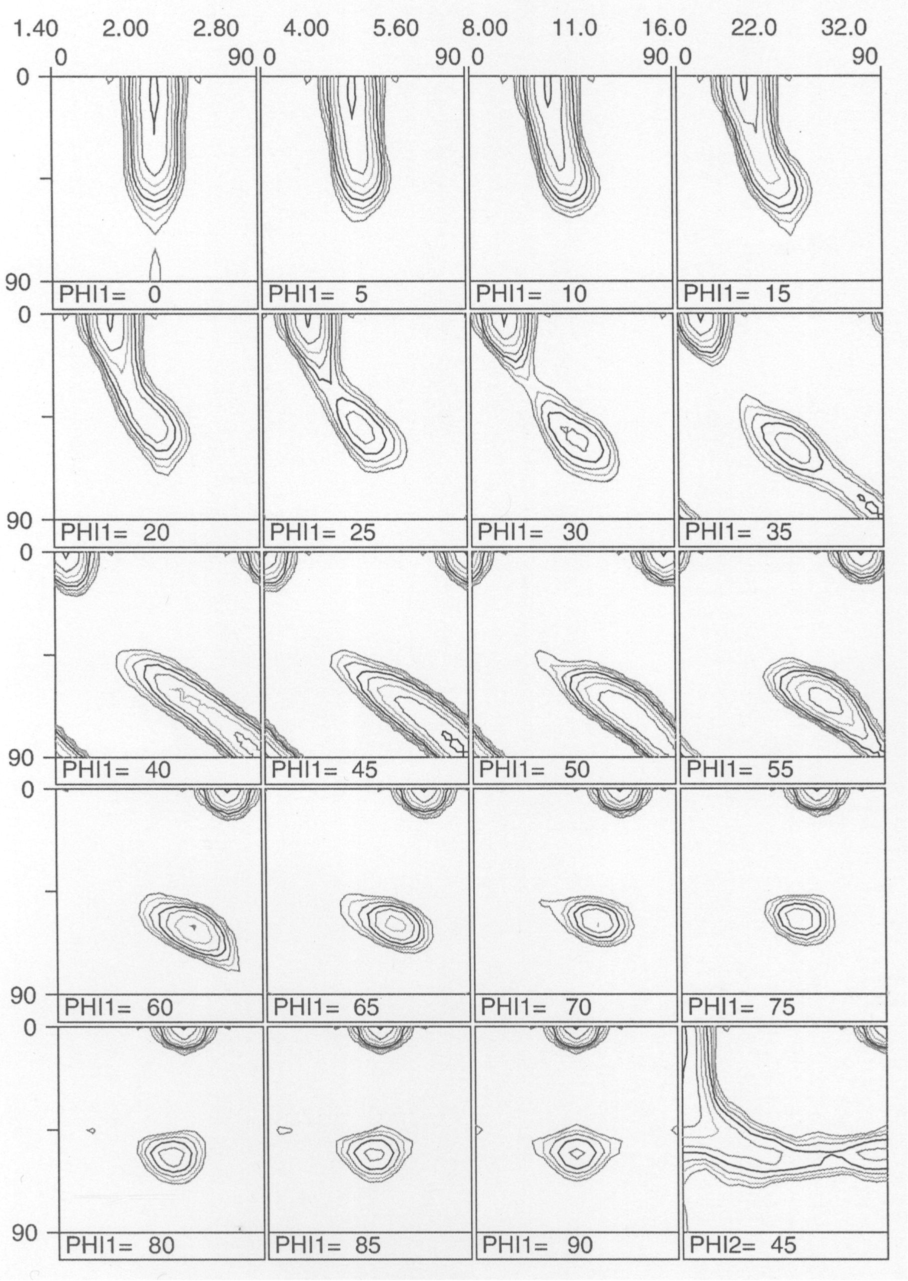

Figure 2.6: ODF (ϕ_1 sections and a ϕ_2 45°section) of an IF steel after hot and cold rolling showing the α and γ-fiber contour levels from 1.4 - 32 [68].

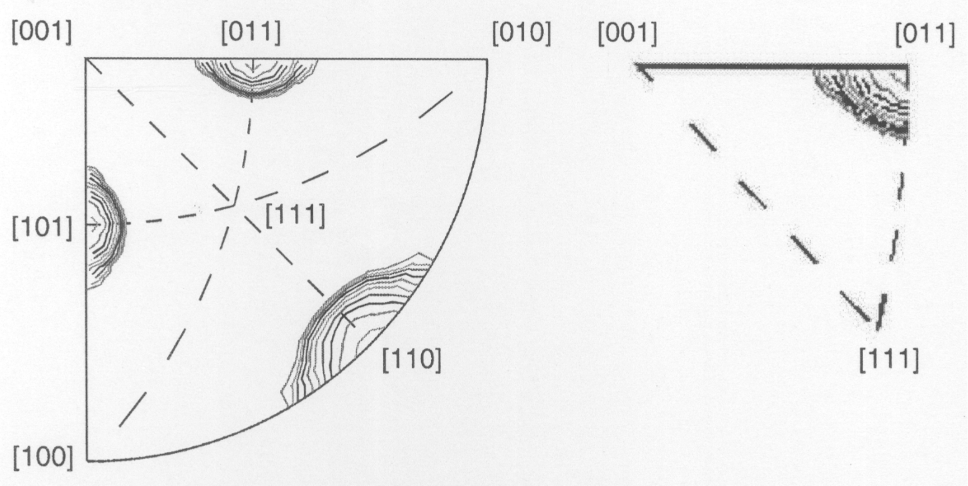

Figure 2.7: $\langle 110\rangle$ Fiber texture in a drawn W-wire in the $[100]\,[010]\,[001]$ quadrant and in a simple unit triangle (contour levels: 1.6, 2.0, 2.5, 3.2, 4.0, 5.0, 6.4, 8.0, 10, 13) [68].

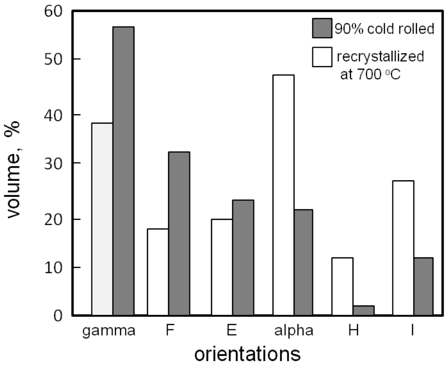

Figure 2.8: Main texture components of IF steel sheet after cold rolling and after recrystallization [68].

E-$\{111\}\,\langle 1\bar{2}1\rangle$ and D-$\{111\}\,\langle 1\bar{1}0\rangle$ recrystallize first. Deformed grains of the α-fiber go through a long period of recovery and start recrystallizing at the end of the recrystallization process. In the mean time, part of them have already been consumed by the growing γ-fiber grains. This results in high volume fraction of γ-grains in the recrystallized sample.

2.5.1. Texture development in bcc based materials

The macrotexture of various bcc metals are summarized in the Table.2.7 [24, 69–72]. Raabe et al. [69] have reviewed rolling and annealing textures of various bcc metals. They have divided bcc materials into two main groups. The first group comprises pure bcc metals (low carbon steel, Ta, Nb, Mo and W) and dilute alloys. The second group includes high alloyed bcc transition metals (steels with 10 -17 % Cr and with 3% Si). It has been shown that the cold rolling texture of all bcc materials have two common features: the formation of a strong but incomplete α-fiber between $\{001\}\langle110\rangle$ and $\{111\}\langle110\rangle$ and the increase in the γ-fibre texture with deformation. For low carbon steels, for deformation <70%, $\{001\}\langle110\rangle$ and $\{112\}\langle110\rangle$ are the dominant components in the α-fiber and a weak preference for $\{111\}\langle112\rangle$ component in the γ-fiber. For deformation $\geq$ 70%, the maximum on the α-fibre shifted to $\{112\}\langle110\rangle$ and for the γ-fiber it shifted from $\{111\}\langle112\rangle$ to $\{111\}\langle110\rangle$. In the case of second group materials, it is observed that strong texture gradient develops from surface to the center. At the center, in the α-fiber increase in $\{001\}\langle110\rangle$ and $\{112\}\langle110\rangle$ and in the γ-fiber strong $\{111\}\langle110\rangle$ component are observed. At the surface, strong $\{001\}\langle110\rangle$ and $\{111\}\langle112\rangle$ components in α and γ-fibers are observed, respectively. The reason for the formation of texture gradient in second group materials is the presence of inhomogeneous microstructure and preference of texture in the predeformed materials (these materials were hot worked prior to room temperature deformation) .

The deformed samples were annealed at homologous temperature ($T/T_m \sim 0.4$). Annealed texture of all the samples were analyzed. It showed orientation density of the α-fiber between $\{001\}\langle110\rangle$ and $\{112\}\langle110\rangle$, especially the strong rolling component $\{112\}\langle110\rangle$, decreased nearly to unity. In the γ-fiber, particularly $\{111\}\langle112\rangle$ is increased. This change in texture is further interpreted using oriented nucleation and oriented growth. They have showed oriented growth plays a major role in the formation of recrystallization texture. The reason for the oriented growth is both the components $\{112\}\langle110\rangle$ and $\{111\}\langle112\rangle$ are related by 32° rotation about a common $\langle110\rangle$ axis, which, according to the lbe and Lucke, is close to a higher growth rate relationship. Therefore, growth of $\{111\}\langle112\rangle$ into $\{112\}\langle110\rangle$ is strongly preferred.

The deformed samples annealed at low temperatures (T/T_m <0.4) resulted increase in $\{001\}\langle110\rangle$ texture component in α-fiber. The $\{001\}\langle110\rangle$ possesses the absolute lowest Taylor factor (ratio of macroscopic stress (σ) to microscopic shear stress (τ) [73]) means they have small energy content. The low energy content grains (low Taylor factor) grains tend to recover, whereas those with high Taylor factor (high energy content) grains tend to recrystallize. At lower annealing temperature, activation energy for grain boundary motion is higher than for dislocation motion. Therefore, material undergoes recovery, and hence, it leads to enhancement of $\{001\}\langle110\rangle$ texture.

The texture development in the second group annealed materials revealed the same features as in first group materials. In addition, it showed strong texture gradient. It is due to the inhomogeneous microstructure present in the deformed samples. Another feature especially in the second group materials annealing texture is the strong occurrence of Goss ((001)[100]) grains, which is particularly relevant in Fe-3%Si. Here it can be noticed that from a strong $\{111\}\langle 112\rangle$ rolling texture, in which shear bands are formed during rolling leads to a strong Goss orientation after annealing treatment.

The reason for observing homogeneous structure/random texture in the first group materials and inhomogeneous microstructure/gradient texture in the second group materials is the difference in the phase diagrams and temperature profiles. In case of first group materials, for example, low carbon steel, hot deformation was carried out in the single (γ) phase region, so that during subsequent cooling complete γ to α transformation takes place and the texture becomes randomized. Whereas, second group steels are hot rolled in the single α phase region. Therefore, no phase transformation occurs and develops texture gradient in the materials.

Development of texture due to crystal lattice rotation by plastic deformation have been simulated using various models [74–77]. Out of these models, Taylor model is very popular due to its simplicity and its ability in predicting deformation texture in many alloy systems. Taylor models uses possible slip systems for deformation and prior deformation texture of the sample as input and predicts the deformation texture [75]. Taylor model assumes that plastic strain in each grain is equal to the macroscopic plastic strain of the specimen (isostrain condition). Taylor model is used in two modes: Full constraint (FC) and Relaxed constraint (RC). The FC Taylor model, neglects the adaptability of the forces at the grain boundaries [69, 78]. The RC Taylor model assumes shear strain to occur microscopically between adjacent grains (relaxes the zero shear strain constraint locally). At low strain, relaxation of the strain component corresponds to a shear in RD (lath model), at high strains additionally in TD (pancake model) [69, 78]. Raabe *et al.* [69] carried out simulations on the aforementioned deformed texture in bcc materials using single $\{110\}\langle 111\rangle$ slip system as well as combination of various slip systems like $\{110\}\langle 111\rangle, \{112\}\langle 111\rangle$ and $\{123\}\langle 111\rangle$ and compared with the experimental texture results. Taylor calculations using the FC model did not match with the experimental results. The results generated using pancake RC model and combination of various slip systems, $\{110\}\langle 111\rangle$, $\{112\}\langle 111\rangle$ and $\{123\}\langle 111\rangle$, matched with the experimental results. It indicates that deformation take place by the activation of $\{110\}\langle 111\rangle$, $\{112\}\langle 111\rangle$ and $\{123\}\langle 111\rangle$ slip systems.

Table 2.7: Texture evolutions in different bcc metals.

Material	**Condition**	**Texture**	**Ref.**
low carbon steel	Deformed $< 70\%$	• In α-fiber:$\{001\}\langle 110\rangle$ and $\{112\}\langle 110\rangle$ are dominant • In γ-fiber: $\{111\}\langle 112\rangle$ is dominant	[67, 69, 79]
	Deformed $> 70\%$	• In α-fiber, intensity maxima shifted to $\{112\}\langle 110\rangle$ • In γ-fiber: $\{111\}\langle 110\rangle$ is dominant	
	Annealed at 800 °C	• In α-fiber, intensity of $\{001\}\langle 110\rangle$, $\{112\}\langle 110\rangle$ decreases to unity and in γ-fiber, intensity of $\{111\}\langle 112\rangle$ increases	
Pure Nb	Deformed <70%	• In α-fiber: $\{001\}\langle 110\rangle$ and $\{112\}\langle 110\rangle$ are dominant • In γ-fiber: $\{111\}\langle 112\rangle$-weak	[69]
	Deformed >70%	• In α-fiber: $\{112\}\langle 110\rangle$ is dominant • In γ-fiber:$\{111\}\langle 110\rangle$ is dominant	
	After annealing	• α-fiber texture becomes weak and γ-fiber becomes dominant	
Pure Nb and Nb alloy (0.5%Zr-0.05%Ti-Nb remainder)	Deformed:91-96%	• $\{100\}\langle 011\rangle$, $\{113\}\langle 011\rangle$,$\{112\}\langle 011\rangle$ components • Pure Nb-$\{113\}$ is dominant • Nb alloy-$\{100\}\langle 110\rangle$ is strong	[70]
	Annealed at 1200 °C for 2 hrs	• Pure Nb:$\{100\}\langle 320\rangle$ is strong • Nb alloy: $\{100\}\langle 011\rangle$ is strong	
	1500°C for 2 hrs	• Pure Nb:$\{100\}\langle 320\rangle$ is strong and original deformation texture becomes week • Nb alloy: two new poles $\{140\}\langle 351\rangle$ strong, $\{113\}\langle 120\rangle$ weak	
Pure niobium	Undeformed	• $\{001\}\langle 110\rangle$ is dominant	[24]
	Deformed-50%	• No change $\{001\}\langle 110\rangle$ is dominant	
	Deformed-70%, 80%	• $\{111\}$ fiber is dominant	
	Deformed-90%	• $\{111\}$ fiber is strong	
	Annealed at 750 °C for 1 hrs	• γ-fiber increased significantly	
Pure niobium	Deformed-30%	• α and γ-fiber exist	[71]
	Deformed-60%	• $(111)\left[\bar{1}21\right]$ and $[001)\left[1\bar{1}0\right]$ become more intense	
	Deformed-80%	• $(001)\left[1\bar{1}0\right]$ more intense $(111)\left[1\bar{2}1\right]$ moves to $(111)\left[0\bar{1}1\right]$	
	Deformed-90%	• $(001)\left[1\bar{1}0\right]$ becomes more dominant $(111)\left[0\bar{1}1\right]$ moves to a position between $(111)\left[0\bar{1}1\right]$ and $(111)\left[1\bar{2}3\right]$	
	80% deformed samples were heat treated at 1200 °C for 1 hrs	• Intensities of $(001)\left[1\bar{1}0\right]$ texture decreased and in the γ-fiber $(001)\left[1\bar{1}0\right]$ spread out about 20° • Preferred texture is $\{100\}\langle 110\rangle$	
Coarse grain Pure Nb	Deformed 33%, 50% and 70% annealed at 800 and 900°C for 1 hrs	• showed the formation of deformation bands during deformation and recrystallization initiated preferentially at deformation bands.	[72]
Pure Tantalum	Deformed-70%	• It has an incomplete α-fiber texture, extending from $\{001\}\langle 110\rangle$,$\{112\}\langle 110\rangle$	[78]
	Annealing at 1000 °C for 1 hrs	• In α-fiber:$\{001\}\langle 110\rangle$ and $\{111\}\langle 110\rangle$ are sharpened $\{112\}\langle 110\rangle$ decreased	
	1100 °C	• Similar tendency as observed in in heat treated sample at 1000 °C for 1 hrs	
	1200 °C	• Intensity of α-fiber is decreased and the γ-fiber exhibits a maximum at $\{111\}\langle 112\rangle$	

2.6. Oxidation behaviour of materials

The major applications of Nb alloys are for structural applications at high temperatures (>900 °C) [2]. However, one of the main problem in using the Nb alloys at high temperatures is their poor oxidation resistance. Hence, it is important to study oxidation behaviour of the Nb alloys at various temperatures. Prior to discuss oxidation behaviour of Nb alloys, a brief discussion on basic principles and kinetics of oxidation have been presented.

2.6.1. Basics of oxidation

The chemical equation for an oxidation reaction between a metal (M) and oxygen (O_2) is shown below [25, 80].

$$aM + \frac{b}{2}O_2 \longrightarrow M_aO_b \tag{2.2}$$

Oxidation of metal is a multi step process. The first step in this metal oxygen reaction involves the adsorption of oxygen on the clean metal surface. In the second stage, the adsorbed oxygen may dissolve in the metal and then oxide is formed on the surface either as a oxide film or as a separate oxide nuclei. The solid reaction product (metal oxide) separates the two reactants, and for the reaction to continue further, in the third stage, one or both reactants (O_2 or Metal) have to diffuse through the oxide layer (scale) by solid state diffusion. This diffusion process involves either oxygen going through the oxide layer to the oxide/metal interface and reacting there, or the metal being transported through the oxide to the oxide/gas interface and reacting there, as shown in Figure 2.9 [81]. For thick compact scales, driving force for transport through the oxide is the chemical potential gradient across the scale, and for thin films it may also be due to electric fields across the film.

In case, metals form porous oxide layer, the oxide scale does not act as a solid-state diffusion barrier between the reactants. In such cases the reaction may be limited by processes occurring at phase boundaries. Oxides at high temperatures may also be volatile or get liquidify [25].

2.6.2. Reaction kinetics of oxidation

The rate of oxidation can be measured experimentally by using three methods. These involve measuring the amount of oxygen consumed, the amount of metal consumed or the amount of

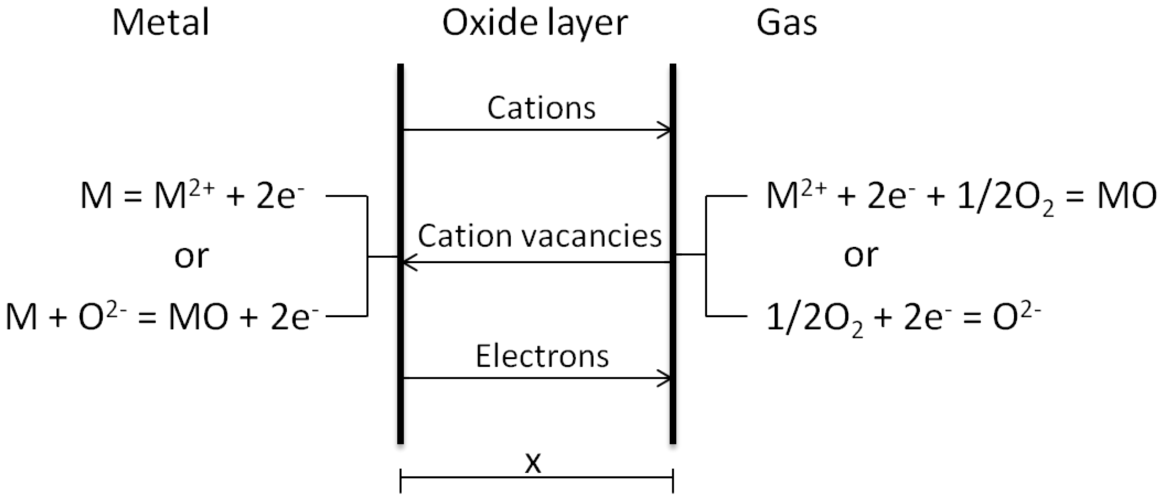

Figure 2.9: Schematic showing diffusion controlled process of oxidation where the cations and cation vacancies have to penetrate the oxide scale for the oxidation reaction to continue [81].

oxide produced. The most general method to study the reaction kinetics is to record the amount of oxide produced by weight change measurements and oxide thickness measurement. All of these variables can be measured as a function of time to show the rate of oxidation [81]. From experimental data, in general, three distinct nature of oxide growth rates have been observed. These are described briefly in the following section.

Linear rate law:

Under this condition, the rate of oxidation remains constant with time and independent to the quantity of metal or gas consumed up to that time. The initial surface reaction step (adsorption) or the diffusion through the gas phase controls the oxidation process. The linear rate law, generally, observed at the very initial stages of oxidation when the fresh metal surface is exposed to the atmosphere for the first time. It can be described by the following equation,

$$\frac{dx}{dt} = k_l \tag{2.3}$$

$$x = k_l t + c_i \tag{2.4}$$

where x is the oxide layer thickness, k_1 is the linear rate constant, c_i is the integration constant and t is the time [81].

Parabolic rate law:

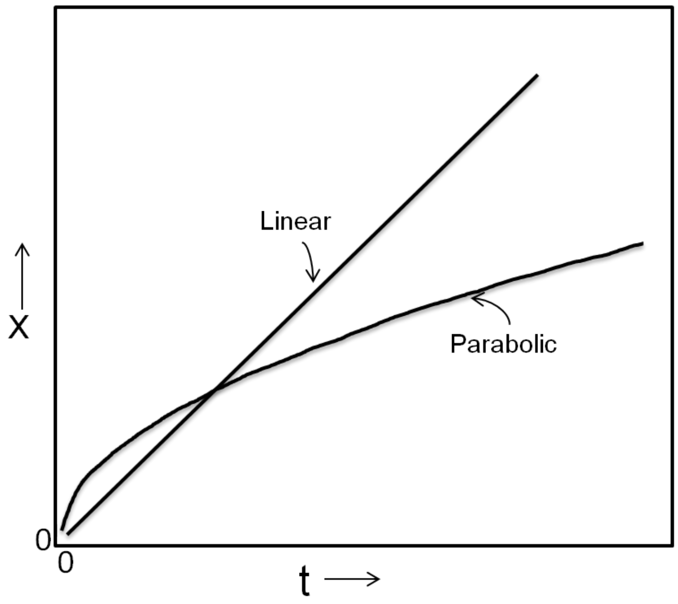

Figure 2.10: A graph showing linear and parabolic oxidation where oxide growth (x) is a function of time (t) [25].

At high temperature many metals are found to follow a parabolic time dependence (Fig.2.10) of oxidation. The differential and integral form of the parabolic rate equation is given by [25]

$$\frac{dx}{dt} = \frac{k_p'}{x} \tag{2.5}$$

$$x^2 = k_p t + c_p \tag{2.6}$$

where k'_p and K_p are the parabolic rate constants, and c_p the integration constant.

In the parabolic oxidation, the diffusion of ions, either metal or gas, through the compact oxide scale is the rate determining step [25]. The metal ions move from the metal/oxide interface to the oxide/gas interface while the oxygen ions moves from gas/oxide interface to the metal/oxide interface.

According to the Wagner's theory, lattice diffusion of reacting atoms or ions (cations, anions) or the transport of electrons through the oxide scale is the rate determining step in oxidation. Wagner's considered the following assumptions:

- Oxide layer is compact and adherent.
- Migration of charged particles, ions (cations and anions), electrons across the oxide is the rate controlling process.

- Thermodynamic equilibrium exists at both the metal/oxide and oxide/gas interfaces.
- The oxide is stoichiometric.
- Oxygen is insoluble in the metal.

With these assumptions, it can be shown parabolic rate constant ($k^{'}$) through calculating flux of charge particles (cations, anions and electrons) and after mass balance that [81].

$$k^{'} = \frac{1}{RT}\int_{\mu_O^{'}}^{\mu_O^{''}} \left[D_O + \frac{Z_M D_M}{Z_O}\right] d\mu_O \tag{2.7}$$

where, D_M = diffusivity of metal in the oxide, D_O = diffusivity of oxygen in the oxide, Z_M = valence of metal, Z_O = valence of oxygen, $\mu_O^{'}$ = chemical potential of oxygen at the metal/oxide interface, $\mu_O^{"}$ = chemical potential of oxygen at the gas/oxide interface

The Wagner theory [82] permits an evaluation of the rate constant of high temperature parabolic oxidation provided the ion and electron mobilities or the diffusion coefficients are known.

Wagner compared the experimentally measured rate constant (equation:2.6) with the calculated rate constant (equation:2.7) with diffusion coefficient for oxidation of copper at 1000 °C and obtained good matching between them. Details could be found in reference [25].

Logarithmic rate law:

It is a characteristic of the oxidation of a lot of metals at low temperatures (usually below 300-400°C) and for the formation of very thin oxide films below tens of nm thick [83]. The reaction is initially quite rapid and then drops off to low or negligibly small values. This rate law can be described by two equations,

$$\text{Direct logarithmic: } x = k_{log} log(t + t_0) + A \tag{2.8}$$

$$\text{Inverse logarithmic: } \frac{1}{x} = B - k_{il} logt \tag{2.9}$$

where k_{log} and k_{il} are rate constants and A and B are constants [25]. These laws can also be shown graphically as seen in Figure 2.11.

Oxidation reactions are frequently found to follow a combination of rate laws [25]. For example, a reaction may be described by a logarithmic rate equation during initial stages at

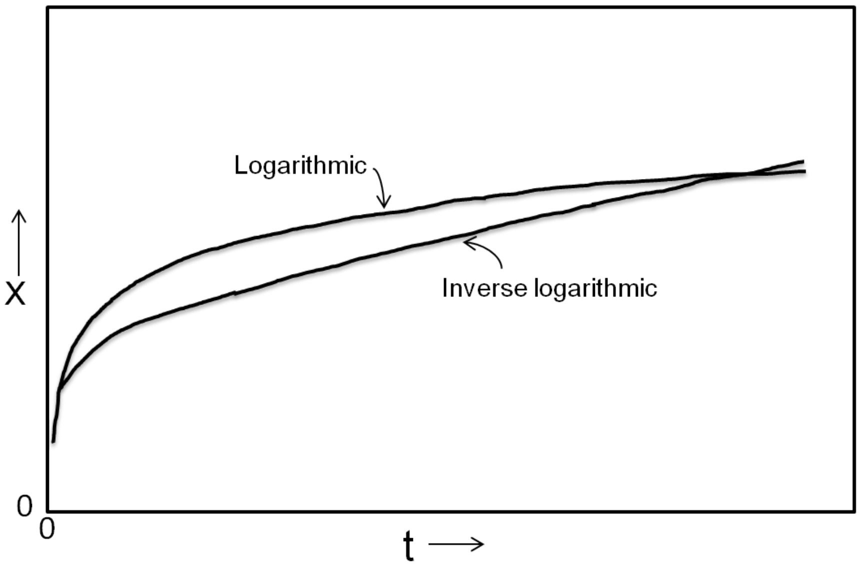

Figure 2.11: A graph showing the logarithmic and inverse logarithmic oxidation kinetics where oxide growth (x) is a function of time (t) [25].

low temperatures due to either electric field induced transport of ions through the film, the rate of reaction by this mechanism will eventually become slower than the rate of reaction due to thermal diffusion of the ions. For this the case the oxidation can be described by a combination of the logarithmic and parabolic rate equations:

$$x = k_{log} log(t + t_0) + k_p t^{\frac{1}{2}} + c \tag{2.10}$$

2.6.3. Oxidation behaviour of refractory materials

Oxidation of niobium with time has been extensively studied in literature [25, 80, 84–87]. All the above mentioned reaction kinetics have been observed in the oxidation of Nb metal. Table.2.8 summarizes the reaction laws observed at various temperatures for refractory materials [87]. It shows that all these refractory materials (Nb, Ta, Mo and W) have similar sequence of reaction laws.

At very low temperatures (<200 °C) a logarithmic or an inverse logarithmic relationship has been found to fit the experimental results for Ta. At 330 °C the surface film on niobium are essentially amorphous consist of Nb_2O_5 oxide layer, but after prolonged oxidation, the presence of suboxides at the metal-oxide interface (NbO and NbO_2) were observed. The suboxides decompose at about 400 °C, X-ray patterns of the pentaoxides become sharp at about 500 °C. In this temperature range, 300 - 500 °C, the oxide film formed during moderate oxide exposures

Table 2.8: Reaction rate laws observed for the oxidation of Nb, Ta, Mo and W metals at various temperature

Metal	100 °C	300 °C	400 °C	500 °C	700 °C	900 °C	1100 °C	1300 °C
Nb		par	par	par - lin	lin	lin	accel.	asym
Ta	log	inv. log	par	par - lin	lin	lin	delayed	
Mo		par	par - lin		lin	lin		
W			par	par	par - lin	par-lin	par-lin	

log = logarithmic oxidation
inv.log = inverse logarithmic oxidation
par = parabolic oxidation
par-lin = parabolic oxidation turning linear after a certain time
accelerated oxidation, i.e. faster than linear
asymptotic oxidation

are adherent, pore free, exhibiting bright temper colour. At 500 °C, in the parabolic-linear transition range, small blister like cracks start forming. Above 500 °C spalling and cracking become quite pronounced, due to this linear oxidation rate laws observed. At 1000 °C, the scale on Nb seems to become more compact, and at 1250 °C, a coherent layer is formed which is, however, non-adherent and easily flakes off at the slightest provocation.

There are five types oxide phases form during oxidation of Nb. Table.2.9 lists the crystal structure information of all the oxide phases.

Table 2.9: Crystallographic information of the various niobium oxide phases forms during oxidation of Nb.

Oxide phase	structure	Lattice constants (A°)
Nb_4O	Tetragonal	a = 3.35, c = 3.24
NbO	cubic	a = 4.21
NbO_2	rutile	a = 4.77, c = 2.96
Nb_2O_5 - α	Orthorhombic	a = 6.19, b = 3.65, c = 3.94
Nb_2O_5 - β	monoclinic	a = 21.34, b = 3.82, c = 19.5, 120.3°

2.6.4. Oxidation mechanisms in refractory materials

As shown above (Table. 2.8), sequence of oxidation of the refractory metals is almost similar. The sequence of oxidation is logarithmic $\longrightarrow$ inverse logarithmic $\longrightarrow$ parabolic $\longrightarrow$ parabolic - linear $\longrightarrow$ linear.

At very low temperatures refractory materials follow logarithmic and then subsequently follow inverse logarithmic oxidation law. Cabrera *et al.* [88] have proposed oxidation mechanism for the low temperature oxidation of refractory materials. According to them, a very thin oxide film on a metal adsorbs oxygen at its surface, and electrons pass through the film from metal to the adsorbed surface layer. In this way a strong electric field is set up which pulls the ions (cations or anions) across the film. Depending on whether the passage of electrons or ions is rate determining step, one obtains a logarithmic or inverse logarithmic relationship.

As the temperature of oxidation is raised (300 - 400 °C), parabolic oxidation follows the logarithmic oxidation. At his stage, the oxidation rate becomes diffusion controlled, the driving force being no longer the electric field but the concentration gradient as in the Wagner mechanism for parabolic oxidation. Most of the lower oxides are metallic conductors in which diffusion rates are fast, and the slowest rate determining diffusion takes place in the highest oxides, which are all cation excess, or rather anion-deficit, conductors.

The parabolic oxidation at intermediate temperatures controlled by the diffusion of O^{-2} ions through the film consisting mainly of the highest oxide (Nb_2O_5), and new oxides (NbO and NbO_2) form at the metal-oxide interface. Pilling-bedworth ratio for Nb_2O_5 is large: 2.45-3.5 [82, 87]. Because of this newly formed oxide expands against the resistance of the existing oxide layer, and severe biaxial stresses develop which eventually lead to rupturing of the film. This is the mechanism (at least for niobium and tantalum) leading to the parabolic into linear ones, at temperatures between 500 and 700 °C. Nb_2O_5 exists in two different forms: α-Nb_2O_5 and β-Nb_2O_5. α-Nb_2O_5 is stable below 700 °C and β-Nb_2O_5 exists at temperature $>$825 °C. Both α-Nb_20_5 and β-Nb_20_5 present between 725 and 825 °C [89]. Formation of β-Nb_20_5 at higher temperature reduces the oxidation rate of Nb [89]. β-Nb_20_5 grows on the surface of the oxide in the form of whiskers (monocrystals). These appear to be produced by evaporation of the high temperature phase followed by deposition on defective sites; the vapor of β-Nb_2O_5 can condense on micropores and cracks, which tend to seal these and thus protects the material from further oxidation.

As the temperature is raised further, the parabolic portion of x - t curves is suppressed and oxidation becomes virtually linear, that is oxygen penetrates through the porous and cracked surface layers and reaction takes place substantially at the unprotected metal surface.

The asymptotic oxidation observed on niobium at 1250 °C may be caused by a separation between the metal and oxide layer due to non-adherence owing to the high pilling-bedworth ratio.

Oxidation reactions often tend to follow a mixture of different rate laws as described above. This behaviour of oxidation of metal is either due to change in the rate determining mechanism or change in the scale chemistry because of allotropic transformation of oxide [25].

2.6.5. Effect of alloying elements on the oxidation behaviour of Nb

It has been observed that addition of titanium, zirconium and tantalum increases the oxidation resistance of Nb alloys. These three metals have higher affinity for oxygen than niobium. Therefore, these metals oxidize preferentially. When these metals are present in sufficient concentration in the Nb alloys, during oxidation, coherent films of TiO_2, ZrO_2 or Ta_2O_3 form. These three oxides are n-type semi conductors with vacant sites in the O^- lattices, and since they would also be saturated with Nb^{5+} ions the number of vacant sites would be considerably reduced. In addition, the molar volume ratio of TiO_2/Ti and ZrO_2/Zr are considerably smaller than that of Nb_2O_5/Nb. Therefore, oxide layers are much less prone to cracking and act as protective oxide layer [87].

Another mechanism of improving oxidation resistance by addition of alloying elements can be by producing double oxides or more complex oxides. It has been shown that the $6ZrO_2$ Nb_2O_5 oxide formed on niobium-zirconium alloys (50/ 50 at.%) does not fall on cooling and is protective for a few hours at 1000 °C. However, if the oxide layer cracks then more rapid oxidation occurs. Further studies on these alloys showed that the addition of 5 at.% titanium to these alloys can suppress this transition and improves the oxidation resistance of Nb alloy by a factor of ten over unalloyed Nb. The effect of chromium addition on the oxidation resistance of Nb has also been considered but chromium has same affinity for oxygen as niobium. Therefore, chromium addition to niobium are effective only above about 20 at.%.

Alloying additions can affect the oxidation behaviour of Nb by expanding or contracting the partially protective Nb_2O_5 layer or forming new oxide layer [90]. Smith et al. [27] have systematically studied the effect of alloying elements on oxidation resistance of niobium alloys. It has been found that addition of 6 at.% titanium to the Nb forms a $3Nb_2O_5.TiO_2$ oxide layer during oxidation. At 1100 °C, oxidation rates of this alloy have been about 1% of that of pure niobium metal. However, addition of Ti in the alloy brings down the creep strength of the alloy to a value as low as of pure niobium [27]. In general, it has been found that by alloy addition, it is very difficult to simultaneously achieve high strength, high workability, high resistance to liquid alkali metals, along with the high oxidation resistance. Therefore, providing environmental coatings appears one of the best option to avoid oxidation as well as getting desired properties.

2.7. Oxidation barrier coatings

2.7.1. Coating requirements

The coating layer allows the total or partial separation of surface and substrate related properties. Therefore, coating systems should be designed to provide a more optimized environmental protection capability, without degrading the mechanical properties of substrate material. Purpose of the coating/surface treatment, is to form a stable, slow growing surface oxide that provides an oxidation barrier between the coating alloy and the environment in which it operates. In order to achieve this oxide scale, it is necessary to have a reservoir of the component that forms it beneath the oxide.

There are several coating techniques available. Among them diffusion coatings provides uniform coating and can be easily applied on the intricate shape and sizes of structural materials. Diffusion coatings are formed through diffusional interaction between the constituents of the coating material (aluminum, chromium or silicon) and the substrate alloy.

Diffusion coatings can be applied to components using a range of techniques: pack cementation, chemical vapor deposition (CVD), gas phase CVD, metallising and fluidized-bed techniques. For pack cementation, the deposition rate and morphology of the coating depend on the pack activity, process time and temperature. Similarly. for CVD coatings, the activity of various species in the vapor phase is equally important. Hence, the properties of a diffusion coating depend upon the process methodology, as well as the substrate composition and the subsequent heat treatments.

2.7.2. Pack cementation coating

Amongst various coating processes, halide activated pack cementation technique (HAPC) is the most widely used process for applying protective coatings on high temperature materials [91]. Pack cementation process is an in-situ chemical vapor deposition (CVD) process which produces coating on substrate by diffusional mechanism [92]. This is a low cost process, particularly, suited for the formation of uniform diffusion coatings on structural alloy components of complex shapes and sizes.

In this process, components to be coated are placed in a pack contained in a sealed re-

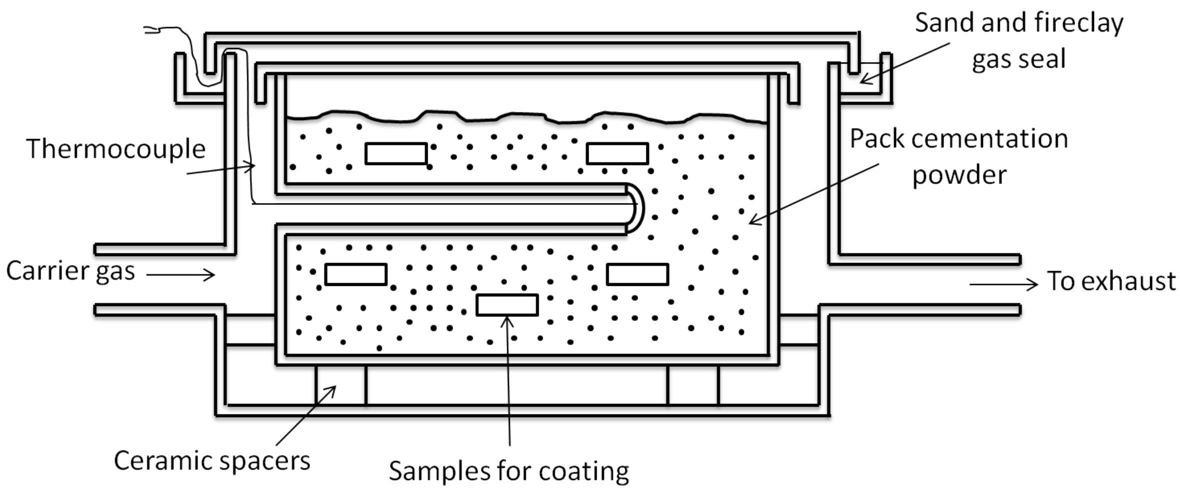

Figure 2.12: Schematic diagram of pack cementation retort [94].

tort, Figure 2.12 [93]. The retort is heated to the desired processing temperature under either an inert gas or hydrogen atmosphere to prevent oxidation. The exact process cycle, time and temperature, is dependent on the required coating, coating thickness and subsequent heat treatments. The pack contains a donor alloy that releases solute material at a known rate (and hence determines the pack activity). A halide activator (NaF, NH_4Cl, NaCl or a mixture) dissociates during the process cycle and acts to transport solute material from the pack to the component to be coated. A inert oxide diluent acts as to prevent pack sintering. Therefore, the diffusion coating is formed as a result of two distinct processing steps:

- The solute elements are brought into contact with the surface of the component to be coated (the role of halide activator).
- The solute diffuses into the component surface to form a surface alloy or compound of different composition (the coating).

After coating, the component may be subjected to a recovery heat treatment, dependent on the substrate used.

Literature shows that among all the elemental coatings, silicide coatings have good oxidation resistance at temperatures higher than 1200 °C, good mechanical properties and high resistance to liquid alkali metals [95, 96]. Levy et al. [95] have studied the oxidation behaviour of a complex disilicide/tantalum-10tungsten alloy system at temperatures of 927 °C to 1482 °C. The silicide coated samples showed very good oxidation resistance at high temperatures due to the formation of SiO_2 oxide layer. It has also been shown that during oxidation, silicide coatings may undergo pesting [97, 98]. Therefore, it is important to provide a suitable silicide coating which can avoid the catastrophic oxidation.

In general, in pack cementation, two kinds of microstructures are observed depending on the activity of the pack. The activity of the pack is related to the concentration of coated material used in the pack. Usually, if the coated element concentration is greater than 60 at.% in the pack it is referred to high activity, otherwise the pack is called low activity pack [99, 100]. Extensive study has been carried out on the aluminide coating on the superalloys by pack cementation technique. Typical microstructure produced by high activity and low activity pack has been very well explained in the literature [100].

CHAPTER 3

Experimental Methods

This chapter describes the experimental details which were used to produce the Nb alloys and their characterization using tools such as X-ray diffraction (XRD), scanning electron microscopy (SEM) and transmission electron microscopy (TEM). In addition, it also describes the experimental techniques used to study the oxidation behaviour of Nb alloys and silicide coating techniques.

3.1. Alloy preparation and fabrication

3.1.1. Melting

Nb is a refractory metal having high melting point (2468 °C) and high reactivity with oxygen and nitrogen. Therefore, melting of Nb was carried out using electron beam (EB) melting facility under high vacuum conditions. Fig.3.1 shows the flow sheet for the preparation of the Nb alloy with desired composition. In order to obtain low level of impurities electron beam refined pure Nb and Zr metals and spectra pure graphite powder were used in the charge. In order to ensure chemical homogeneity, in particular with respect to carbon, throughout the length of ingot, several experiments were carried by placing charge by different methods; e.g., (i) placing of high purity C powder in folded niobium sheets, (ii) placing high purity C powder in a drilled Nb bar or (iii) placing the pure Zr strips below the Nb charge. Several experimental trials were carried out to ensure that the composition of the alloy is within the desired range. For this purpose samples for chemical analysis were collected at least from six different places of the ingot along its length. Based on the variation in the chemical composition, experimental parameters like; extraction rate, current density and vacuum level, etc. were optimized.

A seed ingot for retraction head was developed by carefully preparing the charge specifically for this purpose. The EB melted alloy was hydride, dehydrated and remelted to homogenize the composition of the alloy. The composition of the alloy was verified by combustion

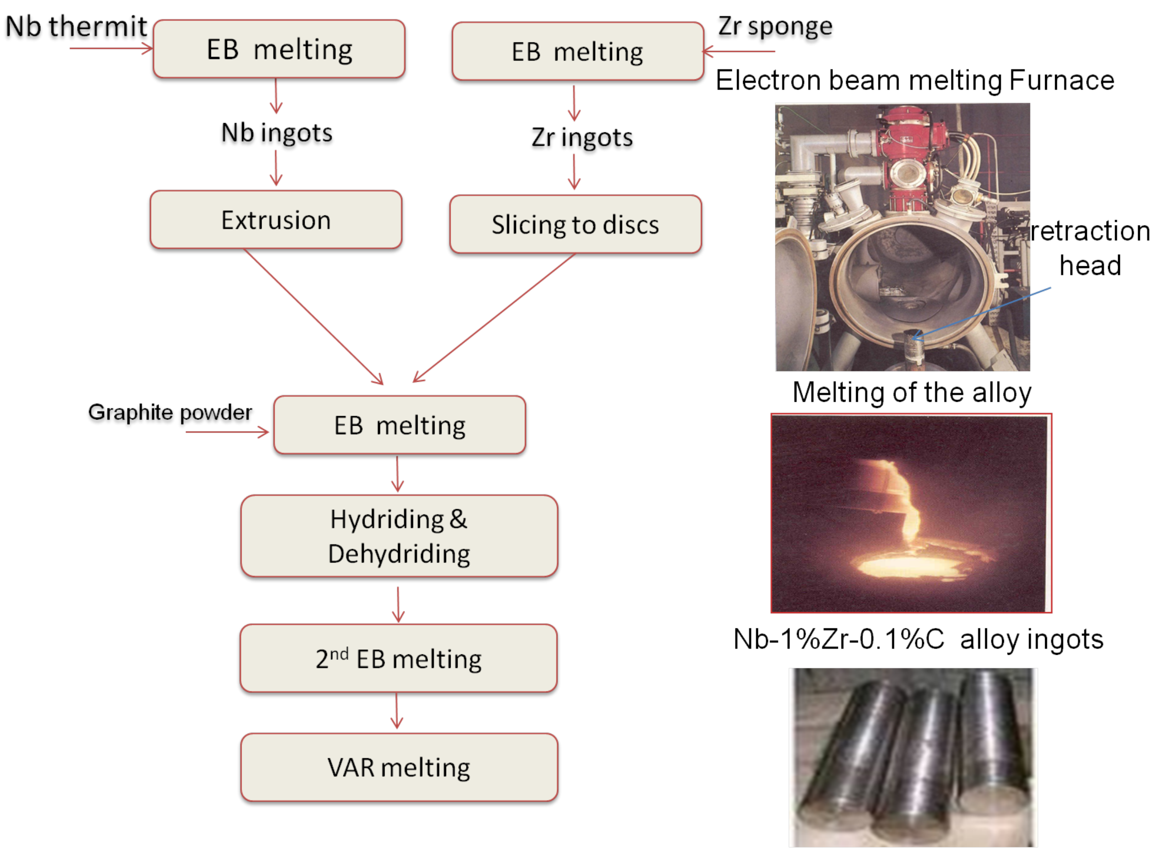

Figure 3.1: Flow sheet for the preparation of Nb-1%Zr-0.1%C alloy

Table 3.1: Chemical compositions of as-solidified Nb alloy.

Zr (wt.%)	C (wt.%	Impurities	Nb (wt.%)
0.9-1.2	0.1-0.13	H - 4 p.p.m	remainder
		N - 41 p.p.m	remainder
		O - 132 p.p.m	remainder

extraction method for carbon and inductively coupled plasma method for zirconium and niobium analysis. Typical chemical composition of the alloy is shown in Table.3.1. Composition of the alloy is within the desired range.

Here after the homogenized electron beam melted Nb alloy is referred as as-solidified Nb alloy.

3.2. High temperature deformation of Nb alloys

In order to brake the as-solidified structure of Nb alloy it was necessary to assess its deformation behavior and for this purpose hot and cold deformation of as-solidified Nb alloy experiments were carried out at different temperatures.

3.2.1. Plastodilatometer

Deformation behavior of the alloy was assessed by carrying out compression testing of as-solidified Nb specimen cylinders (6 mm dia and 7.5 mm length) in a plasto-dilatometer (BAHR Thermoanalyse DIL 805). Deformation was carried out at different temperatures ranging from 800 °C to 1300 °C at 0.01, 0.1, 1 strain rate up to 35% deformation. During experiment vacuum was maintained at 10^{-4} torr.

3.2.2. Hot hardness

The as-solidified Nb alloy samples were subjected to hot hardness tests. Before starting the hot hardness experiments, the instrument was calibrated using a standard (Cu: SRM: National Bureau of Standards, USA) sample. Five indentations were taken on the standard sample using 1 N load. The diagonals were measured on the T.V. screen using the telecomparator. The hardness obtained was found to be within ±0.5% of the actual value.

The specimens and indenter was heated separately to the desired temperature and the variation in temperature during the indentation processes was maintained within less than ±1 °C. At each temperature the specimens were held for at least 0.166 hrs to stabilize the temperature. The load used for hot hardness test was 2 N and the dwell time was 5 s. At each temperature at least five indentations were taken and average hardness value was calculated. The hot hardness experiments were carried out from room temperature to 1000 °C. Above this temperature reaction between specimen and indenter was noticed.

3.2.3. Hot rolling

Hot rolling experiments were carried out on the as-solidified ingot material by taking rectangular (4 cm x 2 cm x 1 cm) slices. These samples were jacketed with low carbon steel and warm worked from 800 to 1000 °C (up to several percentage of thickness reduction).

3.2.4. Extrusion experiments

Extrusion experiments were carried out on hollow billets. For this purpose solid ingots were machined and drilled to make an inner diameter (ID). These hollow billets were mechanically jacketed with seamless copper tubes of thickness 1.6 mm both on OD (outer diameter) and ID side. Copper jacket on the billet has served three purposes (i) prevention of the billet from excessive oxidation, (ii) action as lubricant during extrusion and (iii) prevention any direct contact

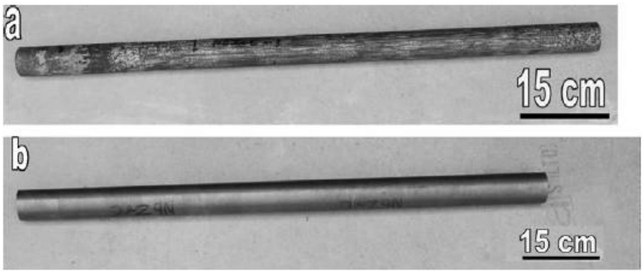

Figure 3.2: Extruded tubular products (a) as-extruded tubular Blank 36 mm OD X 8 mm WT and (b) as-machined tubular Blank 35.2 mm OD X 5.1 mm WT.

of Nb-alloy with tooling surface. Billets were preheated and soaked at a temperature of 800 °C for 2.5 to 3 hrs before extrusion. The selection of temperature was based on the input obtained from the compressive testing. This issue will be discussed in the result part of the thesis. A conical die with semi die angle of 60° was used to reduce the formation of dead metal zone inside the container. Suitable shrinkage allowances were taken into account while deciding the dimensions of the mandrel and the die with respect to the cold dimension of the tubular product. Before the transfer of the preheated billet into the extrusion press container, the container surface, the die and mandrel were lubricated with oil based graphite lubricant. Extrusions of the Nb alloy billets were carried out with extrusion ratio nearly at 6:1-5:1 and mean strain rate of 3.0-5.25 s^{-1}. Subsequent to extrusion copper jacket was removed. As-extruded tubular blank is shown in Fig.3.2.

3.3. Recrystallization experiments

In order to determine the optimum temperature of recrystallization, deformed samples were subjected to various heat treatments starting from 1000 °C to 1500 °C for different soaking time periods. In order to avoid oxidation during annealing, the samples were wrapped in the tantalum foil and heat treated under high purity argon atmosphere. Temperature of the furnace was maintained within ±1 °C.

3.3.1. Experiments for texture and microstructural analysis

For Crystallographic texture studies the recrystallized samples were used and it has been referred in this thesis as as-received Nb alloy. The as-received Nb alloy was subjected to uniaxial rolling at room temperature with multiple passes so that the thickness of the Nb alloy was uniformly reduced to 40%, 60% and 80% of the original thickness. Rolling direction was strictly maintained along the single direction. The 60% deformed sample was annealed at 1300 °C for different soaking time periods (0, 0.5, 1, 1.5, 2, 2.5, 3, 4, 5, 6, 7 hrs). In order to avoid oxidation during annealing, samples were wrapped in tantalum foils and heat treated under high purity argon atmosphere. Mid-thickness section of the deformed and annealed samples was taken for texture and microstructural characterization to avoid surface effects. X-ray diffraction and Electron back scattered diffraction (EBSD) techniques were used for macro and micro texture analysis, respectively.

3.4. Characterization

The deformed and annealed samples were characterized using following methods: (a) optical microscope (b) scanning electron microscope (SEM), (c) electron back scattered diffraction (c) transmission electron microscopy (TEM) techniques.

3.4.1. Optical microscopy

For optical metallography, the specimens were mounted in bakelite and ground using successive grades of emery papers. They were mirror polished and microstructure was revealed using an acid solution containing HNO_3, HF and H_2SO_4 in the ratio of 1:1:3. Optical microstructural investigations were carried out on Leika microscope. Samples were examined in bright field as well as in differential interference contrast mode.

3.4.2. Scanning electron microscopy

Samples prepared for optical microscopy were directly used for SEM examination using the back-scattered electron and secondary electron modes of imaging. A field emission scanning electron microscope (FE-SEM-Zeiss Ultra 55) has been used for this purpose.

3.4.3. X-ray diffraction

X-ray diffraction was used to identify the phases present in the Nb alloy samples. X-ray diffraction patterns were obtained utilizing Cu-kα radiation with a wavelength of 1.5406 A° in a Philips PW 1830 X-ray Diffractometer. Phase identification was also carried out by obtaining X-ray diffraction patterns using a synchrotron as X-ray source (λ= 0.73019 A°) at RRCAT, Indore, India. The XRD patterns were analyzed with the help of PCPDF data base software.

3.4.4. Transmission Electron Microscopy (TEM)

For preparing specimens for TEM, slices of thickness of about 500 μm were cut using a low speed diamond saw which were further thinned down to 100-150 μm by grinding and finally cleaned ultrasonically. Disc specimens of 3 mm diameter were punched out from these slices. TEM samples were prepared by jet thinning technique using Struers Tenupol-5 instrument. In the jet thinning technique, electrolyte solution containing 87.5% methanol and 12.5% sulphuric acid was used at -40 °C and 20 V. TEM examination of these samples did not show the presence of second phase in any of the Nb alloy samples. According to literature the carbide phases should be present in these samples. The reason for the absence of second phase in the TEM samples could be due to the selective dissolution of carbide phases in the electrolyte during jet thinning.

In order to avoid dissolution of second phase, TEM samples were prepared by ion milling technique using Technoorg Linda IV4 instrument. Ion milling was carried out by bombarding argon ions at 6 kV, 1.5 mA current on each side of sample at a grazing angle of 10°. Prior to TEM investigation, samples were plasma cleaned to remove contamination.

Different transmission electron microscopes JEOL2000FX, FEI Tecnai T20 and FEI TITAN were used to completely characterize the second phase present in the Nb samples. Selected area electron diffraction patterns (SAEDP) were analyzed for phase identification. Bright field (BF) and dark field (DF) images were obtained to understand the morphology of phases. Energy dispersive spectrometer (EDS) in STEM (Scanning transmission electron microscopy) mode with the spot size 7 has been used to get the composition of the carbide phases. Electron energy loss spectrometer was also used for composition analysis as well as for TEM sample thickness measurement.

3.5. Macrohardness Test

Macrohardness measurements were conducted on all the deformed and annealed samples using a diamond pyramidal indenter, with Vickers Hardness Tester Model HPO-250 at a load of 5 kgs.

3.6. Silicide coating on Nb alloy by pack cementation

To produce silicide coatings on Nb alloys, thin rectangular slices (10 mm X 6 mm X 2 mm) and cylindrical (5 mm diameter X 1 mm thickness) samples were cut. These samples were mirror polished up to 1 μm diamond. The edges were chamfered manually for better settling of silicide coating on the samples followed by ultrasonic cleaning. The cleaned samples were weighed and subsequently placed in the pack. The pack powder consisted of a mixture of Al_2O_3, Si, and NH_4F in the ratio of 85:10:5. The alumina crucible containing the pack was sealed with an alumina lid using alumina based high-temperature cement. The sealed crucible was left for curing at room temperature for 48 hours, after which it was placed in the uniform heating zone of the high-temperature heating furnace. The coating experiments were conducted at temperatures 1200 °C, 1300 °C, 1400 °C, and 1500 °C for different time periods (6, 9, 12, and 15 hrs). Four samples were coated in each experiment. High purity Ar gas was passed through the furnace tube with the flow rate of 0.33 ml/hrs to protect the pack from oxidation and to provide inert atmosphere. After holding at the coating temperature for a predefined time period, the crucible was furnace cooled. The crucible seal was broken and the coated samples were taken out from the furnace. The coated samples were cleaned ultrasonically in acetone to remove any loosely embedded pack material and were weighed to determine the weight gain. The dimensions of the coated samples were also measured to observe the changes in dimensions.

3.7. Oxidation experiments

To study the oxidation behavior of the Nb alloy and silicide-coated samples, thermogravimetric analysis was carried out in air up to 1200 °C using a NETZSCH thermal analyzer STA 409 PC Luxx at a heating rate of 0.05 °C/hrs.

3.7.1. Isothermal oxidation

Isothermal oxidation experiments were carried out in a horizontal tube furnace in air on the bare Nb alloy at 600 °C for different time intervals up to 6 hours (0.166, 0.333, 0.5, 0.666, 2, 4, and 6 hours) and on silicide-coated samples at 1000 °C up to 64 hours (4, 8, 16, 32, and 64 hours). Each sample was carefully weighed before and after exposure, to determine the weight change during the oxidation process. Each experiment was repeated at least for the four times and the average weight gain is reported.

3.7.2. Characterization

Surfaces of the silicide-coated and oxidized samples were characterized by X-ray diffraction (XRD), optical microscopy, and scanning electron microscopy (SEM). Cross-sectional samples were prepared by taking slices normal to the coated and oxidized surfaces. These samples were metallography polished up to one micron diamond and examined under optical, SEM and EPMA. Composition line scans were performed on the crosssection of oxidized and coated samples of Nb using an energy dispersive spectrometer (EDS) attached to SEM. To find out the morphology of the grains and crystallographic information of silicide coating, electron back scattered diffraction was carried out. For this the same cross-section SEM sample was used. Before going for EBSD analysis, colloidal silica polishing was carried out to remove the deformed layer on the sample.

In order to find out the crystallographic information of silicide phases present in the silicide coating, cross-sectional TEM sample were prepared. For this the rectangular slices (width $\sim$ 0.25 mm and length $\sim$ 1.8 mm) were taken from the cross-section of silicide coatings. The two rectangular slices were sandwiched facing coating layer each other using a fast-curing epoxy. This epoxy has two parts, viz., resin and hardener and both are taken in 10:1 ratio on glass slide and mixed with a toothpick thoroughly for about a minute. The epoxy is applied to the surface of the coating layer for making sandwich. This sandwich was inserted in the slotted titanium grid (slot width and length are 0.6 mm and 1.8 mm,). The left over gaps in the grid were filled with epoxy. The thickness of the cross-section sample (titanium grid) was reduced from 0.3 mm to 0.1 mm using micropol instrument. In order to decrease the time for ion beam thinning as well as obtaining large regions with electron transparent thicknesses, dimpling was performed on both sides of the sample using Gatan dimpler (model 656) up to 40 μm thickness. Further ion milling was carried out using Technoorg linda instrument till the perforation was made at the center of the sandwich in the titanium grid.

3.7.3. Microhardness test

Microhardness measurements were conducted on the cross-section of the oxidized and coated samples using a Knoop indenter and diamond pyramidal indenter, respectively, with Struers microhardness tester Duramin (Struers A/S, Ballerup, Denmark) at a load of 200 gm.

CHAPTER 4

Thermomechanical processing of the alloy

This chapter deals with thermomechanical processing of as-solidified Nb alloy. General understanding about Nb based alloys is that typical deformation temperature should be in the range of 1600 °C and the recrystallization temperatures have been reported to be close to 1400 °C [2, 101]. Nb, however, is known to be a ductile metal which can be deformed substantially at room temperature. Hence, large amount of plastic deformation can be imparted by low temperature deformation. Thereby high strain energy locked inside the deformed sample can be utilized to bring down the recrystallization temperature. Therefore, this chapter has been focused on exploring the possibility of deforming and recrystallizing the Nb alloy at relatively low temperatures. For this, the effect of thermomechanical treatments on the microstructure and mechanical properties of Nb-1%Zr-0.1%C alloy has been studied. It includes studies on the deformation behavior of as-solidified Nb-1%Zr-0.1%C alloy at different temperatures and strain rates, recrystallization behavior at different temperatures and time, and evolution of microstructures at different processing conditions (as-solidified, deformed and recrystallized). Based on these experimental results the flow sheet for the processing of Nb-1%Zr-0.1%C alloy at low temperature ($\leq$ 0.55Tm (Tm - melting point of Nb)) has been developed.

4.1. Introduction

Existing literature on Nb alloys shows that deformation temperatures for the processing and breaking of as-solidified Nb alloy are higher than 1600 °C [2, 101]. Detailed microstructural analysis of thermomechanical treatment of Nb-Zr-C alloys have shown that upon high temperature deformation ($\sim$1625 °C) the carbide phase undergoes dissolution and reprecipitation, and the degree of recrystallization, average grain size increases with increasing number of extrusion steps [9]. The recrystallization temperatures reported for the alloy are in the range of 1450 - 1500 °C. It is also a known fact that Nb alloys are susceptible to oxidation and decarburization above 1400 °C [2, 11]. Any heat treatment above 1400 °C needs special arrangements to keep oxygen concentration extremely low to avoid oxidation. In connection with Nb and its dilute alloys, two points are worth mentioning: (i) Nb alloys are amenable to deformation at lower temperatures. Such an attempt will bring down the fabrication cost of the material low as facilities already existing for the processing of other materials at low temperatures (<1000 °C) can be utilized. (ii) Low temperature deformation in warm deform region would store high strain energy into the material which would bring down the temperature of recrystallization below 1400 °C; making again utilizing the existing facilities available for recrystallizing the other materials at low temperatures (<1350 °C). This twofold benefit - in lowering the cost of fabrication - makes this alloy competitive with respect to other commercial alloys and provides a cost benefit edge over other refractory metals. Therefore, the present work in this chapter focuses on the establishment of a new route for deformation as well as recrystallization of the Nb alloy at lower temperatures which would make the fabricability of the alloy suitable with the existing facilities for processing of materials at low temperatures. The present chapter reports low temperature deformation of the Nb alloy, structural changes to deformation as well as recrystallization of the Nb alloy. Determination of optimized temperature for annealing subsequent to warm working and effects of temperature on deformation has also been reported.

4.2. Characterization of as-solidified microstructure

Fig.4.1 shows optical micrographs of the as-solidified Nb-1%Zr-0.1%C alloy. Very large size of grains (in few of mm) could be noticed from the Fig.4.1(a(i)). Such large grains in as-solidified samples were due to prolonged high temperature exposure during the electron beam melting. Fig.4.1(a(ii)) shows montage of optical micrographs along the longitudinal direction of as-solidified ingot. Presence of columnar microstructure can be noticed from the micrograph. Before, preparing the alloy by electron beam melting, a seed ingot (master alloy) having composition of Nb-1Zr-0.1C was prepared by arc melting technique. The seed ingot was used as a retraction head for the electron beam melting of Nb alloy. In electron beam melting, the Nb alloy was prepared by melting the individual charge materials and solidifying the alloy on the seed ingot. Due to directional solidification, the typical microstructure of the electron beam melted Nb alloy has columnar microstructure. A magnified image of a grain showed uniform distribution of needle shape precipitates in the matrix phase (Fig.4.1(b(i)). Volume fraction of these precipitates was estimated close to 12%. Size distribution of the phase is shown as bar-graph in Fig. 4.1(b(ii)). It shows that high volume fraction of carbides have 10-20 μm length.

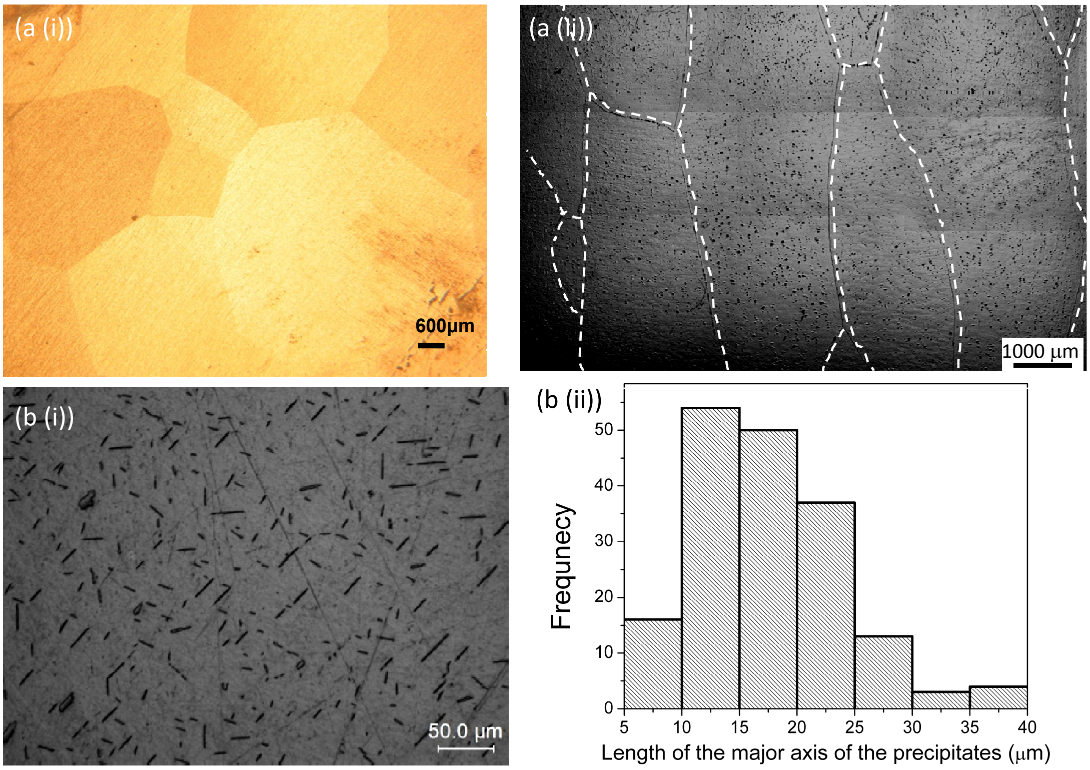

Figure 4.1: Optical micrographs of as-solidified Nb-1%Zr-0.1%C alloy (a) microstructure along (i) transverse and (ii) longitudinal direction showing the presence of large columnar grains (∼ 1 mm) and (b) (i) Magnified image showing needle morphology precipitates within a grain and (ii) precipitate size distribution.

These precipitates appear to have aligned along the specific direction of the matrix phase. Crystal structure and composition of the needle shape precipitates will be discussed in the chapter 5 under carbide phase transformations.

4.3. Deformation behaviour of as-solidified Nb alloy

In order to fabricate the Nb alloy for structural applications it was necessary to assess its deformation behavior and for this purpose compression testing of as-solidified Nb alloy were carried out at different temperatures ranging from 600 to 1300 °C at 0.1 strain rate (s^{-1}) up to 35% deformation. Stress-strain plots and flow curves of these samples are shown in Fig.4.2. As may be noticed from Fig.4.2(b) the flow stress of the alloy remains above 200 MPa up to 1300 °C. In the temperature range from 600-800°C the flow stress dropped from 268 MPa to 241 MPa but between 800 and 1000 °C it increased up to 290 MPa and subsequently exhibited a sharp drop to 200 MPa for testing temperature higher than 1000 °C. In order to verify this behavior hot hardness tests were also carried out which again confirmed sharp rise in hardness for temperature higher than 800 °C (Fig.4.3). Hot hardness tests confirmed this pattern of sharp rise in hardness in the temperature range of 800 - 1000 °C. Reason for such increase in the strength of the alloy was later established as the precipitation of additional carbides at high temperatures.

These experiments established that the alloy exhibits a minimum in strength around 800 °C and, therefore, it was possible to carry out shape forming operations at temperatures close to 800 °C. To establish extrusion parameters for long tubes, it was necessary to determine the strain rate sensitivity of the alloy at the extrusion temperature. For this purpose, samples of as-solidified alloy were compression tested at 800 °C at 0.01, 0.1 and 1 strain rates (s^{-1}) (Fig.4.4). All these curves were superimposed on each other showing that the alloy has very low strain rate sensitivity in this temperature range. Such low stain rate sensitivity indicates that the material has possibility of failure during direct extrusion.

When deformed microstructure was examined under OIM, it showed bimodal grain size distribution (Fig.4.5) where grains could be classified into two families; family-one with grain size lager than 3 μm and family-two with grain size smaller than 3 μm. Fig.4.6(a) shows discrete plot of orientation in Euler space for grains belong to family-two. As may be noticed distribution of these grains is nearly uniform and homogeneous in space. In contrast, grains belong to family-one (Fig.4.6(b)) were mainly aligned along $\langle 100 \rangle$ direction. Grains of family-one appear to resist deformation. The average grain orientation spread is much larger than the grains of family-two indicating these grains have accumulated larger amount of elastic strain (Fig.4.7). Such grains could be the source of stress concentration. In addition, when the material was subjected to tensile stress at room temperature (Fig.4.8) some of the specimen failed in brittle manner exhibiting ductility as low as 2%. It is worth noting that during compressive experiments not a single sample failed even after imparting strain of $\sim$70%. Combining these results it could be inferred that to avoid any chance of cracking of the material the state of compressive stress should be dominating during extrusion. It was, therefore, achieved by drilling a bore on each ingot and extrusion of hollow ingot was carried out with the support of a mandrel at 800 °C. In addition samples were subjected to relatively low strain rates.

In addition to extrusion experiments, deformation experiments by rolling were carried out on the as-solidified ingot material by taking rectangular (4 cm x 2 cm x 1 cm) slices. These

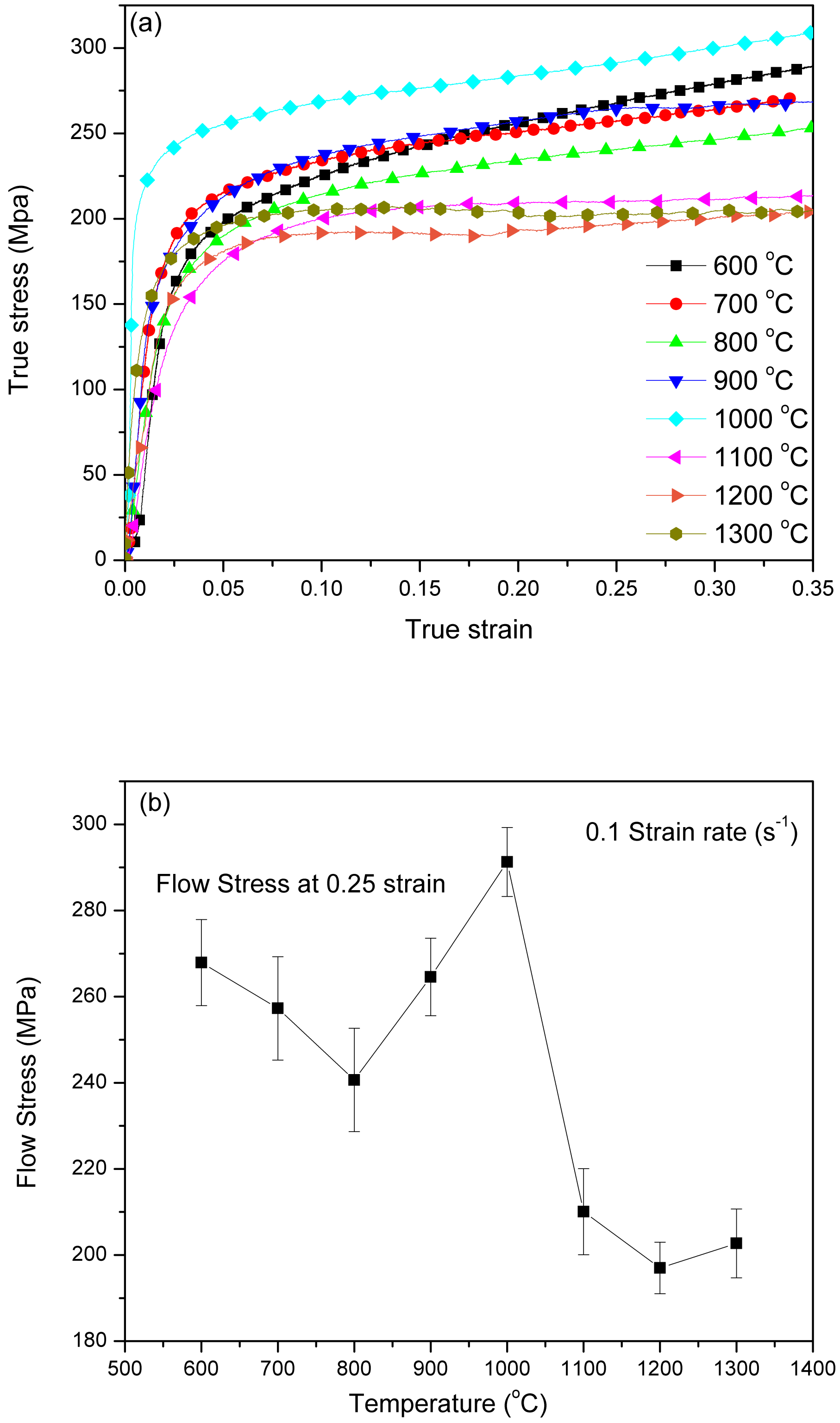

Figure 4.2: Compression (a) stress-strain curve and (b) flow stress as a function of temperature for as-solidified Nb alloy from 600 °C to 1300 °C at 0.1 s^{-1} strain rate. Increase in flow stress in the temperature range of 800 - 1000 °C could be noticed.

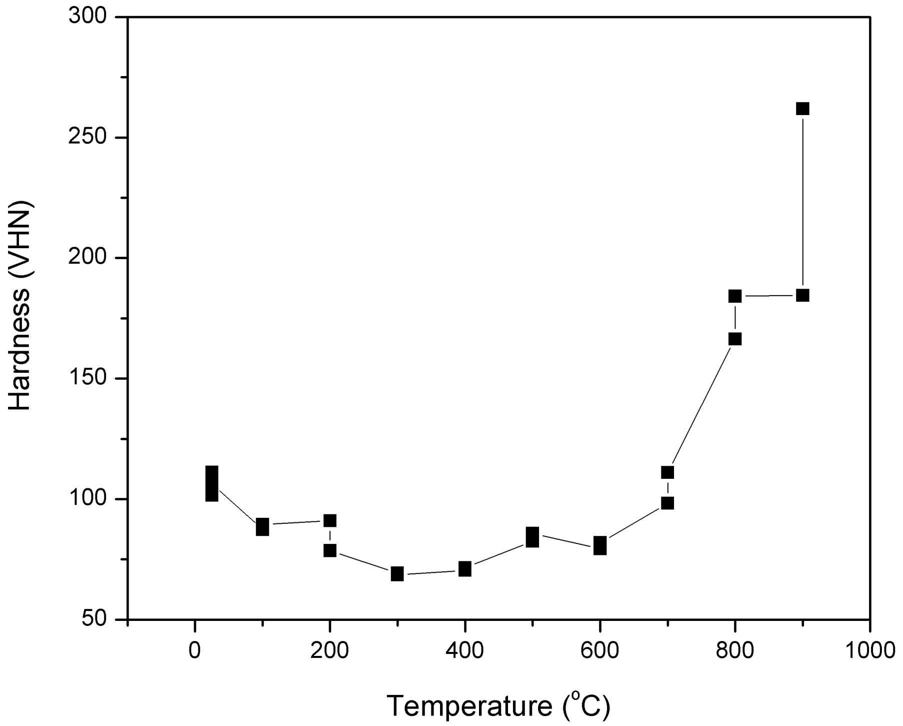

Figure 4.3: Hardness (VHN) vs temperature plot of as-solidified sample. Increase in hardness beyond 800 °C could be noticed. Above 1000 °C Nb alloy started reacting with C of diamond indenter and therefore, hardness experiments were terminated at 1000 °C

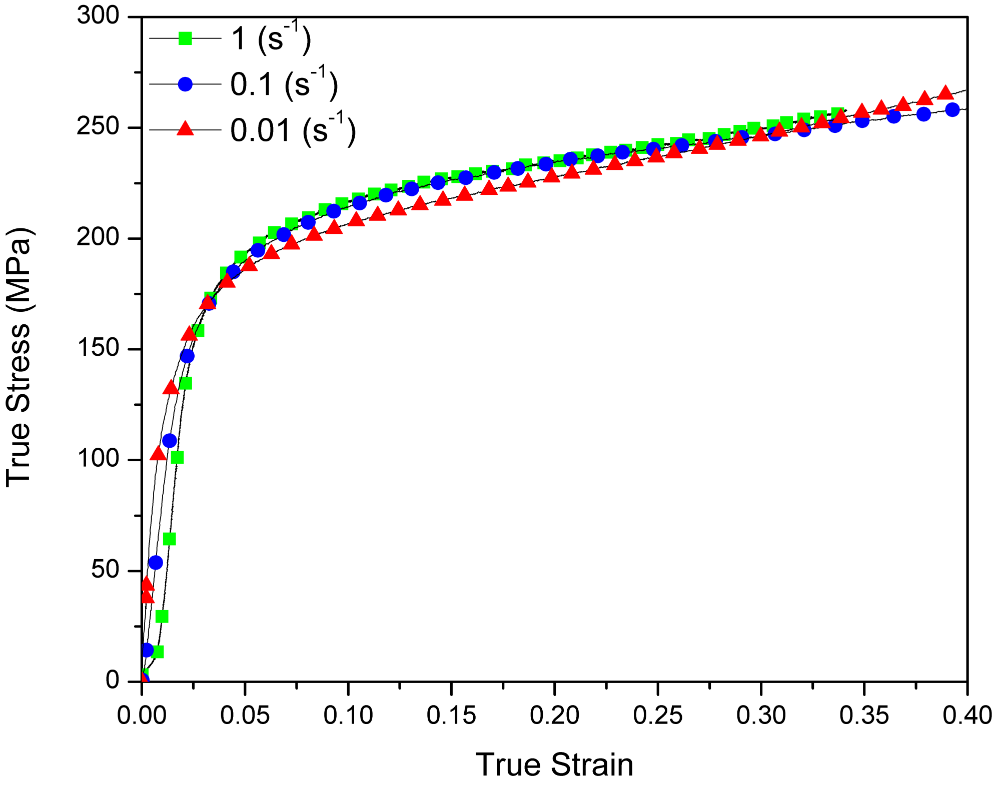

Figure 4.4: Compression stress-strain curves of as-solidified Nb-1%Zr-0.1%C alloy at 800 °C at differant strain rates. All the curves superimposed on each other showing very low strain rate sensitivity of the material at 800 °C

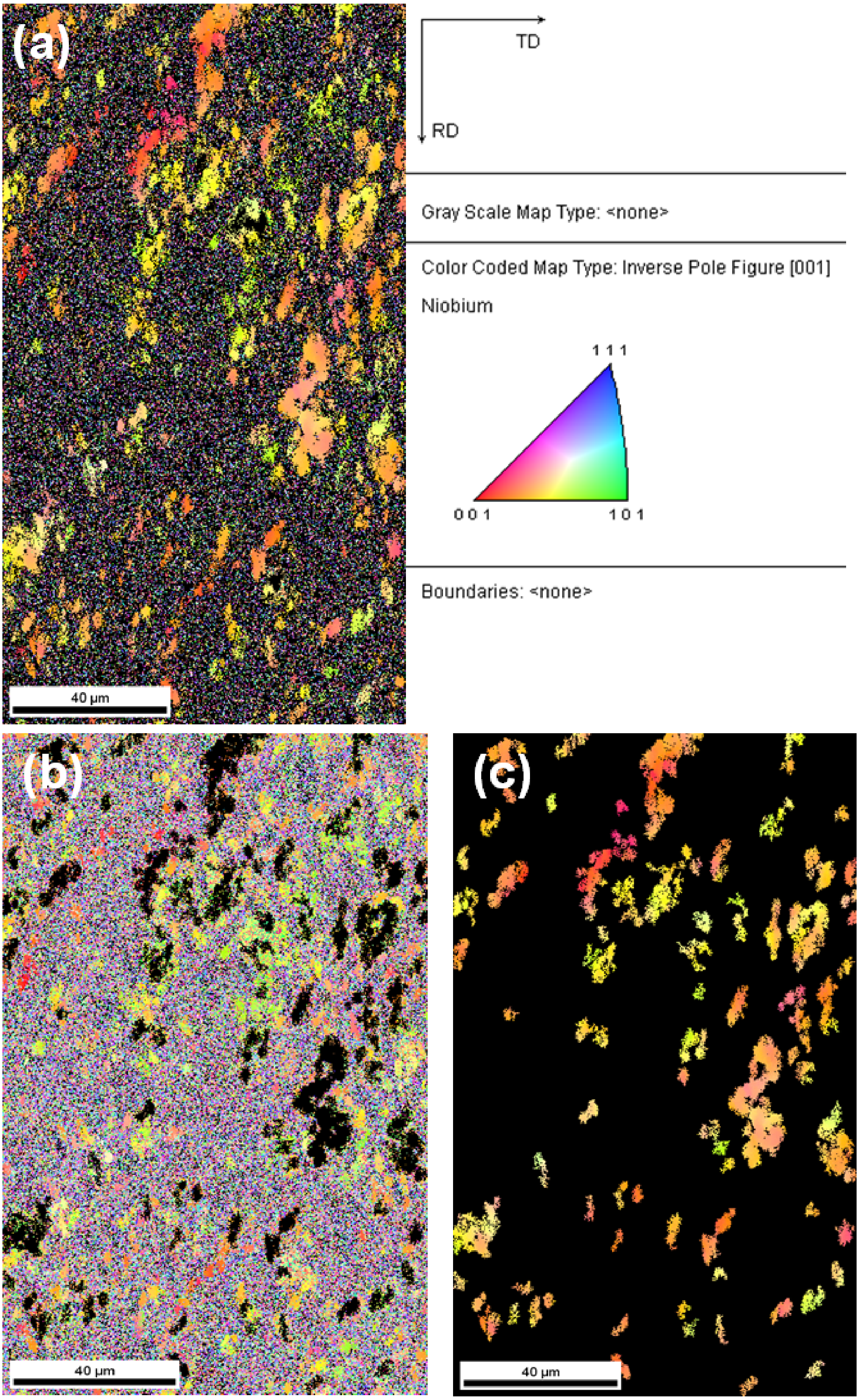

Figure 4.5: (a) Showing deformed microstructure of the Nb-1%Zr-0.1%C alloy. Presence of very fine grains as well as large grains could be noticed. (b) Showing the distribution of small grains (<3 μm) and (c) large grains (>3μm).

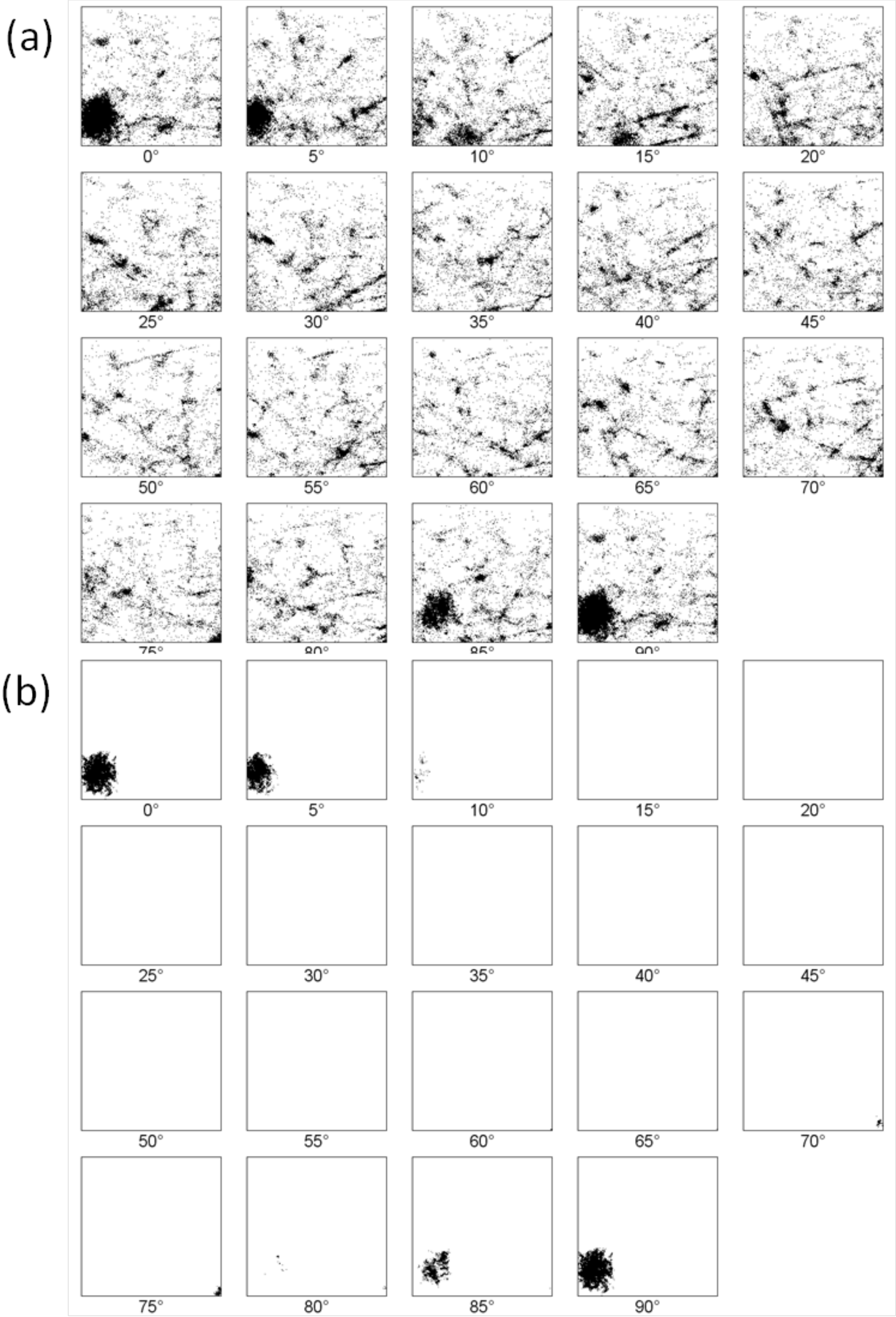

Figure 4.6: Showing the discrete distribution of the orientation in Euler space in the deformed samples of Nb-1%Zr-0.1%C alloy (a) for the grains of dimension smaller than 3 μm. The wide spread of orientation in all section indicates that distribution is nearly random. (b) For the grains of dimensions larger than 3 μm. The narrow spread of orientation indicates most of these grains were have nearly same orientation.

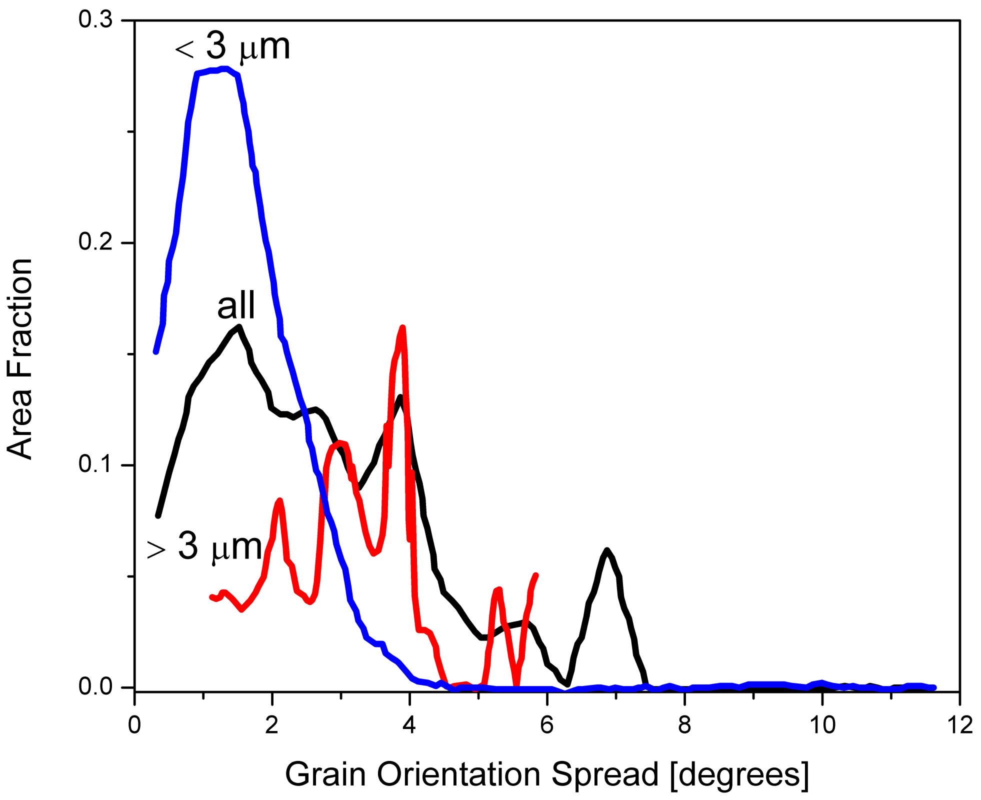

Figure 4.7: Showing grain orientation spread in grains smaller than 3 μm, larger than 3 μm and overall grain orientation spread.

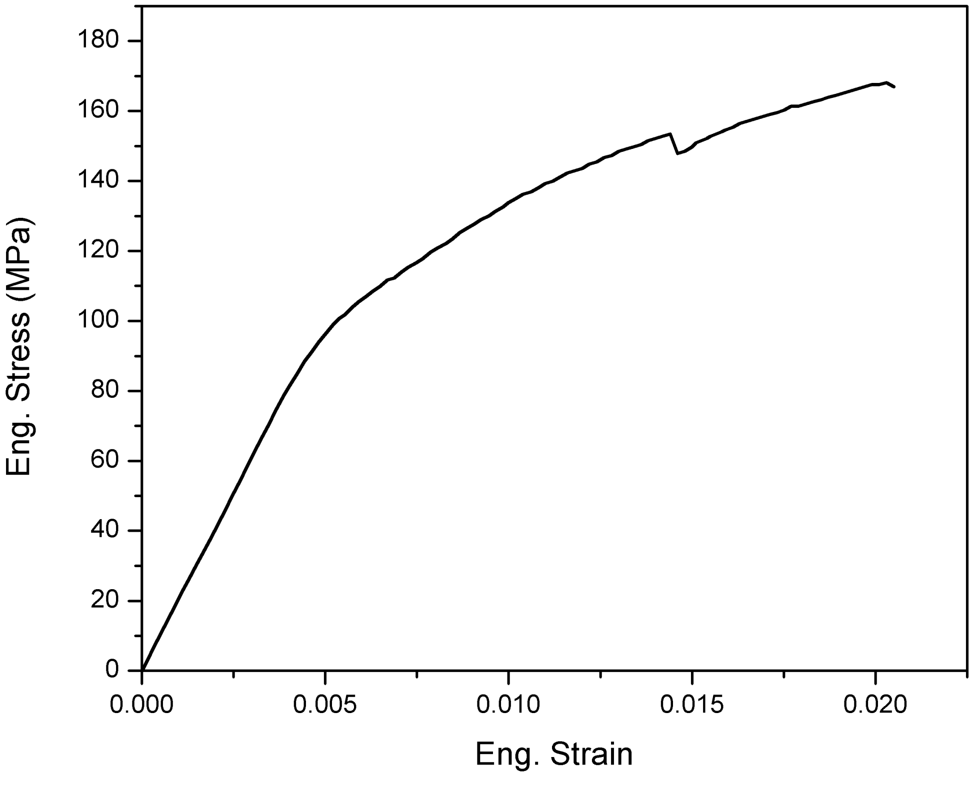

Figure 4.8: Engineering stress-strain graph for as-solidified sample showing low ductility when subjected to room temperature tensile testing.

Table 4.1: Warm working deformation behavior of as-solidified Nb-1%Zr-0.1%C alloy.

Temperature °C	% deformation	Remarks
Room temperature	1%	cracked
800	20%	cracked
900	30%	cracked
1000	35%	No crack, no oxidation
1100	35%	oxidation

samples were jacketed with low carbon steel tube material and warm rolled from 800 to 1000 °C (up to several percentage of thickness reduction). The results and observations are tabulated in the Table.4.1. As could be noticed below 1000 ° cracks were induced even at low strains. Possible reason for such behaviour could be large grain size and distribution of needle morphology precipitates in the Nb matrix. With increase in deformation temperature, propensity for cracking reduces considerably. In contrast, the tendency for oxidation increases with increase in temperature. Because of these two opposing tendencies 1000 °C is the most optimum temperature for the working of Nb as-solidified alloy.

4.3.1. Characterization of deformed microstructure

Fig.4.9 shows a typical optical micrograph of the deformed samples. The presence of deformed grains could be noticed in the optical micrographs of the extruded samples. Extruded microstructure showed (Fig. 4.9(b)) two morphologies of the precipitates; one with rectangular shape and second one with needle shape morphology. The volume fractions of needle and rectangular shape precipitates were estimated as 15% and 6% respectively. Detailed crystallographic analysis of the two phases are explained in the next chapter. The presence of different kind of precipitates as compared to the precipitates present in the as-solidified microstructure indicating that during deformation the precipitates in the as-solidified got dissolved and precipitated into different precipitates. It provides a clue for the presence of two cusps in the graph of flow stress versus temperature (Fig.4.2(b)). The first minimum around 800 °C could be because of dissolution of precipitates present in the as-solidified sample whereas the second minimum above 1000 °C is due to the softening of the Nb matrix. Chemical composition of the extruded alloy was also verified by combustion extraction method and inductively coupled plasma method. It did not show any significant changes in the composition from the as-solidified alloy.

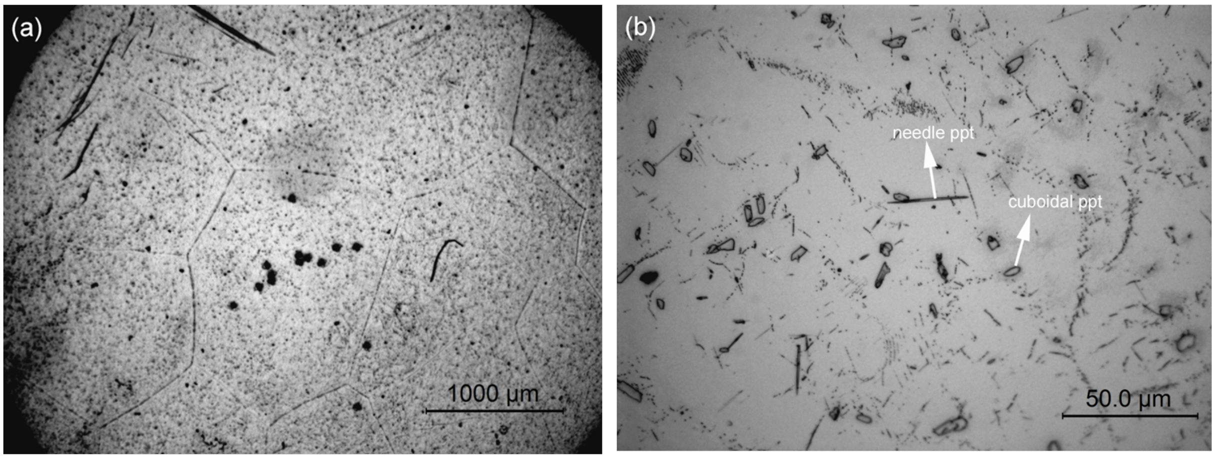

Figure 4.9: Optical micrographs of the deformed Nb alloy (a) low magnified image showing the presence of deformed bigger grains and (b) magnified image of a grain showing the presence of needle and cuboidal morphologies of precipitates within the grain.

Table 4.2: Grain size and percentage of recrystallization of heat treated samples.

Annealing temperature °C	**Grain size (μm)**	**% recrystallization (2deg GOS reference)**
1300 for 3hrs	17.4637	96.1
1200 for 6hrs	4.911	39.6
1200 for 10hrs	8.029	35.1
1200 for 24hrs	5.025	44.1

4.4. Recrystallization behaviour

Subsequent to deformation it was necessary to find out a low temperature recrystallization zone. From this the as-solidified samples were deformed up to 35% at 1000 °C and to determine temperature and time of the recrystallization, several heat treatments were carried out by systematically varying temperature and time of annealing treatments. These annealed samples were subsequently characterized by OIM. Fig.4.10. shows some of the orientation imaging micrographs of samples heat treated at various time and temperature.

As may be noticed from these micrographs annealing at 1200 °C did not yield in a fully recrystallized microstructure even after annealing up to 24 hrs. The annealing treatment of 3 hours at 1300 °C, on the other hand, produced a nearly full annealed microstructure. Grain size of all these samples calculated and tabulated in the Table. 4.2. Percentage of recrystallization has also been calculated by taking GOS as 2^o. A large value of GOS indicates that grains were still under strain and could not recrystallized completely. The recrystallized grains will have low GOS. Based on this criterion percentage of recrystallization has been estimated and shown in the last column of Table.4.2.

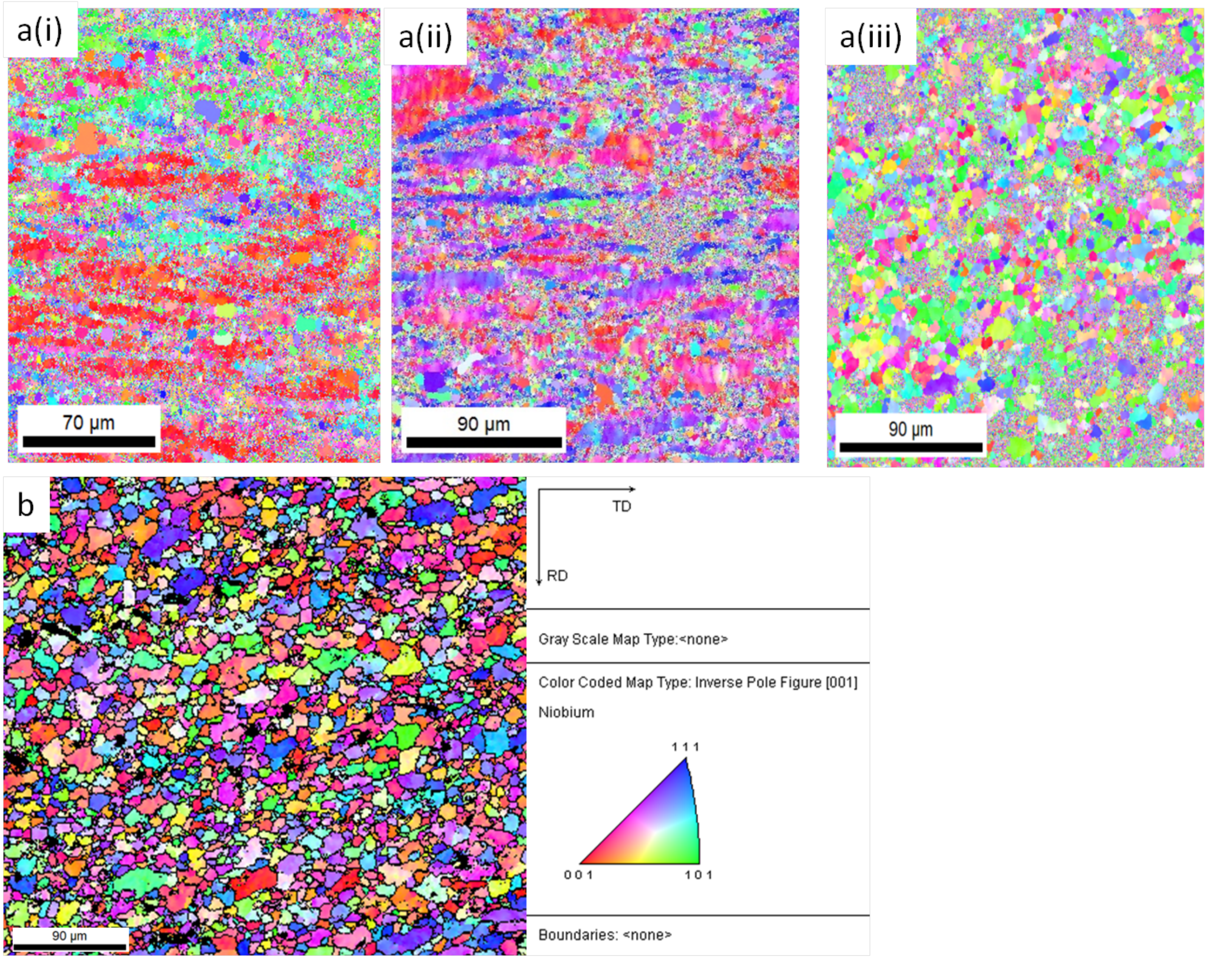

Figure 4.10: EBSD images of heat treated samples at (a) 1200 °C for (i) 6 hrs, (ii) 10 hrs and (iii) 24 hrs, and (b) 1300 °C for 3 hrs.

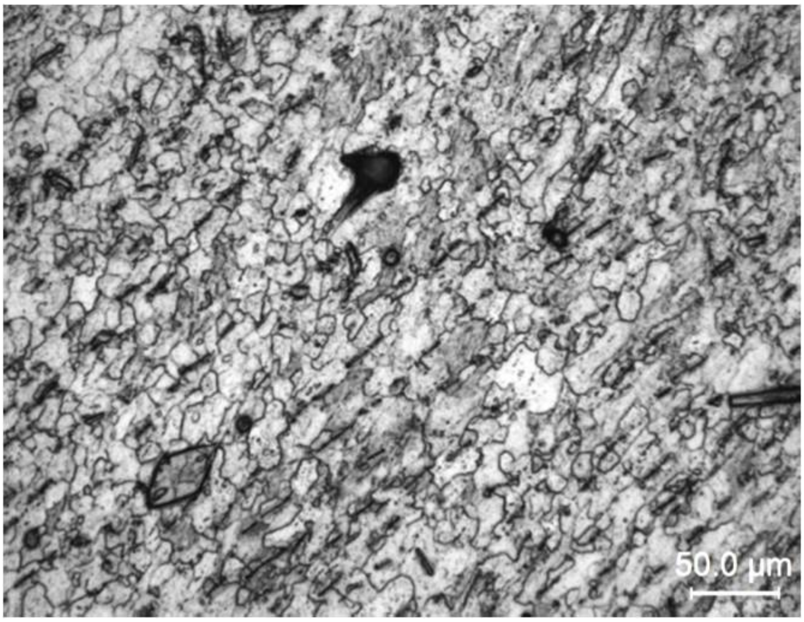

Figure 4.11: Recrystallized microstructure of Nb-1%Zr-0.1%C alloy annealed at 1300 °C for 3 hrs.

From this study it has been established that the as-solidified alloy can be recrystallized by heat treating at 1300 °C for 3 hrs subsequent to warm working at 1000 °C up to 35% deformation.

The optimized recrystallization parameters were also applied on the as-solidified extruded sample at 800 °C. Fig.4.12 shows an EBSD micrograph of the annealed extruded sample. It shows the presence of strain free equiaxed grains of about $\sim$30 μm. Percentage of recrystallization has been calculated using GOS criteria. It showed that 97% of the grains has been recrystallized.

It shows that extrusion at 800 °C provided advantage over deformation at elevated temperature of 1400 °C. Temperature of extrusion being less than 0.35 Tm reduces chances of dynamic recovery or recrystallization. Deformation imparted on material is stored in the form of strain energy which brings down the recrystallization temperature substantially to 1300 °C from the literature showed temperature 1500 °C, as reported in the literature [2].

4.4.1. Mechanical properties of the recrystallized Nb alloy

In order to compare the mechanical properties of the low temperature processed Nb alloy with the high temperature processed material, tensile testing of annealed samples was carried out at room temperature at a strain rate of 8 x 10^{-4} s^{-1}. The Fig.4.13 shows the engineering stress - strain curve of the annealed sample. The tensile properties like, ultimate tensile strength (UTS),

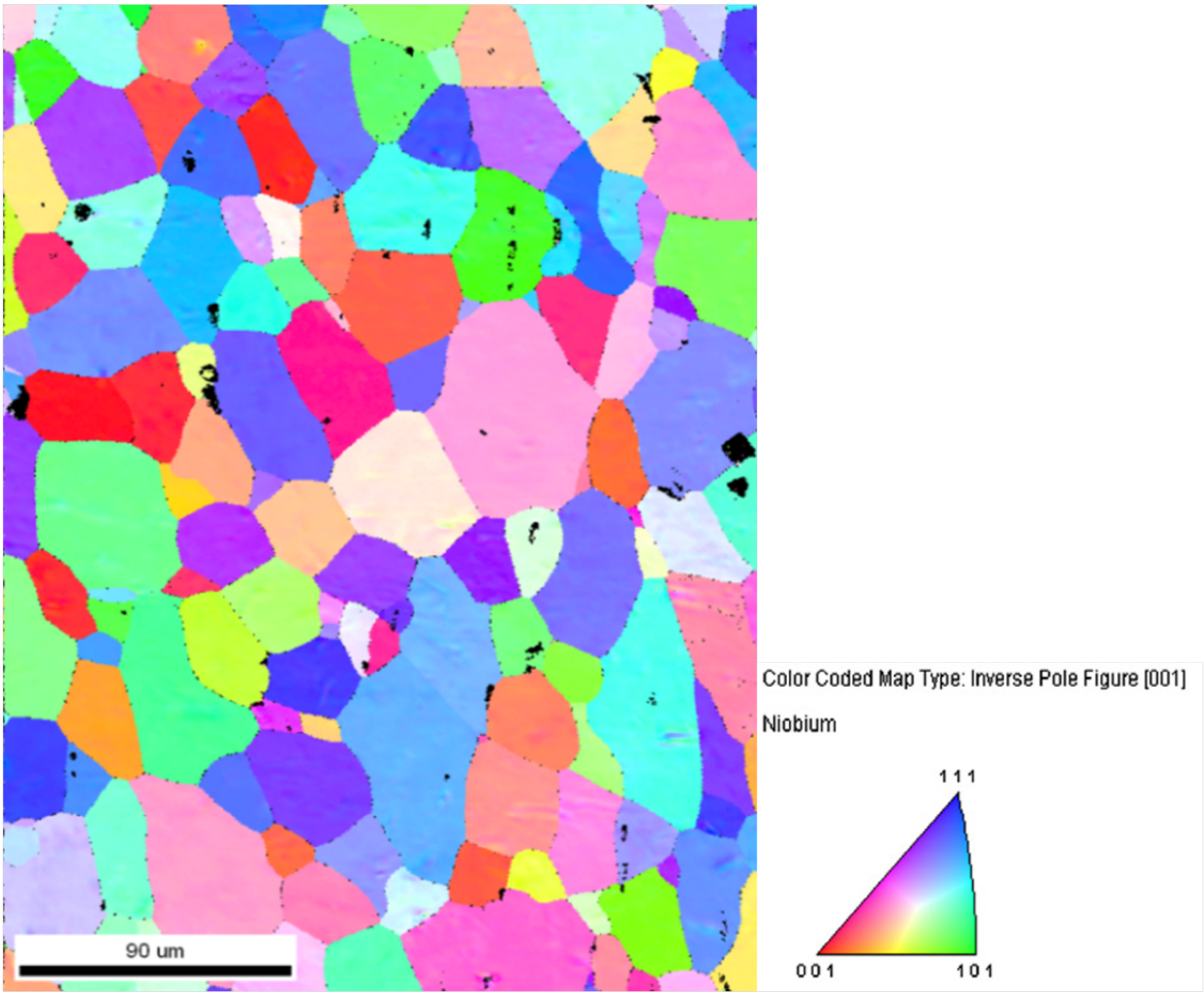

Figure 4.12: EBSD micrograph of extruded Nb-1%Zr-0.1%C alloy annealed at 1300 °C for 3 hrs.

Table 4.3: Mechanical properties of the annealed Nb alloy sample and reported values in the literature.

Sample	**Yield strength (MPa)**	**Ultimate tensile strength (MPa)**	**Total strain (%)**	**Uniform strain (%)**	**Referances**
Annealed sample	98±3	274±5	21±2	11±2	Present work
Literature	114	270	21.9	18.3	[104]
	105-130	250-280	28-35	19-24	[9]

0.2 percent yield strength (YS), ductility and uniform elongation were determined from a load-elongation plot and are reported in Table.4.3. The pure Nb has 60-70 MPa YS, 125-130 MPa UTS [102, 103]. Comparing the mechanical properties of Nb alloy with pure Nb, it can be show that addition of 1% Zr and 0.1%C dramatically increases the strength of the Nb. Improvement in mechanical properties could be attributed to solid strengthening (presence of Zr in the Nb matrix) as well as to precipitation hardening (presence of niobium carbides in the Nb matrix) of Nb alloy. The Nb alloy has high uniform strain in comparison to other refractory materials [15], hence, it is easy to fabricate Nb alloy into different shapes of structural materials.

Mechanical properties of the annealed Nb alloy samples and the reported values in the literature [9] are tabulated in Table.4.3. It shows that the material developed using the low temperature deformation route have similar mechanical properties as that of the material developed using high temperature deformation route. Mechanical properties of a material depends on the microstructure of the material. The low temperature processed material (current study) and the high temperature processed material (reported in the literature) show similar mechanical properties which indicates that both the materials should have similar microstructure though the processing routes are different. The recrystallized Nb alloy reported in literature have ~ 30 μm grain size [9] and presence of cubic (Nb,Zr)C carbides in the Nb matrix. The recrystallized alloy using the low temperature processing condition also shows similar grain size and carbide precipitates (carbide precipitate are discussed in the next chapter). Due to the presence of similar microstructures, both the materials exhibit similar mechanical properties.

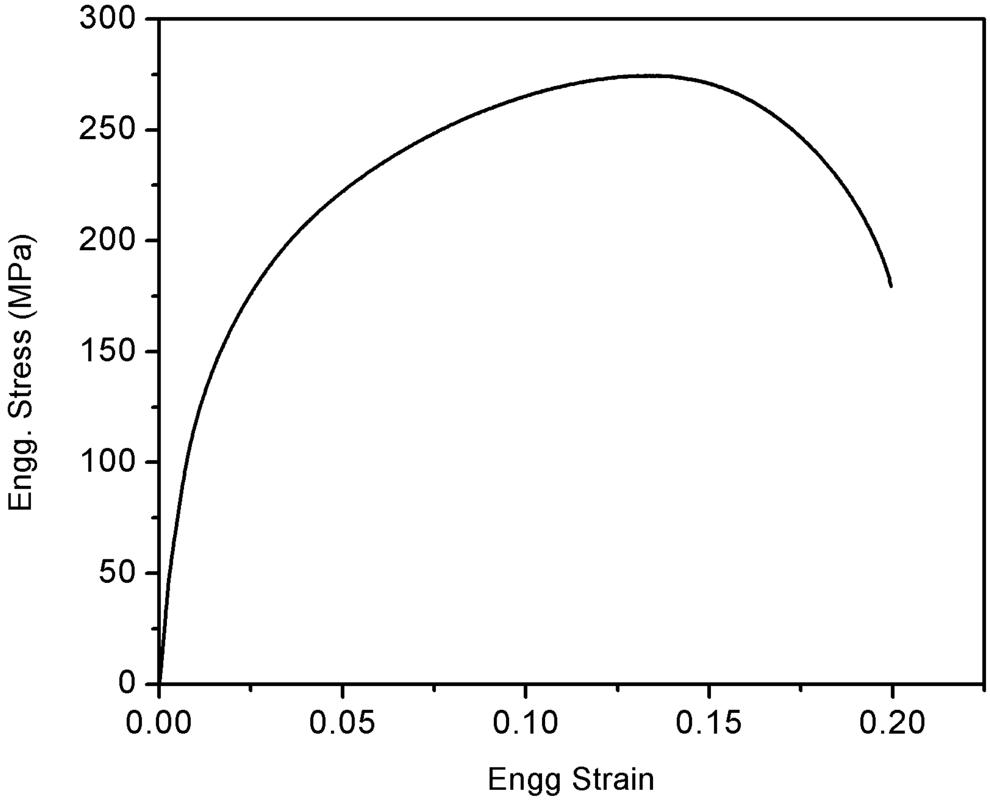

Figure 4.13: Tensile engineering stress-strain curve of annealed Nb alloy sample.

4.5. Fracture surface of the alloy

4.5.1. As-solidified sample

Fracture surface of the tensile tested sample of as-solidified is shown in Fig.4.14. SEM micrograph of the as-solidified sample (Fig.4.14(a)) shows the cleavage fracture. In order to know where from cracks are originating, fractured sample was examined at higher magnification. Fig.4.14(b) shows the grain boundary region. It did not show the presence of cracks at the grain boundaries. Closer observation of SEM micrograph of Fig.4.14(a) has shown the presence of fine cracks at the needle morphology carbide precipitates. High magnified micrographs of the carbide precipitates Fig.4.14(c) & (d) clearly showing the initiation of cracks at the edges of the carbide precipitates. These cracks propagated transgranularly across the grains. The SEM micrographs of the fractured sample had revealed that the main source for poor ductility of as-solidified samples is the presence of needle morphology carbide precipitates. These carbide precipitates acted as stress concentration regions and led to crack initiators. It caused failure of the as-solidified samples with very little plastic deformation.

4.5.2. Annealed sample

Fracture surface of the tensile tested annealed sample was examined under SEM (Fig.4.15). Fig.4.15(a) shows the presence of a lot of voids on the fractured surface. When it was examined at higher magnification (Fig.4.15(b)), it showed the presence of dimple fracture surface indicating the transgranular fracture. The presence of large and deep dimples in the fractured surface of the annealed specimen is an evidence for high ductility of the specimen. The SEM micrograph also shows the presence of voids within the grains. With increasing deformation, these voids expand and join together formed big size voids ((Fig.4.15(c)&(d)). These big size voids caused failure of the sample. The transgranular fracture and presence of dimples and voids in the fractured surface indicating that the annealed sample was fractured under ductile mode.

4.6. Flow sheet for the fabrication of the Nb alloy at low temperatures

Based on the experimental studies on the effect of thermomechanical treatment on microstructure and properties of the Nb alloy, new flow sheet (Fig.4.16) for the low temperature fabrication of tubular products of Nb alloy has been developed. The Nb-1%Zr-0.1%C alloy was prepared

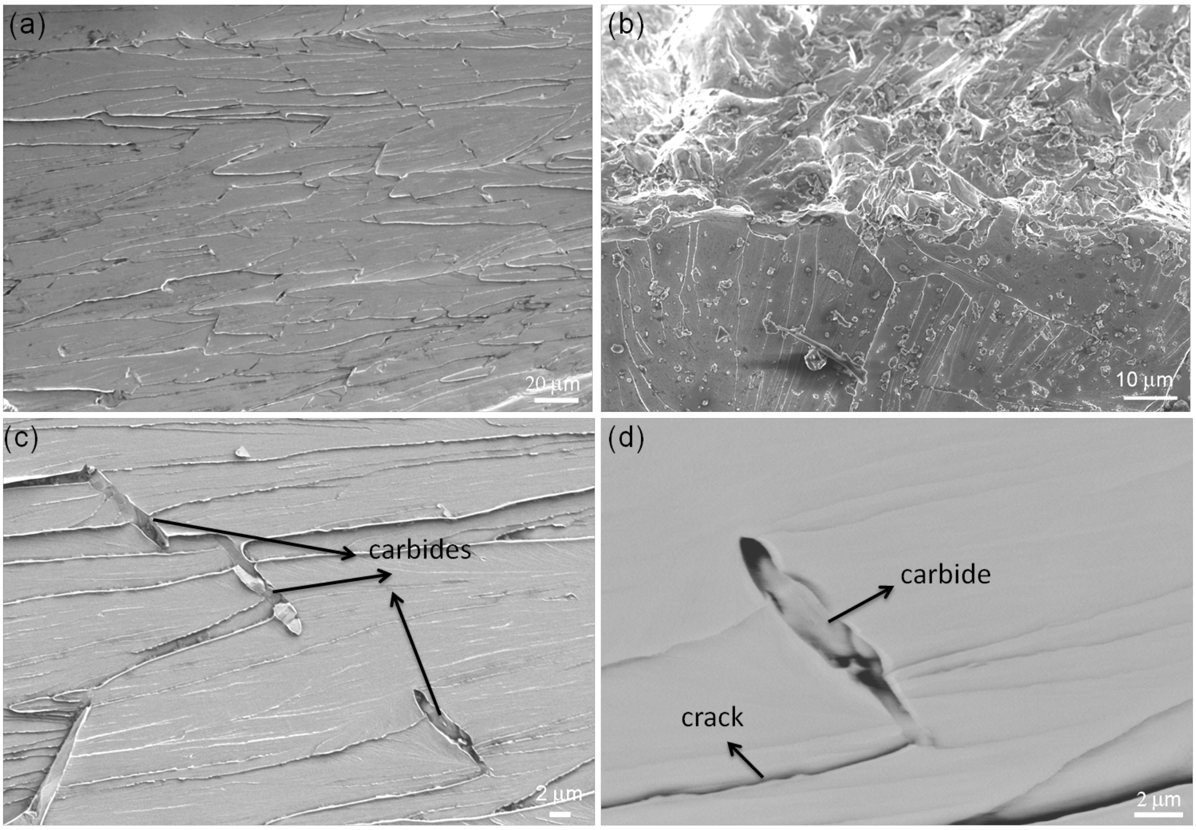

Figure 4.14: Fracture surface of the tensile tested as-solidified sample showing (a) cleavage fracture, (b) absence of cracks at the grain boundaries and (c) & (d) cracks are initiating at the edges of the carbide precipitates.

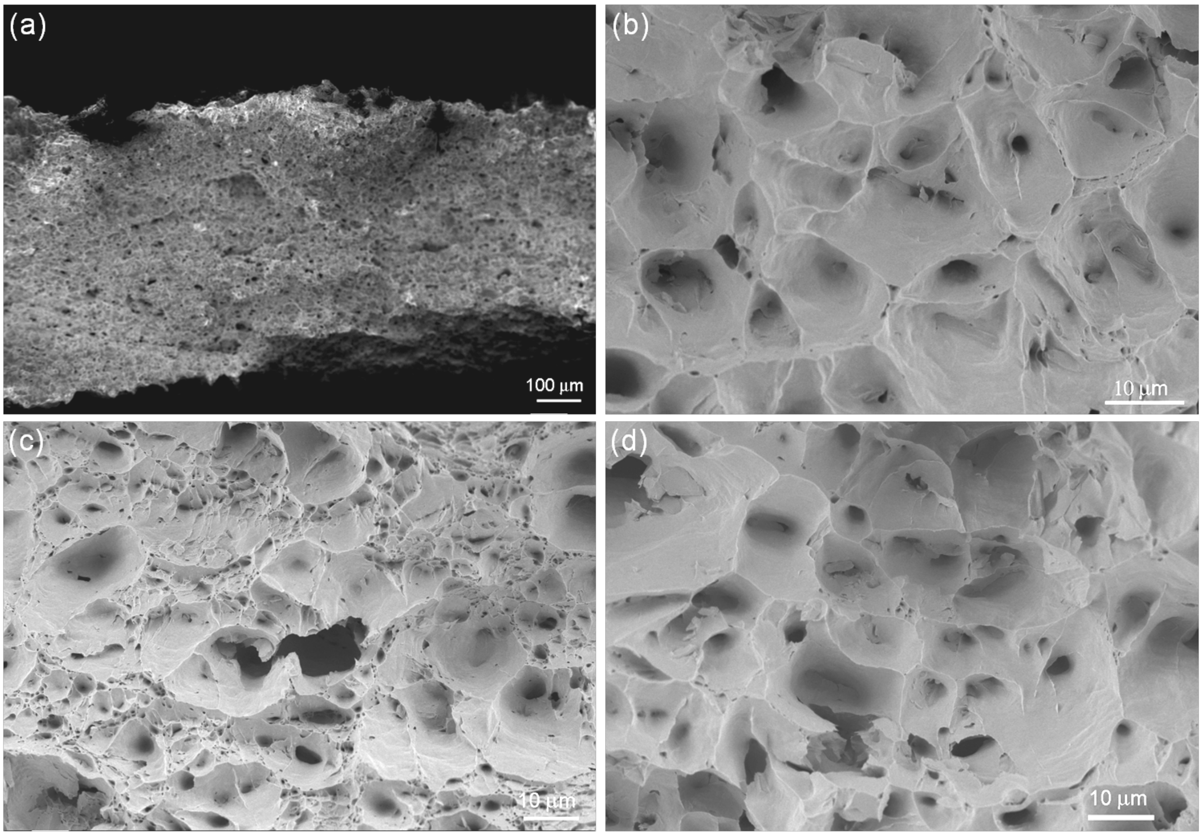

Figure 4.15: Fracture surface of the tensile tested annealed sample showing (a) the presence of voids, (b) transgranular fracture surface and (c) & (d) coalescence of small size voids leading to formation of bigger void.

by the electron-beam melting technique. Detailed procedure for the preparation of alloy including a flow sheet has been given in the experimental chapter. Subsequent to electron beam melting, vacuum arc remelting was carried out to homogenize and refine the grain size of the Nb alloy. In order to confirm the homogeneity of the ingot, chemical composition of samples taken at various locations of the ingot was determined. It showed that variation in composition at all the locations was within accepted limit and confirmed the homogeneity of the Nb alloy ingot.

As discussed earlier to achieve deformation under compressive stresses, a hole was drilled in the solid ingot. The hollow ingot was mechanically jacketed with seamless copper tubes. Subsequently, such billets were preheated and soaked at a temperature of 800 °C for 3 hrs before extrusion. The Cu jacket on the billet prevented the billet from oxidation during preheating. At the same time it also acted as lubricant owing to its lower flow stress and prevented any direct contact of the Nb alloy with tooling surface during extrusion. Extrusion was carried in a preheated container to prevent any major loss of heat from preheated billet to the container during extrusion. A conical die with semi die angle of 60° was used to reduce the formation of dead metal zone inside the container. Extrusion was carried out with an extrusion ratio of 5.8:1 and with a mean strain rate of 5.25 s^{-1}. The copper jacket from both outer and inner diameter of the extruded hollow billet was removed subsequently by immersing the whole blank into acid solution containing 45% HNO_3 where copper jacket dissolved as copper nitrate. Further extruded billets were annealed under vacuum at 1300 °C for 3 hrs to recrystallize the Nb alloy. The recrystallized Nb alloy showed average grain size of 30 μm similar to the grain size observed in the recrystallization experiments carried out on small samples.

Latter, the annealed Nb-1%Zr-0.1%C tubes were cold worked by pilgering at room temperature. Subsequent to each pilgering pass, the Nb alloy tubes were given intermediate annealing of 1300 °C for 3 hrs. A finished Nb alloy tubular product is shown in Fig.4.17.

4.7. Summary

The present work on the effect of thermomechanical processing on the microstructure and mechanical properties of Nb alloy can be summarized by the following highlights:

1. Microstructural investigation of electron beam melted samples showed presence of very large grains and uniform distribution of the needle morphology precipitates in the Nb

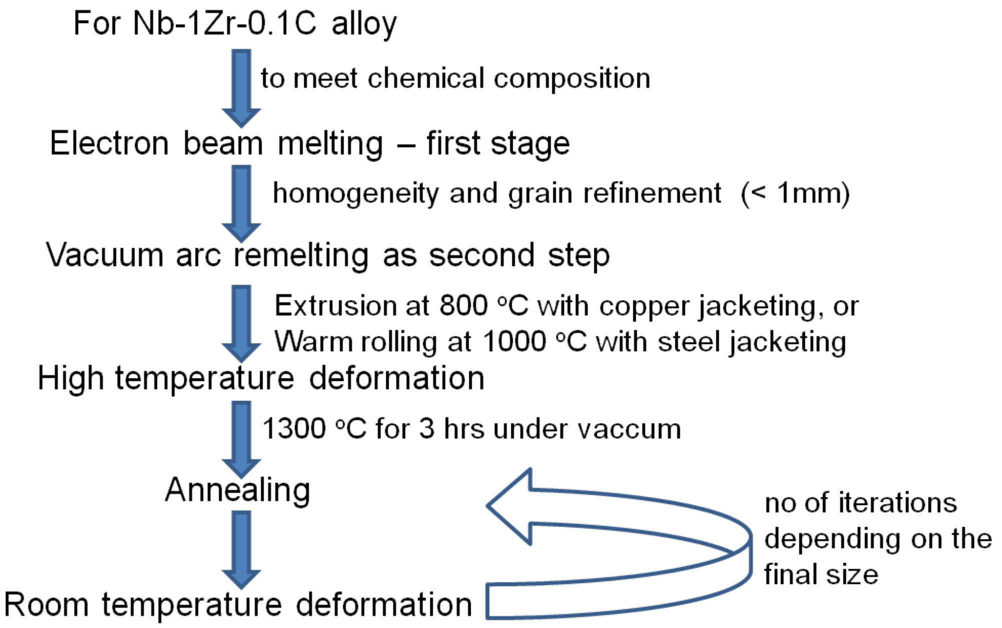

Figure 4.16: A flow sheet for the fabrication of Nb-1%Zr-0.1%C alloy tubular products.

Figure 4.17: Tubular product of Nb alloy obtained using low temperature deformation flow sheet (Fig.4.16).

matrix phase. Mechanical properties of as-solidified Nb alloy showed low ductility $\sim$2%. The fracture surfaces of tensile samples showed that needle morphology of precipitates acted as stress concentration regions and acted as source of crack initiation. It led to low ductility of the as-solidified Nb alloy.

2. Deformation compression tests showed two regions at which the alloy showed low value of flow stress: one at 800 °C and the other one at higher than 1000 °C. At intermediate temperatures, in between 800 - 1000 °C, alloy showed increase in flow stress with increase in temperature. The hot hardness experiments also showed similar tendency of increase in hardness in the intermediate temperature range of 800 - 1000 °C.

3. Since, Nb alloy had low flow stress at 800 °C, extrusion parameters were established by compression testing the as-solidified samples at 800 °C at different strain rates. It showed low strain rate sensitivity and high probability for cracking during extrusion at this temperature. Hence, to avoid cracking, hollow ingots were made and the ingots were successfully extruded at 800 °C without cracking and oxidation. Successful extrusion at 800 °C showed that the temperature for deformation can be brought down to 800 °C from the reported deformation temperature of 1600 °C.

4. Microstructural characterization of the deformed samples showed the presence of needle morphology and cuboidal morphology of precipitates in the Nb alloy. These microstructural changes were established reasons for change in flow stress with temperature. Decrease in flow stress up to 800 °C was due to dissolution of the precipitates present in the as-solidified samples whereas low flow stress at higher temperatures (>1000 °C) was due to the dominance of softening of the Nb matrix. Increase in the flow stress between 800 to 1000 °C was due to the precipitation of the additional cuboidal precipitates in the Nb matrix.

5. In addition to compression testings, warm rolling experiments were carried out on metal jacketed as-solidified Nb alloy at different temperatures (room temperature to 1100 °C). It showed high propensity for cracking below working temperature of 1000 °C and oxidation at higher than 1000 °C. It showed that as-solidified Nb alloy can be deformed by rolling up to 35% with out cracking and oxidation at 1000 °C. This study showed that the optimized temperatures for rolling and extrusion were 1000 °C and 800 °C, respec-

tively. It showed that deformation temperature for rolling was higher than the extrusion temperature.

6. Systematic annealing experiments at different temperatures were carried out. These experiments showed that the deformed Nb alloy either by rolling or by extrusion can be recrystallized by heat treating at 1300 °C for 3 hrs. The annealed samples showed average uniform grain size of $\sim$ 30 μm. EBSD analysis of the annealed sample showed that $\sim$ 97% of the grains were completely recrystallized.

7. Tensile testings of the annealed samples showed that after recrystallization, the Nb alloy showed improvement in mechanical properties and these mechanical properties matched with the Nb alloy material processed at higher temperatures. Examination of the fracture surface of the tensile tested annealed sample showed typical ductile fracture behaviour.

8. Based on deformation and annealing studies, a flow-sheet for the fabrication of tubular product of the Nb alloy at low temperatures ($<$0.5 T_m) has been developed.

CHAPTER 5

Formation of different carbide phases in the Nb alloy

In the Nb-1%Zr-0.1%C alloy, carbon has been added to increase the strength of the alloy by forming carbide precipitates in the alloy. Formation of various carbides in the Nb alloy reported in literature are listed in Table.2.5. Many of the carbides reported in literature are metastable in nature. Presence of many of these carbides provide an unique opportunity to tailor the microstructure suitable for a desirable materials property. In addition, these carbides also provide alternate pathways to achieve the microstructures through modifying heat treatments. Therefore, to exploit the role of carbides in determining high temperature properties, it is necessary to determine the crystal structure, their chemical composition, orientation relationship and their interrelation with other carbides. Keeping this in view, this chapter focuses on the formation of various carbides in the Nb-1%Zr-0.1%C alloy. Microstructural characterization (includes identification of the precipitate phase, grain size distribution etc) of the as-solidified, deformed and annealed Nb alloy samples was carried out using optical microscopy, XRD, TEM and HRTEM (High resolution transmission electron microscopy) techniques. Orientation relationship between precipitate phase and Nb matrix was also estimated and discussed in the present chapter. Composition analysis of the carbides was carried out using EDS technique in STEM mode. The present study has shown that formation of type of carbide phase depends on the processing condition of the alloy.

5.1. Background

In Nb-Zr-C alloys, formation of carbide phases is a multi stage process [19, 20, 49, 105–107]. The key to the development of a Nb-Zr-C alloy lies in the evolution of these carbide phases. Investigations on various carbide phases suggest that metastable carbides form during initial stages of the carbide formation. Since the solubility of carbon in niobium is limited at low temperatures (0.1 at.% at 1200 °C) [55], during cooling from high temperatures excess carbon atoms separate out to form carbon rich Nb-C phases aided by rapid interstitial diffusion. Details of the formation of these phases, especially the formation of different metastable precipitates, prior to the formation of equilibrium phase and the subsequent structural changes have not been investigated either theoretically or experimentally. In this respect the equilibrium ternary phase diagram of Nb-Zr-C is not complete enough for understanding of the aging process because the intermediate metastable phases are not represented in the equilibrium phase diagram. In a Nb-Zr-C alloy, with carbon content is well below the stoichiometry, there may be a pre-precipitation phenomenon whereby a carbon rich phase can form in conformity with a phase of the matrix crystal structure. The evolution of an ordered phase, for example, Nb_2C, may in all probability be preceded by clustering of carbon atoms to local active centers yielding subsequently ordered metastable intermediate phases containing less carbon than needed for the equilibrium phase [55]. Such an early stage of precipitation is a well documented phenomenon in substitutional alloys and relatively less reported, definitely not an unreported one, in the case of interstitial alloys [55, 108]. A detailed description of various carbide phases has already been presented in Chapter.2, where phase fields and composition details have been tabulated in Table.2.5.

Nb_2C is the stable carbide phase and exists in two allotropic forms, the hexagonal β phase above 1230 °C and the orthorhombic α phase below 1230 °C. The other Nb_3C_2 carbide phase is a metastable phase and exists in Nb-C alloys only when the alloy was quenched from high temperatures ($T > 1750$ °C). Alloying additions to binary Nb-C are known to modify the sequence of carbide formation. For example, early investigations have shown that additions of Zr, W to Nb-C (low carbon concentration) alloys enhance the formation of another carbide phase; i.e NbC (fcc) phase [19, 20, 49, 109]. The precipitation sequence in the D-43 alloy (Nb-10W-1Zr-0.1C) exhibited the presence of Nb_3C_2 and Nb_2C type carbides in the Nb matrix. After prolonged aging treatments these carbides were found to transform to the NbC phase [19, 49]. The Nb-11W-3Mo-2Hf-0.08C and Nb-17W-3.5Hf-0.12C [20] alloys have shown similar sequence of carbide precipitations.

Among all the carbides of Nb, formation of Nb_2C is most intriguing. The Nb_2C phase forms directly from the liquid phase as well as through a solid state reaction. At least three crystal structures of the Nb_2C phase have been identified. (1) α-Nb_2C, it has orthorhombic structure with lattice parameters of a = 1.09060, b = 0.30960, c = 0.49688 nm, (2) β-Nb_2C, ordered hexagonal structure with lattice parameter of a = 0.5407, c = 0.4968 nm, (3) γ-Nb_2C, disordered hexagonal structure with lattice parameter of a = 0.312, c = 0.4957 nm. Rudy *et al.* [54] have shown multistage carbide phase transformation in the Nb_2C phase. At above 1230 °C, α-Nb_2C carbide transforms to β-Nb_2C and at 2500 °C, β-Nb_2C transforms to γ-Nb_2C. These studies show that at room temperature, α-Nb_2C is the stable carbide phase in the Nb-C system. Titran *et al.* [110] have carried out microstructural characterization of Nb-1%Zr-0.1%C alloy. They have shown that the microstructure of vacuum arc melted cast ingots of Nb alloy have orthorhombic α-Nb_2C precipitates in the Nb matrix. Vishwanadham *et al.* [55], who studied formation of the carbide phase in the Nb-0.3 at% C alloy during the aging in the supersaturated stage, have observed that carbide precipitation is a multi-stage process. The initial precipitates have bcc structure with lattice parameters very close to the niobium matrix and remain coherent with the matrix. The final precipitate phase is the equilibrium hexagonal γ-Nb_2C phase and incoherent with the matrix phase. The orientation relationship between the Nb_2C and the matrix observed by Vishwanadham *et al.* [55] is $(0001)_{Nb_2C}$//$(011)_{Nb}$; $[11\bar{2}0]_{Nb_2C}$ // $[11\bar{1}]_{Nb}$. These observations are not in commensurate with the observation of formation of α-Nb_2C below 1230 °C. It highlights a fact that formation mechanism of Nb_2C is still not clear and further investigations on the formation of Nb_2C phase are required.

Brauer *et al.* [53] have found formation of ζ-Nb_4C_3 phase in the Nb alloy. It is isostructural with the Ta_4C_3 and V_4C_3 but actual stoichiometry near to Ta_3C_2 and V_3C_2. Crane *et al.* [23] have also reported on the similar phase formation in Nb-3.1 at.%C alloy. The XRD patterns obtained for this alloy matched with the XRD pattern obtained by Brauer *et al.* [53] for the Nb_4C_3 phase. However, there are some additional XRD peaks in the XRD pattern which remained unindexed. Latter, crane *et al.* [23] have reanalyzed it and confirmed that the phase has chemical composition as Nb_3C_2 with hexagonal structure having lattice parameters as a = 1.16 nm and c = 1.830 nm.

These studies indicate that identification carbides in the Nb alloy and their transformation mechanism is incomplete. Therefore, further analysis on morphology, crystallography and composition of the carbides is required. The present chapter is focused on the microstructural characterization of carbides (or second phase as mentioned in the previous chapter) present in the as-solidified, deformed and annealed Nb-1%Zr-0.1%C alloy. Based on the results, the underlying mechanism for the formation of carbides has been discussed.

5.2. Carbide formation in as-solidified microstructure

The optical micrographs of the as-solidified sample are shown in Fig.4.1 (Chapter.4). It showed the presence of large grain size and needle morphology precipitates in the Nb matrix. To identify the precipitate phase, the as-solidified sample was further characterized using XRD and TEM techniques. Fig.5.1 shows a conventional bright-field TEM image of the as-solidified specimen. The micrograph reveals a needle morphology of the second phase with dimensions of about 500 nm in width and up to several micrometers in length within the matrix phase. Dimensions of these needles matched well with those observed in optical micrographs. Filipleva *et al.* [59] have reported a similar needle morphology of the carbide phase in the as-cast Nb-Mo-Zr-C alloys. Fig.5.1 shows the presence of linear features within the precipitate inclined at 45° to the needle axis, indicating the presence of a high concentration of planar faults in the needle phase. Similar features are observed in other types of carbides in stainless steel [109]. To identify the precipitate phase, SAED patterns were collected at different zone axes from a single precipitate by systematically varying tilt angles (Fig.5.2). All these patterns could be successfully indexed in terms of a hexagonal lattice and lattice parameters are found to be a = 0.315 and c = 0.4957 nm. These lattice parameters were compared with the lattice parameters of various niobium carbides (listed in Table.2.5) and best match was found with the γ - Nb_2C carbide phase. SAED patterns collected from other needles (nearly 25 in numbers); could again be indexed in terms of aforementioned hexagonal lattice. Smith *et al.* [20] have reviewed the presence of various carbides in the Nb-C system. It has been reported that structure of the γ-Nb_2C is isostructural with β-W_2C and Mo_2C phases. It has $P6_3/mmc$ space group with the atom positions in the unit cell, two Nb atoms occupy the 2(c) positions with the coordinates (1/3 2/3 1/4), (2/3 1/3 3/4) and one C atom statistically occupies the positions 2(a) with the coordinates (0 0 0) and (0 0 1/2). When SAED patterns were simulated using JEMS software by providing atom positions of prototype hexagonal W_2C phase as input (shown in 2.5), a good match between the simulated and experimental patterns (shown in Fig.5.2(b)) ensured correct identification of Nb_2C phase. In addition, based on tilt angle separation between the two zone axes, angular separation between various zone axes was estimated using formulation (equation.5.1) developed by Xiaodong Zou *et al.* [111] and these are tabulated in Table.5.1.

$$\theta = \cos^{-1}\left(\cos x_1 \cos y_1 \cos x_2 \cos y_2 + \cos x_1 \sin y_1 \cos x_2 \sin y_2 + \sin x_1 \sin x_2\right) \tag{5.1}$$

Table 5.1: Tilt angle between zone axes.

Zone axis	Double tilt specimen holder		Angle between zone axes	
	α	β	Experimental	Theoretical
$[11\bar{2}0]$	1°	12.5°	30.105°	30°
$[10\bar{1}0]$	30°	4°		
$[30\bar{3}\bar{1}]$	23°	-14°	0°	0°
$[44\bar{8}\bar{3}]$	-4°	-9°		
$[22\bar{4}\bar{3}]$	-7°	-28°	50.21°	47.30°
$[01\bar{1}\bar{0}]$	-29°	20°		

Where, $(x_1, y_1), (x_2, y_2)$ correspond to α and β tilt angles of the two zone axes having angular separation θ.

These estimated angular separations matched well with the angular separation between zone axes of a hexagonal lattice. Tilt angles required to move from one zone to another zone in a hexagonal lattice are shown in Fig.5.3. When conventional X-ray diffraction patterns were acquired using various sources (Cu-K$_\alpha$, Mo-K$_\alpha$, Cr-K$_\alpha$) it could reveal only the bcc matrix phase. In order to get the X-ray diffraction peaks of carbide phase, synchrotron X-ray source (λ=0.73 A°) was used. The XRD pattern was obtained on the image plate and is shown in the Fig.5.4(a). It shows high intensity rings which correspond to Nb and in addition it shows some low intensity additional rings in the image which correspond to the second phase present in the as-solidified Nb alloy. Using FIT2D open source software, the XRD image was converted in to the standard X-ray diffraction pattern (intensity versus 2θ) and is shown in Fig.5.4(b). In the XRD pattern, first peak has very high intensity, it is due to the presence of large grains. Therefore, it is introducing the texture effect in the XRD pattern. Because of the high intensity of Nb peaks, the second phase XRD peaks are not visible in the patterns. This could be the reason for not obtaining the second phase XRD peaks in the conventional XRD pattern. When the low intensity region was enlarged (Fig.5.4), it showed the presence of additional peaks. These peaks could be successfully indexed in terms of the hexagonal lattice with the same lattice parameters which was established by SAED patterns.

EDS analysis of several carbide precipitates was carried out and the average composition of the phase was determined to be Nb: 63.5 ± 2 at%, C: 36.5 ± 1.5 at%. EDS analysis reconfirmed the identification of the carbide phase as Nb_2C. Composite SAED patterns having reflections from both the carbide phase as well as from the Nb matrix exhibited the presence of a common diffraction vector between the carbides and the matrix phase. By carrying out

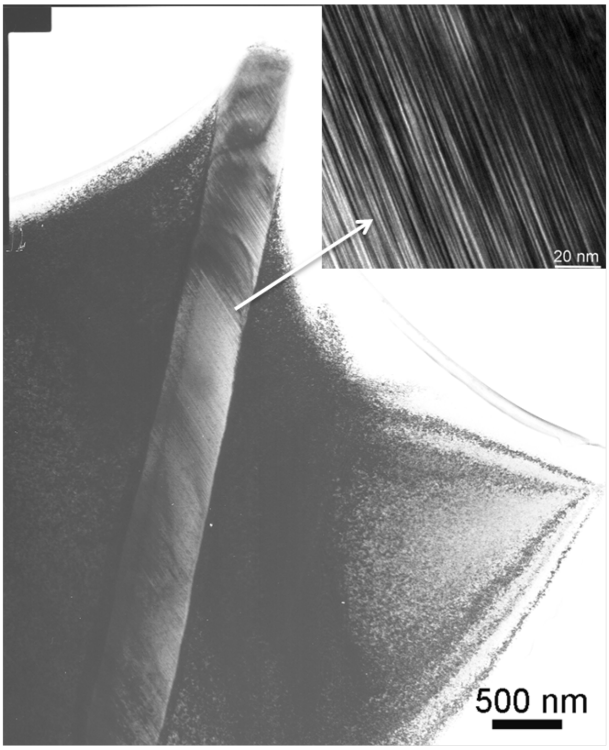

Figure 5.1: A typical bright field TEM micrograph of precipitates present in the as-solidified Nb alloy. The inset figure shows the presence of heavy faults within the precipitate.

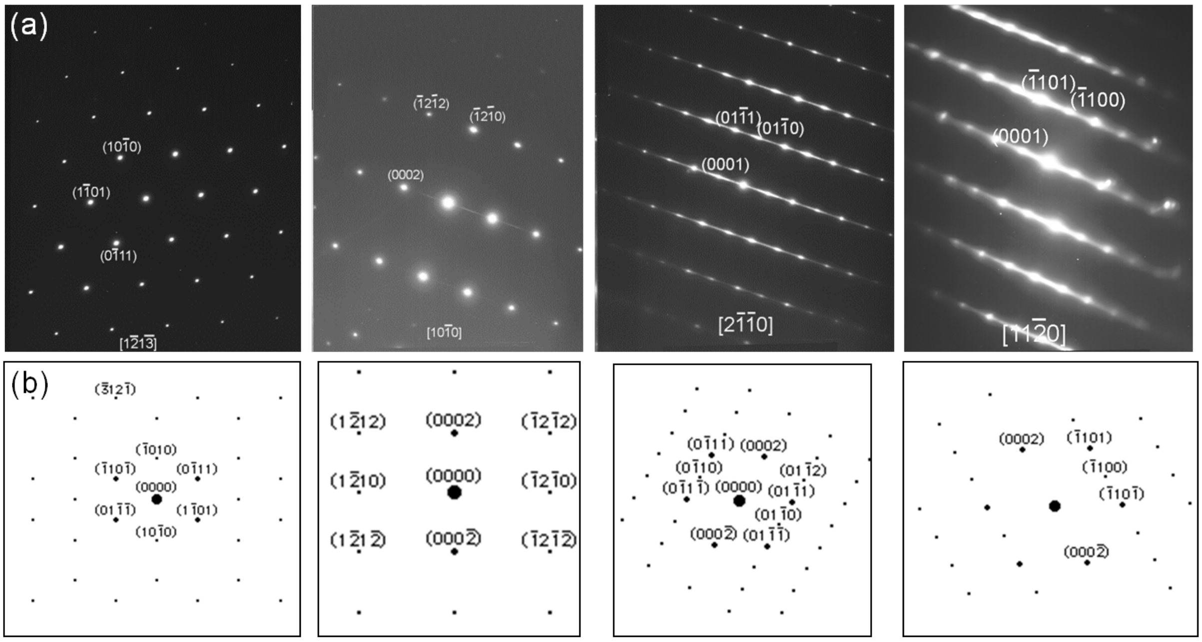

Figure 5.2: (a) SAED patterns obtained from the precipitates in as-solidified Nb alloy having needle like morphology. These SAED patterns were indexed with the Nb_2C phase and (b) Simulated SAED patterns using JEMS software by providing atom positions of prototype hexagonal W_2C phase [22, 112] as input, a good match between the simulated and experimental patterns ensured correct identification of Nb_2C phase.

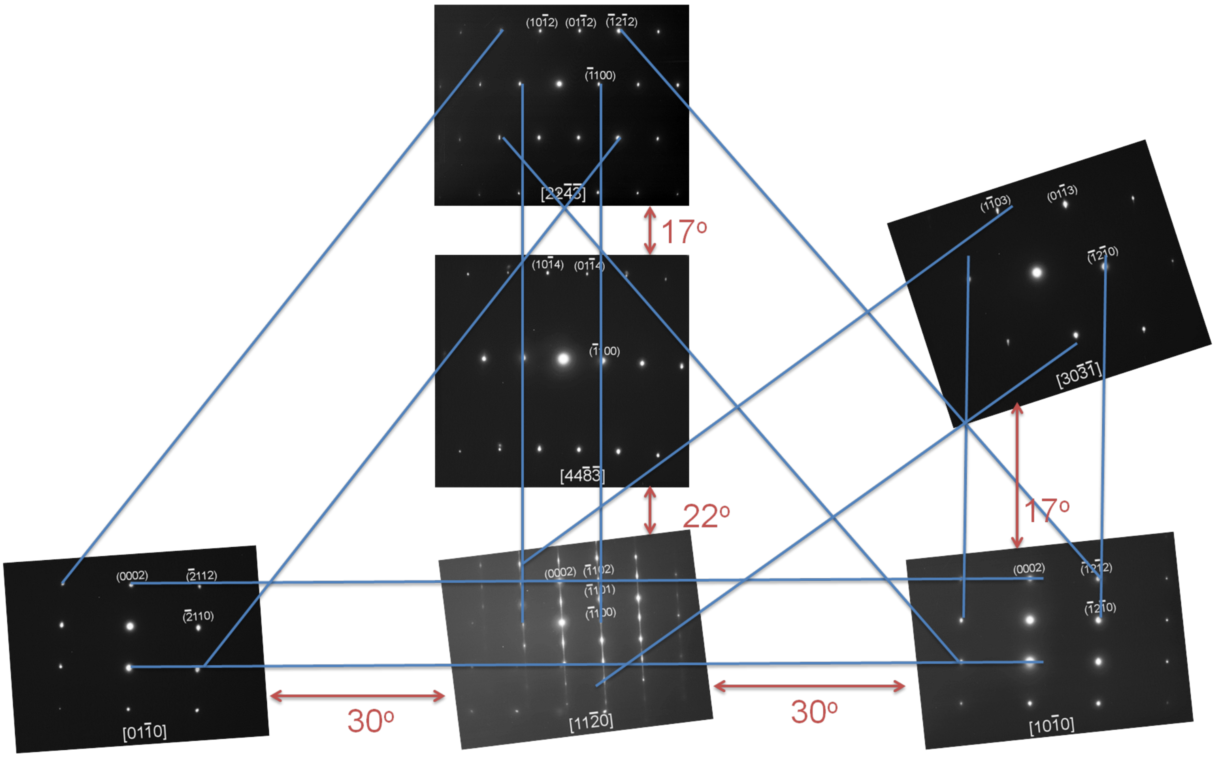

Figure 5.3: SAED patterns of the precipitate at different zones showing tilt angles required to move from one zone axis to another zone axis with Kikuchi lines.

systematic tilting experiments, several composite SAED patterns were obtained, as shown in Fig.5.5. This indicates a possibility of an orientation relationship (OR) to exist between the matrix and the precipitate, as was noticed in the optical micrographs. For example, when the sample was tilted in such a way that $[001]$ direction of the matrix phase got aligned with $[11\bar{2}0]$ axis of the precipitate phase, $(000\bar{1})$ plane of precipitate phase was found deviated nearly 5° from $(1\bar{1}0)$ plane of the matrix phase. The calculation of lattice parameter of the matrix phase from this relationship $(a_\beta = c/\sqrt{2})$ turns out to be 3.53 ± 0.07 A°, which is within 7% of the lattice parameter of pure Nb (a = 3.30 A°). By translating these relative orientations of SAED reflections pertaining to both the phases on stereogram (shown in Fig.5.6), a single OR between the precipitates and the matrix could be determined as shown below:

$$[1\bar{1}\bar{1}]_{Nb} \, // \, [\bar{1}\bar{1}23]_{Nb_2C} \, , (0\bar{1}1)_{Nb} \, // \, (01\bar{1}1)_{Nb_2C} \, and \, (12\bar{1})_{Nb} \, // \, (1\bar{2}1\bar{1})_{Nb_2C} \qquad (5.2)$$

This OR seems to be specific as evaluating the composite diffraction patterns from several other (25) carbide particles did not lead to the observation of any other OR. Based on this OR, the correspondence transformation matrix in reciprocal space relating vectors [uvw] of Nb matrix to vectors [u’ v’ w’] of Nb_2C precipitate has been derived. This can be expressed as:

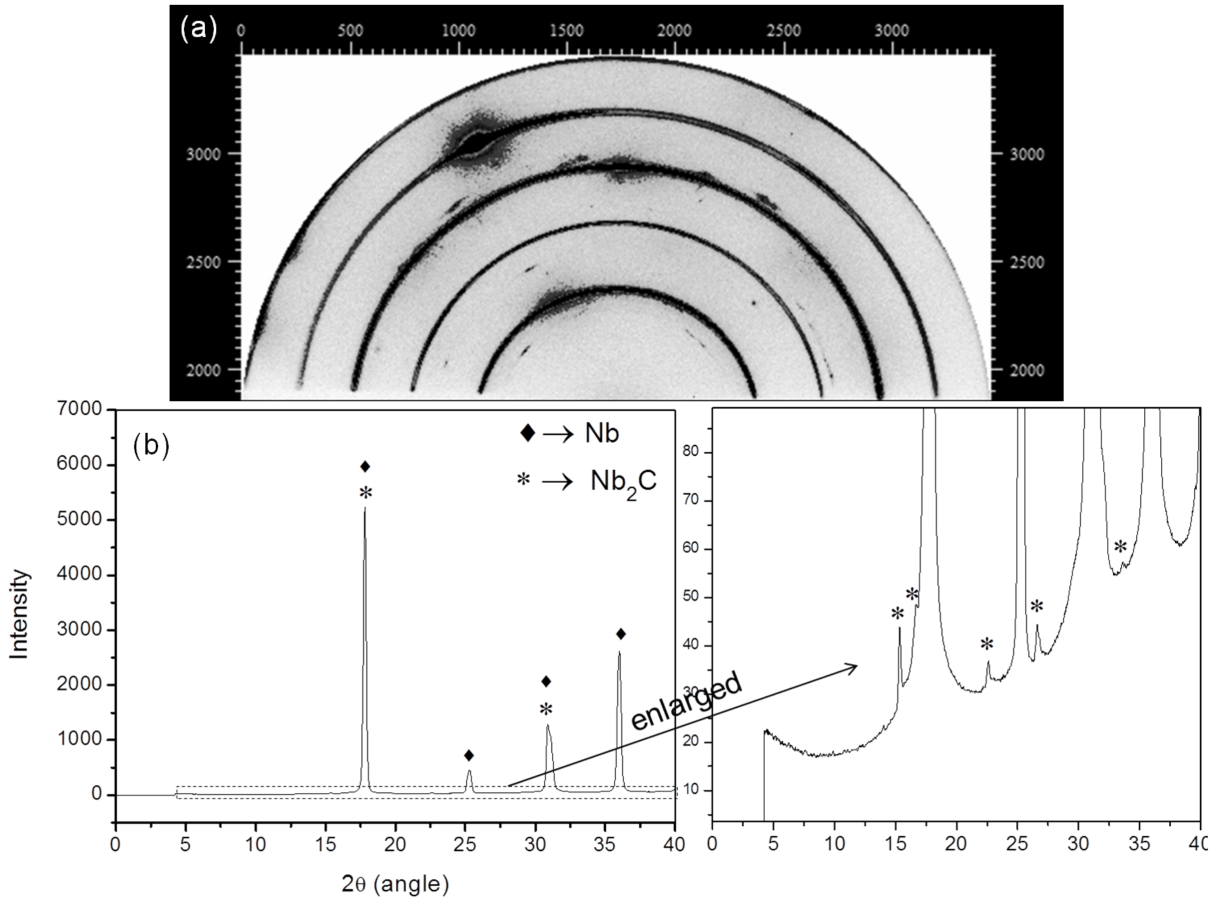

Figure 5.4: X-ray diffraction pattern of as-solidified Nb alloy obtained using synchrotron X-ray source (a) showing XRD image obtained on the image plate, it shows the presence of high intensity and low intensity rings corresponds to Nb and second phase precipitates present in the as-solidified Nb alloy and (b) showing intensity versus 2θ plot extracted form XRD image (a) showing the diffraction peaks for Nb and Nb_2C phases. An enlarged view of the area marked by dashed line shows the presence of Nb_2C peaks.

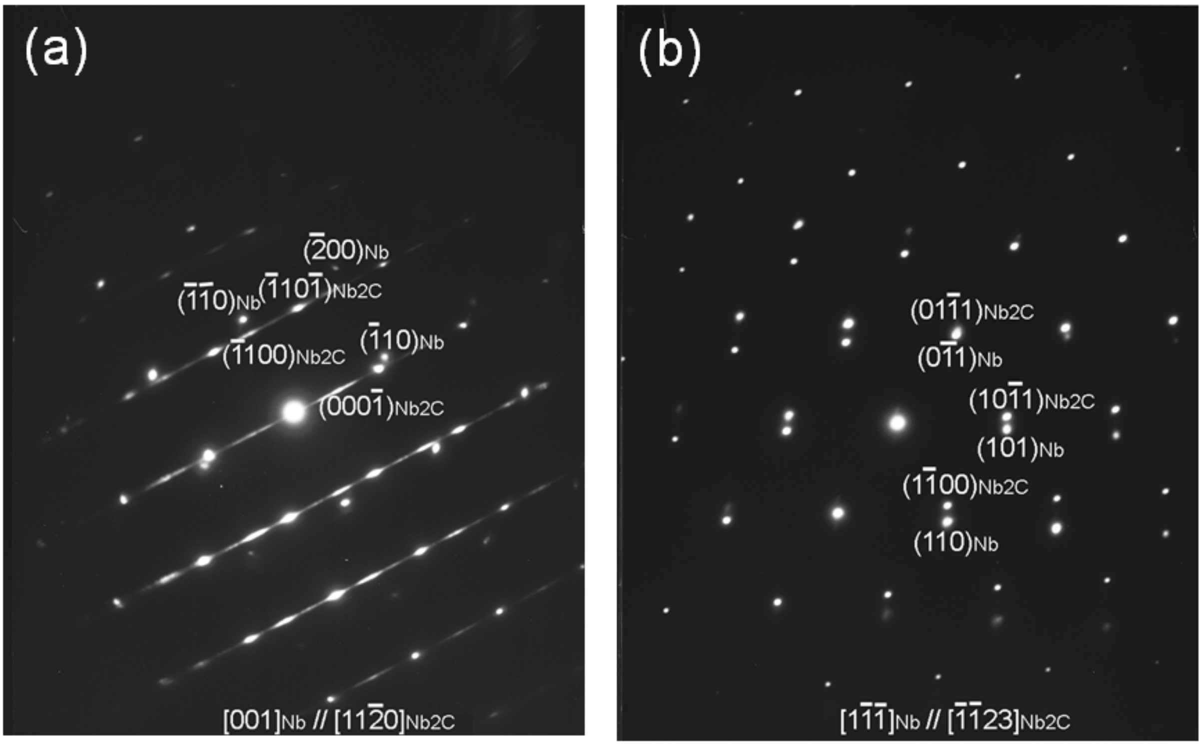

Figure 5.5: Composite selected area electron diffraction patterns of Nb matrix and Nb_2C precipitate showing the existence of orientation relationship between the two phases.

$$\begin{bmatrix} u' \\ v' \\ w' \end{bmatrix}_{Nb2C} = \begin{bmatrix} 0.4436 & 0.3306 & 1.0888 \\ -0.4524 & -0.4965 & 1.0200 \\ 0.4524 & -0.4870 & -0.0364 \end{bmatrix} \begin{bmatrix} u \\ v \\ w \end{bmatrix}_{Nb}$$

Using the correspondence transformation matrix (Equation.5.2) three additional orientation relations between other directions could be derived as:

$$[100]_{Nb} // [1\bar{1}01]_{Nb_2C} \tag{5.3}$$

$$[001]_{Nb} // [11\bar{2}0]_{Nb_2C} \tag{5.4}$$

$$[1\bar{1}1]_{Nb} // [\bar{2}110]_{Nb_2C} \tag{5.5}$$

Orientations (5.2,5.3,5.4,5.5) are shown in the stereographic projection (Fig.5.6) confirming that Nb_2C precipitates have a specific orientation relationship with the Nb matrix.

The TEM micrographs also suggest towards the alignment of the long axis of the carbide phase along a particular crystallographic direction of the matrix phase. The fine streaks at each reflection in Fig.5.5(a) originate from the planar faults present normal to the long axes of the

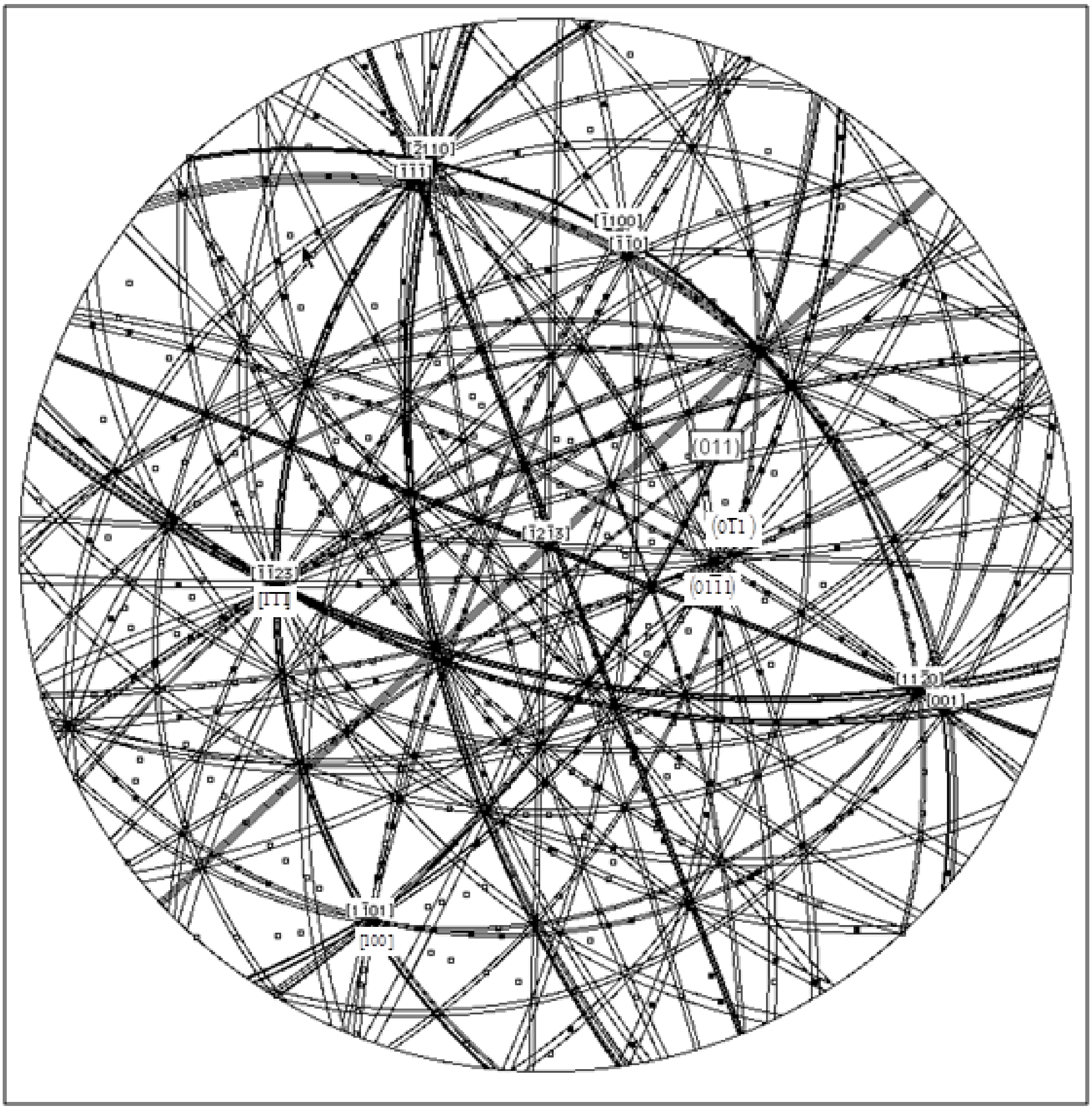

Figure 5.6: Stereographic projection showing trace of the planes and directions parallel to both the phases. Based on these traces a unique orientation relationship between the matrix and the precipitate phase was determined.

carbide needles; our analysis indicates that they are oriented orthogonal to the fault plane.

In order to find out the true growth direction and habit plane of the carbide precipitate, trace analysis method described by Andrews et al. [113, 114] was followed. For example, this sample was tilted until electron beam direction became parallel to zone axes $[100]$, $[1\bar{1}\bar{1}]$ of the matrix phase and SAED patterns and corresponding bright field images were acquired. Rotation of bright field image in relation to the diffraction pattern was calibrated using MoO_3 standard sample. The overlapped BF images and SAED patterns are shown in Fig.5.7. The precipitate growth direction and normal to growth direction are marked as A and B. [100] standard stereographic projection is taken for the trace analysis (Fig.5.7). Position of the reference directions (A & B) were calculated from the SAED patterns (Fig.5.7(a)) and are marked on the great circles of [100] and $[1\bar{1}\bar{1}]$ as A_1, A_2 and B_1, B_2 in Fig.5.7(b). The great circle has been drawn through projected direction A_1 and zone axis [100]. Similarly another great circle has been drawn through A_2, $[1\bar{1}\bar{1}]$. These two great circles intersected at the point T.D (true growth direction). This point was found out to be [131], this is the true growth direction of the carbide precipitate. To find out the habit plane, similar trace analyis has been applied for B_1 and B_2 and it was found to be $(11\bar{3})$.

High resolution images of the carbide phase were obtained after aligning along different zone axes (Figs. 5.8, 5.9). Fig. 5.8 shows the lattice fringes of the Nb_2C phase when viewed along the $[11\bar{2}0]$ zone axis of the phase. The inset figure shows enlarged view of the marked region. Interplanar distances of (0001) ($d_{(0001)}$= 0.4957 nm) and $(\bar{1}100)$ ($d_{(\bar{1}100)}$ = 0.2702 nm) are marked in it. Fig.5.8 also contains the simulated image of Nb_2C carbide phase along the $[11\bar{2}0]$ zone axis. This simulated HRTEM image, which was obtained at a defocus value of -7 nm and a thickness of about 9.67 nm, matched well with the experimental image of the Nb_2C phase. It showed that when viewed along $[11\bar{2}0]$, the Nb_2C structure exhibits three layered structure where a composite layer of Nb-C is sandwiched between two niobium layers. When carbide needles were viewed along $[\bar{1}\bar{1}23]$ direction their interface with the matrix (Fig.5.9), though, not atomistically flat, did not contain any discontinuity. Continuity of planes across the interface was even more evident when the interface was viewed under edge on condition (Fig.5.9). Under this condition planar defects, which were seen in HRTEM image of Fig.5.8, were nearly invisible as the vector of defects was aligned in the viewing direction.

Microstructural observations carried out on Nb_2C phase could be summarized as:

1. Diffraction patterns and the HRTEM (high resolution TEM) images were consistent with

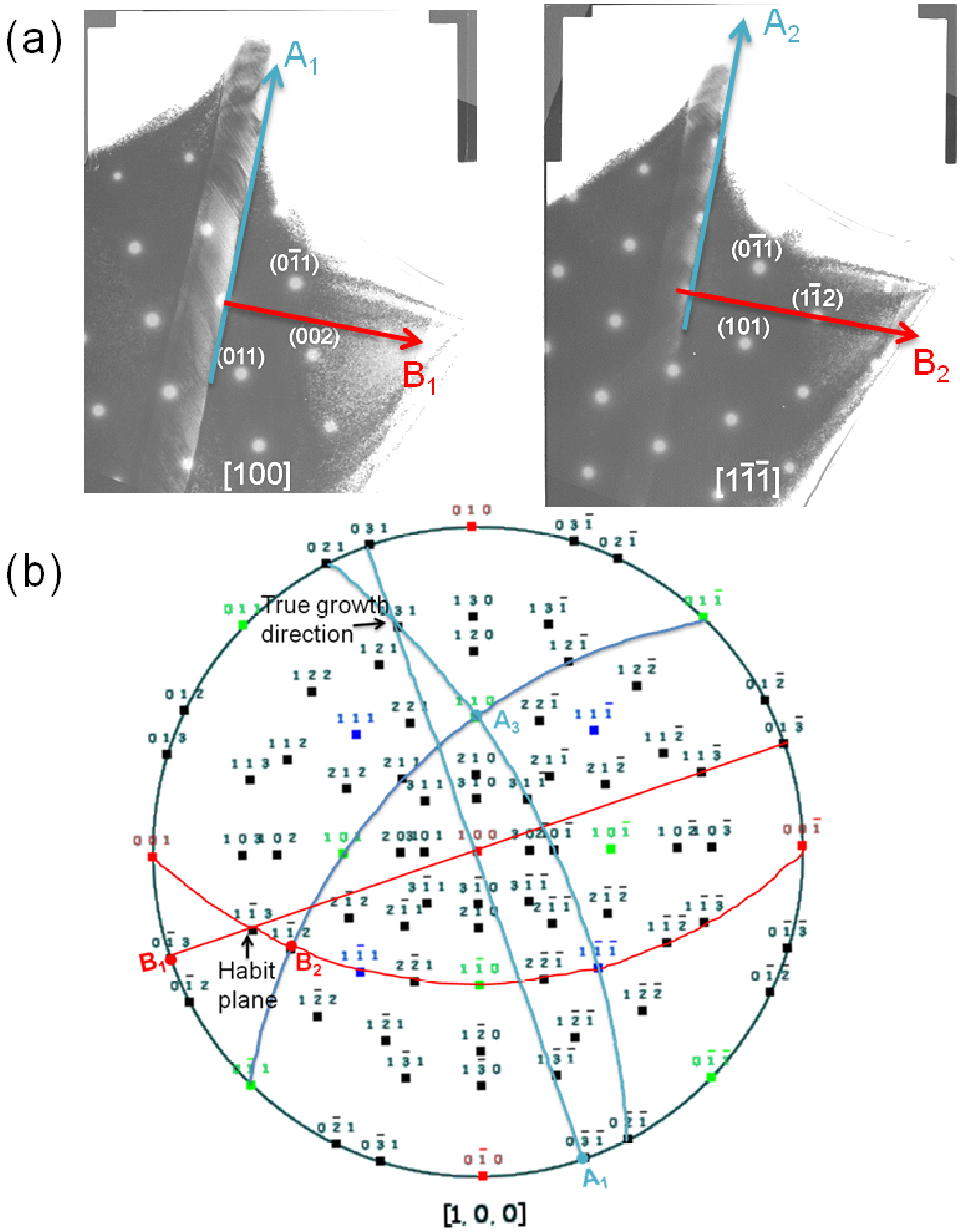

Figure 5.7: Overlapped electron micrographs of SAED patterns and corresponding bright field images to determine the true growth direction (A) and habit plane (B) of the carbide precipitate and (b) Standard [100] stereographic projection showing the true growth direction and habit plane of the precipitate.

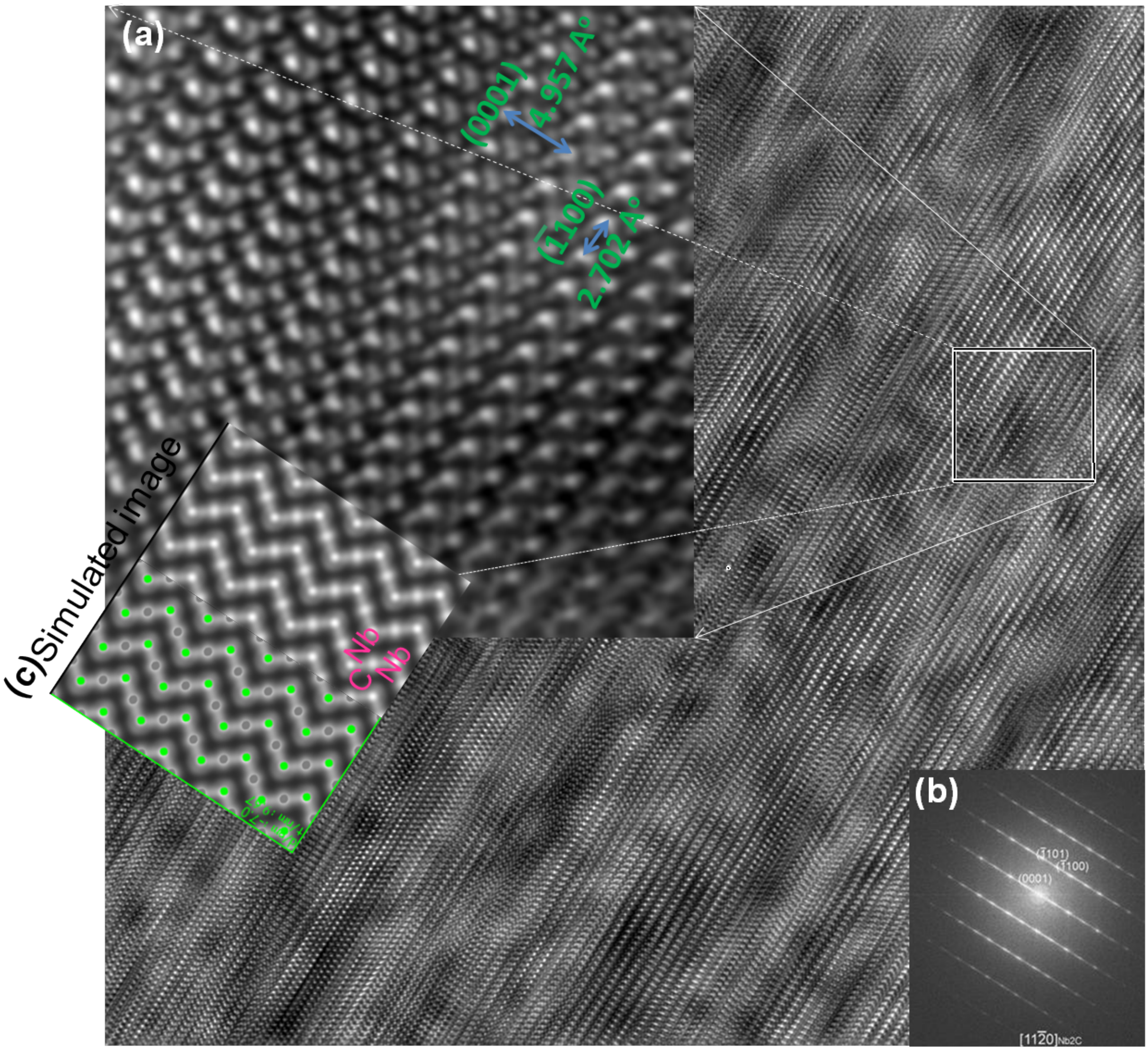

Figure 5.8: High resolution transmission electron micrograph of the carbide precipitate at the zone axis of $[11\bar{2}0]$, the inset figure shows (a) magnified image of the marked area, (b) corresponding FFT pattern of the HRTEM and (c) simulated HRTEM image of the Nb_2C at $[11\bar{2}0]$ zone axis.

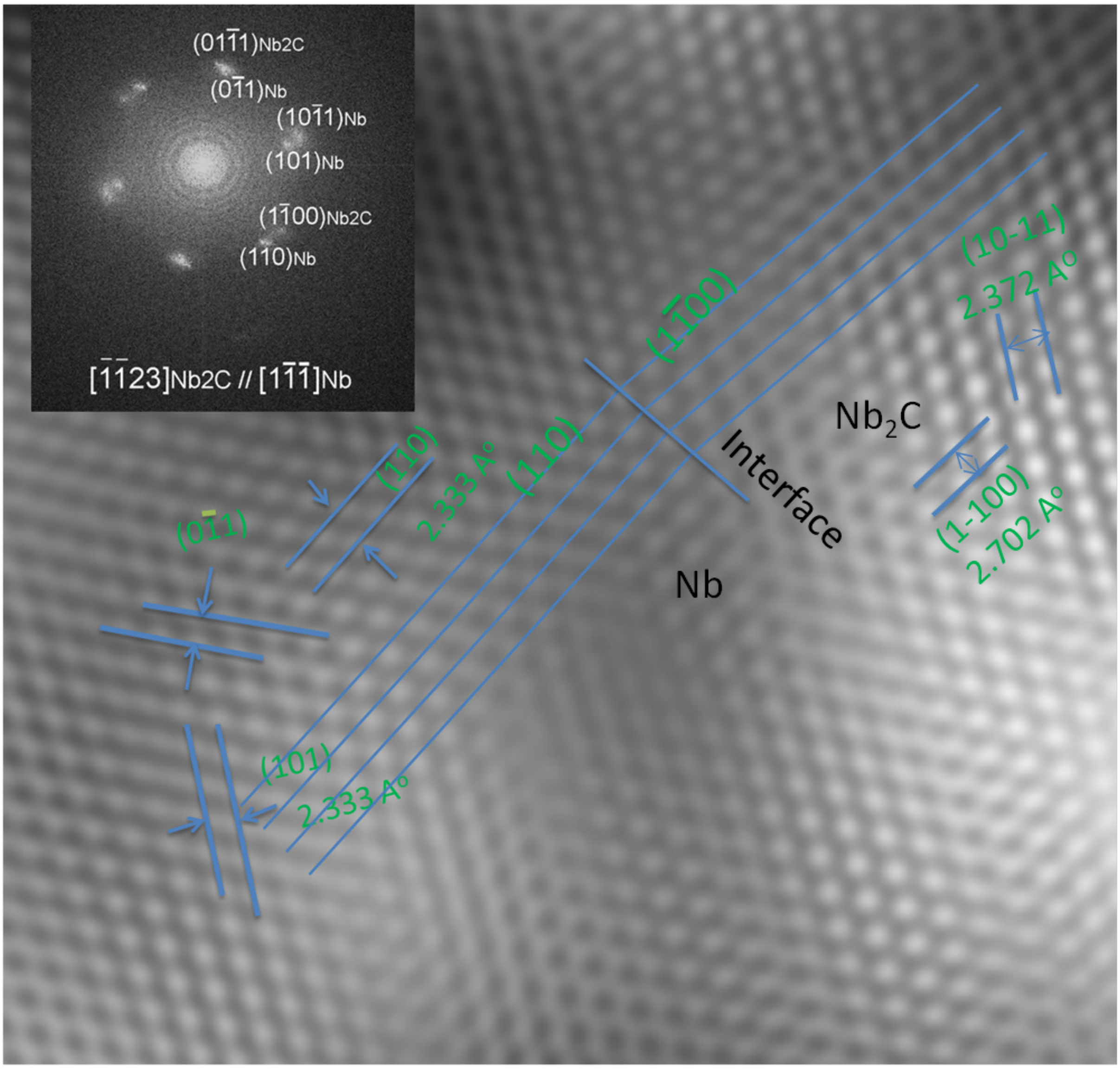

Figure 5.9: High resolution image of the interface between Nb matrix and Nb$_2$C carbide. The view of HRTEM is the $[1\bar{1}\bar{1}]$ zone axis of Nb which is parallel to $[\bar{1}\bar{1}23]$ zone axis of Nb$_2$C. The inset figure shows corresponding FFT pattern of the HRTEM image.

that of a hexagonal Nb_2C structure and the OR with the matrix determined as $[1\bar{1}\bar{1}]_{Nb} // [\bar{1}\bar{1}23]_{Nb_2C}$, $[001]_{Nb} // [11\bar{2}0]_{Nb_2C}$ and $(0\bar{1}1)_{Nb} // (01\bar{1}1)_{Nb_2C}$ appears specific, as all the composite SAD patterns of carbide needles with the matrix phase could be successfully indexed. This OR is apparently different from the one reported in literature [55, 115]. This difference in OR could be attributed to the difference in the processing and preparation of the alloy.

2. Chemical composition analysis of several carbide needles showed that Zr concentration in the carbide phase was nearly same as it was estimated in the matrix phase. This observation is not unexpected as at high temperature Zr has high solid solubility in the Nb matrix but during cooling it could not get partitioned to carbides due to insufficient time. Lattice parameter of the matrix phase determined from XRD patterns was 0.3418 nm which is nearly $\sim 3.5\%$ larger than the pure Nb lattice parameter (a = 0.3303 nm). Such variations in lattice parameter also provide evidence of the presence of Zr and C in the matrix phase. In short, the Nb_2C precipitates in the present study could be considered as a binary phase for most of the treatment.

5.2.1. Structural relationship between Nb and γ-Nb_2C carbide phase

Crystal structure of Nb_2C drawn with Nb atom at origin position and shown in Fig.5.10(a). Lattices of the Nb matrix and Nb_2C phase have been drawn in accordance with the aforementioned OR and shown in Fig.5.10(b). From this figure it could be noticed that the distance between two Nb atoms along [100] direction of the bcc - Nb is 0.33 nm which is nearly same as the distance between two Nb atoms along $[1\bar{1}01]$ in the Nb_2C precipitates. Similarly, the distance between two Nb atoms of 0.57 nm along $[1\bar{1}\bar{1}]$ direction is almost same as the distance between two Nb atoms of 0.58 nm along $[11\bar{2}3]$ direction. Similarly relationships can be shown to exist between other Nb atom positions also. This structural relationship between bcc - Nb and the Nb_2C carbide phase shows that the transformation of Nb to Nb_2C requires very small movement of Nb atoms. This fact could be better realized when the carbide phase is viewed along $[1\bar{1}\bar{1}]$ direction of the bcc Nb matrix. Fig.5.9 shows the high resolution image of the interface between the matrix and the carbide phase. The matching of the planes across the interface is so well that the interface become indistinguishable. Rotation of the planes (marked on Fig.5.9) is nearly of the order of $\sim 10^\circ$. Examination of the entire interface shows that matching remained as seamless as shown in Fig. 5.9. In order to further clarify the small shift of Nb atoms during

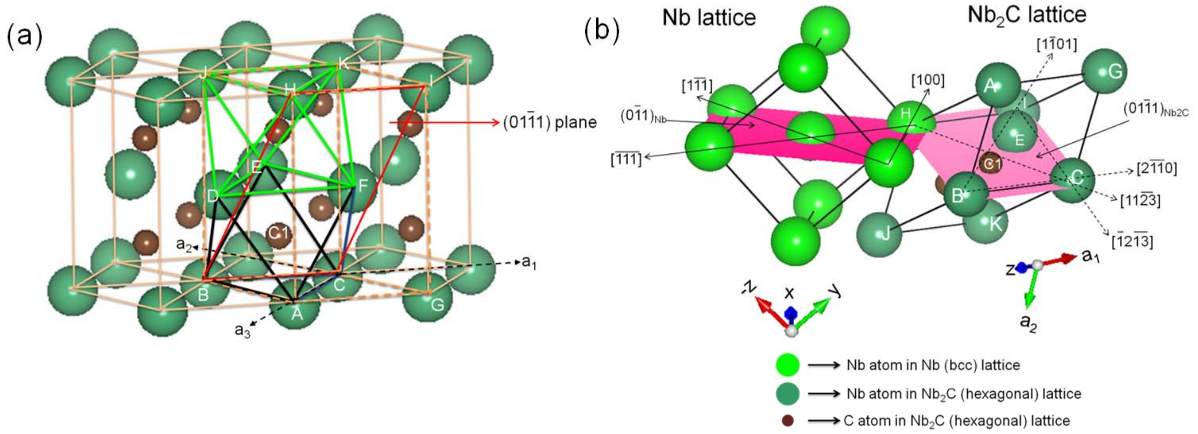

Figure 5.10: (a) Crystal structure of Nb_2C, showing the presence of carbon atoms at octahedral sites in hexagonal unit cell, (b) schematic of the orientation relationship ($[1\bar{1}\bar{1}]_{Nb} // [\bar{1}\bar{1}23]_{Nb_2C}$, $(0\bar{1}1)_{Nb} // (01\bar{1}1)_{Nb_2C}$) between Nb_2C carbide and bcc Nb matrix phase (Nb_2C unit cell shown in Fig. 5.10(b) is marked with alphabets as shown in Fig. 5.10(a)).

transformation of Nb to Nb_2C, the Nb and Nb_2C lattices are superimposed after orienting in accordance with their above mentioned OR (Fig.5.11(a)). In this figure some of the atoms are deleted to avoid confusion in visualization. It shows that all the Nb atoms in the Nb_2C lattice are shared with the Nb atoms in the Nb lattice except for a small shift in the atom positions. This clearly indicates that the transformation of Nb to Nb_2C takes place with very small movement of Nb atoms.

The HRTEM image (Fig.5.9) shows that habit plane for the carbide precipitate is $(1\bar{1}2)$, whereas the habit plane found from the trace analysis is $(1\bar{1}3)$. Angle between $(1\bar{1}2)$ and $(1\bar{1}3)$ is 10°. This small difference could be due to the error in drawing traces and finding accurate position of reference direction on the SAED pattern. The trace analysis is further confirming that the habit plane for the carbide phase is very close to $(1\bar{1}2)$ plane.

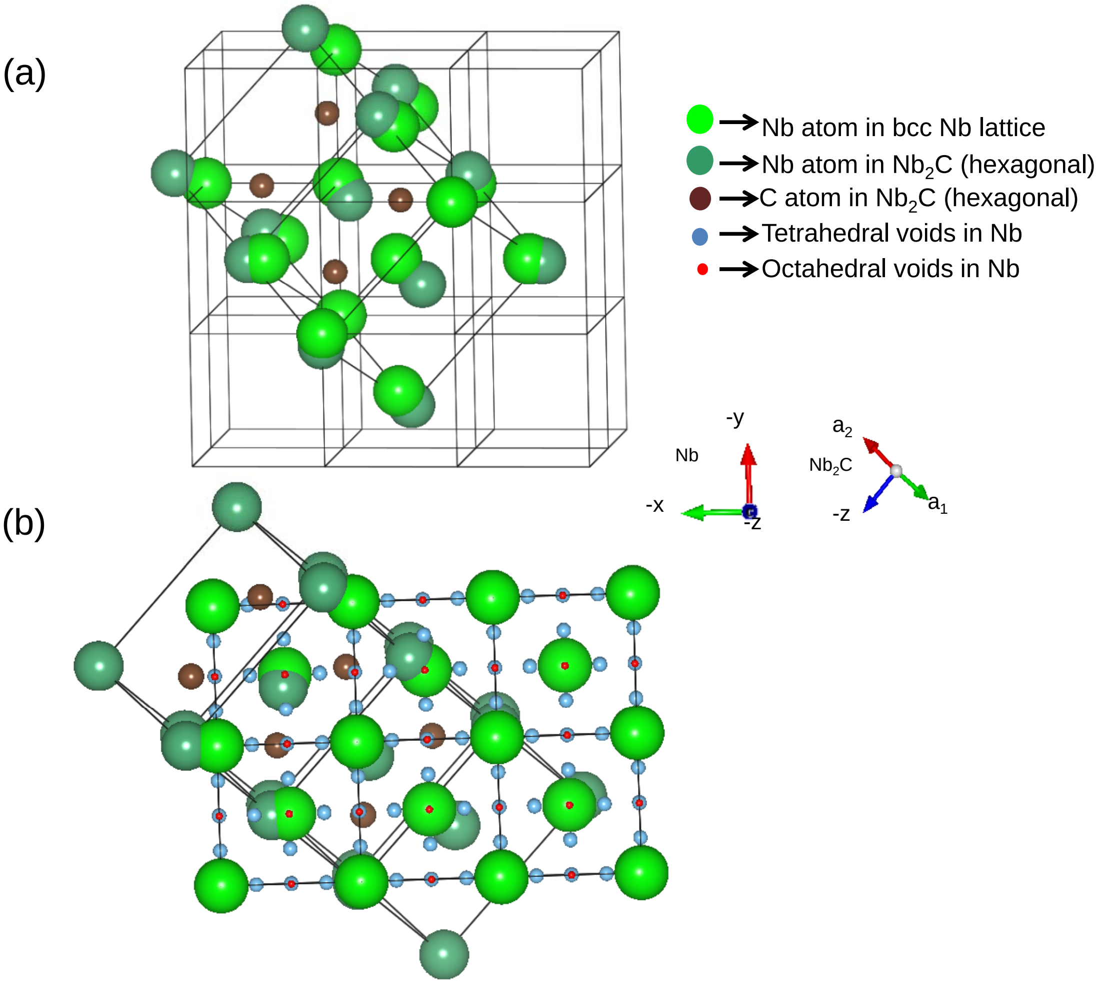

Figure 5.11: (a) Pictorial representation of overlapping of Nb and Nb$_2$C crystal structure with their orientation relationship showing that the transformation from bcc Nb to Nb$_2$C requires small movement of Nb atoms and (b) showing carbon atoms in the Nb$_2$C unit cell occupy the face center of Nb bcc unit cell and it is closer to octahedral void position in Nb lattice.

5.2.2. Atomistic mechanism of γ-Nb_2C formation

As positions of Nb atoms remained nearly unaltered, interstitial carbon atoms must play a key role in the formation of the Nb_2C phase. By examining the unit cell of Nb_2C it can be noticed that positions of carbon atoms are the positions of octahedral voids in the hexagonal lattice (Fig.5.11(a)). This means that carbon atoms are occupying the interstitial sites. In order to identify the location of carbon atoms with respect to Nb lattice, Nb lattice was redrawn schematically with octahedral and tetrahedral vacancy positions marked on it and Nb_2C lattice was overlapped with the properly oriented matrix lattice described by the orientation relationship (Fig.5.11(a)). It clearly shows that the carbon atoms are occupying position on the face of the bcc Nb lattice. Upon closer examination it showed that carbon atoms in the Nb_2C lattice are located very close to the octahedral voids of bcc Nb (Fig.5.11(b)). It is a well known fact that carbon atoms occupy octahedral voids because octahedral voids are more favorably placed for the relief of the strain due to the occupation of carbon atom in it than tetrahedral void. It is well reported in case of iron. The similar behavior is noticed in the present case.

As orientation relationship between bcc Nb and Nb_2C (equation.5.2) suggests that $(0\bar{1}1)$ planes of bcc Nb is parallel to $(01\bar{1}1)$ plane of Nb_2C (Fig.5.10(b)). It could be envisaged that $(0\bar{1}1)$ plane of Nb can transform into $(01\bar{1}1)$ plane of Nb_2C lattice. Fig.5.10(a) shows the atomic arrangement of an octahedral void and Nb atoms surrounding the voids are marked as A,B,C,D,E,F. Fig.5.12 shows atomic arrangements of $(0\bar{1}1)$ plane in Nb and $(01\bar{1}1)$ plane of Nb_2C lattices superimposed on each other. Three atoms out of the six atoms (B, C and F) surrounding the octahedral void (marked in Fig.11) lie on this $(0\bar{1}1)$ plane. Two atoms (C & F) out of these three atoms fall along the closest packed direction ($[1\bar{1}\bar{1}]$ in the present case). Therefore any displacement along closest pack direction shifts atoms away from the direction. In the present case out of the two Nb atoms, one atom (e.g., the atom marked as F) is displaced out of the $(01\bar{1}1)$ plane by an amount of 0.09 nm and the other atom (marked as C) shifts by an amount of 0.014 nm along $[\bar{1}11]$. Due to this shifting of atoms, parallel to $[\bar{1}\bar{1}23]$ direction of Nb_2C, one row of Nb atoms (marked as a in Fig.5.12) shifts in plane and the second row of Nb atoms (marked as b) shifts out of plane. This shifting of atomic row repeats itself. Similar behavior could also be observed when viewed parallel to $[\bar{2}110]$ direction. Another insight of small shifting of atoms out of the $(0\bar{1}1)$ plane in bcc Nb lattice to convert it into Nb_2C can be viewed from the Fig.5.13. Fig.5.13(b) shows the arrangement of atoms around an octahedral void in Nb bcc lattice. An octahedral void in bcc is not symmetrical. It has one shorter vertex length as compare to other two vertex lengths. Because of this the maximum space along the shorter vertex in bcc Nb lattice is $\sim$ 0.036 nm (direction EF) and along other two vertices is $\sim$ 0.172 nm (directions AD & CB). Therefore, the maximum sizes of the atom that can fit in the octahedral void without distortion along EF and AD are 0.036 and 0.172 nm respectively. Size of the carbon atom is 0.154 nm. Therefore, if a carbon atom occupies a octahedral void in the bcc Nb lattice, as shown in Fig.5.13(b), it does not distort the lattice along AD or CB but produces a distortion of 0.059 nm along EF. Due to this distortion, Nb atoms marked as E and F shift out of the $(0\bar{1}1)$ plane.

Nb_2C unit cell from Fig.5.11(a) is shown separately in Fig.5.14 to show the transformation behavior from Nb to Nb_2C. It shows that the vectors $[111]\,, [001]\,, [\bar{1}\bar{1}1]$ and $[\bar{1}10]$ in bcc Nb lattice become $[2\bar{1}\bar{1}0]\,, [11\bar{2}0]\,, [\bar{1}2\bar{1}0]$ and $[000\bar{1}]$ vectors in the Nb_2C lattice with small rotation and shifting. Distance between two Nb atoms along [111] direction in Nb lattice is 2.85 A°, it becomes 3.12 A° along $[2\bar{1}\bar{1}0]$ direction in Nb_2C lattice. Similarly, distance between Nb atoms along $[\bar{1}10]$ is 4.66 A°, it becomes 4.957 A° along $[000\bar{1}]$ direction in Nb_2C lattice. It indicates that occupation of octahedral voids in Nb lattice by carbon atoms makes minor changes in the Nb lattice and it becomes Nb_2C lattice.

5.2.3. Origin of strain during transformation

Using lattice parameters of the Nb_2C phase typical radius of an octahedral void was estimated as 0.0716 nm [116]. This size of an octahedral void is smaller than the size of a carbon atom (0.077 nm). It is therefore obvious that introduction of a carbon atom results in significant strain which is estimated to be a dilatation strain (δ) of 8.45%. This strain can be conveniently resolved along three of the basis vectors of the host lattice by equation.5.6.

$$\epsilon_{a_i} = dot\left(\epsilon_u, \vec{a}_i\right) \tag{5.6}$$

where ϵ_u is given by, $\epsilon_u = \delta\frac{\vec{u}}{|\vec{u}|}$, in which u is the vector connecting the octahedral void to unit cell origin. In the present case magnitudes of the ϵ_{a_i} along the three basis vectors (X = $[2\bar{1}\bar{1}0]_{Nb2C}$, Y = $[\bar{1}2\bar{1}0]_{Nb2C}$ and Z = $[0001]_{Nb2C}$) of the hexagonal lattice, due to a carbon atom at the octahedral position (2/3, 1/3, 1/4) estimated to be 0.0717, 0.0358 and 0.0269. Fig.5.10(a). shows relative arrangement of octahedral voids within a unit cell of Nb_2C. Their relative inclination along the unit cell is so arranged that if the other octahedral position (i.e., 2/3, 1/3, 3/4) is occupied by another carbon atom it would produce strain -0.0717, -0.0358 and 0.0269 along the

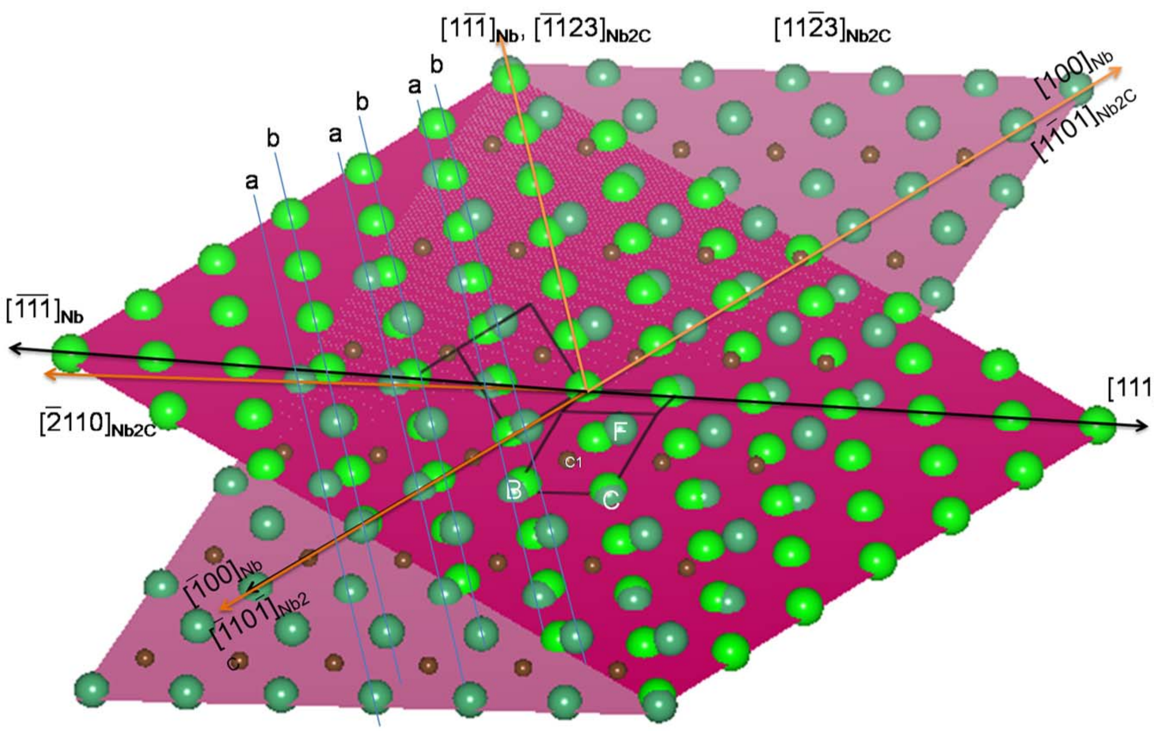

Figure 5.12: Superimposed planes of Nb $(0\bar{1}1)$ and Nb_2C $(01\bar{1}1)$, according to their orientation relationship $[1\bar{1}\bar{1}]_{Nb} \,//\, [\bar{1}\bar{1}23]_{Nb_2C}$, $(0\bar{1}1) \,//\, (01\bar{1}1)_{Nb_2C}$ showing atomic arrangement in both the planes and crystallographic orientations.

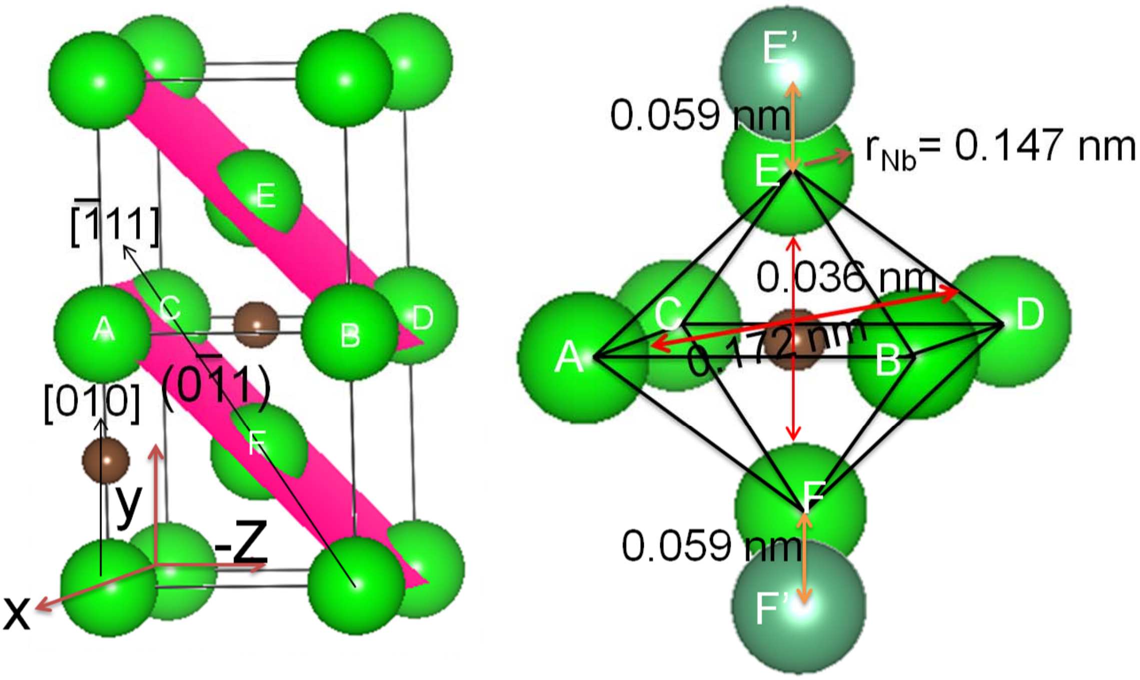

Figure 5.13: Illustrating occupation of carbon atoms at octahedral sites (face centered and edge centered) in the bcc lattice and it shows (b) large distortion necessary to accommodate a carbon atom in the face centered octahedral void, due to this the Nb atoms (E and F) shifts away from $(0\bar{1}1)$ plane.

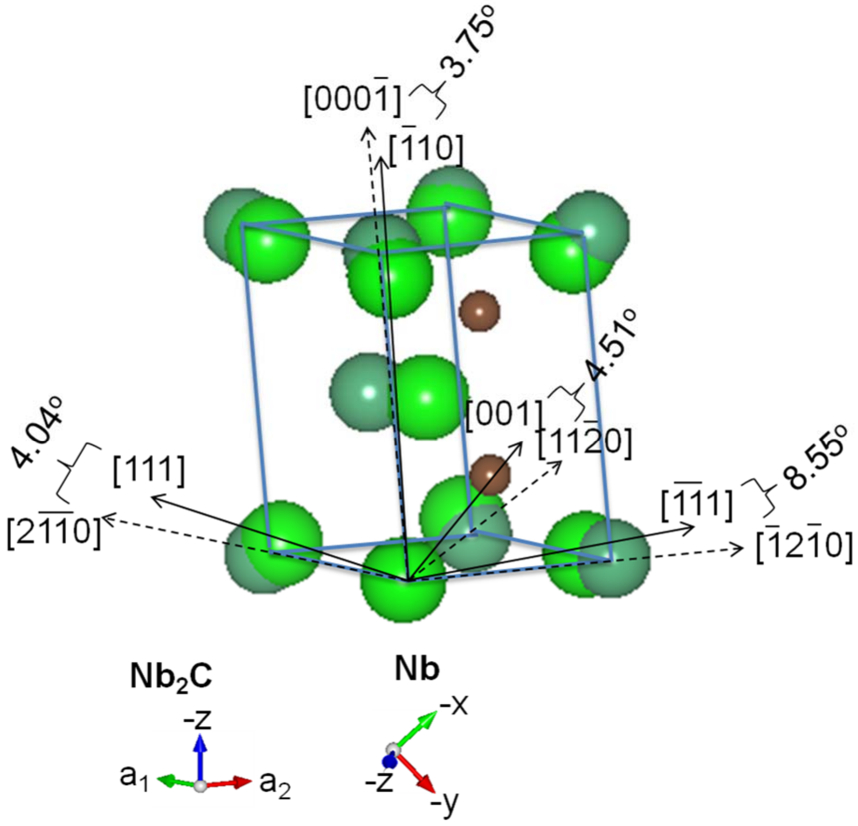

Figure 5.14: Schematic diagram showing transformation of bcc Nb unit cell to hexagonal Nb_2C unit cell. It shows that with small shifting of Nb atoms due to the occupation carbon at the interstitial sites, Nb unit cell transforms to Nb_2C unit cell.

X, Y and Z directions, respectively. Therefore, under the condition of simultaneous occupation of both the octahedral positions within unit cell by carbon atoms, strains along X and Y directions would be cancel out whereas along the Z direction it would add up. However, to achieve the stoichiometry of the Nb_2C composition both the octahedral positions need not to be simultaneously occupied by carbon atoms. Under the two opposing condition distribution of carbon atom is achieved by minimizing the overall energy of the phase. This led to the condition of imbalanced strain by the creation of defects along the plane normal to the Z direction. Copious presence of defects along the (0001) plane (shown in Fig.5.8) supports this conjecture.

5.3. Carbide formation in the deformed microstructure

As mentioned in the previous chapter (chapter.4) that deformed samples (extruded Nb alloy at 800 °C (Fig.4.9) showed two morphologies of the precipitates; one with needle morphology and second one with cuboidal morphology. The conventional XRD could not reveal the type of secondary phases present in the extruded sample. Hence, synchrotron XRD was carried out on the deformed sample (Fig.5.15). Similar to the XRD image of the as-solidified sample, it showed the presence of high intensity and low intensity rings correspond to Nb and second phase precipitates present in the microstructure of the deformed sample. Intensity versus 2θ information extracted from this figure is shown in Fig.5.15(b). In order to identify the second phase, XRD pattern was compared with the as-solidified synchrotron XRD pattern (Fig.5.4). It shows the presence of additional carbide diffraction peaks which were not present in the as-solidified sample. It indicates that the deformed sample has different carbide phases. The optical micrographs and XRD pattern showed the possibility of formation of at least two carbide phases in the deformed sample. Due to the presence of multiple carbide phases, it is very difficult to identify accurately what type of carbide phases present in the extruded sample based only on the XRD result. Therefore, the deformed samples were examined under transmission electron microscopy.

TEM micrographs of the deformed samples are shown in Fig.5.16. Typical dimensions of the cuboidal morphology precipitates were $\sim$100 nm width and $\sim$300 nm long. The needle shape precipitates were typically $\sim$200 nm wide and $\sim$2500 nm long. These two precipitates are described separately in the following sections:

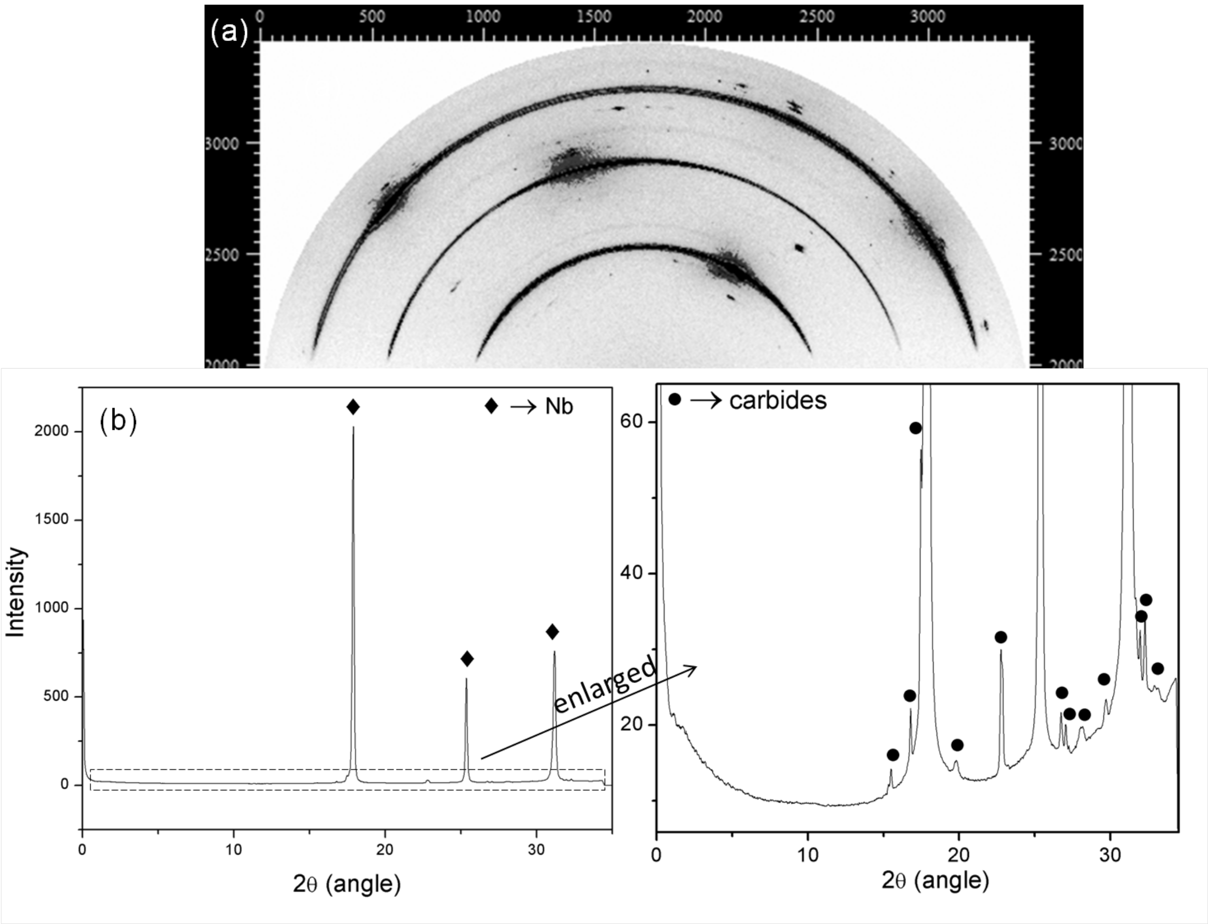

Figure 5.15: Synchrotron XRD of the deformed Nb alloy sample showing the presence of Nb phase and second phase diffraction peaks.

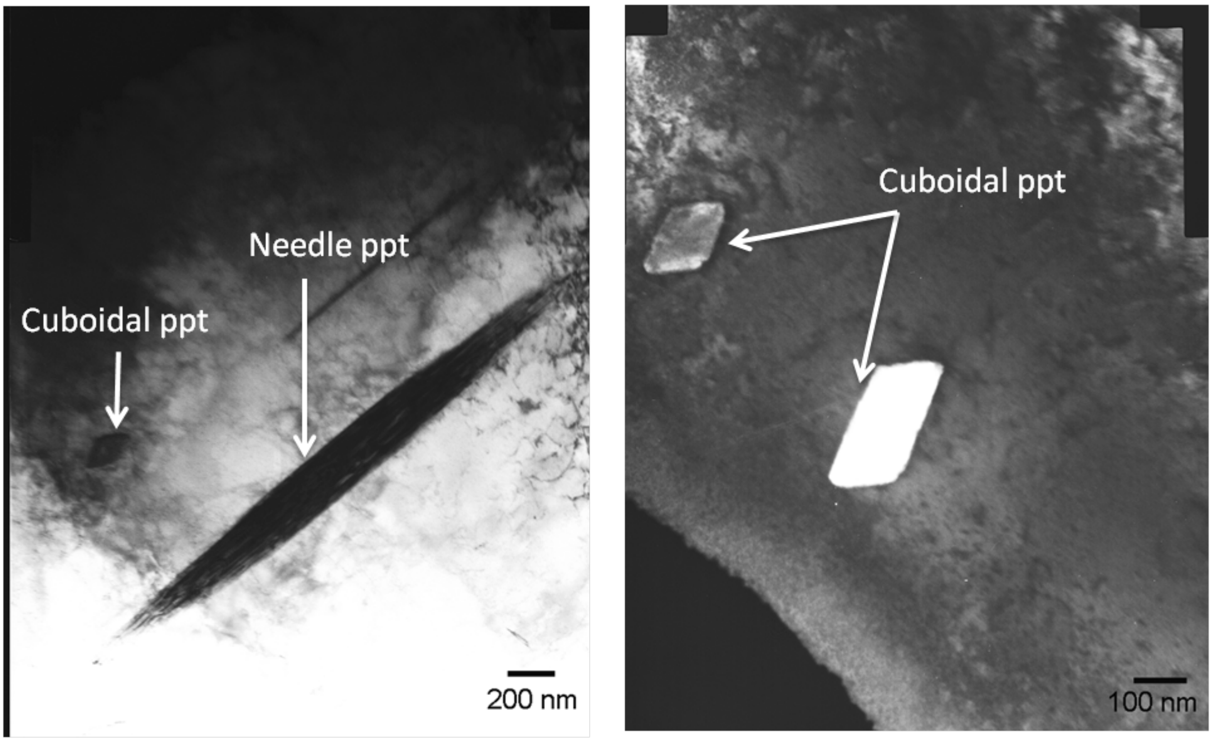

Figure 5.16: TEM micrographs of the deformed Nb alloy sample showing the presence of (a) needle and (b) cuboidal morphology precipitates.

5.3.1. Needle morphology precipitates

Fig.5.17 shows the SAED patterns acquired at different zone axes of the needle morphology precipitates. These patterns were analyzed with the crystal structure mentioned in the Table.2.5. It matches with the SAED patterns of α-Nb$_2$C orthorhombic crystal structure with lattice parameters a = 10.89, b = 12.36 and c = 4.956 A°. The indexed SAED patterns with the α-Nb$_2$C are shown in Fig.5.17. In order to further confirm the carbide phase of the the needle morphology precipitate, SAED patterns were simulated using JEMS software and shown in Fig.5.18. The experimentally acquired SAED patterns (Fig.5.17) matched well with the simulated SAED patterns (Fig.5.18) confirming the identification of needle morphology precipitates as the (Nb,Zr)$_2$C phase. In addition, EDS was carried out on these precipitates in the STEM mode. Typical composition of these precipitates was found to be 53.48 ± 2 at.% Nb, 12.51 ± 1.5 at.% Zr and 34 ± 5 at.%C. Based on composition analysis needle precipitates matched with the composition of (Nb, Zr)$_2$C. Diffraction patterns and EDS analysis have confirmed that the needle morphology precipitate is orthorhombic-α-(Nb,Zr)$_2$C carbide phase.

To know the orientation relationship between the Nb and α-(Nb,Zr)$_2$C, composite SAED patterns were obtained and shown in Fig.5.19. It clearly shows the existence of orientation

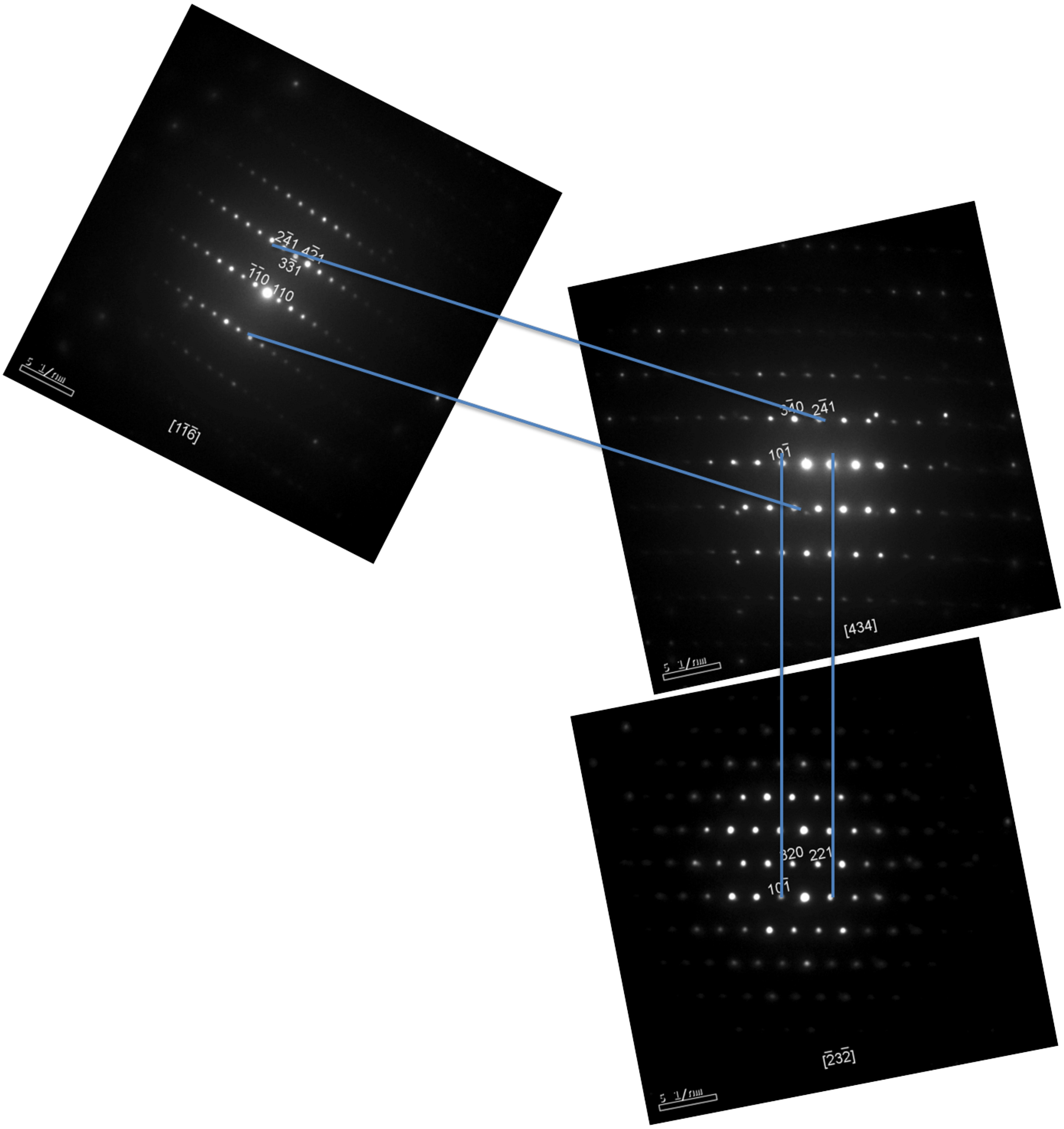

Figure 5.17: SAED patterns acquired at different zone axis of the needle morphology precipitates. These SAED patterns were indexed with α-(Nb,Zr)$_2$C crystal structure.

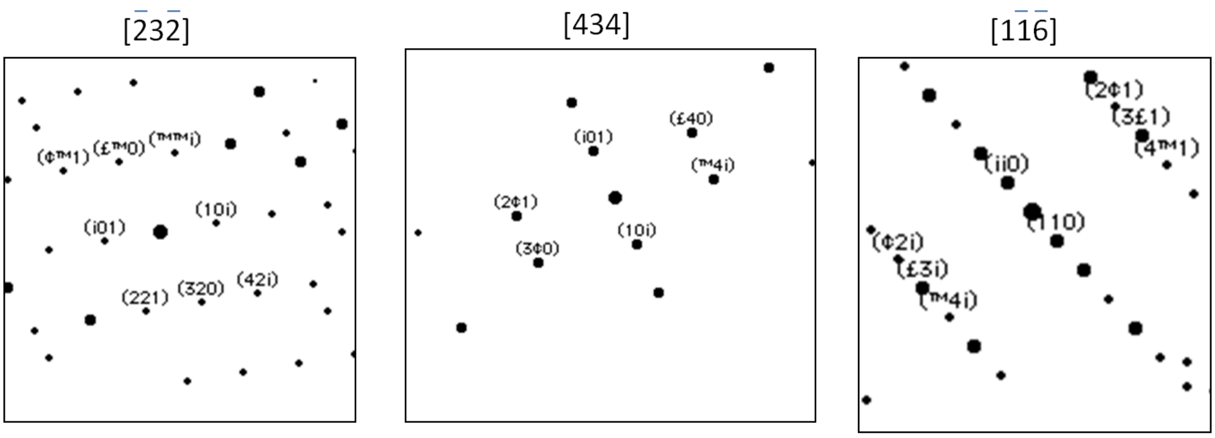

Figure 5.18: SAED patterns acquired at different zone axis of the needle morphology precipitates. These SAED patterns were indexed with α-(Nb,Zr)$_2$C crystal structure.

relationship (equation.5.7 between Nb matrix and α-(Nb,Zr)$_2$C carbide.

$$[001]_{Nb} \,//\, [2\bar{3}2]_{(Nb,Zr)_2C}\,, (\bar{2}00)_{Nb} \,//\, (\bar{1}01)_{(Nb,Zr)_2C} \qquad (5.7)$$

The correspondence transformation matrix between α-$(Nb, Zr)_2C$ and Nb has been estimated using above mentioned orientation relationship (equation.5.7).

$$\begin{bmatrix} u' \\ v' \\ w' \end{bmatrix}_{(Nb,Zr)_2C} = \begin{bmatrix} 0.125521 & 0.231744 & 0.149555 \\ 0.000000 & 0.144772 & -0.224332 \\ -0.606050 & 0.231744 & 0.149555 \end{bmatrix} \begin{bmatrix} u \\ v \\ w \end{bmatrix}_{Nb}$$

To study the transformation mechanism for the formation of α-(Nb,Zr)$_2$C, high resolution electron microscopy was carried out. Fig.5.20 shows the HRTEM image of interface between α-(Nb,Zr)$_2$C and Nb matrix. It shows the presence of coherent interface between Nb and α-(Nb,Zr)$_2$C carbide phase.

5.3.2. Formation mechanism of α-(Nb,Zr)$_2$C phase

According to the binary Nb-C phase diagram, γ-Nb$_2$C is a stable phase only at higher temperatures (2500 °C). At $\sim$ 2500 °C, γ-Nb$_2$C transforms to β-Nb$_2$C and at $\sim$ 1200 °C, β-Nb$_2$C transforms to α-Nb$_2$C. Crystallographic information of all the Nb$_2$C phases are given in Table.2.5 and their unit cells are shown in the Fig.5.21. In the case of α-Nb$_2$C there are at least five different space groups of the orthorhombic structures have been reported (Table.2.5). Here the stable α-Nb$_2$C(4) is considered for comparision purpose. When the crystal structures of β and α-Nb$_2$C are drawn with Nb atom positions as the origin, they match closely with the γ-Nb$_2$C of hexagonal structure (Fig.5.21(b)). This indicates that three Nb$_2$C lattices (γ, β, α) have

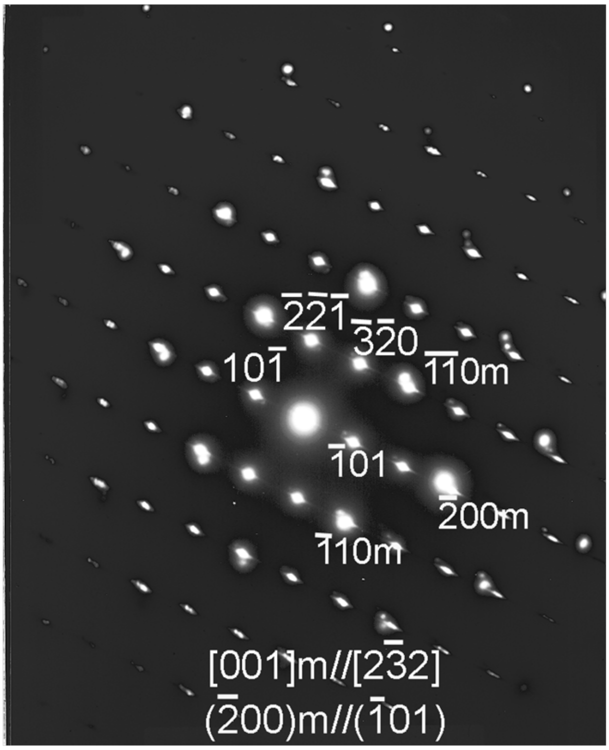

Figure 5.19: Composite selected area electron diffraction patterns showing the presence of orientation relationship between Nb matrix and α-(Nb,Zr)$_2$C.

the same hexagonal niobium sublattice. This matching can be viewed in details when β-Nb$_2$C and α-Nb$_2$C lattices are rotated along c-axis by 30° and along the a-axis by 45° respectively (Fig.5.21). Under this viewing direction dimension of all crystal structures matched with the γ-Nb$_2$C crystal when viewed along a $[11\bar{2}0]$ direction. This indicates that the γ-Nb$_2$C can transform to β or α-Nb$_2$C directly by changing ordering of C atoms and vacancies. The ordering of the C atoms brings changes in the volumes of the unit cell and accordingly lattice parameters of β and α-Nb$_2$C changed.

In the present study, formation of the β-Nb$_2$C carbide phase was not observed. It, therefore, can be inferred that γ-Nb$_2$C transformed directly into α-Nb$_2$C carbide phase. Reason of such direct transformation could be attributed to the low deformation temperature (800 °C) at which α-Nb$_2$C is stable. The lattice parameters of α-Nb$_2$C obtained by SAED patterns analysis are a=10.89, b=12.36, c=4.956 A°, which match with the α-Nb$_2$C(3) (Table.2.5). However, the atom positions for this crystal structure are not available in the literature. If the lattice parameters of a & c are interchanged it become a=4.956, b=12.36 and c=10.89 A°. When these lattice parameters compared with the lattice parameters of the α-Nb$_2$C(1) (Table.2.5 for which atom positions are known), it shows that b and c are 2 times of the α-Nb$_2$C(1). In order to

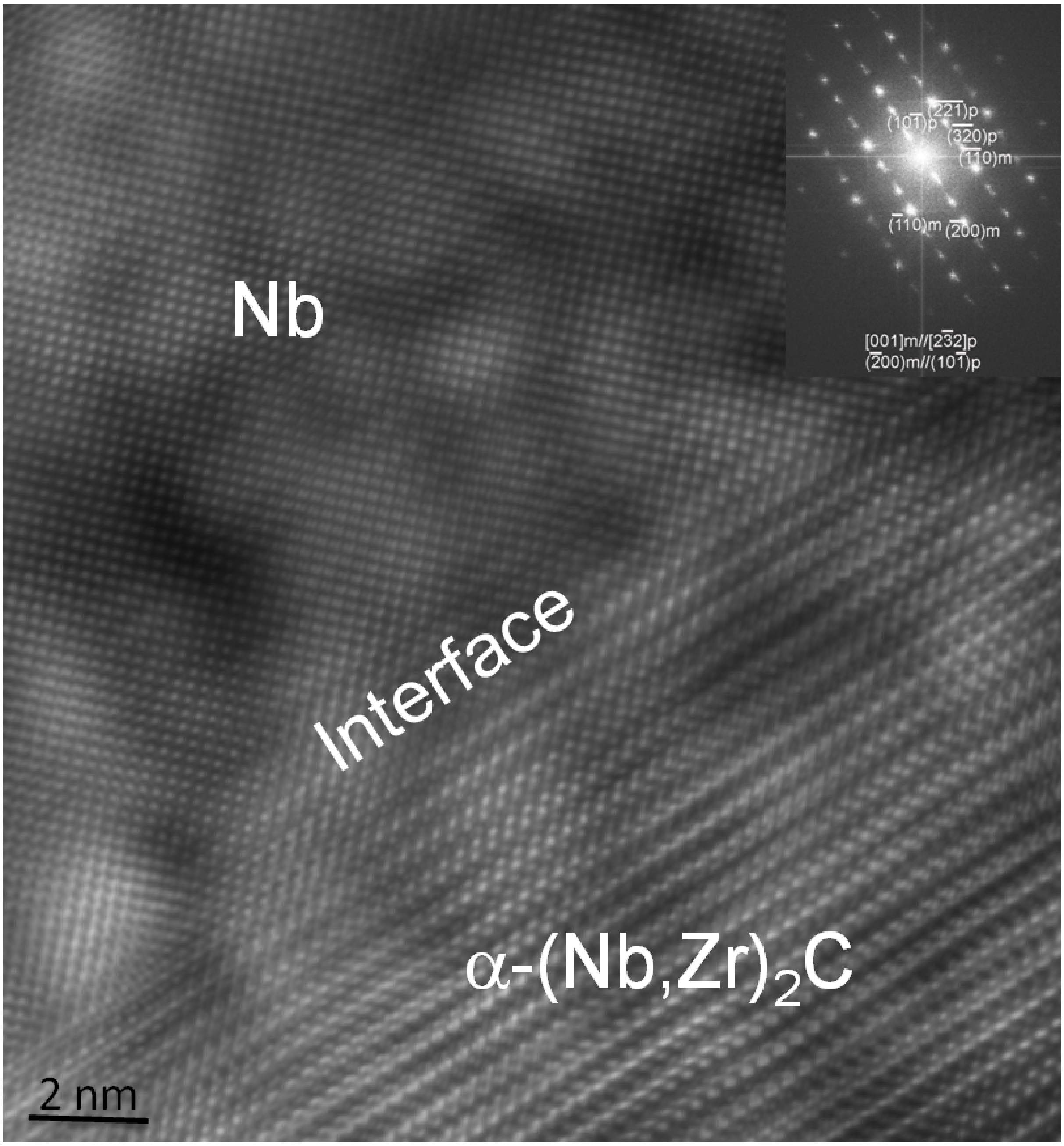

Figure 5.20: High resolution image of the interface between Nb matrix and α-(Nb,Zr)$_2$C carbide. The view of HRTEM is the $[001]$ zone axis of Nb which is parallel to $[2\bar{3}2]$ zone axis of α-(Nb,Zr)$_2$C. The inset figure shows corresponding FFT pattern of the HRTEM image.

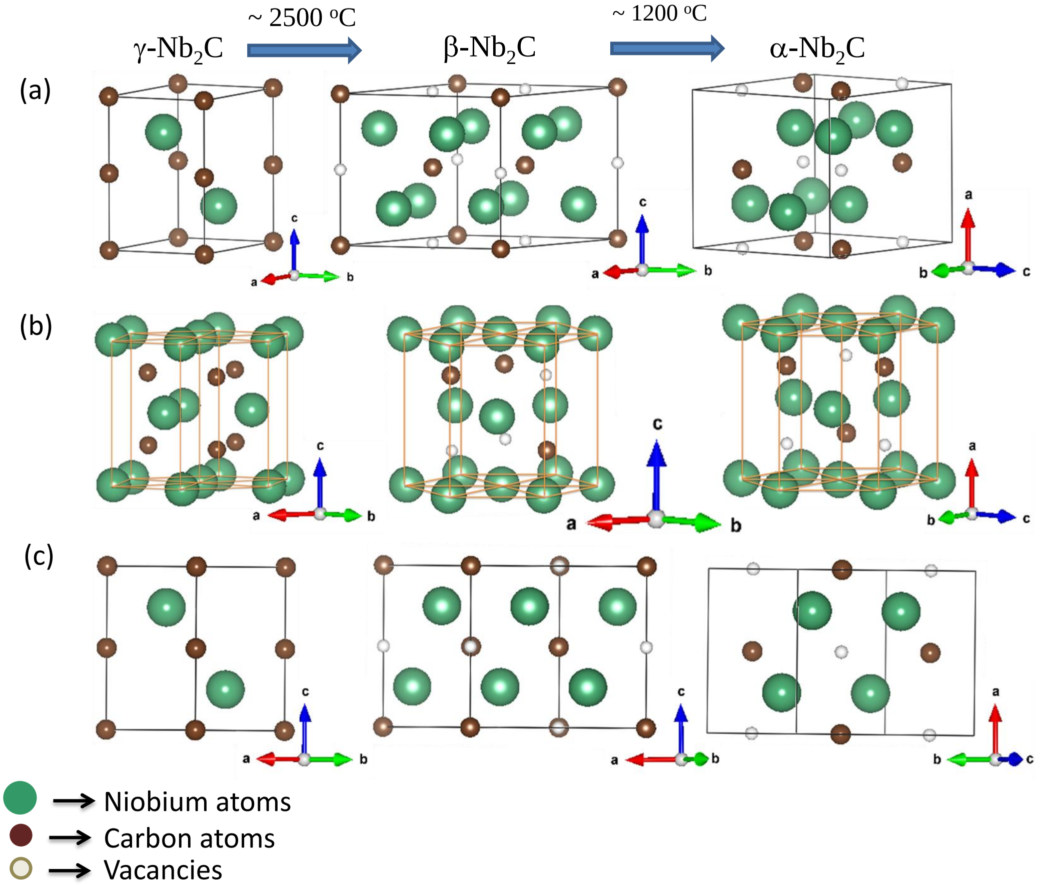

Figure 5.21: (a) Crystal structures of γ, β and α-Nb_2C phases, (b) The unit cells of γ, β and α-Nb_2C phases are drawn with Nb atom positions as the origin and it shows similar crystal structures, and (c) γ-Nb_2C unit cell shown along $[11\bar{2}0]$ direction, similarly β-Nb_2C (rotated along c-axis by 30°) and α-Nb_2C (rotated along a-axis by 45°) unit cells are drawn at an orientation showing similar crystal structure with γ-Nb_2C along $[11\bar{2}0]$ direction.

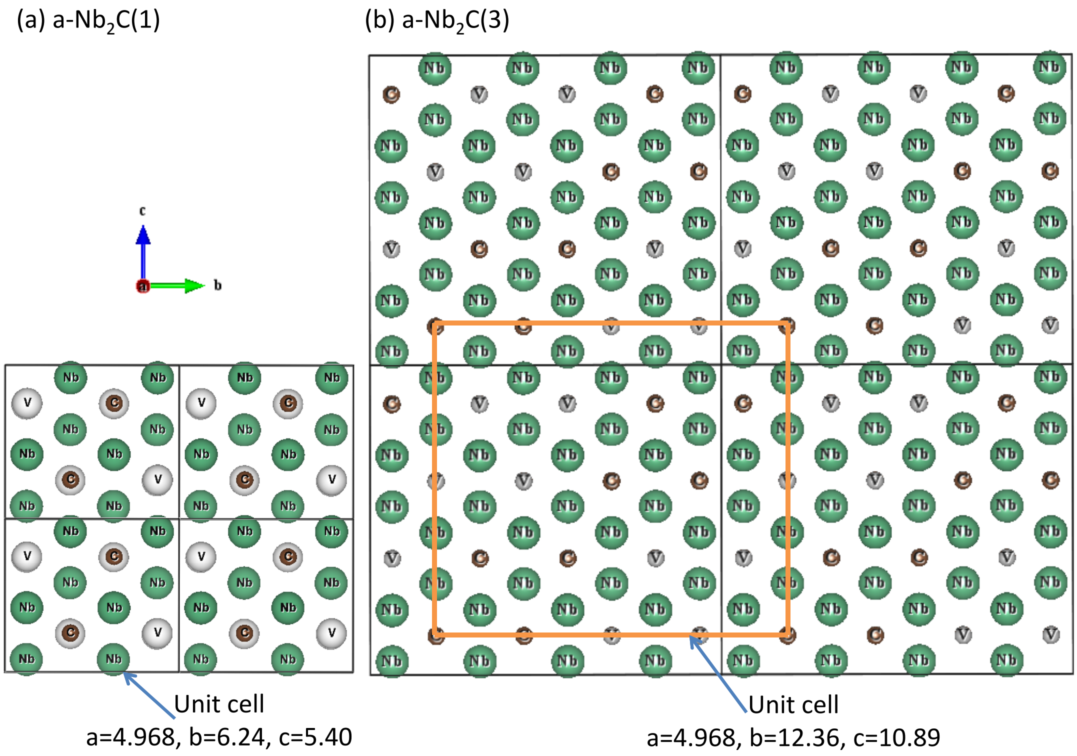

Figure 5.22: Unit cell of (a) α-$Nb_2C(1)$ and (b) α-$Nb_2C(3)$ along $[001]$ projection. It shows the difference in C and vacancy ordering in both the unit cells.

produce the α-$Nb_2C(3)$ from α-$Nb_2C(1)$, the C and vacancy ordering has been changed without changing the Nb atom positions. Fig.5.22 shows that in the α-Nb2C(1), the sequence of C and vacancy ordering along b-direction is C,V,C,V this has been changed to C,C,V,V,C,C in the α-$Nb_2C(3)$ by keeping the same Nb atom positions. Due to changing the C and vacancy ordering, the α-$Nb_2C(1)$ unit cell become $Nb_2C(3)$. In order to confirm the existence of this structure, the projected crystal structure along $[0\bar{1}1]$ and the simulated HRTEM image along $[0\bar{1}1]$ from α-Nb_2C structure are compared with the experimental HRTEM image along $[0\bar{1}1]$ (Fig.5.23). It shows good matching between them. It confirms the formation of α-Nb_2 with the a=10.89, b=12.36, c=4.956 A° lattice parameters.

Finally, the microstructural characterization of γ-Nb_2C and α-Nb_2C show that for the formation of Nb_2C from Nb, it does not require large movement of Nb atoms.

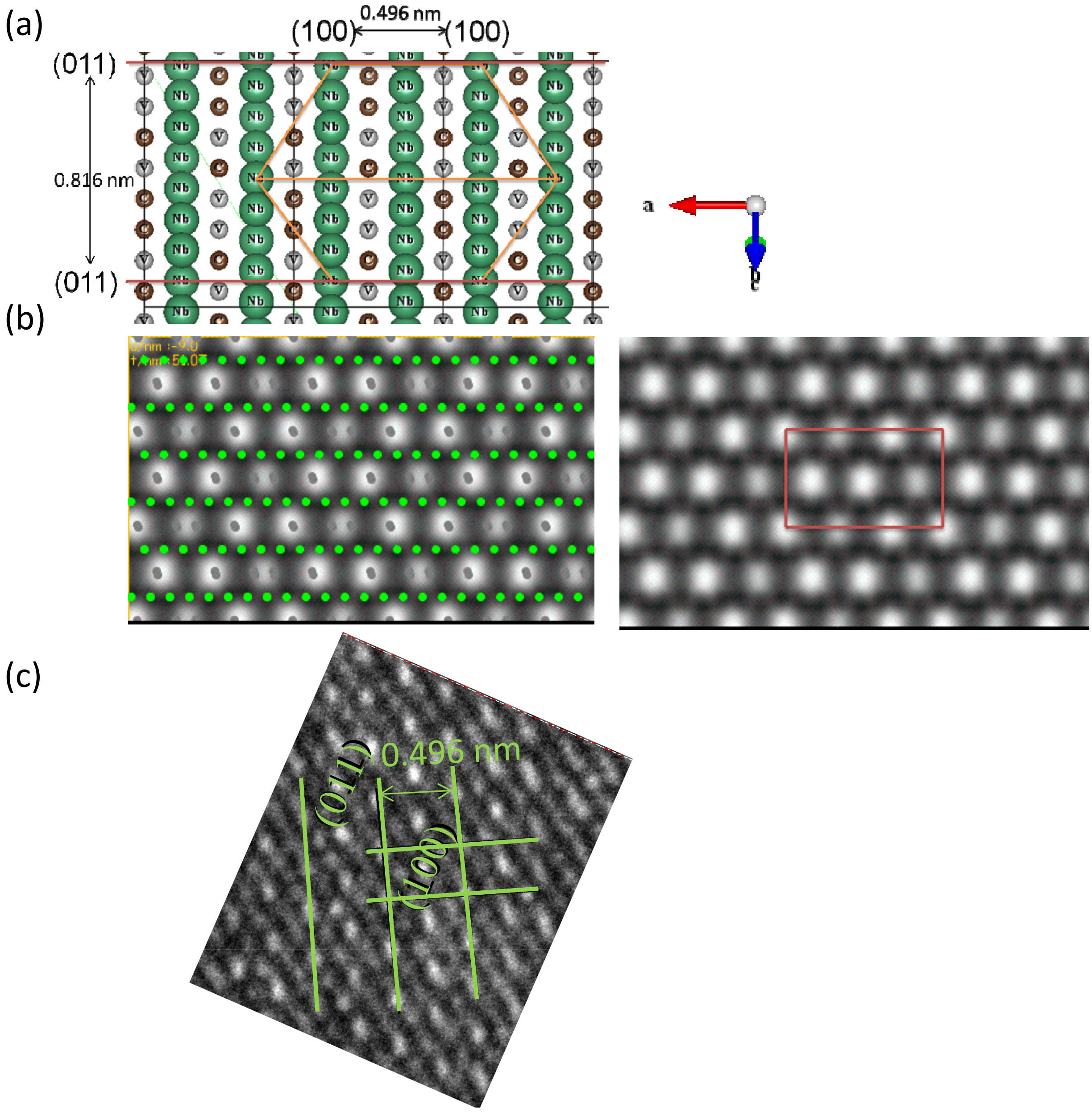

Figure 5.23: (a) α-Nb_2C unit cell shown along $[0\bar{1}1]$ direction, (b) simulated HRTEM image of the α-Nb_2C at $[0\bar{1}1]$ direction zone axis and (c) experimental HRTEM image of the α-Nb_2C at $[0\bar{1}1]$ direction zone axis, showing matching between all three figures.

5.3.3. Cuboidal morphology precipitates

Similarly, to identify the crystal structure of cuboidal shape of precipitate, SAED patterns were collected at different tilt angles (Fig.5.24). The SAED pattern (Fig.5.24(b)) shows the presence of three fold symmetry in the crystal structure of the precipitate. It indicates that the precipitate is having either cubic or hexagonal crystal structure. Further analysis of the SAED patterns showed that all the SAED patterns can be indexed with hexagonal crystal structure. From these indexed patterns, lattice parameters of hexagonal crystal structure are found to be a = 11.46 A° and c = 18.30 A°. These lattice parameters matched with the lattice parameters of Nb_3C_2 (a=11.46 and c=18.30 A) given in Table.2.5. Further to confirm the Nb_3C_2 carbide phase, EDS was carried out. EDS analysis showed that the cuboidal precipitate has 45.97 ± 2 at.% Nb, 10.11 1 at.% Zr and 43.9 ± 4 at.% C and it closely matches with the $(Nb,Zr)_3C_2$.

The SAED patterns shown in Fig.5.24 also shows the diffraction reflections from the Nb matrix. The Nb SAED patterns are also indexed in Fig.5.25 to show the orientation relationship between Nb_3C_2 and Nb matrix. The orientation relationship between Nb_3C_2 and Nb matrix is (equation:5.8):

$$[001]_{Nb} // [0001]_{(Nb,Zr)_3C_2}, (020)_{Nb} // (11\bar{2}0)_{(Nb,Zr)_3C_2} \tag{5.8}$$

The coordinate transformation matrix has been calculated from the above mentioned orientation relationship (equation.5.8)

$$\begin{bmatrix} u' \\ v' \\ w' \end{bmatrix}_{(Nb,Zr)_3C_2} = \begin{bmatrix} 0.166253 & 0.287958 & 0.000000 \\ -0.166253 & 0.287958 & 0.000000 \\ 0.000000 & 0.000000 & 0.180328 \end{bmatrix} \begin{bmatrix} u \\ v \\ w \end{bmatrix}_{Nb}$$

From the transformation matrix (equation:5.3.3), the presence of other orientations were verified which matched well with the orientation as shown in Fig.5.25. Upon aligning [001] cubic stereographic projection with [0001] stereographic projection (Fig.5.26), other inter relationships observed in different selected area diffraction patterns (Fig.5.25) were obtained. It indicates the presence of unique orientation relationship between $(Nb,Zr)_3C_2$ carbide phase and Nb matrix.

In order to understand formation mechanism of $(Nb,Zr)_3C_2$ in the deformed Nb alloy, carbide phase has been observed under high resolution electron microscopy. Fig.5.27 shows the HRTEM image of the interface between Nb and Nb_3C_2. Interface shows the presence of strain between Nb and $(Nb,Zr)_3C_2$. Due to this the interface was not clear. The HRTEM images of

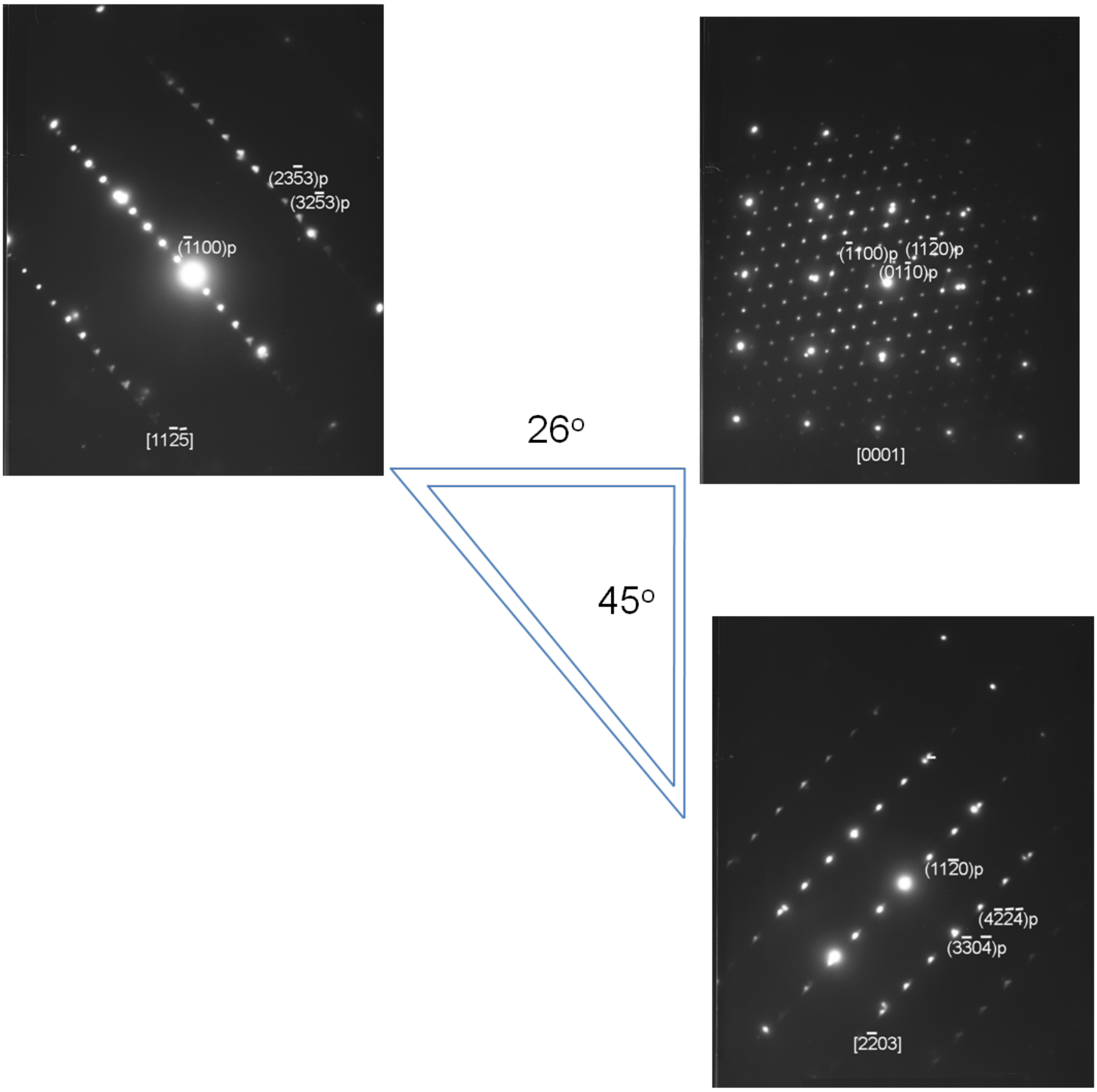

Figure 5.24: SAED patterns acquired at different zone axis from the cuboidal morphology precipitates present in the deformed Nb alloy.

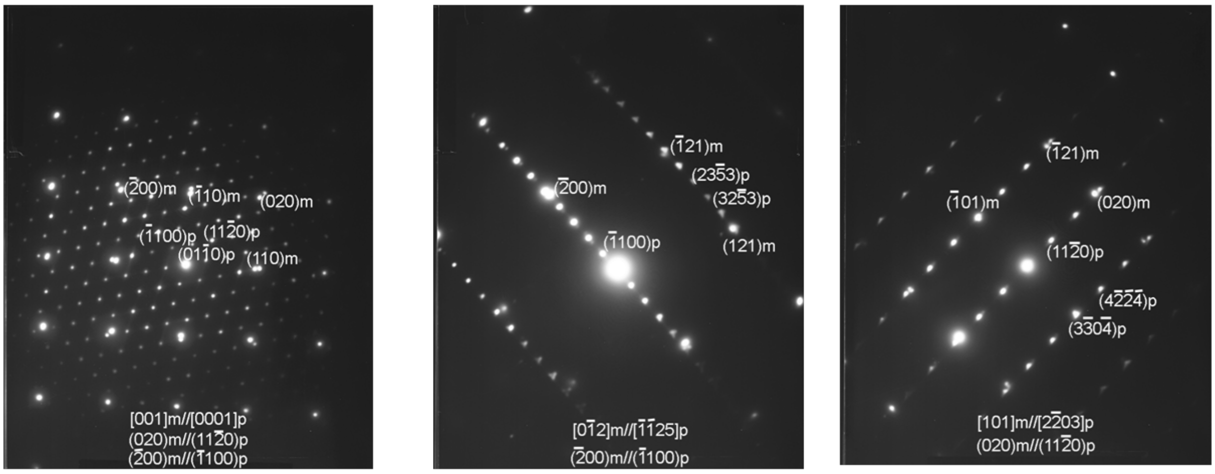

Figure 5.25: Composite SAED patterns obtained from Nb_3C_2 carbide precipitate and Nb matrix showing the orientation relationship between them.

both the carbide phases $(Nb,Zr)_2C$ and $(Nb,Zr)_3C_2$ did not shows the presence of defects in the carbide phases.

Microstructural characterization of the deformed sample did not show the presence γ-Nb_2C particles, which are observed in the as-solidified microstructure. It indicates that the carbide particles present in the as-solidified microstructure were dissolved during the extrusion experiments and reprecipitated in the form of α-$(Nb,Zr)_2C$, $(Nb,Zr)_3C_2$ particles. All the results shows that Zr present in the Nb matrix phase got partitioned in to the carbide particles and it destabilizes the as-solidified microstructure and forms deformed microstructure with the formation of two new carbide phases (α-$(Nb,Zr)_2C$ and $(Nb,Zr)_3C_2$). Carbon concentration in the Nb_3C_2 phase is higher than in the Nb_2C phase. It clearly shows that low carbon concentration phases are unstable in the Nb alloy.

5.4. Carbide formation in the annealed microstructure

To find out the number of phases present in the annealed sample (recrystallized by heat treating the deformed sample at 1300 °C for 3 hrs), synchrotron XRD was carried out. Fig.5.28 shows the synchrotron XRD of the annealed sample. It clearly shows the presence of additional diffraction rings correspond to second phase precipitates in the annealed sample (Fig.5.28(a)). Due to the recrystallization, it has strain free 30μm$\pm$5 grains and reduced texture effect. It lead to formation of visible diffraction rings corresponds to second phase precipitates in the annealed Nb alloy sample. These diffraction peaks were analyzed and it was found that these correspond to fcc-NbC phase (Fig.5.28(b)). The optical micrographs and OIM images of the

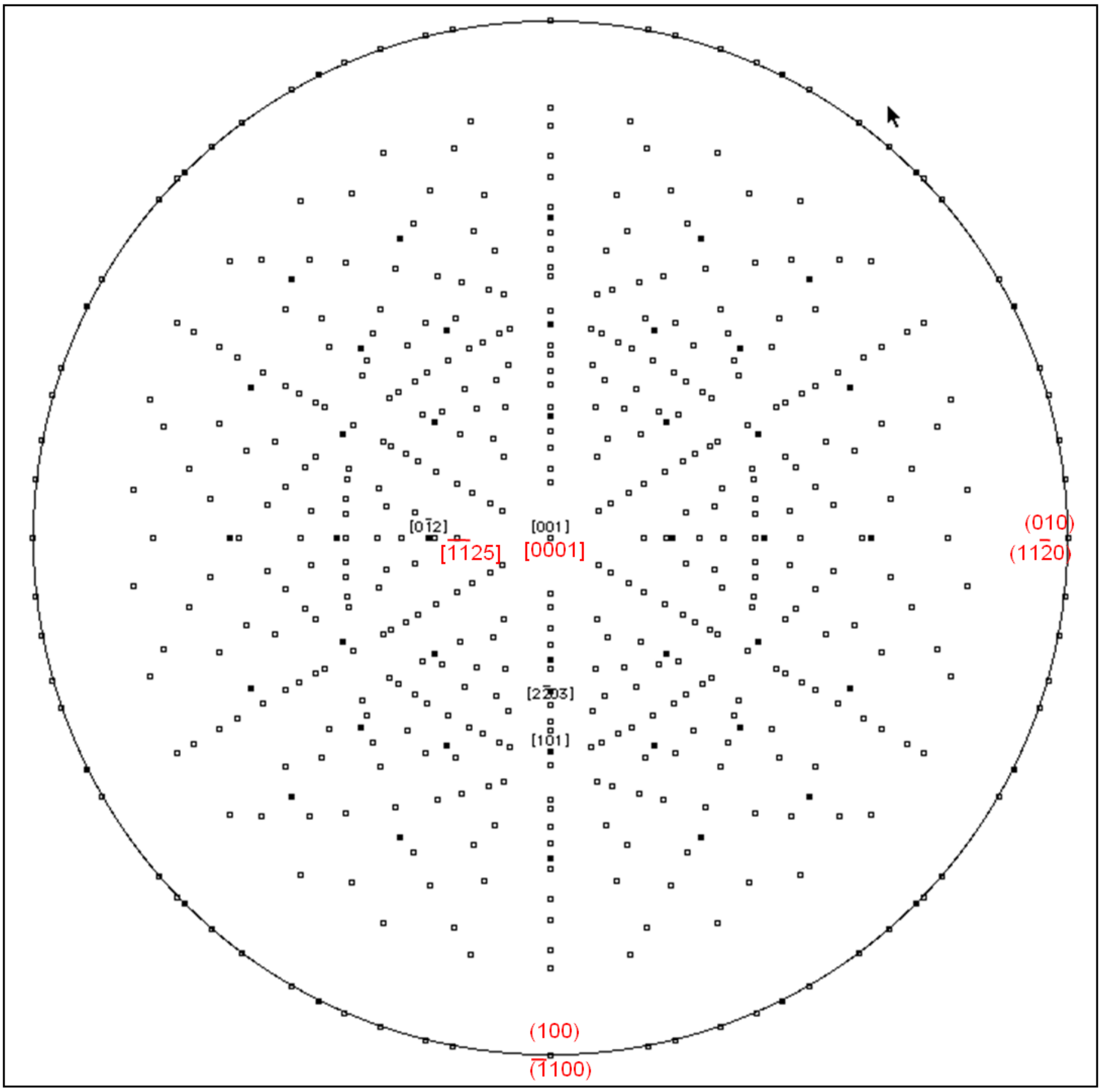

Figure 5.26: Stereographic projection showing the presence of all the orientation observed in the composite SAED patterns (Fig.5.25).

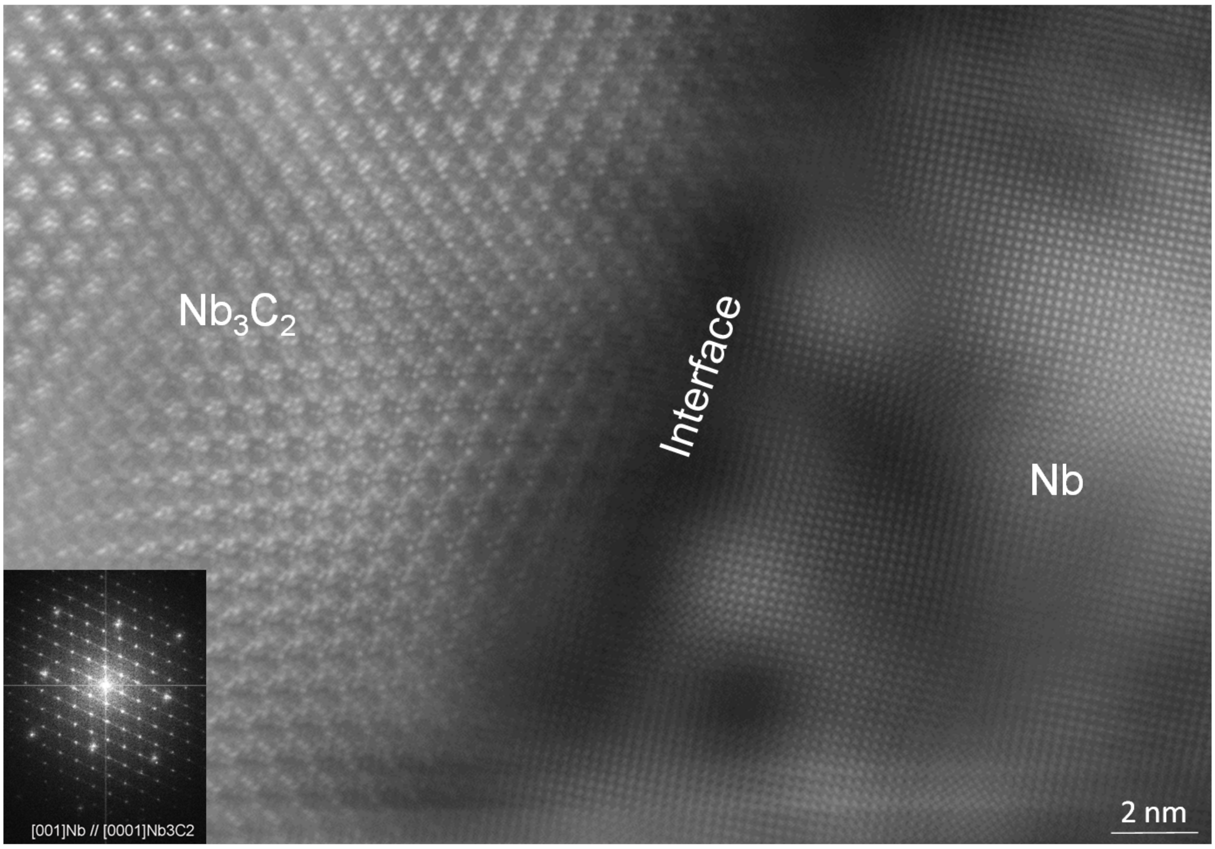

Figure 5.27: HRTEM image of the interface between (Nb,Zr)$_3C_2$ and Nb matrix.

annealed samples shown in the previous chapter, did not show the presence of second phase precipitates. In order to examine the presence of carbide precipitates of smaller dimensions, the annealed samples were examined under TEM. Fig.5.29 shows a bright field image of the annealed sample. It shows the presence of very fine spherical shape precipitates (∼100 nm). To identify the precipitate phase, SAED patterns were collected from different zones from a single precipitate by carrying out systematic tilting experiments (Fig.5.30). All these patterns could be successfully indexed in terms of fcc lattice with a lattice parameter as a = 4.75 A°. After carrying out EDS analysis of several precipitates, the average composition of the phase was determined as Nb(at%)-34.32±2, Zr(at%)-17±3 and C(at%)-48.68±5. Combining information of crystallographic and chemical analysis of these precipitates, precipitate phase was identified as the (Nb,Zr)C carbide phase. Composite SAED patterns (Fig.5.31) having reflections from both the carbide phase and the Nb matrix exhibited the presence of a common diffraction vector between the carbides and the matrix phase. A unique orientation relationship (OR) between the precipitates and matrix was determined which can be expressed as:

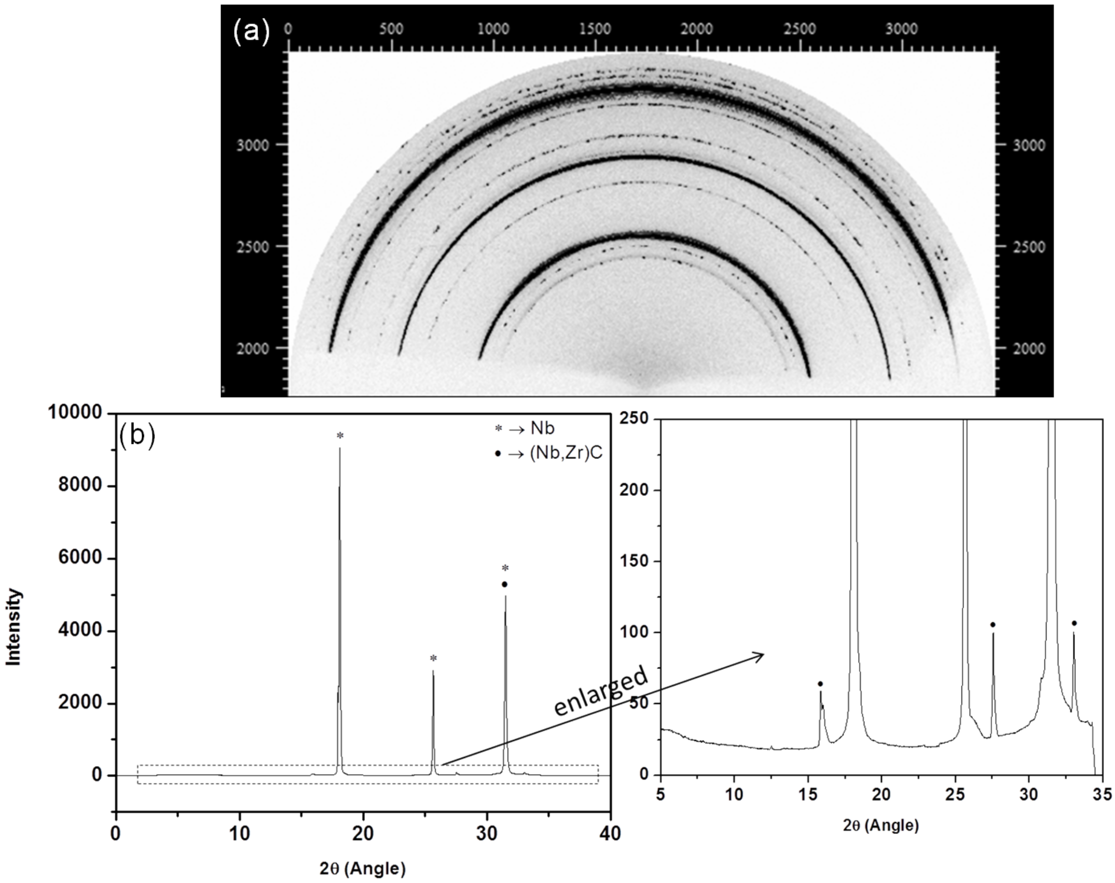

Figure 5.28: Synchrotron XRD of the annealed sample (a) showing the formation diffraction rings of Nb alloy and second phase precipitates present in the annealed sample and (b) showing intensity versus 2θ plot showing the presence Nb and NbC phases.

$$[\bar{1}10]_{Nb}\,//\,[\bar{1}11]_{(Nb,Zr)C}\,,\,(002)_{Nb}\,//\,(0\bar{2}2)_{(Nb,Zr)C} \tag{5.9}$$

This orientation relationship matches with the orientation relationship established by Nishiyama and Wasserman between fcc and bcc phases [117, 118].

Crystal structure of the fcc-NbC is shown in Fig.5.32(a). Since, the carbide contains Zr, half of the atom positions occupied by Nb are occupied by Zr. Fig.5.32(b) shows the schematic of the orientation relationship between Nb and (Nb,Zr)C phases. It has been carefully observed to see sharing of Nb atoms between Nb and (Nb,Zr)C (as observed between Nb_2C and Nb (Fig.5.33)). It did not show sharing of Nb atoms between Nb and (Nb,Zr)C. In addition, it shows that to transform Nb alloy to (Nb,Zr)C, it requires high diffusion of Nb, Zr and C atoms is required. The formation of (Nb,Zr)C carbide phase is a diffusional phase transformation. This indicates that the carbide phases $(Nb,Zr)_2C$, Nb_3C_2 present in the deformed sample were dissolved during annealing and re-precipitated in the form of (Nb,Zr)C carbide phase.

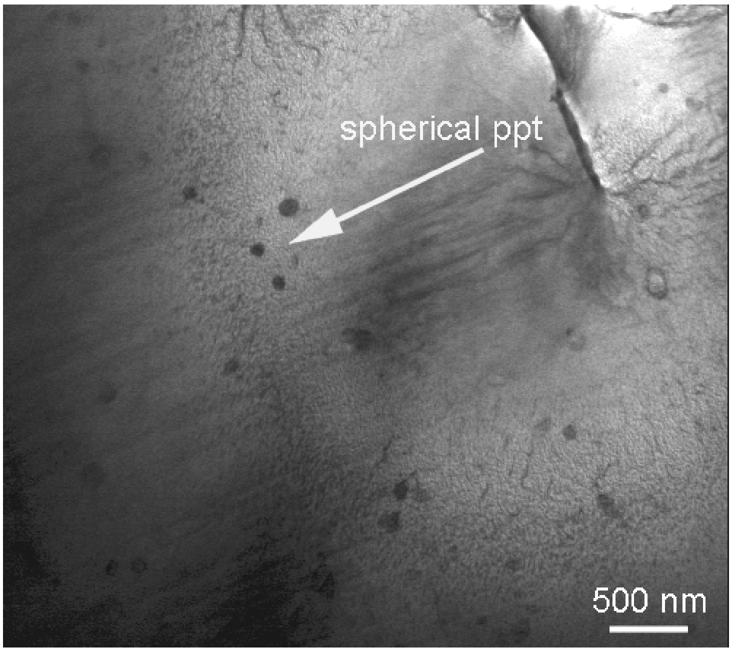

Figure 5.29: Bright field TEM image of the annealed sample showing the presence of fine spherical morphology precipitates.

In order to observe the interface between Nb and (Nb,Zr)C, the annealed samples were examined under high resolution electron microscopy. Fig.5.34 shows the HRTEM image of the interface between Nb and (Nb,Zr)C phases. Fast Fourier transform (FFT) has been taken at all the locations. The FFT shows [111], [101] zone axis for the matrix and carbide phase respectively. At the interface completely different FFT was observed. Further, this FFT was analyzed. It matched with the [001] zone axis of the hexagonal $(Nb,Zr)_3C_2$ phase having lattice parameter of a = 11.46 and c = 18.30 A°. It indicates that (Nb,Zr)C has formed at the vicinity of the $(Nb,Zr)_3C_2$ phase. The reason for the formation of (Nb,Zr)C at these location could be lesser driving force requires to form than the driving force required to form through out the Nb matrix. This was due to the availability of carbon from decomposing metastable $((Nb,Zr)_3C_2)$ phases. Therefore, driving force required for the formation of (Nb,Zr)C at the vicinity of $(Nb,Zr)_3C_2$ is lower than formation of (Nb,Zr)C through out the Nb matrix. To further confirm the presence of $(Nb,Zr)_3C_2$ at the interface of (Nb,Zr)C an Nb matrix, EDS line profile has been carried out. Fig.5.35 shows the line profile of the annealed sample from the (Nb,Zr)C carbide to matrix region. It shows the presence of three regions. The first region which has lowest Zr concentration corresponds to Nb matrix. At interface Zr concentration is maximum and reduces upon moving towards the core of the carbide phase. However, concentration of Zr at the core of the carbide phase remained higher as compare to the matrix phase. It indicates that the interface has higher

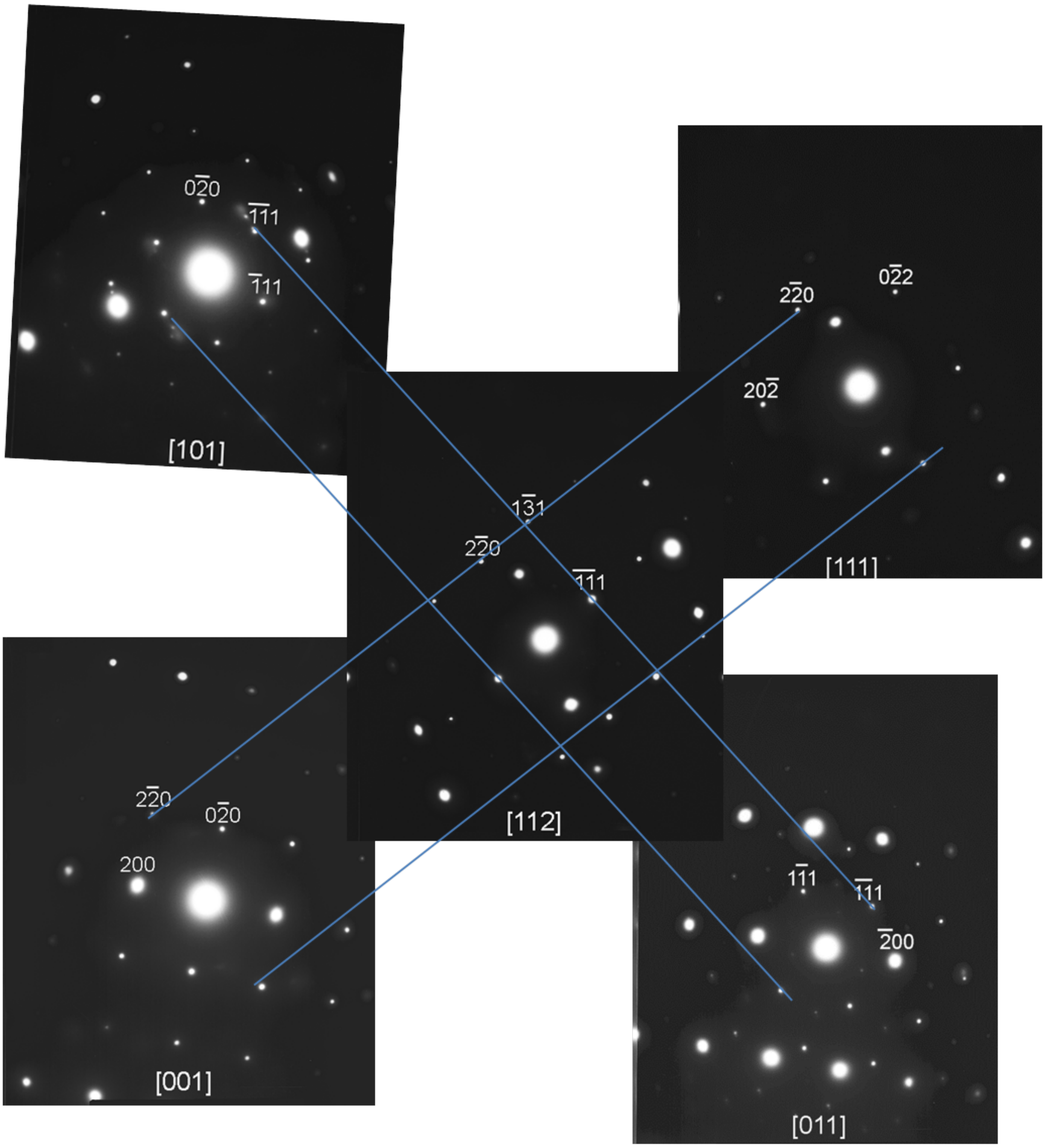

Figure 5.30: SAED patterns acquired from different zone axis from the annealed sample.

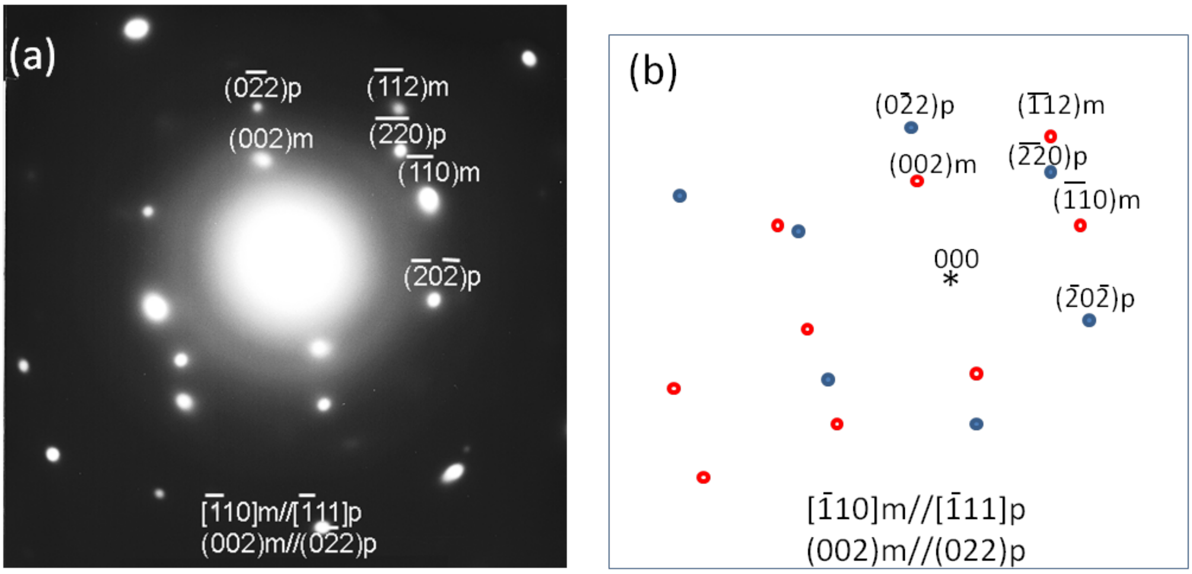

Figure 5.31: Composite SAED patterns acquired from the annealed sample showing the presence orientation relationship between Nb and NbC precipitate.

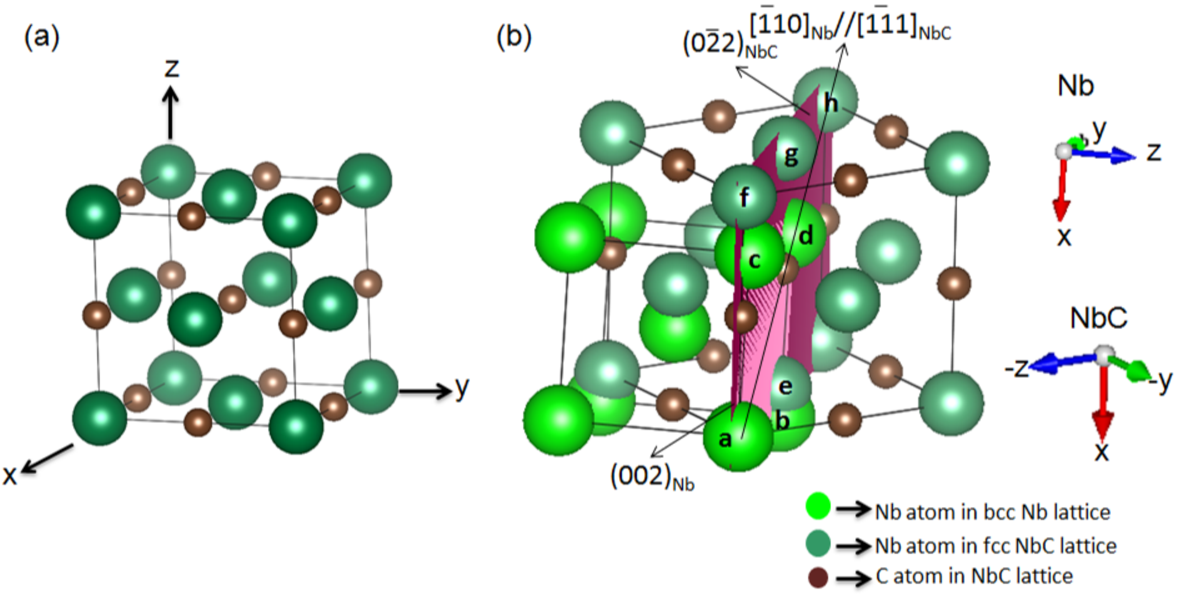

Figure 5.32: (a) Crystal structure of fcc - NbC, (b) schematic of the orientation relationship ($[\bar{1}10]_{Nb} // [\bar{1}11]_{(Nb,Zr)C}$, $(002)_{Nb} // (0\bar{2}2)_{(Nb,Zr)C}$) between (Nb,Zr)C carbide and bcc Nb matrix phase.

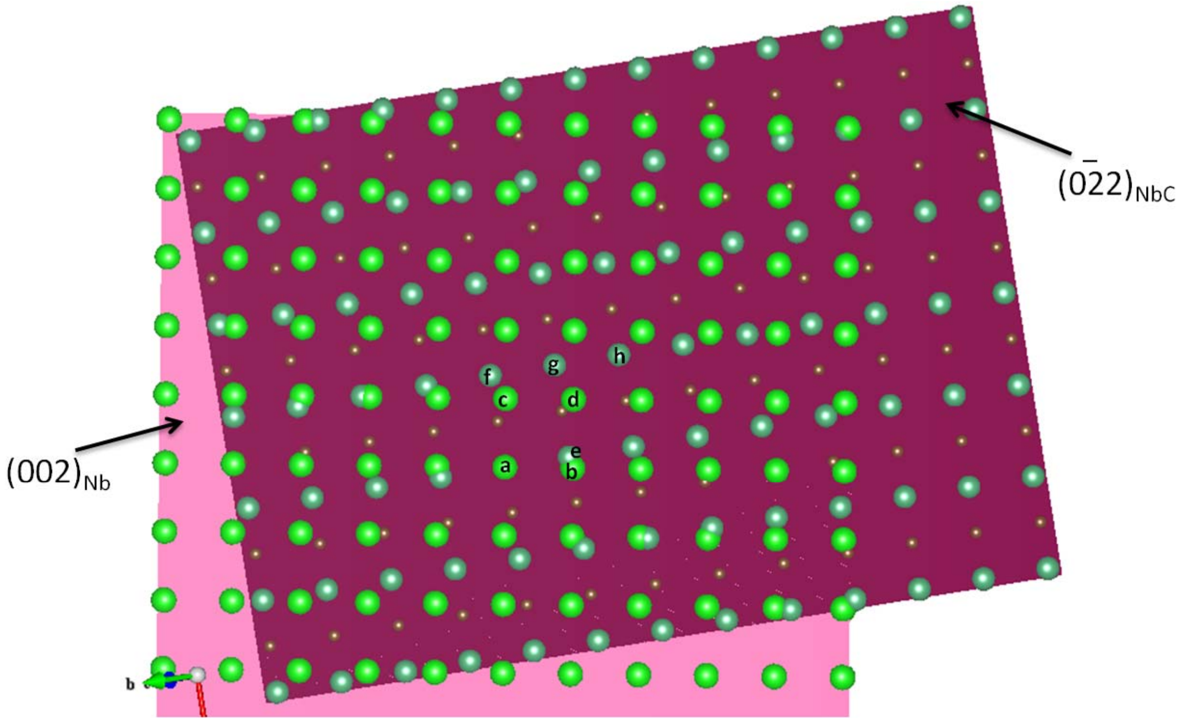

Figure 5.33: Superimposed planes of Nb (002) and (Nb,Zr)C $(0\bar{2}2)$, according to their orientation relationship $([\bar{1}10]_{Nb} // [\bar{1}11]_{(Nb,Zr)C}$, $(002)_{Nb} // (0\bar{2}2)_{(Nb,Zr)C})$ showing atomic arrangement in both the planes (Nb atoms in Nb and NbC are marked with alphabets as shown in Fig. 5.32(b)).

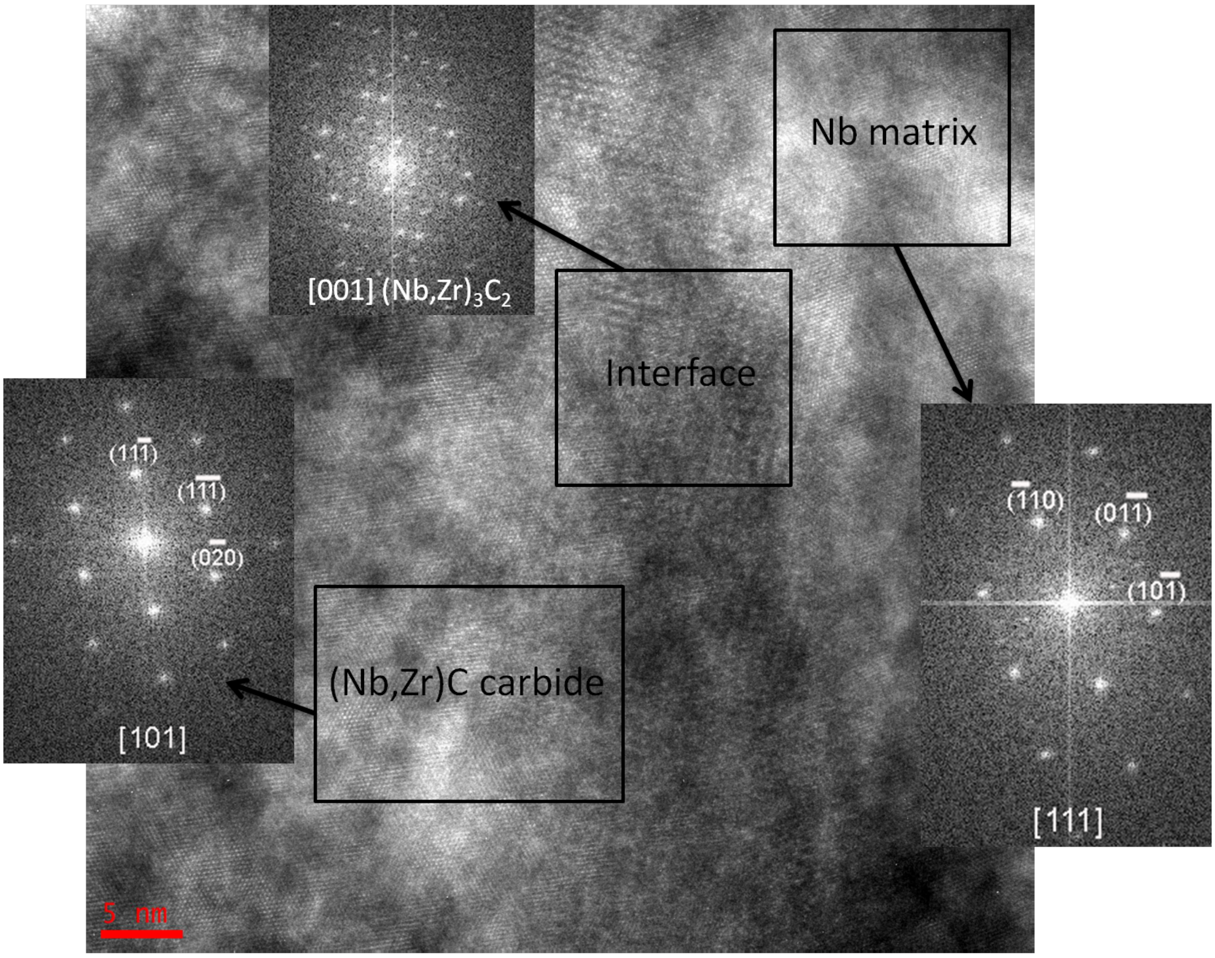

Figure 5.34: HRTEM image of the interface between (Nb,Zr)C carbide and Nb matrix. Inset figures shows the FFT of the selected regions. It shows the formation of $(Nb,Zr)_3C_2$ phase at the interface.

Zr than the carbide phase. The HRTEM investigations showed that interface has $(Nb,Zr)_3C_2$ carbide phase and the core of carbide phase is (Nb,Zr)C. The EDS and HRTEM results show that interface has $(Nb,Zr)_3C_2$ carbide phase.

Farkas *et al.* [107] has carried out thermodynamic analysis of carbide precipitates in Nb-Zr-C alloy. They have calculated the free energy formation of Nb_2C, NbC and ZrC using the standard free energy values of pure Nb, Zr and C components. They have assumed ideal solution for the free energy calculations. Fig.5.36 shows the free energy diagram for Nb_2C , NbC and ZrC phases. It shows that at lower concentrations of NbC, free energy for the formation of NbC is lower than the Nb_2C. Similarly, with increasing temperature, NbC becomes more stable. The present results matches with their results showing the transformation of Nb_2C to (Nb,Zr)C carbide phase. The present study also shows formation of the intermediate metastable phases $(Nb,Zr)_2C$ and $(Nb,Zr)_3C_2$ before formation of the (Nb,Zr)C carbide phase.

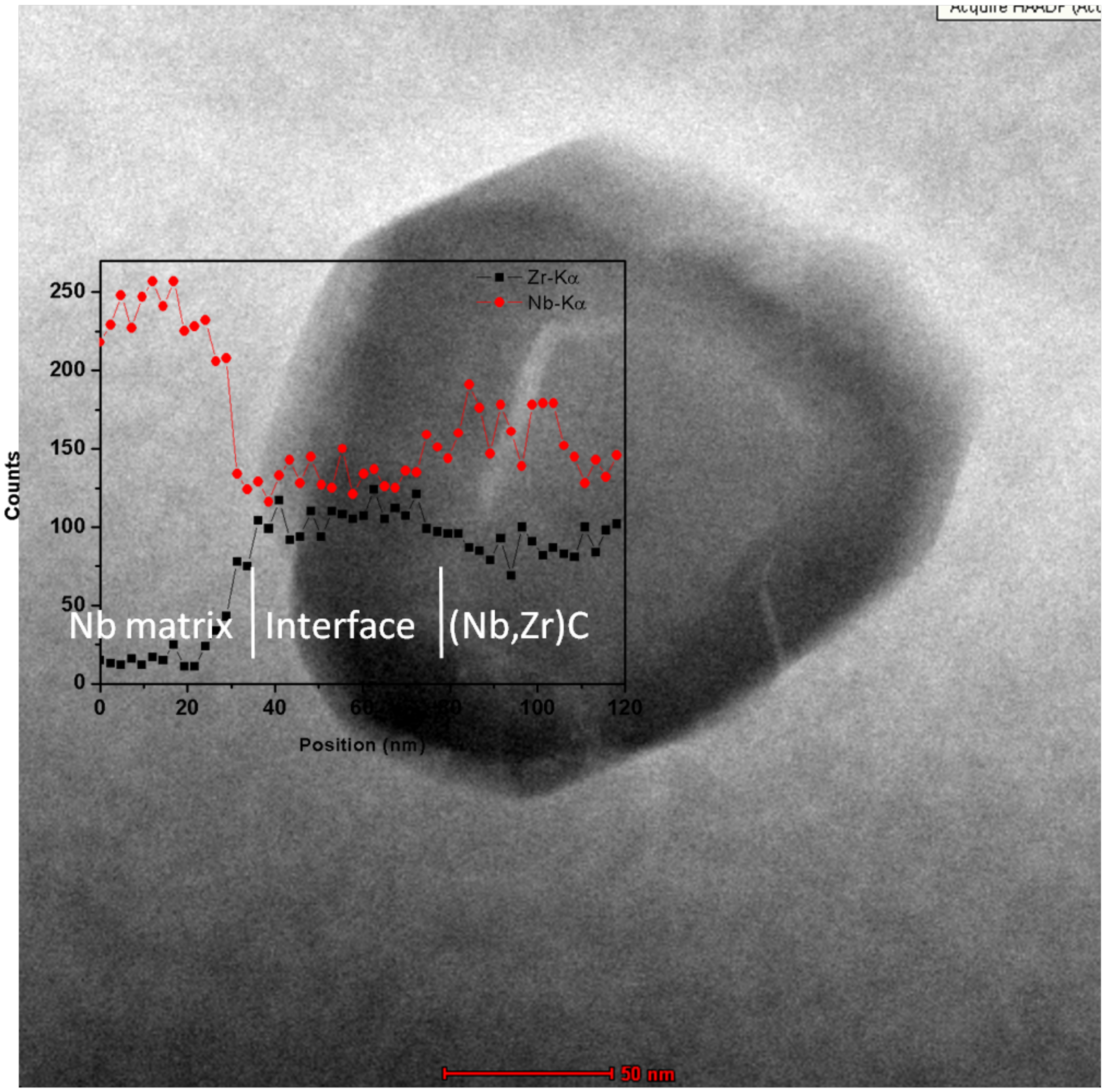

Figure 5.35: EDS line profile across the interface between Nb matrix and $(Nb,Zr)_2C$, showing the presence of three regions: (1) low Zr (Nb matrix region), (2) high Zr (interface) and (3) Zr concentration lower than the previous two regions ((Nb,Zr)C region).

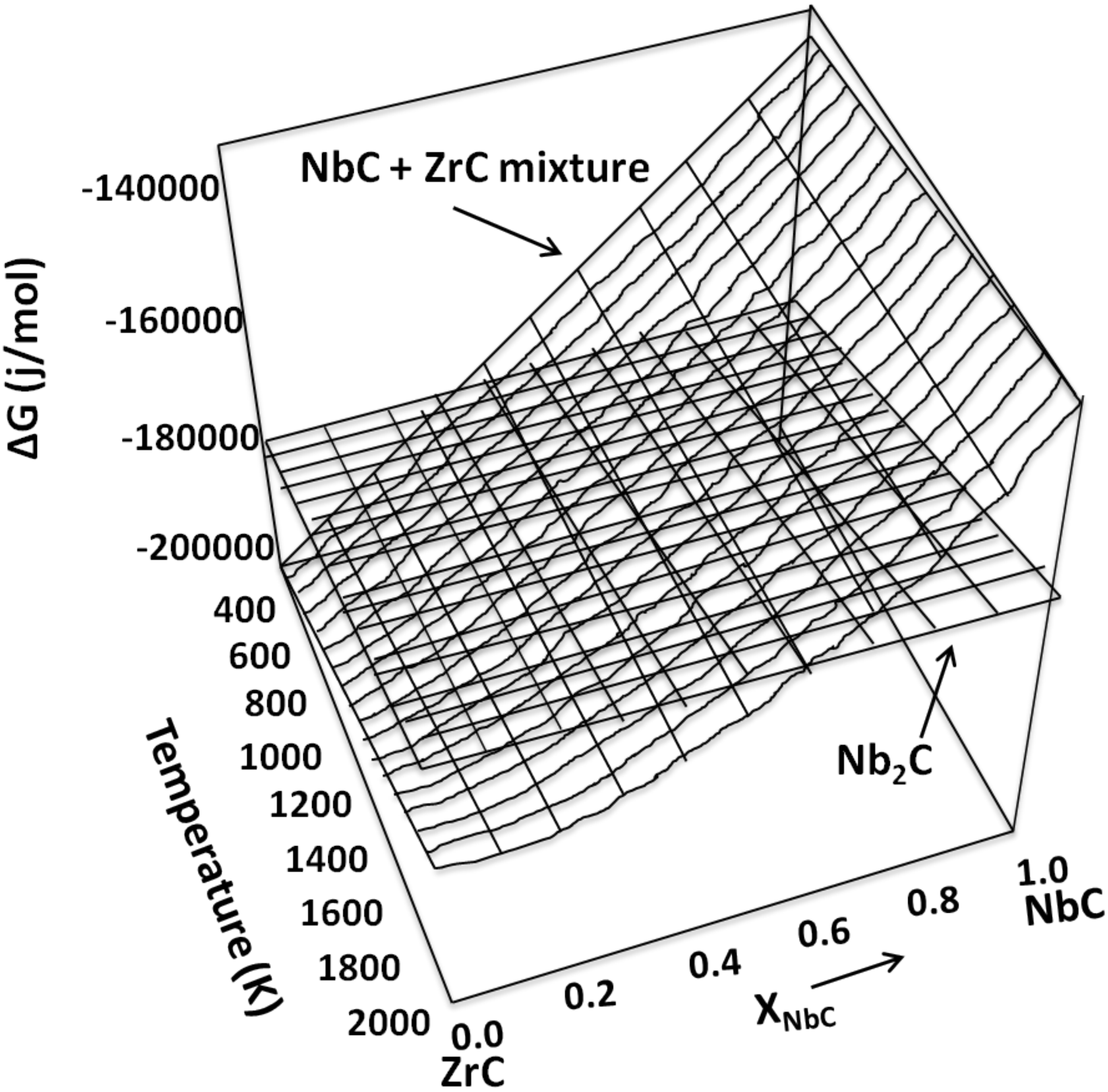

Figure 5.36: Free energy surfaces of Nb_2C and NbC + ZrC mixture when $a_{Zr} = 1$. Intersection specifies the equilibrium ZrC(NbC) concentration [107].

5.5. Summary

The present study on the microstructural characterization of the Nb-1Zr-0.1C alloy was focused on various carbides which formed during thermomechanical treatments. This study can be summarized by the following points:

1. The as-solidified Nb alloy had needle morphology of second phase precipitates in the Nb matrix. These precipitates had high concentration of planar faults. Using, XRD and TEM, these precipitates were identified as γ-Nb_2C carbides. Orientation relationship between carbide phase and matrix was determined using composite SAED patterns of carbide and the matrix phase. After arranging the Nb and Nb_2C according to the orientation relationship and incorporating crystallographic details of the structures of Nb and Nb_2C, it was shown that transformation of Nb to Nb_2C take place by occupation of carbon atoms at octahedral sites in Nb lattice whereas for this transformation large movement of Nb atoms is not required. The lattice strain calculations showed that during the formation of Nb_2C, strain builds up on (0001) planes due to which formation of defects in the Nb_2C phase occurs.

2. The microstructural characterization of the deformed samples showed that the needle and cuboidal morphology of carbides correspond to α-$(Nb,Zr)_2C$ and $(Nb,Zr)_3C_2$ carbides, respectively. It showed that after deformation of the as-solidified alloy at 800 °C, the γ-Nb_2C carbides which was present in the as-solidified sample disappeared nearly and transformed to other carbides in the form of α-$(Nb,Zr)_2C$ and $(Nb,Zr)_3C_2$ carbide phases.

3. The microstructure of the recrystallized samples showed the presence of fine scale ($\sim$ 100 nm) spherical morphology of precipitates. Using synchrotron XRD and TEM, these precipitates were identified as (Nb,Zr)C type of carbide phase. HRTEM analysis of the (Nb,Zr)C phase showed that most of these carbides precipitated in the vicinity of the $(Nb,Zr)_3C_2$ carbide phase in the Nb matrix. It did not show the presence of $(Nb,Zr)_2C$ and $(Nb,Zr)_3C_2$ carbides in the annealed samples. It indicated that the prior existing carbides in deformed samples were dissolved and a new fcc carbide phase ((Nb,Zr)C) precipitated at the vicinity of the $(Nb,Zr)_3C_2$ metastable carbide phase in the Nb matrix. The orientation relationship between (Nb,Zr)C and Nb matched with Nishiyama-Wasserman orientation relationship between fcc and bcc phases. The detailed crystallographic anal-

ysis of this structure based on orientation relationship showed that (Nb,Zr)C has formed by diffusional phase transformation and to form (Nb,Zr)C carbide phase, large movement of Nb and C atoms required.

4. Finally, this study has shown that the sequence of the formation of stable (Nb,Zr)C carbide phase as: $Nb_2C \rightarrow (Nb,Zr)_2C + (Nb,Zr)_3C_2 \rightarrow (Nb,Zr)C$.

CHAPTER 6

Textural and microstructural evolutions during deformation and annealing of the Nb alloy

During deformation depending upon the external conditions, various modes of slip systems get activated which result in development of different textures in the material. Among various materials, bcc based materials show high propensity for texture because of large differences in the activation energies of various slip systems. Even Nb is not an exception to this, therefore, special attention has been paid to study the development of texture during deformation and annealing treatments. In this chapter, deformation and annealed textures were simulated with various slip systems and compared with the experimentally developed textures. Based on the analysis, mechanism for the development of texture is proposed. In addition, the influence of annealing temperature and time on the stability of carbide phases has also been discussed.

6.1. Background

In order to fabricate the material into different shapes and sizes for structural applications, material is required to exhibit good formability. Development of texture during deformation and annealing decides the properties of the material. In addition, crystallographic texture of the material can also be exploited in improving the formability of a material [24]. Therefore, it is important to study texture developments during deformation and annealing of a material.

According to Raabe *et al.* [69] and Jiang *et al.* [24], in pure niobium, up to 70% deformation α-fiber is the dominant fiber and for deformation greater than 70%, γ-fiber is the dominant fiber. Borodkina *et al.* [70] and Abreu *et al.* [71] have observed different texture in pure Nb. According to them [70, 71], beyond 70% deformation, α-fibre is the dominant fiber. The reason for difference in the texture in the same type of material has been attributed to the differences in their microstructures. These differences in the microstructures include grain size, size of the precipitates etc., For example, coarse grain microstructure leads to heterogeneous deformation resulting in the generation of shear bands. These shear bands facilitate nucleation of randomly oriented grains during recrystallization. Therefore, increasing grain size leads to weakening of the α and γ-fiber texture [72].

Borodkina *et al.* [70] have investigated the effect of addition of alloying elements (0.5% Zr, 0.05% Ti) on the texture of pure niobium [70]. In pure Nb beyond 90% deformation, $\{113\}$ fiber texture was the dominant texture component, whereas for the same amount of deformation, the Nb-0.5%Zr-0.05%Ti alloy showed predominantly $\{100\}\ \langle 110\rangle$ texture. Annealing has also shown differences in the texture between pure Nb and alloyed niobium. These observations clearly show that even addition of small percentage of alloying elements can change the texture of pure material considerably. It also emphasizes necessity for studying the textural evolutions for each of the material separately.

Titran *et al.* [16, 62] have studied the effects of thermal aging and processing on the microstructure of the Nb-1%Zr-0.1%C alloy. These studies have shown that with increasing annealing time, the orthorhombic precipitates of Nb_2C completely transformed into face centered cubic carbides of Nb and Zr. Zr concentration in the cubic carbide is reported to vary from 25 to 75 wt.%. In spite of having such potential importance, very few studies have been reported in literature on textural and microstructural evolution for the Nb alloy (Table.2.7) and no systematic work has been carried out on texture and microstructural evolutions during deformation and annealing of the Nb-1%Zr-0.1%C alloy. Therefore, the present chapter is focused on the investigation of texture and microstructure evolutions during deformation and annealing of Nb-1%Zr-0.1%C alloy.

6.2. Textural evolutions in the Nb alloy

6.2.1. Deformed texture

In order to study the evolution of texture during deformation, it was necessary to have random texture in the beginning. As-solidified structure was having very large grain size, it does not represent a truly random texture. To initiate the study, well annealed samples having randomly oriented grains of 40 μm size were used. The recrystallized samples used for the texture studies have been referred in this chapter as the as-received sample.

The as-received samples were deformed up to 40%, 60% and 80% of the original thickness. Rolling direction was strictly maintained along the single direction. For bulk texture measurements, (200), (220) and (111) pole figures were taken from deformed specimens using the X-ray diffractometer. Subsequently, pole figures, sample orientation distribution function (ODF), texture fiber volume fractions and their intensities were computed using orthorhombic sample symmetry in the MTex open source texture analysis software. In general bcc materials have predominant α and γ-fiber textures. These textures appear in the ϕ_2-45° and ϕ_1-0° sections of ODF plots. Therefore to analyze these textures ϕ_2-45° and ϕ_1-0° sections were taken from the ODF plots. Figs.6.1 and 6.2 show the Bunge ODF ϕ_2 45° and ϕ_1 0° sections of as-received, deformed and annealed samples. It was observed that the as-received and 40% deformed samples have low difference between the maximum and minimum values of intensity ($\sim$ 2). It indicates that up to 40% deformation, development of the strong texture does not take place. The samples deformed up to 60% and 80% showed large difference in the maximum and minimum intensity, 4 and 5.8, respectively (Fig. 6.1 and 6.2(ii), (iii)). It led to predominant development of α and γ-fiber textures in the samples [68]. Volume fractions of α and γ-fibers were estimated from ODF and are shown in Fig.6.3. The as-received and 40% deformed samples (Fig.6.3(a)) have nearly equal volume fractions of α and γ-fibers with very low values (0.1-0.15). However, there is a significant build up of α and γ-fiber components in samples deformed beyond 40%. In these samples increase in the strength of the γ-fiber was found to be more than that of the α-fiber. In order to verify the variation of intensities of individual orientations present in the α and γ-fibers, the ODF intensities were plotted along the α and γ-fibers and are presented in Fig.6.4. In the case of 60% deformed sample, Fig.6.4(a) shows the evolution of three texture components in the α-fiber and these were $\{001\}\langle110\rangle, \{112\}\langle110\rangle$ and a third texture component at $(0°(\phi_1), 45°(\phi), 45°(\phi_2))$. The orientation at $(0°, 45°, 45°)$ corresponds to miller indices of $\{1, 1, 1.41\}\langle110\rangle$. Among these three orientations, orientation intensities of $\{001\}\langle110\rangle, \{112\}\langle110\rangle$ are same while the intensity of $\{1, 1, 1.41\}\langle110\rangle$ component exceeded the former two components. After 80% deformation, the maximum intensity shifted to $\{111\}\langle110\rangle$ texture component. In the case of γ-fiber, for the sample deformed beyond 40% reduction, all the orientations present in the γ-fiber have increased and a weak preference for $\{111\}\langle110\rangle$ texture component was observed.

Fig.6.5 shows the inverse pole figures (IPF) of as-received and deformed samples, which are taken in the direction parallel to the rolling direction (RD) and rolling plane normal direction (ND), respectively. IPF map of rolling direction in the as-received sample shows (Fig.6.5(a)) two high intensity regions. First region is very close to $\langle001\rangle$ and second region is in between

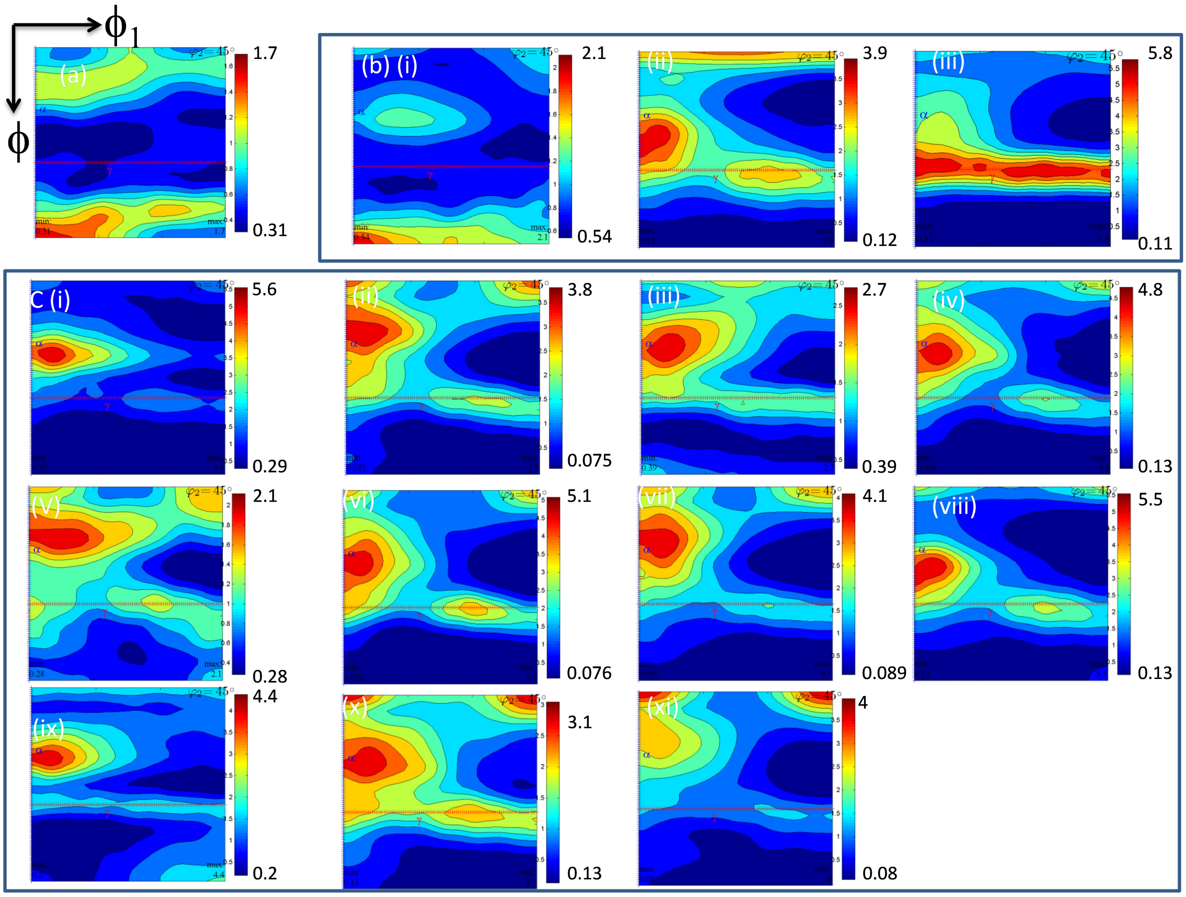

Figure 6.1: ϕ_2 45° sections of (a) as-received, (b) deformed (i) 40% reduction, (ii) 60% reduction, (iii) 80% reduction and (c) annealed samples of 60% deformed samples at 1300 °C for different soaking time (i) 0, (ii) 0.5, (iii)1, (iv) 1.5, (v) 2, (vi) 2.5, (vii) 3, (viii) 4, (ix) 5, (x) 6, (xi) 7 hrs showing the presence of α and γ-fiber texture at ϕ_1 0° and ϕ 54.7°, respectively.

$\langle 111 \rangle$ and $\langle 011 \rangle$. The IPF map of rolling plane normal (Fig.6.5(b)) is close to $\langle 011 \rangle$ direction. After 40% thickness reduction, the first and second components present in the as-received sample are shifted to center of the $\langle 001 \rangle$, $\langle 111 \rangle$ and $\langle 111 \rangle$, $\langle 011 \rangle$ directions. The direction parallel to rolling plane normal became highly texture with respect to $\langle 011 \rangle$ direction. With increasing the percentage of deformation (>40%), deformed samples become highly textured with the rolling direction parallel to $\langle 011 \rangle$ and rolling plane normal parallel to $\{111\}$.

6.2.2. Annealed texture

The 60% deformed sample was annealed at 1300 °C for different soaking time periods (0, 0.5, 1, 1.5, 2, 2.5, 3, 4, 5, 6, 7 hrs). It was shown in the previous chapter (Chapter.4) that annealing of the deformed samples at 1300 °C clearly showed the recrystallization evidence. Based on this data, the recrystallization temperature as 1300 °C was considered for the annealing treatments.

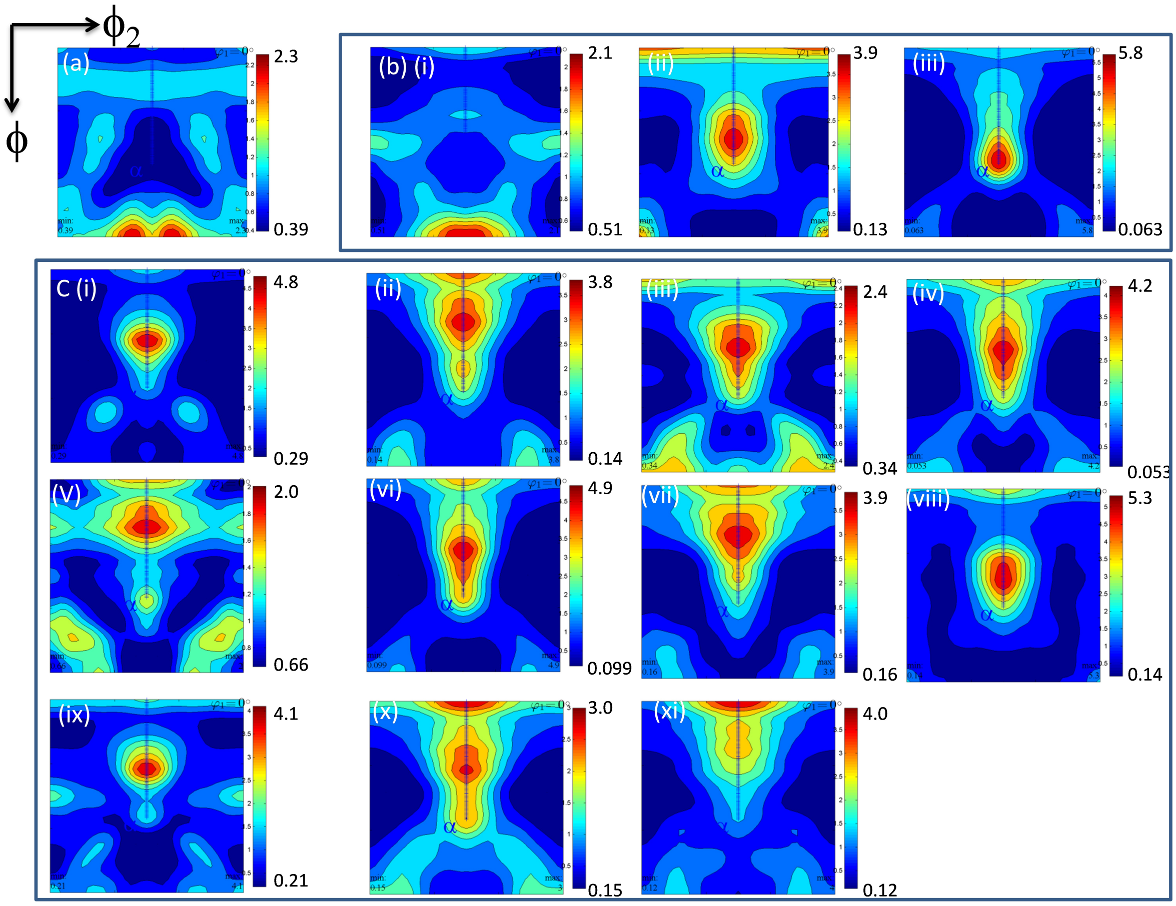

Figure 6.2: ϕ_1 0° sections of (a) as-received, (b) deformed (i) 40% reduction, (ii) 60% reduction, (iii) 80% reduction and (c) annealed samples of 60% deformed samples at 1300 °C for different soaking time (i) 0, (ii) 0.5, (iii)1, (iv) 1.5, (v) 2, (vi) 2.5, (vii) 3, (viii) 4, (ix) 5, (x) 6, (xi) 7 hrs showing the presence of α-fiber texture at ϕ_2 45°.

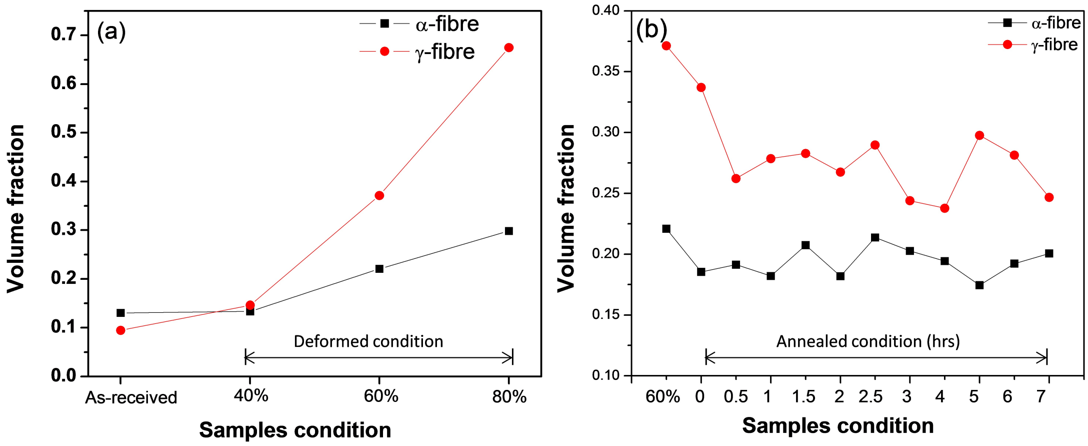

Figure 6.3: α and γ-fiber fractions of (a) as-received and deformed samples, (b) 60% deformed and annealed samples of Nb alloys.

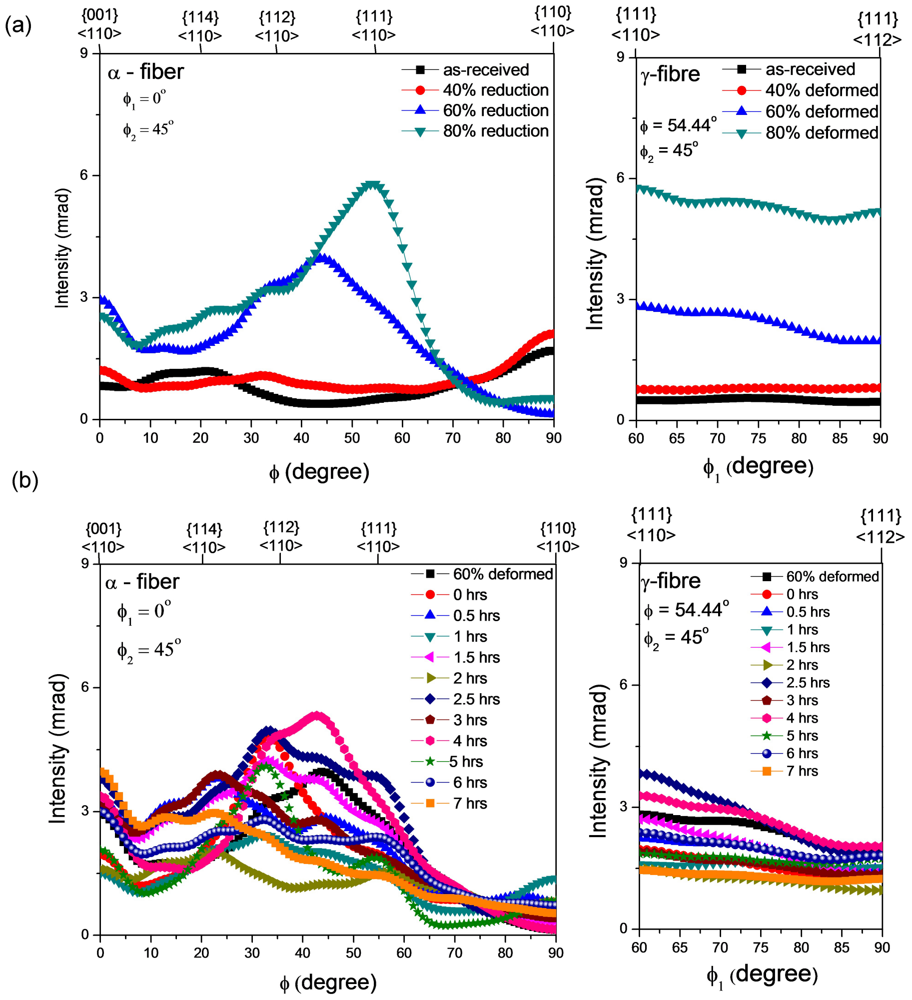

Figure 6.4: ODF intensities of individual orientations present in the α and γ-fibers in (a) as-received and deformed samples, (b) 60% deformed and annealed samples.

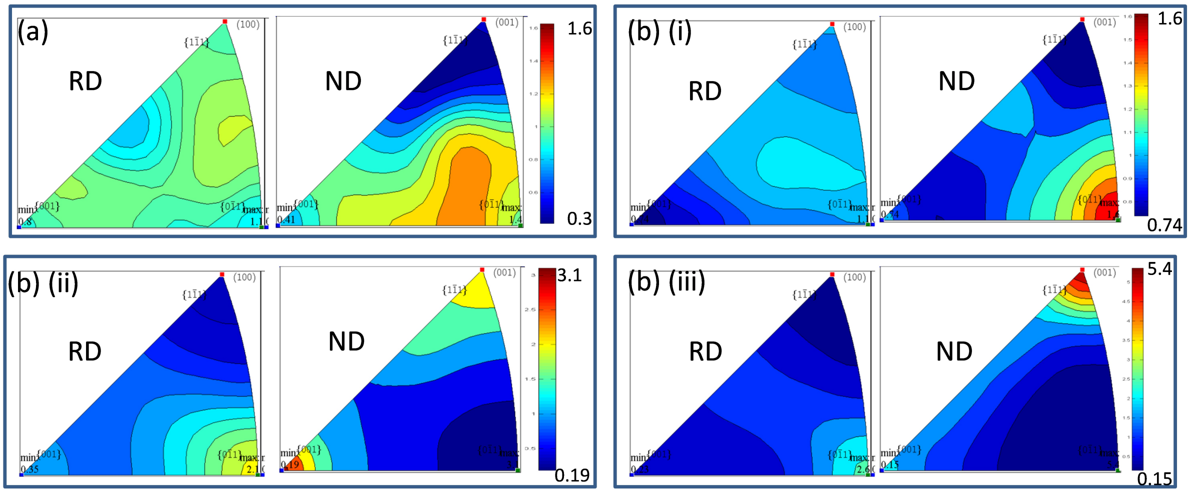

Figure 6.5: Inverse pole figures of (a) as-received and (b) deformed samples of (i) 40% reduction, (ii) 60% reduction and (iii) 80% reduction.

These annealed sample were characterized by XRD for bulk texture analysis.

ϕ_2-45° and ϕ_1-0° sections of annealed samples are shown in Figs.6.1 and 6.2. These figures show the presence of α and γ-fibers in the annealed samples. Fig.6.3(b) shows variation of fiber intensity for the 60% deformed and annealed samples. It reveals that after annealing, there is no significant change in the α-fiber intensity, whereas, the intensity of γ-fiber, up to 0.5 hrs soaking time, has decreased but thereafter it remained unchanged during subsequent annealing treatment. Thus it can be inferred that the annealing treatment dilutes the deformation texture. When the intensity of individual orientation component was observed (in Fig.6.4(b)) an increase in $\{001\}\langle 110\rangle$ orientation and decrease in two orientations $\{112\}\langle 110\rangle$, $\{111\}\langle 110\rangle$ in the α-fiber were noticed. However, in the case of γ-fiber, there was no such change in the texture components. It remained similar to as it was present in the deformed sample i.e.,$\{111\}\langle 110\rangle$ component intensity is slightly higher than the $\{111\}\langle 112\rangle$. It also shows that annealing reduced the intensities of all the orientations. Fig.6.6 shows the IPF maps of the annealed samples. It showed modifications in the deformation texture as a function of annealing time. Fig.6.6. clearly shows that with increasing annealing time, the direction parallel to rolling plane normal shifted to $\langle 001\rangle$, whereas rolling direction remained same as in the deformation texture i.e., $\langle 011\rangle$ direction. This behaviour shows that the annealed samples developed $\{001\}\langle 110\rangle$ texture.

6.2.3. Microtexture study on deformed and annealed samples

To study the microtexture of the deformed and annealed samples, all the samples were characterized by EBSD. Figs.6.7 and 6.8 show EBSD images of deformed and annealed samples of the Nb alloy, respectively. The as-received sample (Fig.6.7(a)) has an average grain size of 40 μm. The EBSD images of deformed samples (Fig. 6.7(b)) showed that with increasing the extent of deformation, volume fraction of the $\{111\}$ grains increased. γ-fiber represents a texture condition where $\{111\}$ planes are aligned along the rolling plane [68]. Therefore, increasing volume fraction of the $\{111\}$ grains indicates that the deformed samples have predominant γ-fiber texture. This observation is in agreement with the bulk texture results. In order to quantify the percentage of recrystallization in annealed samples, GOS (grain orientation spread) has been calculated from the EBSD data. A large value of GOS indicates that grains still have remnant plastic strain and could not recrystallize completely. For typical recrystallized grains the value of GOS should be less than 1°. Based on this criterion, percentage of recrystallization

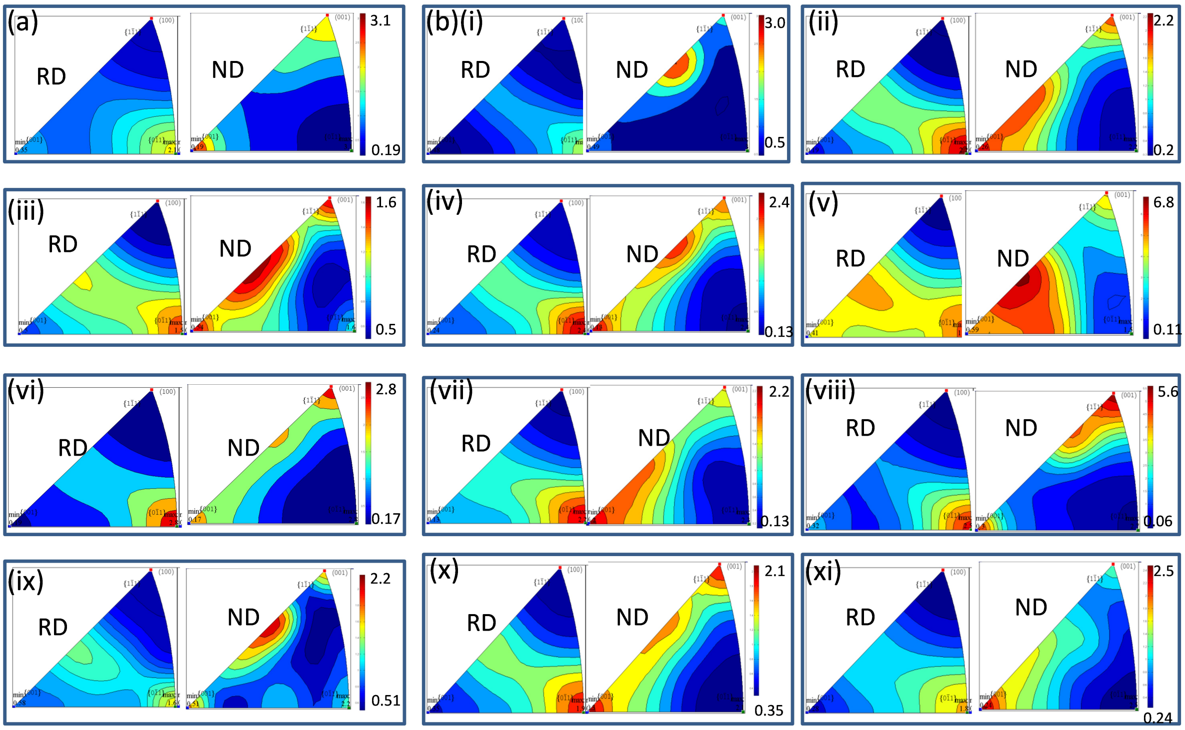

Figure 6.6: Inverse pole figures of (a) 60% deformed sample and (b) annealed samples at 1300 °C for different soaking times (i) 0, (ii) 0.5, (iii) 1, (iv) 1.5, (v) 2, (vi) 2.5, (vii) 3, (viii) 4, (ix) 5, (x) 6, (xi) 7 hrs.

was estimated and is plotted in Fig.6.9(a). It shows that the 97% of the grains present in the the annealed samples, with out soaking time (soaking time = 0 sec) got recrystallized. Upon increasing the soaking time, percentage of recrystallization remained more or less constant. It indicates that the deformed samples are got completely recrystallized during the heating period. Grain size variation as a function of annealing time has been plotted in Fig.6.9(b). It shows no noticeable variation in the grain size, indicating nearly negligible grain growth during annealing treatments.

6.2.4. Study of second phase precipitation

The OIM images (Figs.6.7,6.8) did not show the presence of any precipitates in the as-received and annealed samples. In order to verify the presence of second phase, the as-received and annealed samples were examined under TEM. Fig.6.10(a) shows a bright field (BF) image of the recrystallized sample. It shows the presence of very fine spherical morphology precipitates (∼ 100 nm). To identify the precipitate phase, SAED patterns were collected from different zones from a single precipitate by carrying out systematic tilting experiments (Fig.6.10(b)). All these patterns could be successfully indexed in terms of a fcc lattice with a lattice parameter as a =

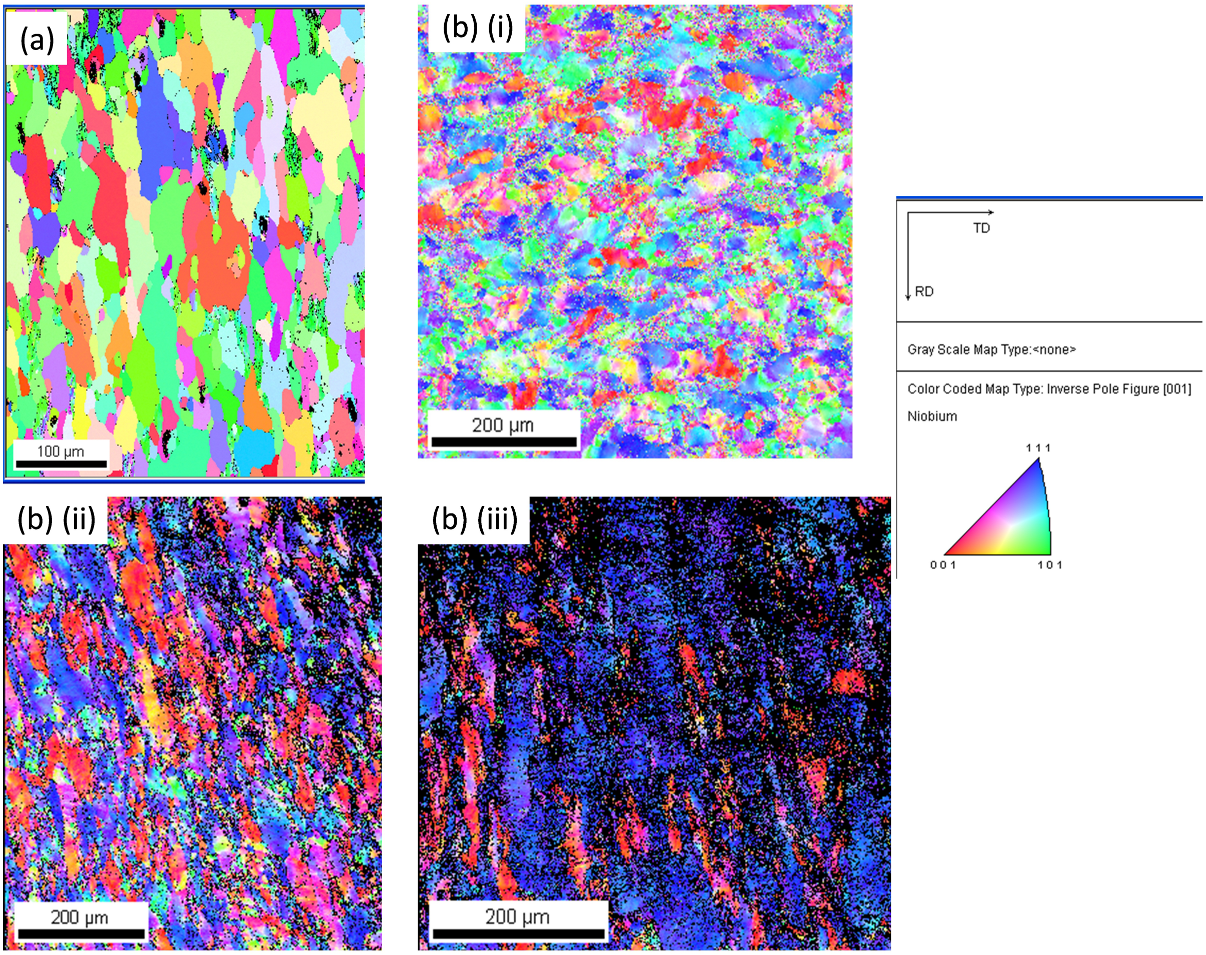

Figure 6.7: EBSD images of (a) as-received and (b) deformed samples of (i) 40% reduction, (ii) 60% reduction and (iii) 80% reduction.

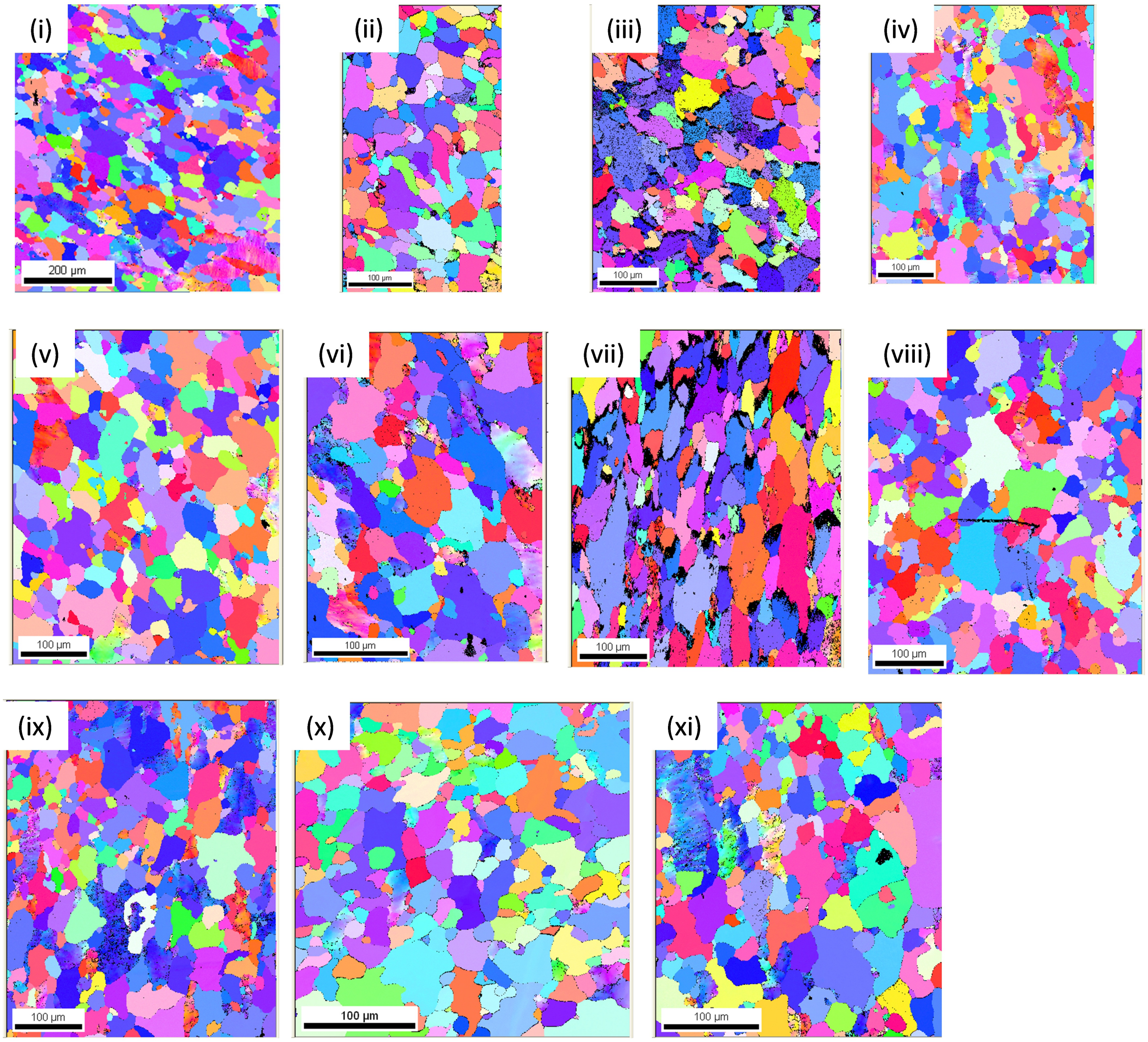

Figure 6.8: EBSD images of annealed samples of 60% deformed samples at 1300 °C for different soaking time (i) 0, (ii) 0.5, (iii) 1, (iv) 1.5, (v) 2, (vi) 2.5, (vii) 3, (viii) 4, (ix) 5, (x) 6, (xi) 7 hrs.

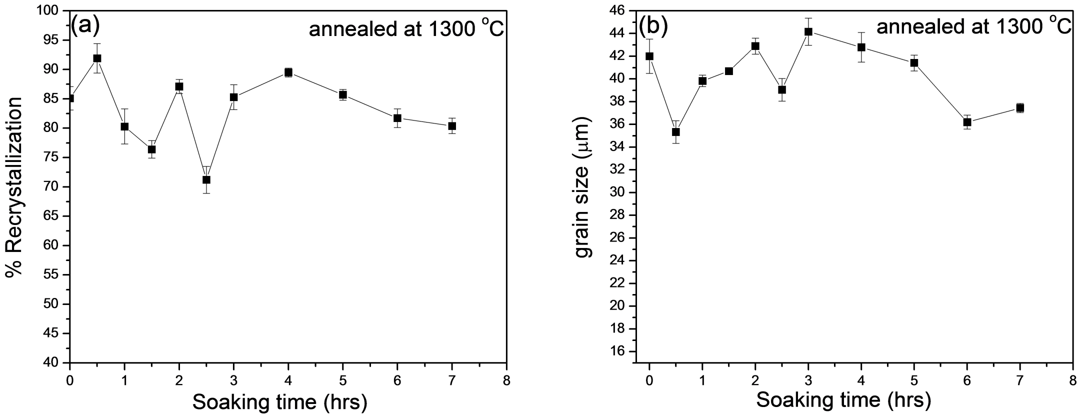

Figure 6.9: Variation of (a) grain size and (b) percentage of recrystallization of annealed samples at 1300 °C as a function of soaking time (hrs).

Table 6.1: Carbide precipitate size and its chemical composition in as-received and annealed samples of Nb alloy.

Samples		Size	Chemical composition (at.%)		Ratio of Nb/Zr
			Nb	Zr	
As-received		90-100 nm	66.23 ± 4	33.76 ± 2.7	1.96
Annealed	0.5 hrs	150-200 nm	59.72 ± 2.6	40.26 ± 4.2	1.48
	2.5 hrs	150-200 nm	45.63 ± 3.2	54.36 ± 3.7	0.84
	7 hrs	150-200 nm	20.70 ± 2.7	79.28 ± 2.3	0.26

4.75 A°. After carrying out EDS analysis of several precipitates, the average composition of the phase was determined as Nb(at.%) - 34.32±2 , Zr(at.%) - 16.99±3 and C(at.%) - 48.68±5. Combining information of crystallographic and chemical analysis of these precipitates, precipitate phase was identified as the (Nb,Zr)C carbide phase. These carbides are similar to the carbide precipitates found before in the recrystallized sample (mentioned in the Chapter.5).

In order to examine the effect of annealing treatment on these precipitates, the annealed samples of different soaking time 0.5, 2.5, 7 hrs were also examined in TEM. Fig.6.11 shows the bright field images of the annealed samples and the size of the second phase were tabulated in Table.6.1. It shows that with increasing the soaking time, the size of the second phase has not increased substantially. Chemical analysis of the precipitates carried out by EDS in STEM mode and is tabulated in Table.6.1. Chemical analysis has revealed that with increasing annealing time, Nb/Zr ratio in the precipitate has decreased. It indicates that Zr present in the Nb alloy has preferentially partitioned into precipitates.

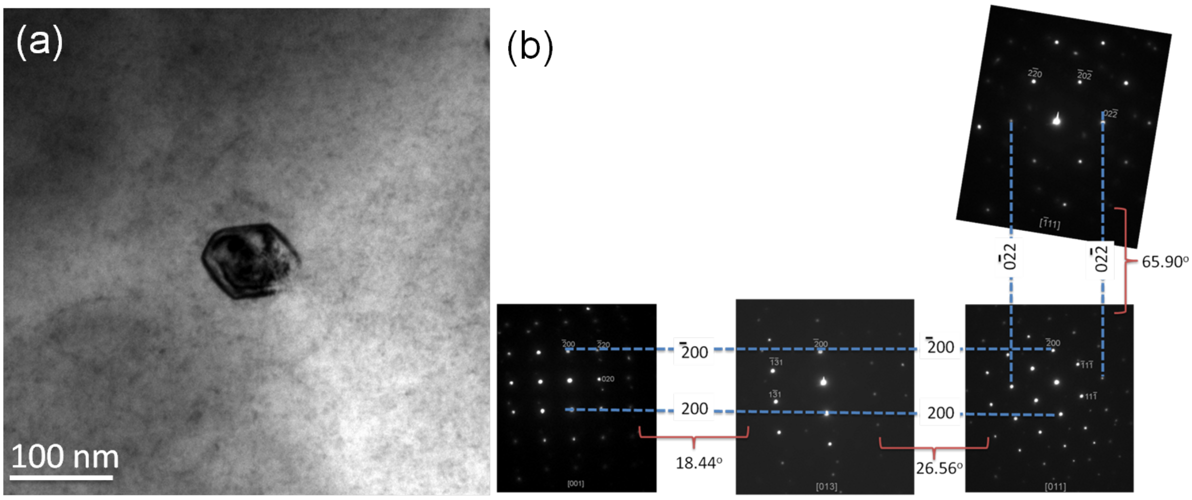

Figure 6.10: TEM images of as-received Nb alloy sample (a) bright filed image, (b) SAED patterns of precipitate at different zone axes and (c) composite SAED pattern of matrix and precipitate.

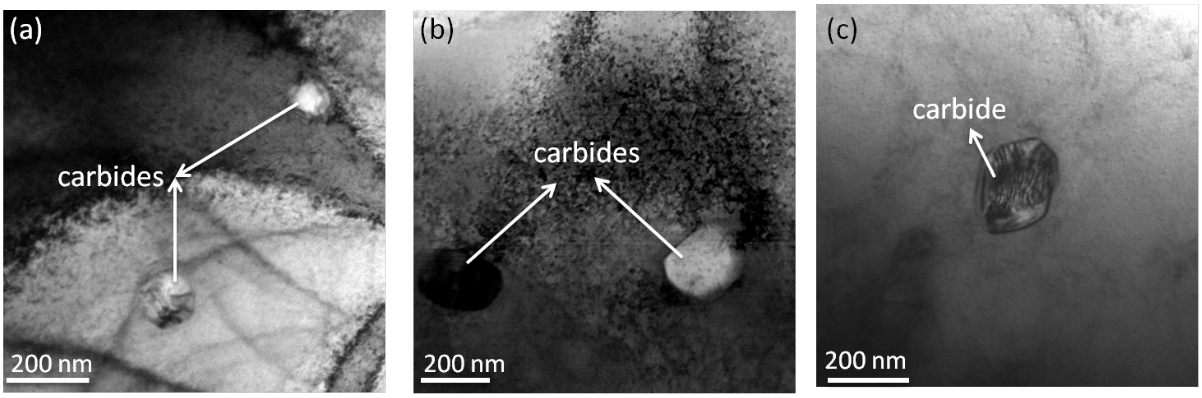

Figure 6.11: Bright filed images of annealed samples at 1300 °C for (a) 0.5 hrs, (b) 2.5 hrs and (c) 7 hrs.

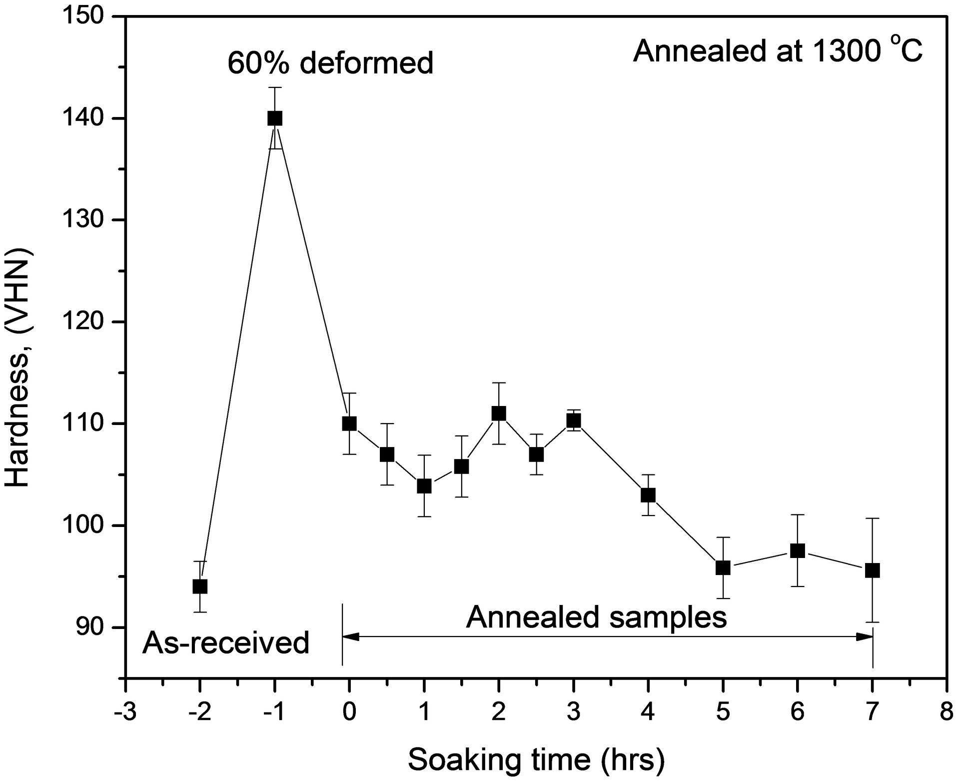

Figure 6.12: Variation of macrohardness (VHN) with soaking time (hrs) for annealed samples of Nb alloys.

6.2.5. Macrohardness of deformed and annealed samples

Fig.6.12 shows changes in macrohardness of 60% deformed sample during annealed treatment at 1300°C for different soaking times (hrs). The 60% deformed samples had a hardness of 140 ± 3 VHN. After annealing at 1300 °C with out any soaking time (0 hrs), the hardness of the sample decreased to 110 ± 3 VHN. Further, with increasing the soaking time up to 3 hrs the hardness of the sample remained constant thereafter. Again, the hardness of the sample decreased up to 95 ± 3 VHN with increase in the soaking time up to 5 hrs and remained constant up to 7 hrs soaking time. Thus two regions of hardness response (1) 0-3 hrs region and (2) 5-7 hrs could be identified.

6.3. Discussion

6.3.1. Texture evolutions in deformed samples

Study of macrotexture development in deformed samples showed that strong texture development takes place only on samples deformed up to 60% thickness and beyond. It remained nearly unaltered for samples deformed up to 40% thickness. Strong α and γ-fiber texture developed in the 60 and 80% deformed samples. Within the α-fiber, the $\{111\}\langle 110\rangle$ texture component was dominant and in the γ-fiber, increase in texture gradient from $\{111\}\langle 112\rangle$ to $\{111\}\langle 110\rangle$ were observed. It could be noticed from Table.2.7 that the deformed texture of the Nb alloy did not match with other bcc materials. Deformed samples of Nb alloy showed strong γ-fiber and unlike steel there is no significant α-fiber intensity [119]. Differences in the texture between different bcc materials have been attributed to differences in various parameters like, alloying elements, starting texture, percentage of deformation, type of heat treatment and second phase [67, 69]. The texture of the Nb alloy is not an exceptional to these variations. Although its deformation texture differs from the texture reported in other bcc materials, it does show some similarities with other bcc materials. For example, the trend observed in Nb alloy in the γ-fiber i.e., increasing texture gradient from $\{111\}\langle 112\rangle$ to $\{111\}\langle 110\rangle$, also exists in steels if deformed beyond 70%. However, intensities of the texture components present in the Nb alloy are weaker than those observed in steels. It indicating that there is much more of a random component in texture evolution in the Nb alloy. Nemat Nasser *et al.* [120] indicated that niobium has a tendency to form shear bands, which causes heterogeneous local rotations leading to a much wider range of crystal orientations. These orientations apparently weakens the classical bcc deformation texture characteristics. In order to understand the development of textures during rolling, the rolling textures of Nb alloy were simulated using Taylor type full constraint (FC) and relaxed constraint (RC) models.

In the FC model each grain is assumed to experience the same strain as that of the macroscopically whole sample, neglecting the adaptability of forces at the grain boundaries [69]. On the other hand, The RC model assumes shear strains to occur locally between adjacent grains (thus relaxes the zero shear constraint locally). At low strains shear is relaxed only in rolling direction (lath model) and at high strains additionally it is relaxed in tangential direction (pancake model) [69, 78]. For large strains, the pancake RC model gives comparable results with the experimental results than the lath model [79]. Therefore, in the present work, FC model and RC pancake model were used for simulation. MTM-FHM software developed by Van Houtte was used for simulation of deformation texture. EBSD data of 1465 grains in as-received sample (Fig.6.7(a)) were used for the simulation. In bcc materials, deformation takes place by activation of various types of slip systems $\{110\}\langle111\rangle$, $\{112\}\langle111\rangle$ and $\{123\}\langle111\rangle$. Therefore, simulations were carried out for all the possible slip systems for 80% deformation of as-recieved Nb alloy. Identical critical resolved shear stress was used for all types of slip systems. The ϕ_2 45° sections of all the simulations are shown in Fig.6.13 and 6.14. It shows that results of the RC model generated using $\{110\}\langle111\rangle$ and $\{112\}\langle111\rangle$ slip systems showed the fibre type texture whereas remaining all the simulations in RC and FC model showed the peak type texture. Variation in intensity along the γ-fiber between ϕ_2 45° sections generated using slip system $\{110\}\langle111\rangle$ and $\{112\}\langle111\rangle$, the ϕ_2 section of slip system $\{110\}\langle111\rangle$ shows lower intensity variation. Comparing simulation and experimental results of the ϕ_2 section images of 80% deformed samples of Nb alloy, simulation carried out using the pancake RC model with $\{110\}\langle111\rangle$ slip system matched closely with the experimental results. Further simulations were carried out for 10-80% deformation using FC and RC models with $\{110\}\langle111\rangle$ slip systems. Fig.6.15 show the ODF intensity variation along the α and γ-fibers. In FC and RC simulations, in α-fiber, the maximum intensity was at $\{112\}\langle110\rangle$ and $\{111\}\langle110\rangle$ orientations, respectively. In γ-fiber, in FC model, the ODF intensity at $\{111\}\langle112\rangle$ was higher than the intensity at the $\{111\}\langle110\rangle$, whereas, in the RC model, the ODF intensity at $\{111\}\langle110\rangle$ was higher than the intensity at the $\{111\}\langle112\rangle$ orientation. Comparing the experimental ODF intensity results (Fig.6.4)(a) with the simulated results, results generated by pancake RC model using $\{110\}\langle111\rangle$ slip systems are in good accordance with the experimental results. As shown by experimental ODF results, simulation ODF results (Fig.6.15) also showed that texture develops in the Nb alloys when the deformation percentage is $>$40%.

Dillamore *et al.* . [121] have shown that in bcc materials, activation of $\{110\}\langle111\rangle$ type of slip systems under biaxial stress (tensile and compression) condition leads most of the grains present in the material to rotate to $\{112\}\langle110\rangle$ component texture. This texture was successfully simulated by the FC Taylor model. It is worth mentioning here that the the basic assumption taken in their study was insignificant contribution of deformation occurring at grain boundary regions in the development of the texture. As Taylor FC model neglects the adaptability of the forces at the grain boundaries, simulation of the two results matched. However, the present experimental results do not match with the simulated FC results. In fact, they matched better

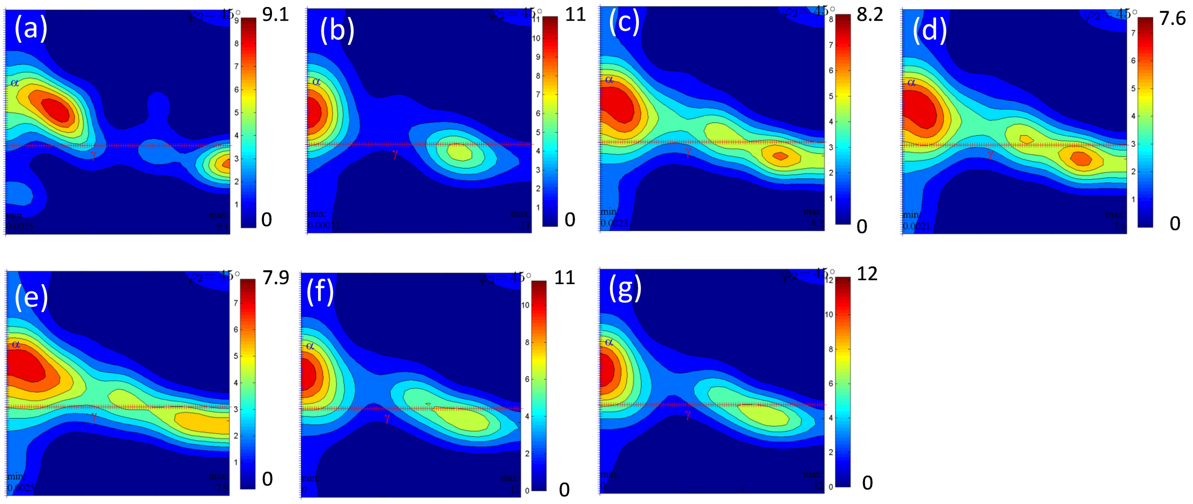

Figure 6.13: Simulated ϕ_2 45° sections of 80% deformed texture using full constraint Taylor type model consideration of slip on various combination slip systems in 110, 112 and 123 planes (a) $\{110\}\langle111\rangle$, (b) $\{112\}\langle111\rangle$, (c) $\{123\}\langle111\rangle$, (d) $\{110\}\langle111\rangle + \{112\}\langle111\rangle$, (e) $\{110\}\langle111\rangle + \{123\}\langle111\rangle$, (f) $\{112\}\langle110\rangle + \{123\}\langle111\rangle$ and (g)$\{110\}\langle111\rangle + \{112\}\langle111\rangle + \{123\}\langle111\rangle$.

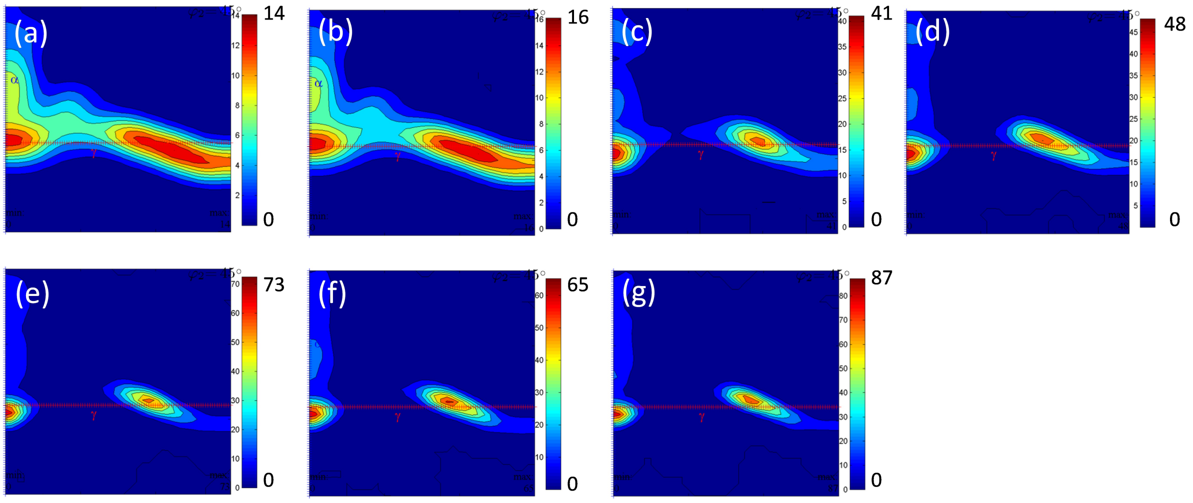

Figure 6.14: Simulated ϕ_2 45° sections of 80% deformed texture using relaxed constraint pancake Taylor type model consideration of slip on various combination slip systems in 110, 112 and 123 planes (a) $\{110\}\langle111\rangle$, (b) $\{112\}\langle111\rangle$, (c) $\{123\}\langle111\rangle$, (d) $\{110\}\langle111\rangle + \{112\}\langle111\rangle$, (e) $\{110\}\langle111\rangle + \{123\}\langle111\rangle$, (f) $\{112\}\langle110\rangle + \{123\}\langle111\rangle$ and (g) $\{110\}\langle111\rangle + \{112\}\langle111\rangle + \{123\}\langle111\rangle$.

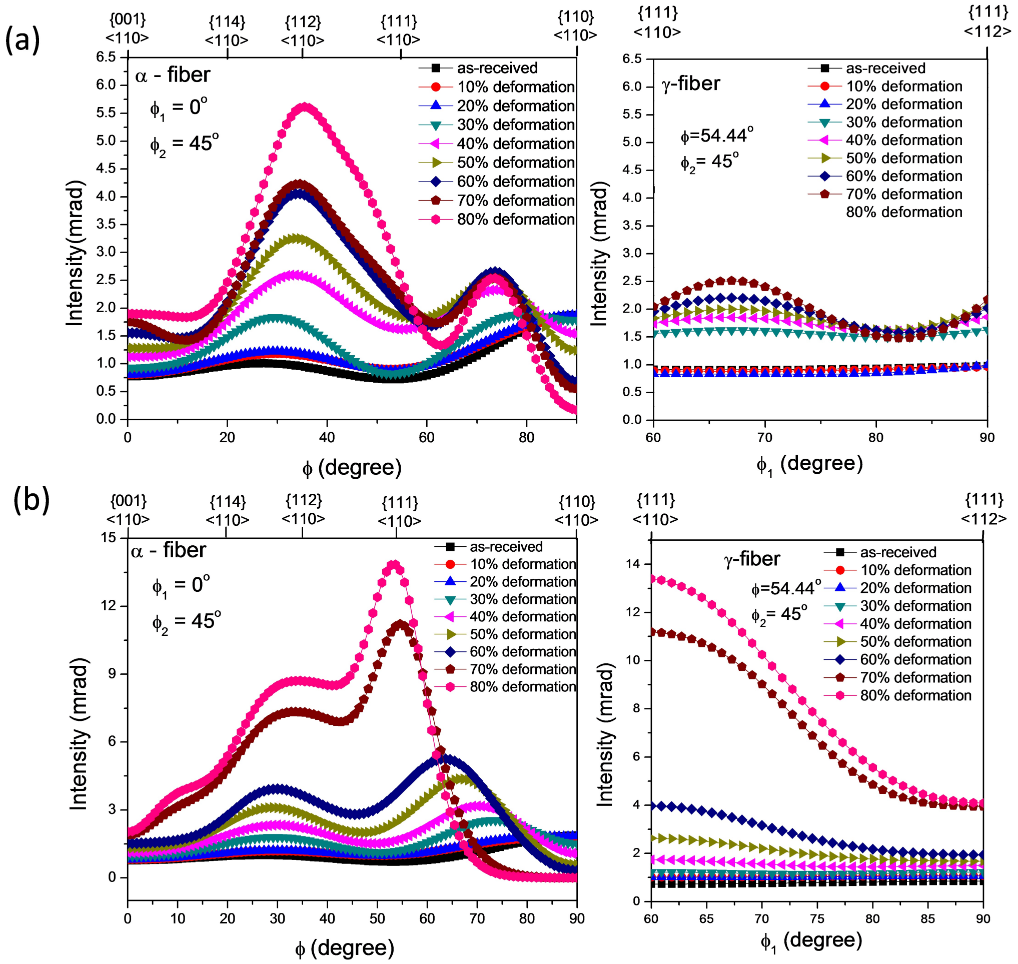

Figure 6.15: ODF intensities of individual orientations present in the α and γ fibers in simulated deformed texture of Nb alloy using as-received EBSD data simulated using Taylor type model (a) full constraint and (b) relaxed constraint Pancake model consideration of slip on $\{111\}\ \langle 110\rangle$ slip system.

with the simulation obtained using pancake RC model. The pancake model relaxes the shear strain along the rolling direction and tangential direction at grain boundary regions [78]. Hence, the present results clearly shows that in Nb alloys deformation at grain boundaries plays a vital role in the development of rolling texture in the Nb alloy which can not be neglected.

6.3.2. Texture evolutions in annealed samples

Annealing of the 60% deformed sample showed two major changes in the annealed texture with respect to deformed texture. First, the enhancement of $\{001\}\langle 110\rangle$ component in the α-fiber and decrease in the other two components $\{111\}\langle 110\rangle$ and $\{112\}\langle 110\rangle$. Secondly, decrease in the intensity of the γ-fiber. These changes lead to the development of a random texture in the annealed samples with a weak $\{001\}\langle 110\rangle$ texture. This change in texture between deformed and annealed samples indicates that different mechanisms were involved in the reformation of the microstructure during annealing. The $\{001\}\langle 110\rangle$ orientation has low Taylor factor [78]. Therefore, the formation of $\{001\}\langle 110\rangle$ texture in the annealed sample could be due to continuous recrystallization [78]. The recrystallized texture matches with the reported texture of the annealed Nb alloy (Nb-0.5%Zr-0.05%Ti).

Development of recrystallization textures during annealing in most of the bcc materials is characterized by a strong increase in the γ-fiber and disappearance of α-fiber. Recrystallization textures in steel can be explained by the criterion of release of strain energy based on elastic anisotropy [24]. Niobium has elastic anisotropy which is opposite to steel [122]. Therefore, evolution of recrystallization texture in Nb alloy is different from the texture observed in steel.

6.3.3. Microstructural evolutions in deformed and annealed samples

EBSD results showed that annealing temperature of 1300 °C is adequate for recrystallization. At the same time it is sufficiently low for noticeable competitive grain coarsening. Fig.6.9(a) shows low variation in grain size with increasing soaking time. Nearly constant grain size indicates low grain growth. Low grain growth could be attributed either to precipitation pinning grain boundaries or to low grain boundary mobility. In order to verify the precipitate pinning of grain boundaries, grain boundaries in various annealed samples were examined under TEM. Fig.6.16 show a typical example of grain boundaries in some of the annealed samples. Most of the precipitates were present within the grains and preferable presence of any kind of precipitates at the grain boundaries could not be observed in any of these micrographs. These observations

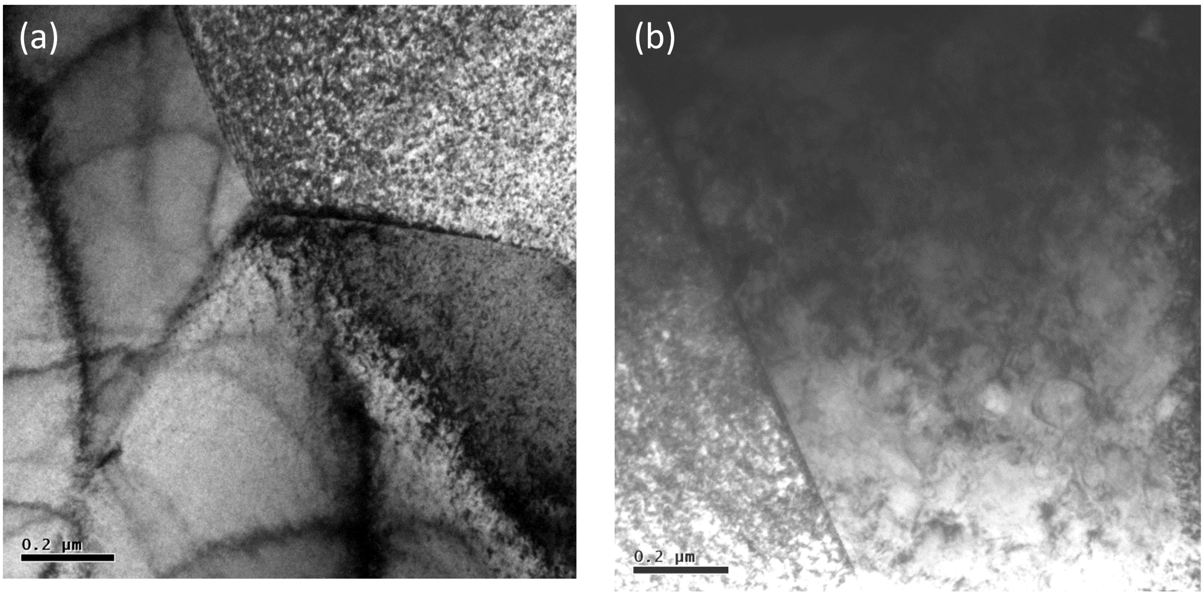

Figure 6.16: Grain boundary in the annealed samples (a) 0.5 hrs and (b) 2.5 hrs showing the absence of precipitates at the grain boundary.

clearly ruled out the possibility of precipitates pinning grain boundaries. Therefore, the reason of nearly constant grain size could be due to the low grain boundary mobility.

ATEM examination of annealed samples showed that with increasing soaking time, size of the precipitates did not increased but composition in terms of Nb/Zr ratio in the carbides has changed. Mehmet Uz et al [16, 63] have studied stability of various carbide phases at different temperatures between 1077 °C to 1482 °C up to 34,500 hrs. They have shown that (Zr,Nb)C is more stable in comparison to Nb_2C phase and also upon increasing the aging temperature and time the Nb/Zr ratio in (Zr,Nb)C carbide changes from 62/38 to 25/75. The present results show a similar trend in concentration variation where Zr/Nb ratio varied from 1.96 to 0.26. Farkas *et al.* [107] have carried out thermodynamic analysis of carbide precipitates in Nb-Zr-C alloy. They have shown that Zr rich (Zr,Nb)C is more stable carbide than Nb rich (Zr,Nb)C carbide. Therefore, the formation of Zr rich (Zr,Nb)C carbide could be attributed to the low free energy for the carbide in comparison to other carbide phases.

The above microstructural studies give evidences for decrease in macrohardness of the annealed samples. Fig.6.12 showed two regions (0 hrs, 4 hrs) where decrease in macrohardness of the annealed samples was observed. EBSD examination of annealed samples showed that during heating period, the deformed sample gets completely recrystallized. This led to decrease in macrohardness of the annealed sample at 1300 °C with negligible soaking time. Further decrease in the macrohardness of the annealed sample at 1300 °C for 4 hrs soaking time could be attributed to the decrease in the zirconium content in the matrix due to enrichment of zirconium in the carbide phase.

6.4. Summary

The present study on the macro and micro-texture development and microstructural evolutions in deformed and annealed samples of Nb alloy (Nb-1%Zr-0.1%C) can be summarized by the following highlight points.

- The macro and micro-texture studies of deformed samples showed that up to 40% of thickness reduction, deformation did not induce strong texture in the Nb alloy. However, at and beyond 60% deformation, the samples showed predominant development of α and γ-fiber textures in the samples. Among α and γ-fibre texture, γ-fiber texture was dominant and unlike steel there was no significant α-fiber intensity.
- Within the α-fiber, the $\{111\}\langle 110\rangle$ texture component was dominant and in the γ-fiber, increase in texture gradient from $\{111\}\langle 112\rangle$ to $\{111\}\langle 110\rangle$ was observed.
- Results produced by simulation using pancake relaxed constraint Taylor model considering $\{110\}\langle 111\rangle$ slip systems were in good agreement with the experimental results showing that deformation at the vicinity of grain boundary plays an important role in developing the deformation texture in the Nb alloys.
- Upon annealing at 1300 °C the deformed samples texture got randomized and weak $\{001\}\langle 110\rangle$ type of texture developed.
- With increasing annealing time, there was no substantial change in the grain size, indicating low grain growth for Nb alloy at 1300 °C due to low grain boundary mobility.
- With increasing annealing soaking time at 1300 °C, Zr concentration in the carbide precipitates increased and in the matrix region decreased. It led to decrease in the macro-hardness of the Nb alloy.

CHAPTER 7

Silicide coating on the Nb alloy and its oxidation behaviour

One of the main concerns of using Nb based alloys for high temperature applications is their poor oxidation resistance. Pure Nb undergoes severe oxidation at higher temperatures due to non protective oxide film formation. Oxidation resistance of Nb alloy can be improved either by alloying addition or by providing an oxidation barrier coating. As nuclear applications restrict the addition of alloying elements due to non favourable nuclear properties of many elements, therefore, in the present work, oxidation protection coatings have been attempted. In order to access the performance of coatings, silicide coated Nb alloy samples were produced using pack cementation technique and their oxidation behavior has been studied at higher temperatures. Oxidation behaviour of Nb-1%Zr-0.1%C alloy has been studied under atmospheric condition up to 1000 °C and compared with the oxidation behaviour of the silicide coated samples. Subsequently, From these results, the underlying mechanism for the prevention of high temperature oxidation of silicide coated samples has been discussed.

7.1. Background

The isothermal oxidation behaviour of the pure Nb metal has shown at least two distinct sequences of oxidation [25, 80, 84–86]. One sequence was observed when alloy was oxidized below 650 °C. Hurlen et al. [85] have proposed a sequence of oxidation events at and below 650 °C to explain the oxidation behaviour of the alloy. The sequence of oxidation events is linear $\rightarrow$ parabolic $\rightarrow$ linear $\rightarrow$ parabolic $\rightarrow$ parabolic. The initial linear rate of oxidation was due to the dissolution of oxygen in the niobium metal. Further oxidation led to the formation of NbO_x and NbO_z oxides which resulted into a parabolic rate of oxidation [123]. Upon further oxidation, both the oxides, NbO_x and NbO_z transformed into the stable Nb_2O_5 phase, which being a porous oxide phase enhanced the oxidation rate and produced a linear rate of oxidation [82, 85]. The two final parabolic stages were due to the formation of thick oxide scales, which might obstruct the gaseous flow of oxygen to the metal/oxygen interface. It has also been reported that with increasing temperature transition period from parabolic to linear becomes shorter.

The other sequence of oxidation of Nb alloy has been reported at higher temperatures (>650 °C). The reaction sequence during oxidation at higher temperatures (>650 °C) follow linear → parabolic → linear [25]. At higher temperatures, NbO_z is not a stable phase, instead a mixture of NbO and NbO_2 forms as an intermediate reaction product [25, 124]. The formation of NbO and NbO_2 led to a parabolic rate of oxidation. Arbuzov et al [89] have found that oxidation rate of the niobium metal increased with increase in temperature up to 900 °C, beyond 900 °C, oxidation rate is decreased. The reduction in the oxidation rate is due to the transformation of α-Nb_2O_5 to β-Nb_2O_5 [89].

Delgrosso et al. [125] have studied the oxidation characteristics of the Nb-1%Zr alloy up to 1200 °C in air under different condition of samples (as-cast, deformed and annealed) . All the samples showed parabolic oxidation behaviour up to 315 °C. At 371 and 399 °C, initial oxidation reaction rates were high and reduced progressively up to 60 hrs. Beyond 60 hrs, oxidation behaviour had changed from parabolic to linear. In the temperature region of 426 to 871 °C, oxidation rates remained linear and increased with increase in temperature. Beyond 871 °C, linear oxidation rate is independent of temperature. The reason for the change from parabolic to linear oxidation is the formation of oxides which have higher Pilling-Bedworth ratio [90].

Studies on the oxidation bahaviour of Nb alloys, which are meant for high temperature applications have shown that these alloys are susceptible to oxidation at temperatures as low as 500 °C [15]. Therefore, various approaches are being tried to improve the oxidation resistance at higher operating temperatures (>1000 °C). One approach is to develop improved alloys with alloying additions and the second approach is to provide an oxidation barrier coating to the existing alloys [26, 27]. In general, it has been found that by alloy addition, it is very difficult to simultaneously achieve high strength, good workability, high resistance to liquid alkali metals as well as better oxidation resistance. Therefore, the second approach of improving the oxidation resistance by external coating appears attractive. Literature shows that among all the elemental coatings, silicide coatings have good oxidation resistance, mechanical properties and high resistance to liquid alkali metals [95, 96]. Levy et al. [95] have studied the oxidation behaviour of a complex disilicide/tantalum-10tungsten alloy system at temperatures of 927 °C to 1482 °C. The silicide coated samples showed very good oxidation resistance at high temperatures due to the formation of SiO_2 oxide layer. It has also been shown that during oxidation, silicide coatings may undergo pesting [97, 98]. Therefore, it is important to provide a suitable silicide coating which can avoid the catastrophic oxidation.

Amongst various coating techniques, halide activated pack cementation technique (HAPC) is the most widely used process for applying protective coatings on high temperature materials [91]. Pack cementation process is an in-situ chemical vapor deposition (CVD) process which produces coating on substrate by diffusional mechanism [92]. It is a low cost process, particularly, suited for the formation of uniform diffusion coatings on structural alloy components of complex shapes and larger sizes.

Most of the oxidation behaviour studies focused on Nb and Nb-1Zr alloy and the work on the oxidation behaviour of Nb-1Zr-0.1C alloy and also on coated niobium alloys are very limited [84, 96, 126–129]. Therefore, present work is focused on studying oxidation behaviour of bare Nb-1Zr-0.1C alloy and silicide coated alloys. HAPC technique was used to produce the silicide coatings on the Nb alloy. The coating parameters were optimized to produce a two layer (Nb_5Si_3 and $NbSi_2$) coating on the Nb alloy. The oxidation behaviour of the bare Nb alloy and silicide coated samples was studied using thermogravimetric analysis (TGA). To study the oxidation kinetics of both the samples, isothermal oxidation experiments were carried out in air at different temperatures for different time periods. The oxide layers formed on the samples of Nb alloy and silicide coated sample were characterized by XRD, SEM, EBSD and TEM.

7.2. Characterization of silicide coated samples

The silicide coatings on Nb alloy was carried out by pack cementation technique at different temperatures 1200 °C, 1300 °C, 1400 °C and 1500 °C for different time periods (6, 9, 12, and 15 hrs). These coated samples were characterized by SEM, TEM and EBSD techniques.

7.2.1. Microstructural investigation under SEM

Surface and cross-section of the silicide coated samples was examined under SEM. Fig.7.1 shows the surface morphology of the coated layers produced at different temperatures. The sample coated at 1200 °C (Fig.7.1(a)) showed grainy nature of the coating surface. A wide variation in the size of grains indicates simultaneous precipitation and coalescence of silicide

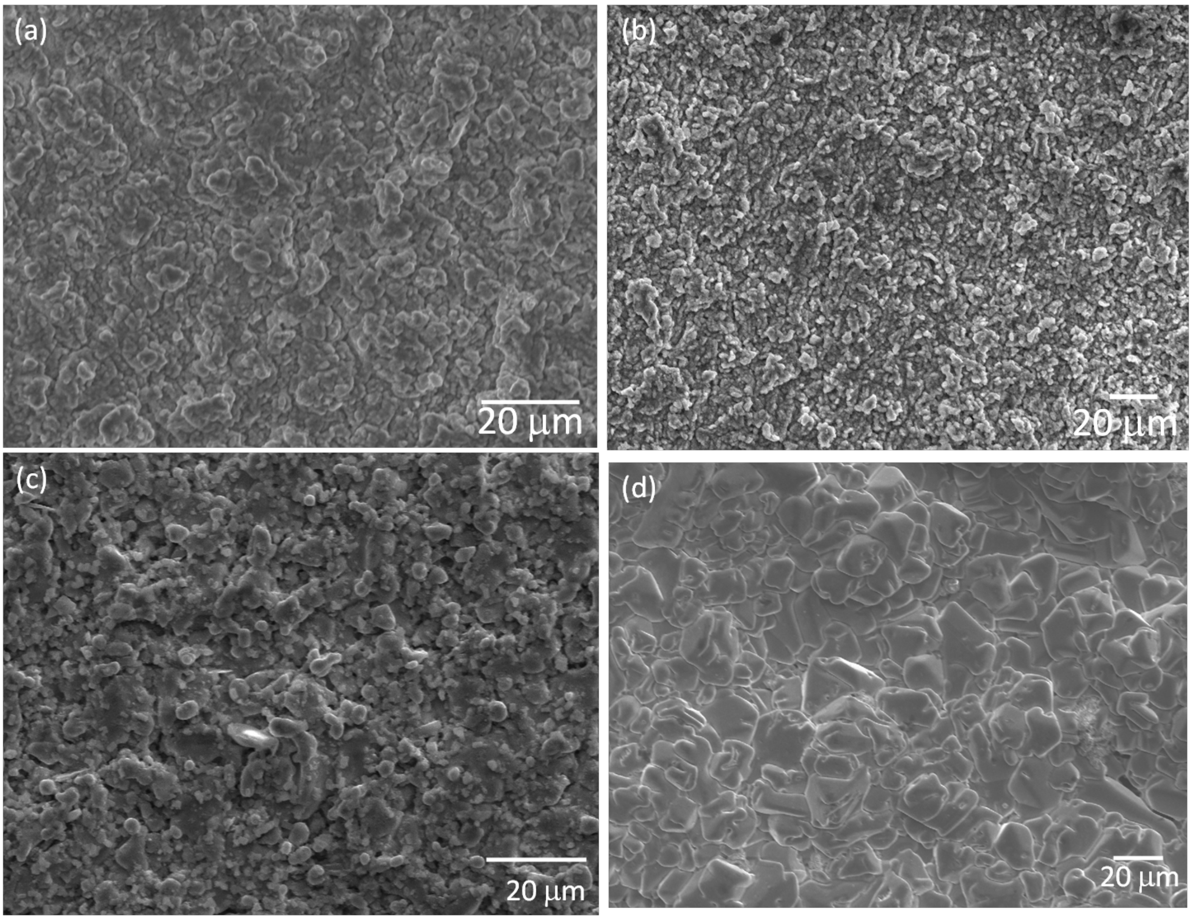

Figure 7.1: Secondary electron micrographs showing the surface morphology of silicide coated samples at (a) 1200 °C, (b) 1300 °C, (c) 1400 °C and (d) 1500 °C for 6 hrs.

grains. The grainy nature of coating could also be observed in the sample coated at 1300 °C (Fig.7.1(b)). In addition some uneven surfaces and cracks on the top surface were also noticed. The surface morphology of the silicide coating produced at 1400 °C (Fig.7.1(c)) appeared nearly similar to the morphology observed in coatings produced at 1300 °C (Fig.7.1(b)). Upon closer examination, however, subtle differences like increase in the average size of individual grain were noticed. The surface of the sample coated at 1500 °C appeared much smoother and the grains had much sharper interfaces of the crystallite. The surface morphology of the samples coated at 1500 °C, in comparison to previous two cases, shows substantial increase in the grain size. There are additional notable changes in the morphology of the grains; there are no holes or cracks on the surface as these were filled by the molten silicon. Silicon accumulated over the complete surface.

Fig.7.2 show SEM micrographs of typical cross-sectional views of silicide coatings carried out between 1200 °C to 1500 °C for 6 hrs. It may be noticed from these micrographs that

Table 7.1: Chemical composition determined by EDS at the positions marked on the BSE micrographs Fig.7.3.

Sample	Position	Elements (at.%)			Phase
		Nb	Zr	Si	
1200 °C	1	96.82	3.18	0	Nb alloy
	2	97.35	2.65	0	Nb alloy
	3	34.15	0	65.85	~ $NbSi_2$
	4	35.12	0	64.88	~ $NbSi_2$
1300 °C	1	94.58	5.42	0	Nb alloy
	2	93.89	6.11	0	Nb alloy
	3	63.14	0	36.86	~ Nb_5Si_3
	4	63.70	0	36.30	~ Nb_5Si_3
	5	33.80	0	66.20	~ $NbSi_2$
	6	33.89	0	66.11	~ $NbSi_2$

all the coatings produced at different temperatures were having uniform coating thicknesses. Coating produced at 1200 °C has a single phase whereas coatings produced at higher temperatures (1300-1500 °C) have two phases in the coating layer. When EDS line profiles of the cross-section were superimposed on the BSE micrographs (Fig.7.3) of samples coated at 1200 °C and 1300 °C, EDS analysis for 1200 °C sample showed a sharp drop at the interface indicating the existence of two phases (a silicide phase and a matrix phase) in the sample. Whereas, the composition profile for 1300 °C shows clearly the presence of three distinct regions in the microstructure. Chemical composition at the specific locations on cross-sections are tabulated in Table.7.1. Based on the stoichiometric analysis it was possible to identify all the phases in the microstructure. The stoichiometry of the coating layer matched with the $NbSi_2$ in 1200 °C sample. In the case of 1300 °C sample, stoichiometry of the outer layer coating matched with $NbSi_2$ phase and the intermediate layer between outer layer and substrate (Nb alloy) matched with Nb_5Si_3. The composition analysis obtained by EDS showing the presence of $NbSi_2$ single coating layer in 1200 °C sample, whereas for 1300 °C, the coating layer consisted of $NbSi_2$ and Nb_5Si_3 phases. The composition profiles obtained for the samples of 1400 and 1500 °C were found to be similar to 1300 °C sample showing the presence of two coating layers ($NbSi_2$ and Nb_5Si_3). However in 1500 °C sample, coating cross-section (Fig.7.2(d)) showed the presence of white precipitates in the $NbSi_2$ phase and above the Nb_5Si_3 phase. This was identified as pure silicon formed from molten Si. Melting point of silicon is 1414 °C, so during the heat treatment at 1500 °C, silicon got melted and deposited directly on the surface of the coating.

Average coating thickness of the silicide phases produced at different temperatures are

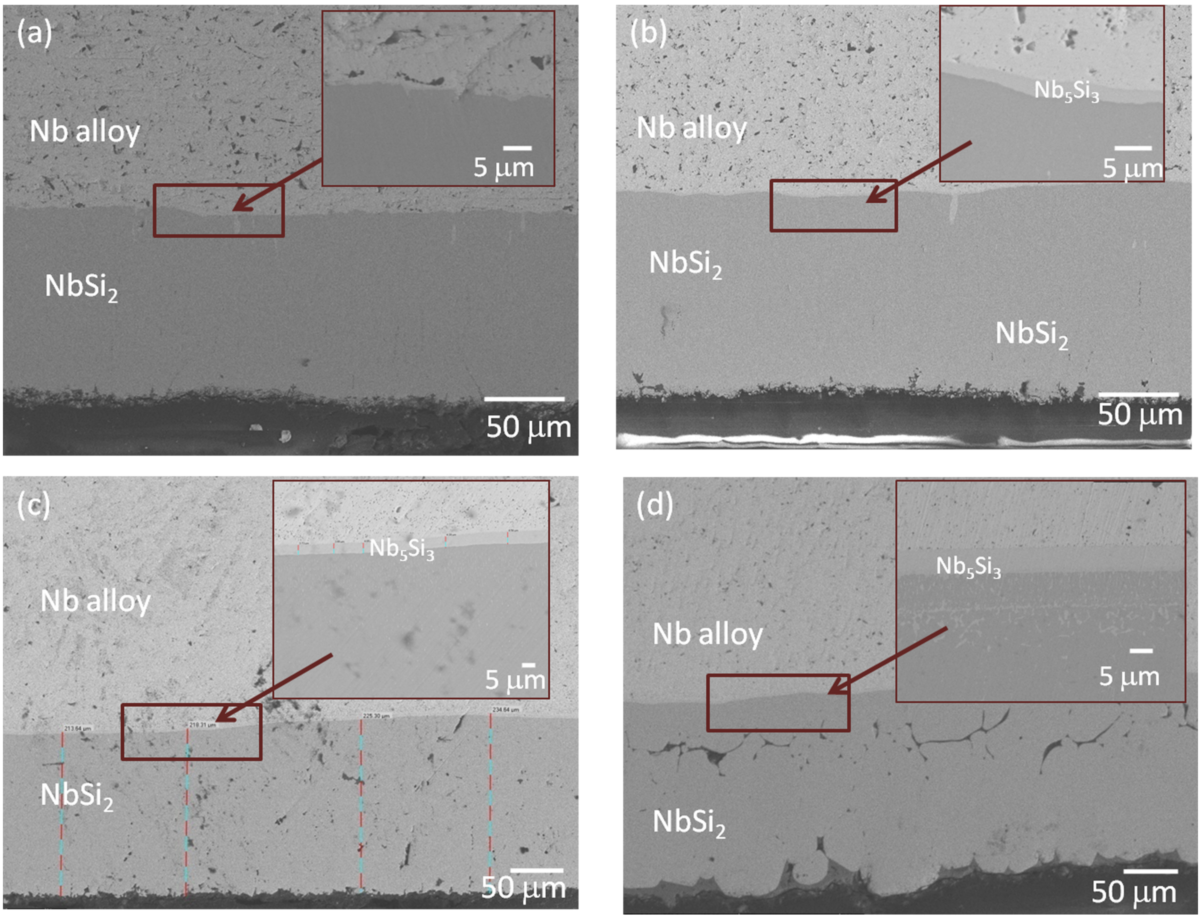

Figure 7.2: Secondary electron micrographs of cross-sectional view of silicide coatings produced by pack cementation technique at different temperatures (a)1200 °C, (b) 1300 °C, (c) 1400 °C and (d) 1500 °C for 6 hr. (a) shows the formation of a single phase in the coating whereas (b,c and d) shows formation of two phases in the coating.

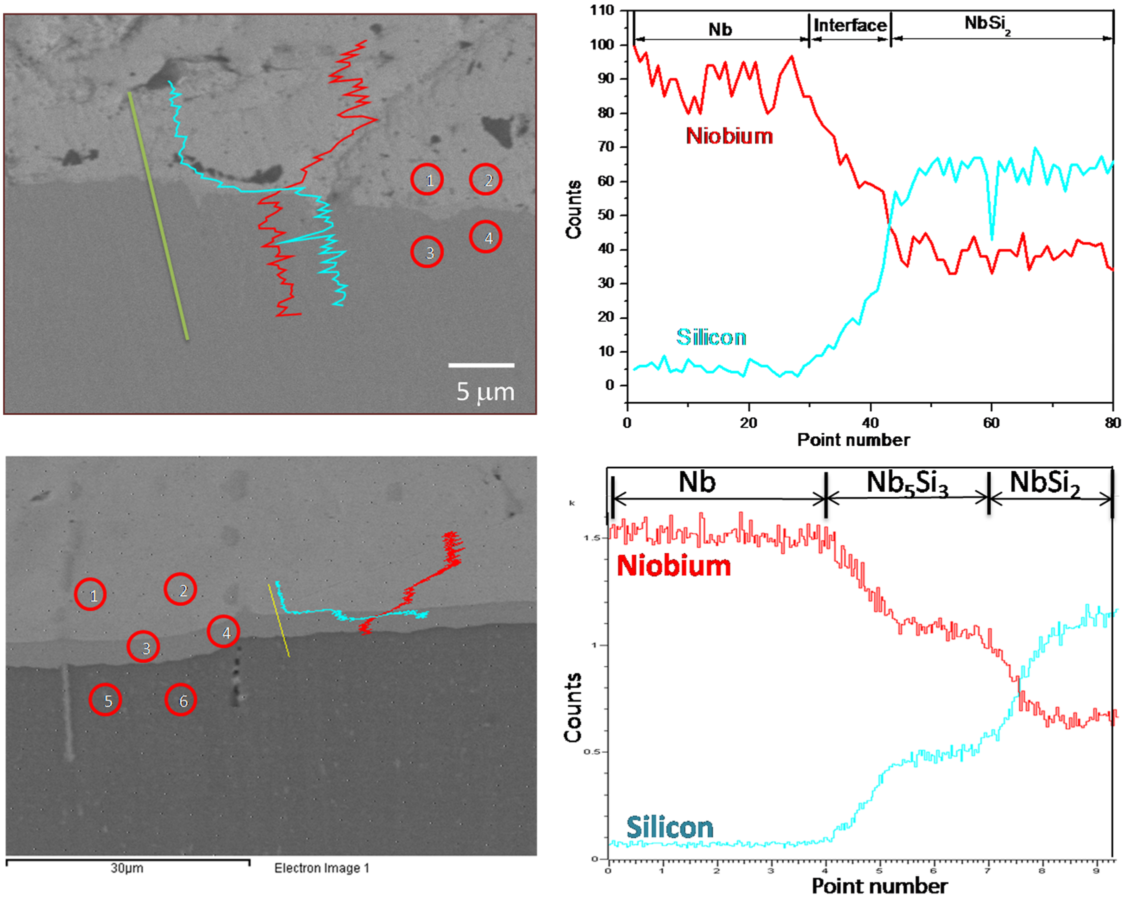

Figure 7.3: BSE micrograph and EDS composition profile of the cross-section of silicide coated sample at (a) 1200 °C and (b) 1300 °C for 6 hrs showing the presence of two phases (Nb, $NbSi_2$) and three phases (Nb, Nb_5Si_3 and $NbSi_2$) in 1200 °C and 1300 °C samples, respectively.

Table 7.2: Average coating thicknesses of the $NbSi_2$ and Nb_5Si_3 phases present in the microstructures shown in Fig.7.2.

Coating condition	**Thickness (μm)** **$NbSi_2$**	 **Nb_5Si_3**
1200 for 6hrs	110±2	—-
1300 for 6hrs	120±5	1.75±0.5
1400 for 6hrs	152±4	4±0.75
1500 for 6hrs	185±5	5.7±0.6

Table 7.3: Average coating thicknesses of $NbSi_2$ and Nb_5Si_3 phases present in the silicide coated samples at 1300 °C and 1400 °C for different time periods (6, 9, 12 and 15 hrs).

	Thickness of $NbSi_2$ (μm)		**Thickness of Nb_5Si_3 (μm)**	
Time (hrs)	**1300 °C**	**1400 °C**	**1300 °C**	**1400 °C**
6	120±5	152.2±3	1.75±0.5	4±0.75
9	157±2	187.98±2	3.2±0.25	9.76±0.75
12	200±3	230±3	4.5±0.5	12.75±0.5
15	210.41±2	241±3	5.12±0.75	15.32±0.5

tabulated in the Table.7.2. It shows that with increasing temperature of coating, thicknesses of $NbSi_2$ and Nb_5Si_3 were increased. This is attributed to increase in Si diffusion rate in the Nb matrix due to increase in temperature. Table.7.2 and SEM micrographs (Fig.7.2) also show that for every temperature, the layer of $NbSi_2$ phase is thicker than the Nb_5Si_3 layer. This shows that the $NbSi_2$ phase grows at a much faster rate compared to the Nb_5Si_3 phase.

In order to estimate the kinetics of coatings, silicide coatings were carried out at 1300 and 1400 °C for different time periods (6, 9, 12 and 15 hrs). Thickness of both the silicide layers ($NbSi_2$ and Nb_5Si_3) as a function of time for temperatures 1300 °C and 1400 °C are tabulated in Table.7.3. In order to understand the kinetics of the coatings, the data were analyzed using the parabolic law, (i.e.x^2=kt), where x, k and t are the thickness of reaction layer, parabolic rate constant and coating time, respectively. Fig.7.4 showing the linear plot of thickness square (x^2) of reaction layer of $NbSi_2$ and Nb_5Si_3 against reaction time (t) indicates that the growth of reaction layer controlled by diffusion controlled mechanism. The observation is in agreement with those reported in literature [126].

7.2.2. Microstructural investigation under TEM

Although EDS has provided the chemical composition information about the phases and based on this information, presence of Nb_5Si_3 and $NbSi_2$ phases in the silicide coating have been

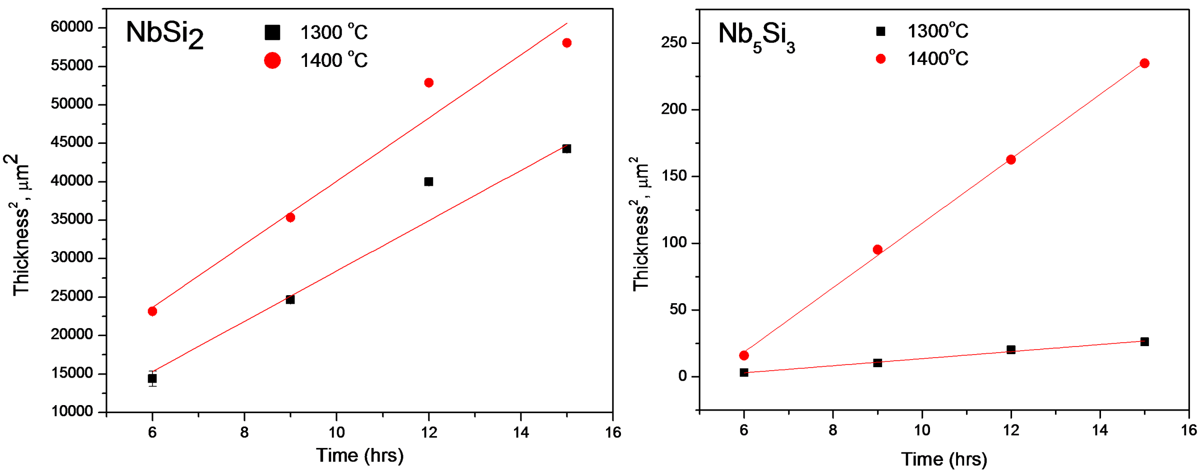

Figure 7.4: Plot of coating thickness versus time for (a) $NbSi_2$ and (b) Nb_5Si_3 phases produced at two different temperatures 1300 °C and 1400 °C for different time periods (6, 9,12 and 15 hrs).

identified. However, it did not reveal the crystallographic information of the silicide phases. Table.7.4 shows the crystallographic information of the various kinds of crystal structures present in the Nb_5Si_3 and $NbSi_2$ phases [51]. Hence, to determine the exact crystallographic information of the silicide phases, cross-sectional TEM samples from the silicide coated sample at 1300 °C for 6 hrs were prepared. These samples were further observed under TEM.

Fig.7.5. shows the presence of two distinct morphologies (equiaxed and columnar) of grains in the silicide coated TEM sample. EDS analysis of each grain morphologies showed that the equiaxed grains were having Nb - 64.42 ± 2, Si - 35.5 ± 2 (at.%) and the columnar grains were having Nb - 37.7 ± 2, Si - 62.3 ± 1 (at.%). EDS, therefore, confirmed that equiaxed grain morphology corresponds to the Nb_5Si_3 phase and columnar grains morphology corresponds to the $NbSi_2$ phase. To find out the crystal structure of both the silicide phases, SAED patterns were obtained from different zone axes on a single grain by systematically varying tilt angles (Fig.7.6). The SAED patterns obtained from the equiaxed and columnar grains were successfully indexed in terms of tetragonal and hexagonal crystal structures, respectively. Based on tilt angle separation between the two zone axes, angular separation between various zone axes were estimated using formulation developed by Xiaodong Zou et al. [111] and these are tabulated in Table.7.5, 7.6. These experimental angles matched very well with the theoretically calculated angular separation between zone axes of tetragonal lattice and hexagonal lattice of Nb_5Si_3 and $NbSi_2$ phases, respectively. It has further confirmed the proper identification of silicide phases. Lattice parameters determined from these SAED patterns, established that the Nb_5Si_3 (tetrago-

Table 7.4: Crystallographic information of the various kinds of crystal structures present in the Nb_5Si_3 and $NbSi_2$ phases [51].

Phase	Crystal structure	Lattice parameter (nm)	Space group	Wyckoff letter
$NbSi_2$	Hexagonal	a = 0.4794 c = 0.6589	$P6_422$	Nb - 3C Si - 6i
	Hexagonal	a = 0.4819 c = 0.6592	$P6_222$	Nb - 3d Si - 6j
Nb_5Si_3	Hexagonal	a = 0.7536 c = 0.5249	$P6_3$/mcm	Nb_1 - 4d Nb_2 - 6g Si - 6g
	Tetragonal	a = 1.0026 c = 0.5249	I4/mcm	Nb_1 - 4b Nb_2 - 16k Si_1 - 4a Si_2 - 8h
	Tetragonal	a = 0.6570 c = 1.1884	I4/mcm	Nb_1 - 4c Nb_2 - 16l Si_1-4a Si_2-8h

Table 7.5: Angular separation between various zone axes of Nb_5Si_3, estimated based on experimental (exp.) tilt angles of double tilt specimen holder [111] and theoretically (the.) calculated based on equations. It shows good matching between experimental and theoretical estimations.

Zone axis	Tilt angles of double tilt specimen holder		Angle between zone axes (deg)	
	alpha (deg)	beta (deg)	experimental	theoretical
{001}	14	-23	38.8243	38.0197
{111}	38	11.5	51.2151	51.6381
$\{\bar{1}11\}$	-13	6.5		

nal) phase has lattice parameters of a = 0.65 nm, c = 1.19 nm and for $NbSi_2$ (hexagonal) lattice parameters were of a = 0.48 nm, c = 0.66 nm. These crystallographic information of the silicide phases are compared with the silicide phases mentioned in the Table.7.4. It showed that Nb_5Si_3 matched with the I4/mcm space group of Nb_5Si_3 silicide phase and $NbSi_2$ matched with the $P6_222$ space group of $NbSi_2$ phase.

7.2.3. Microstructural investigation under OIM

Fig.7.7 shows the EBSD image of the silicide coated sample produced at 1300 °C for 6 hrs. In the input data for EBSD analysis, the crystallographic information obtained from the TEM has been provided. Fig.7.7 shows the inverse pole figure images of three phases in the sample:

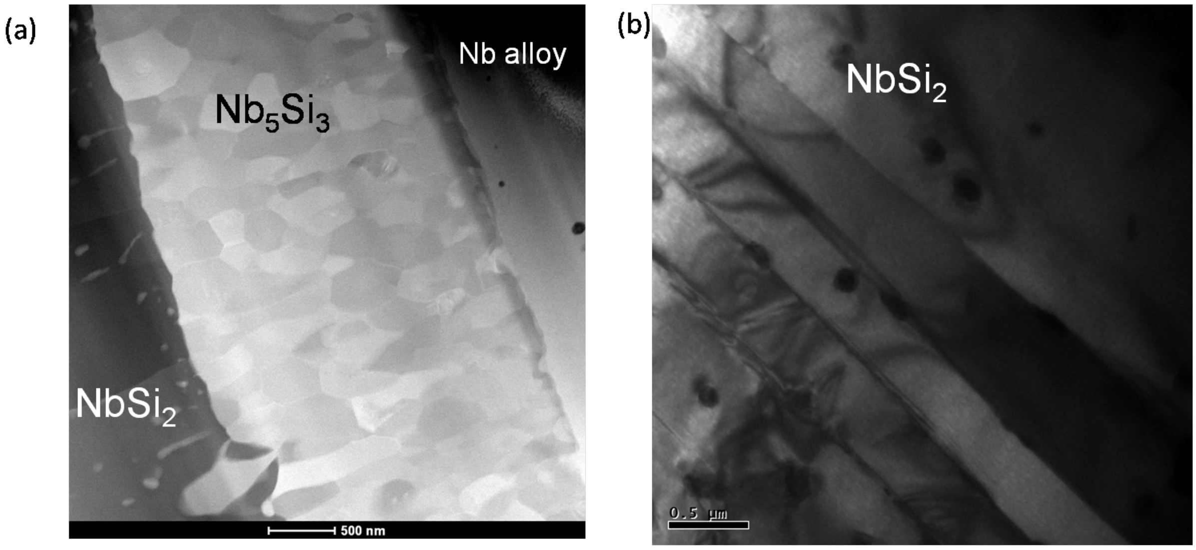

Figure 7.5: TEM micrographs of two silicide phases in silicide coated samples at 1300 °C for 3 hrs showing the presence of (a) equiaxed grain morphology in one silicide phase and (b) columnar grain morphology in the another silicide phase.

Table 7.6: Angular separation between various zone axes of $NbSi_2$, estimated based on experimental (exp.) tilt angles of double tilt specimen holder [111] and theoretically (the.) calculated based on equations. It shows good matching between experimental and theoretical estimations.

Zone axis	Tilt angles of double tilt specimen holder		Angle between zone axes (deg)	
	alpha (deg)	beta (deg)	experimental	theoretical
$\{0001\}$	22	16.5	22.6807	22.8829
$\{0\bar{1}13\}$	2	5.5	16.19	9.4549
$\{0\bar{1}12\}$	-14	8	21.3387	17.1623
$\{1\bar{2}13\}$	-14	-14		

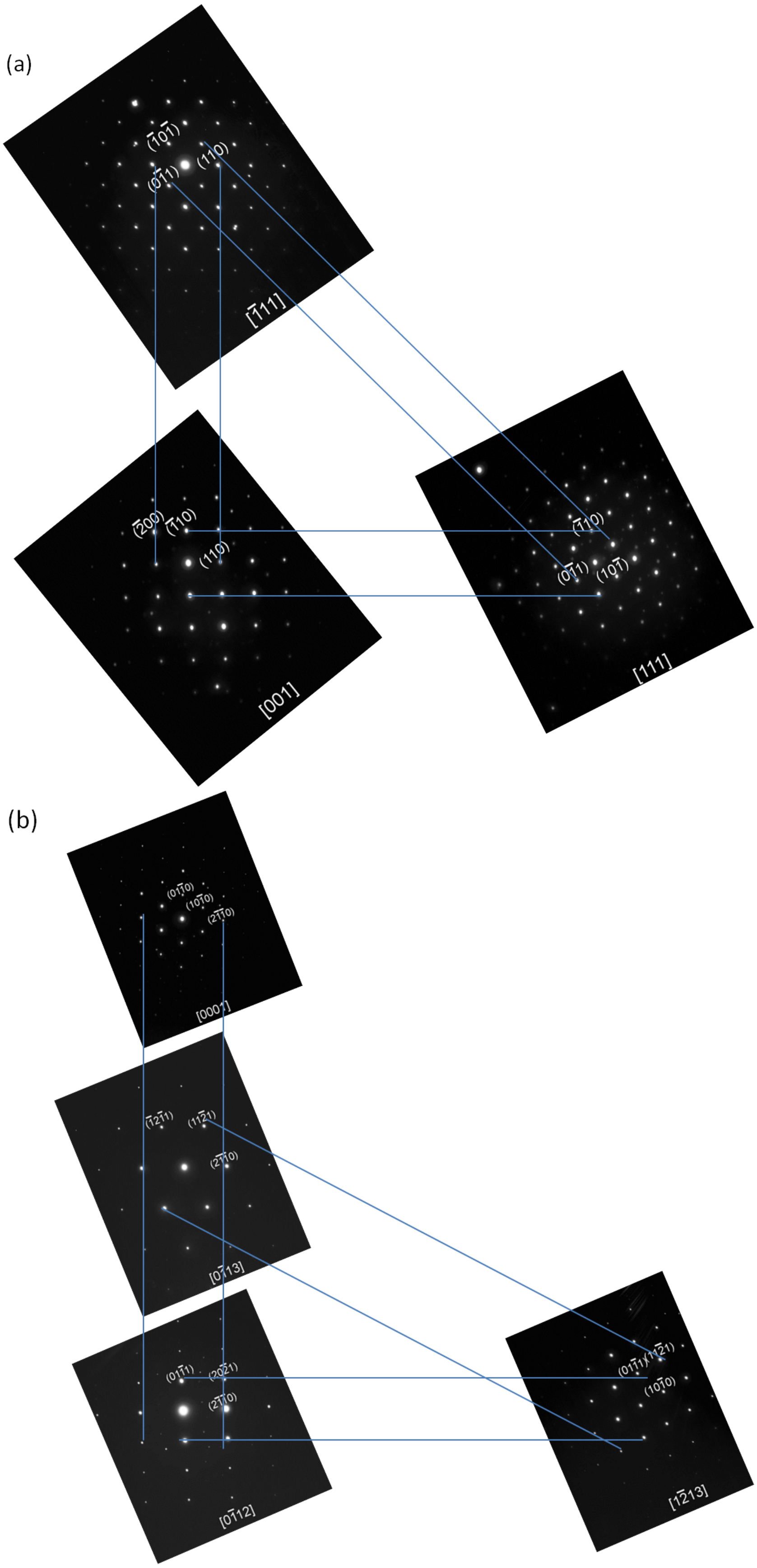

Figure 7.6: SAED patterns obtained at different zone axes from the single grain of (a) Nb_5Si_3 equiaxed grains and (b) $NbSi_2$ columnar grains.

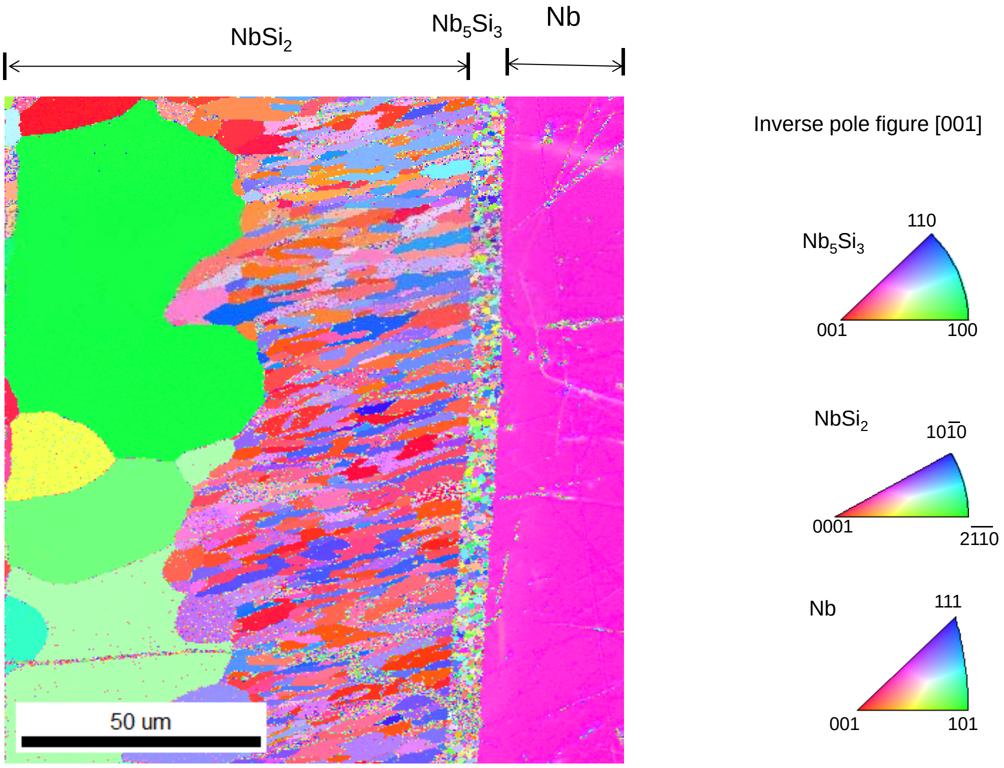

Figure 7.7: EBSD image of the cross-section of silicide coated sample showing the presence of $NbSi_2$, Nb_5Si_3 and Nb phases.

Nb, Nb_5Si_3 and $NbSi_2$. EBSD could index all the three phases very clearly with the crystallographic data provided from the TEM analysis. The EBSD image also shows the equiaxed grain morphology of Nb_5Si_3 and columnar grain morphology of the $NbSi_2$ as observed under TEM. In addition, EBSD also showed that the $NbSi_2$ has two grain morphologies: one columnar morphology which has formed near to the Nb_5Si_3 phase and second bigger equiaxed grain morphology near to the surface of the sample. The EBSD shows the extra features in the $NbSi_2$ phase which could not be observed in the TEM due to difficulty in preparation of large thin area in TEM samples.

7.3. Growth of silicide phases in the silicide coating

In the current study, formation of the $NbSi_2$ phase indicates that the reaction starts from the Si rich side of the phase diagram. The reason for the formation of silicon rich phase is that there exists a depletion zone of certain depth near the substrate surface where Si is completely consumed [130]. Due to the formation of a depletion zone near the substrate, a chemical potential gradient develops providing a driving force for the gas phase diffusion of silicon fluorides for surface deposition [130]. Formation mechanisms for different silicide phases ($NbSi_2$, Nb_5Si_3) in the coating layer during the pack cementation at different temperatures are explained in literature [91, 126, 130]. The silicide coated sample at 1200 °C for 6 hrs has thickness of 110 ± 2 μm of the $NbSi_2$ layer. The formation of Nb_5Si_3 could not be observed in this sample. The thickness of the silicide coating layer in the sample coated at 1300 °C for 6 hrs is 120 ± 5 μm. In this silicide layer, the presence of Nb_5Si_3 phase has been noticed (thickness 1.75 ± 0.5 μm). As the coating temperature and time increased, the total coating thickness and the thickness of both the coating phases increased and followed parabolic growth behaviour. This indicates that the the growth of $NbSi_2$ and Nb_5Si_3 are diffusion controlled. All the silicide coated micrographs (Fig.7.2) show that the thickness of Nb_5Si_3 is lower than that of the $NbSi_2$. It indicates that the growth rate of Nb_5Si_3 is lower as compared to $NbSi_2$.

In general, coatings produced by high activity pack cementation technique consist of three layers [100]. The first layer which forms at the surface of the sample will be rich in coated element. The second layer which forms below the first layer will have low concentration of coating element in comparison to top or first layer. The growth of the second layer leads to the depletion of the major element in the substrate material which in turn leads to formation of the inner diffused layer or third layer.

The microstructure observed in the present silicide coated sample is a typical microstructure of the coatings produced by high activity pack cementation technique. The first surface layer comprising $NbSi_2$ is rich in coated element (Si). The second layer or intermediate layer i.e., Nb_5Si_3 which has lower Si content than the $NbSi_2$ phase. The sample did not show the presence of inner diffused layer or third layer. It is due to fact that the base material is almost pure Nb and hence there is no depletion of the Nb in the base material.

The EBSD image of the silicide coated sample at 1300 °C for 6 hrs showed the presence of duplex grain morphology of the $NbSi_2$ phase. Columnar grain morphology has been observed near the Nb_5Si_3 silicide phase and big equiaxed grains are observed near the outer surface of sample. The Nb_5Si_3 phase has small equiaxed grain morphology. In general, coating produces single morphology of the grains but in the in the present sample, $NbSi_2$ showed duplex grain morphology. This duplex morphology of the $NbSi_2$ phase can be explained on the basis of physiochemical approach developed by Prasad *et al.* [131]. In this method, thickness of the coating layers are related to the reaction and dissociation of atoms at different interfaces and flux through the phases.

The schematic of formation mechanism of $NbSi_2$ and Nb_5Si_3 is shown in Fig.7.8. Entire silcide layer can be divided into three regions (Nb, Nb_5Si_3, $NbSi_2$) which are separated by three interfaces (marked as I, II and III in Fig.7.8). As shown in Fig.7.8, the $NbSi_2$ and Nb_5Si_3 are formed by diffusion of Nb and Si from substrate and coating layer, respectively. Δ x_{k1}^{I}, Δ x_{k1}^{II}, Δ x_{k2}^{II}, Δ x_{k2}^{III} are the different sublayers grown from different interfaces. p and q are the total moles per unit area of the diffusing species Nb and Si, respectively diffused through the phase Nb_5Si_3, and r and s are the total moles per unit area of Nb and Si, respectively, diffused through the $NbSi_2$ phase during the total annealing time.

Entire sequence of formation of silicide phases can be written in the following equations 7.1 - 7.6. Nb from interface I diffuses through the Nb_5Si_3 phase, reacts with the $NbSi_2$ phase at interface II and forms Nb_5Si_3 phase (equation.7.1). In addition, Nb_5Si_3 dissociates at interface II and produces Nb and $NbSi_2$ (equation.7.2). The produced Nb diffuses through the $NbSi_2$ phase to reacts with Si at interface III and produces $NbSi_2$ (equation.7.5).

Similarly, Si from interface III diffuses through the $NbSi_2$ phase to react with the Nb_5Si_3 phase and produced $NbSi_2$ (equation.7.3). Further, Si dissociated at interface II from the $NbSi_2$ phase diffused through the Nb_5Si_3 (equation.7.4) and reacted with Nb at interface I to produce the Nb_5Si_3 (equation.7.6). Dissociation of Si at interface II also leads to the formation of Nb_5Si_3 (equation.7.4). The reactions are given below.

Reactions at Interface II for the formation of Nb_5Si_3 and $NbSi_2$:

$$\frac{9}{7}pNb_{\frac{1}{3}}Si_{\frac{2}{3}} + p\left[Nb\right]_d \Rightarrow \frac{16}{7}pNb_{\frac{5}{8}}Si_{\frac{3}{8}} \tag{7.1}$$

$$\frac{16}{7}rNb_{\frac{5}{8}}Si_{\frac{3}{8}} \Rightarrow r\left[Nb\right]_d + \frac{9}{7}rNb_{\frac{1}{3}}Si_{\frac{2}{3}} \tag{7.2}$$

$$\frac{8}{7}sNb_{\frac{5}{8}}Si_{\frac{3}{8}} + s\left[Si\right]_d \Rightarrow \frac{15}{7}sNb_{\frac{1}{3}}Si_{\frac{2}{3}} \tag{7.3}$$

$$\frac{15}{7}qNb_{\frac{1}{3}}Si_{\frac{2}{3}} \Rightarrow q\left[Si\right]_d + \frac{8}{7}qNb_{\frac{5}{8}}Si_{\frac{3}{8}} \tag{7.4}$$

Reactions at Interface III

$$2rSi + r\left[Nb\right]_d \Rightarrow 3rNb_{\frac{1}{3}}Si_{\frac{2}{3}} \tag{7.5}$$

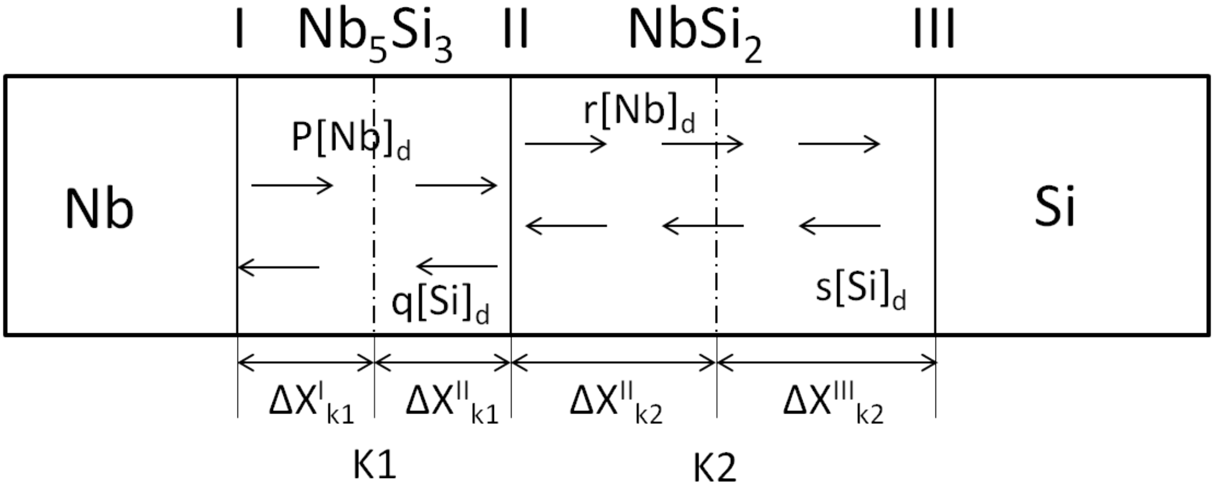

Figure 7.8: Schematic representation of the growth of silicide phase in silicide coated samples. K_1 and K_2 are the mid thickness of the silicide phases. Δ x^I_{k1}, Δ x^{II}_{k1}, Δ x^{II}_{k2}, Δ x^{III}_{k2} are the different sublayers grown from different interfaces, p and r denote the flux of Nb, and q and s denote the flux of Si [131].

Reactions at Interface I

$$\frac{5}{3}qNb + q\left[Si\right]_d \Rightarrow \frac{8}{3}qNb_{\frac{5}{8}}Si_{\frac{3}{8}} \tag{7.6}$$

The constants (p, r, s, q) and the thickness of the sublayers (Δ x^I_{k1}, Δ x^{II}_{k1}, Δ x^{II}_{k2}, Δ x^{III}_{k2} shown in Fig.7.8) grown from different interfaces are estimated for the present silicide coated condition (silicide coated at 1300°C for 6 hrs) using the similar equations used by Prasad *et al.* [131]. The calculated values are:

p = 0.112 mol/m^2, r = 2.033 mol/m^2, s = 7.44 mol/m^2, q = 3.4194 mol/m^2 and

x^I_{k1} = 87.54 μm, x^{II}_{k1} = -86.1 μm, x^{II}_{k2} = 96.45 μm, x^{III}_{k2} = 53.06 μm

All the sublayer thickness values are positive except x^{II}_{k1} which has negative value. It indicates that the Nb_5Si_3 sublayer near to the $NbSi_2$ was consumed by the $NbSi_2$ phase and it shows that the growth of the Nb_5Si_3 phase by outward diffusion of Nb from the substrate is not a realistic mode. Therefore, the growth of Nb_5Si_3 take place only by inward diffusion of Si. The Nb_5Si_3 forms according to the reaction.7.6. The growth of $NbSi_2$, on the other hand, occurs by inward diffusion of Si (according to equation.7.3) as well as by outward diffusion of Nb element (according to equation.7.5). Due to this fact the growth rate or thickness of the $NbSi_2$ layer is higher than the Nb_5Si_3layer. The another reason for the higher rate of growth for $NbSi_2$ than Nb_5Si_3 is the diffusivity of both the elements (Si, Nb) is higher in $NbSi_2$ as compared in Nb_5Si_3.[131]. The ratio of diffusivity of Si and Nb in $NbSi_2$ and Nb_5Si_3 phases are

3.6, 30.53 respectively [131]. This also indicates the possibility of single element Si diffusion in Nb_5Si_3 and diffusion of both the elements (Nb,Si) in the $NbSi_2$ phase. Due to single element diffusion, the Nb_5Si_3 grows from a single interface (I) and it leads to development of mono-morphological grains of the phase. Whereas, in the case of $NbSi_2$, diffusion of both of elements takes place. Therefore, $NbSi_2$ grows from two interfaces (II and III) and it leads to duplex grain morphology. The equiaxed grain morphology at the surface of the coated sample is due to the outward diffusion of Nb, and the columnar grain morphology is due to the inward diffusion of Si.

7.4. Microhardness of the silicide phases

In order to find out the microhardness of the silicide phases, microhardness testing has been carried out on the cross-section of the silicide coated sample. Microhardness values across the cross-section of the coatings are shown in Fig.7.9. For the sample coated at 1200 °C, hardness of the single $NbSi_2$ phase remained nearly constant at 950 HK in comparison to 145 HK hardness of the matrix phase. In the case of samples coated beyond 1200 °C (1300 °C, 1400 °C), upon moving towards the substrate, hardness raised from initial value of 733 HK (for 1300 °C sample) to a maximum of 1034 HK at the interface between the coating and substrate, then decreased sharply to 155 HK and became constant as the distance from the interface increased. Out of the two silicide phases ($NbSi_2$ and Nb_5Si_3), Nb_5Si_3 showed higher hardness. Microhardness of the sample coated at 1500 °C showed fluctuations in the hardness values. This fluctuation could be attributed to non uniform composition due to melting of Si above 1414 °C. Owing to the melting of silicon above 1414 °C the diffusion was not uniform between the silicon and the Nb substrate and hence the phases formed were not uniform in composition. It was clearly manifested in terms of large fluctuations in the microhardness plot obtained on the sample coated at 1500 °C. From all the above plots it can be observed that the coating produced at 1200 °C has the highest hardness.

7.5. Oxidation studies of Nb alloy and silicide coated samples

To study the oxidation behaviour of the Nb alloy and silicide coated samples TGA has been carried out.

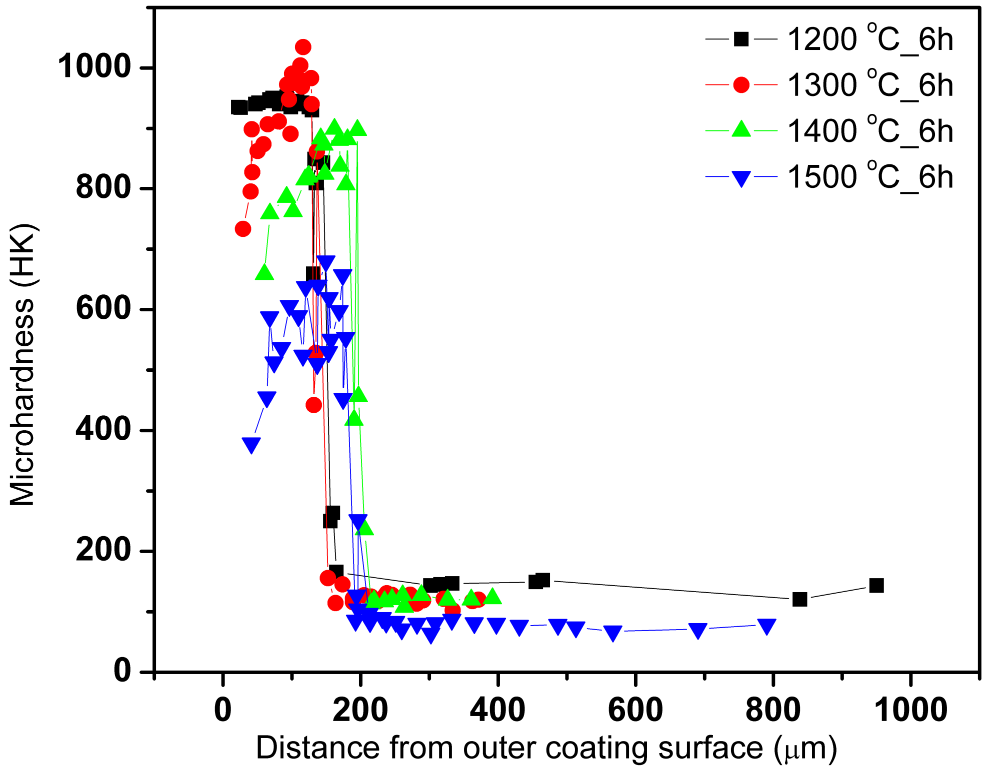

Figure 7.9: Microhardness obtained along the cross-section of the coatings produced at different temperatures 1200 °C, 1300 °C, 1400 °C and 1500 °C for 6 hrs.

7.5.1. Oxidation behaviour of the uncoated Nb alloy

Fig.7.10. shows the weight gain versus temperature curve obtained from bare niobium samples oxidized in air in a thermogravimetric analyzer (TGA). This graph shows three distinct temperature regions of weight gain, (1) negligible change in the weight up to 500 °C, (2) gradual weight gain between 500 to 630 °C and (3) steep weight gain above 630 °C. This indicates that accelerated oxidation of Nb alloy starts at 500 °C.

Sudden increase in the weight gain at and above 630 °C could be attributed to the formation of non protective layer of oxide phase. It has been shown that the protective nature of the oxide layer depends on two factors: (1) relative atomic volumes of metal and oxide and (2) relative thermal coefficients of expansion of the metal and oxide [125]. In the case of bare Nb alloy, both the factors are unfavorable. Nb alloy undergoes oxidation with the formation of Nb_2O_5 phase which has high Pilling-Bedworth ratio of 2.68 [82]. The reported coefficient of thermal expansion of Nb and Nb_2O_5 are 7-8x10^{-6} °C^{-1}, 1-2x10^{-6} °C^{-1} [132, 133], respectively. Due to this vast difference in coefficient of thermal expansion ($\sim$4 times), during a heating and cooling cycle, stresses develop in the oxide film. Being brittle in nature, the oxide film (VHN-557 ± 7) failed to accommodate the stresses generated during heating and cooling leading to the formation of cracks and spallation of the oxide film. Hence, in the present case both high Pilling-Bedworth ratio and large differences in the coefficient of thermal expansion lead to cracking and spallation of oxide phase which had increased oxidation of the Nb alloy at higher temperatures (>600 °C).

In order to understand the oxidation kinetics of the bare Nb alloy, isothermal oxidation studies were carried out at 600 °C in air for time period up to 6 hrs (0.166, 0.333, 0.5, 0.666, 2, 4, 6 hrs). Oxidation plot of weight gain per unit surface area versus time is shown in Fig.7.11. It shows that oxidation of Nb alloy at 600 °C in air follows a linear rate behaviour. Cross-sectional microstructure of oxide samples are shown in Fig.7.12. Fig.7.12(a) showed that with increase in the oxidation time, thickness of the oxide layer increased linearly with time. Microstructural examination of the oxide layer was not possible for samples oxidized beyond 0.5 hrs because of difficulty in sample handling without damaging the oxide layer. Fig.7.12(b) shows a SEM micrograph of typical cross-sectional view of the oxidized sample. It shows the presence of cracks in the oxide phase. EDS analysis (Fig.7.12(c)) revealed that the oxide layer had composition of Nb-74.83 at%±3 and O-25.16 at%±2. Thus composition closely matched with the Nb_2O_5 phase. The EDS results showed that the samples of bare Nb alloys have undergone oxidization

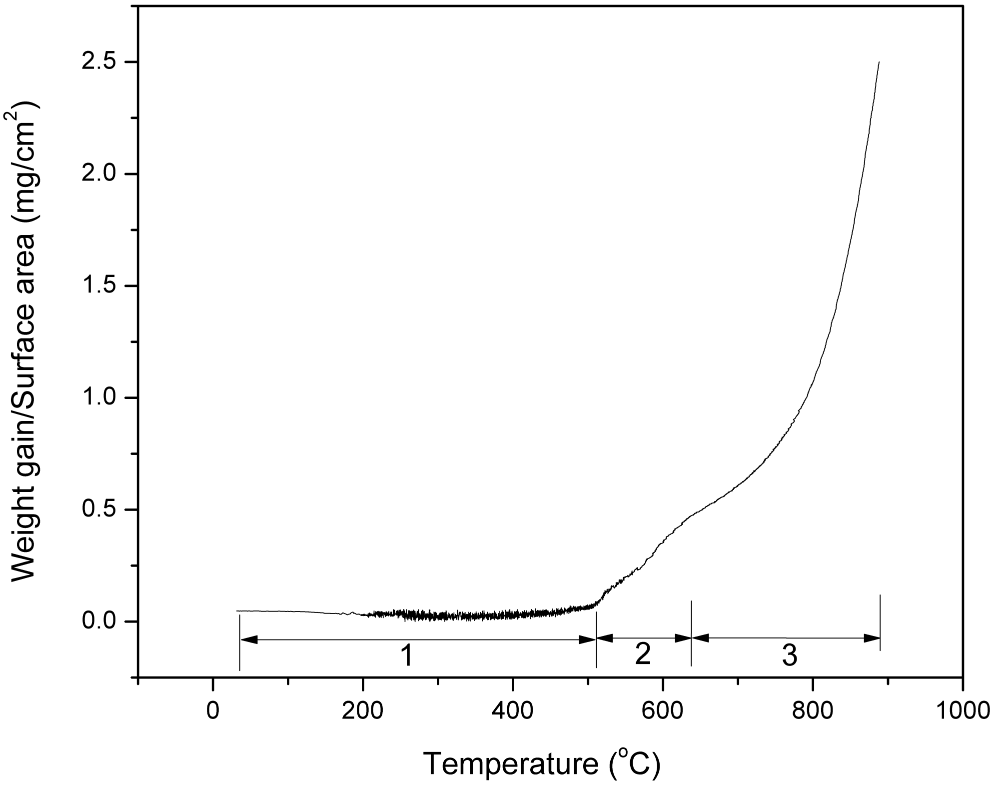

Figure 7.10: TGA analysis of Nb alloy heated in air environment. Three distinct oxidation regimes have been marked as (1), (2) and (3): (1) negligible change in the weight up to 500 °C, (2) gradual weight gain between 500 to 630 °C and (3) steep weight gain above 630 °C.

with the formation of Nb_2O_5 oxide phase. Efforts were made to find out the hardness of the oxide phase. The measured hardness values for oxide phase and bare samples were 557±10 and 118±7 VHN, respectively.

Isothermal oxidation experiments showed that the Nb-1Zr-0.1C alloy undergoes linear rate of oxidation. Similar linear rates of oxidation have been observed in the case of Nb-1Zr alloy and pure Nb [25, 85, 125, 134]. In the present work, the oxidation rate estimated for Nb-1Zr-0.1C alloy was 0.10834±0.003 Kg/m^2/hrs. This oxidation rate for Nb-1Zr-0.1C alloy is higher than the reported oxidation rate for Nb-1Zr (0.05±0.01 Kg/m^2/hrs at 593 °C [125]). This indicates that the presence of carbides in the Nb-1Zr-0.1C alloy reduces oxidation resistance of the Nb-1Zr-0.1C alloy. The rate of oxidation of Nb-1Zr-0.1C alloy at 600 °C is lower than the oxidation rate of pure Nb (0.357 Kg/m^2/hrs at 600 °C [85, 89, 134]). Improvement in the oxidation resistance of the Nb-1%Zr-0.1%C alloy in comparison to pure Nb metal could be the effect of Zr addition in the Nb alloy.

In general Nb and its alloys undergo oxidation with the formation of NbO_x and Nb_2O_5 oxide phases. The morphology of NbO_x and Nb_2O_5 appear in the form of plate and spherical shape, respectively. The SEM micrographs shown in Fig.7.12(b) matched with the Nb_2O_5 morphology as reported in literature [135, 136]. The EDS results also confirmed that at higher temperature (>600 °C), Nb alloy undergoes oxidation with the formation of Nb_2O_5 oxide phase.

7.5.2. Oxidation behaviour of the silicide coated Nb alloy

To study the oxidation behavior of the silicide coatings, samples were heated in TGA in air up to 1200 °C (all the oxidation experiments were carried out on the silicide coated sample at 1300 °C for 6 hrs because these samples have two layers of silicide phases with homogeneous microstructure and crack free coating). Fig.7.13 shows the TGA graph of silicide coated sample. For the purpose of comparison, TGA graph of bare Nb sample has also been shown. It showed that up to 1200 °C there is no substantial change in the weight of the silicide coated sample, whereas the bare Nb alloy undergoes heavy oxidation at 500 °C. This showed that silicide coating has effectively provided the resistance against oxidation.

As these Nb alloys are designed for application temperature of 1000 °C, isothermal oxidation behaviour of silicide coated samples was studied at 1000 °C up to 64 hrs. The weight gain data obtained during oxidation at 1000 °C as a function of time is shown in Fig.7.14. These isothermal oxidation studies showed marginal weight gain of silicide coated samples (0.020

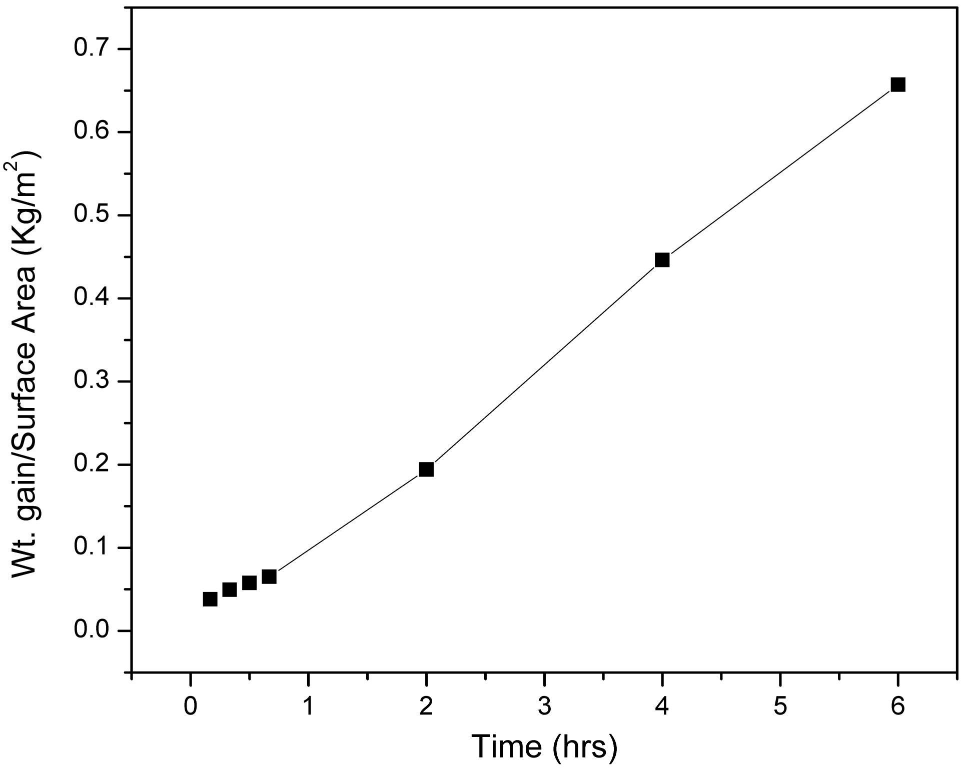

Figure 7.11: Weight gain curve for oxidation of Nb alloy in air atmosphere at 600 °C.

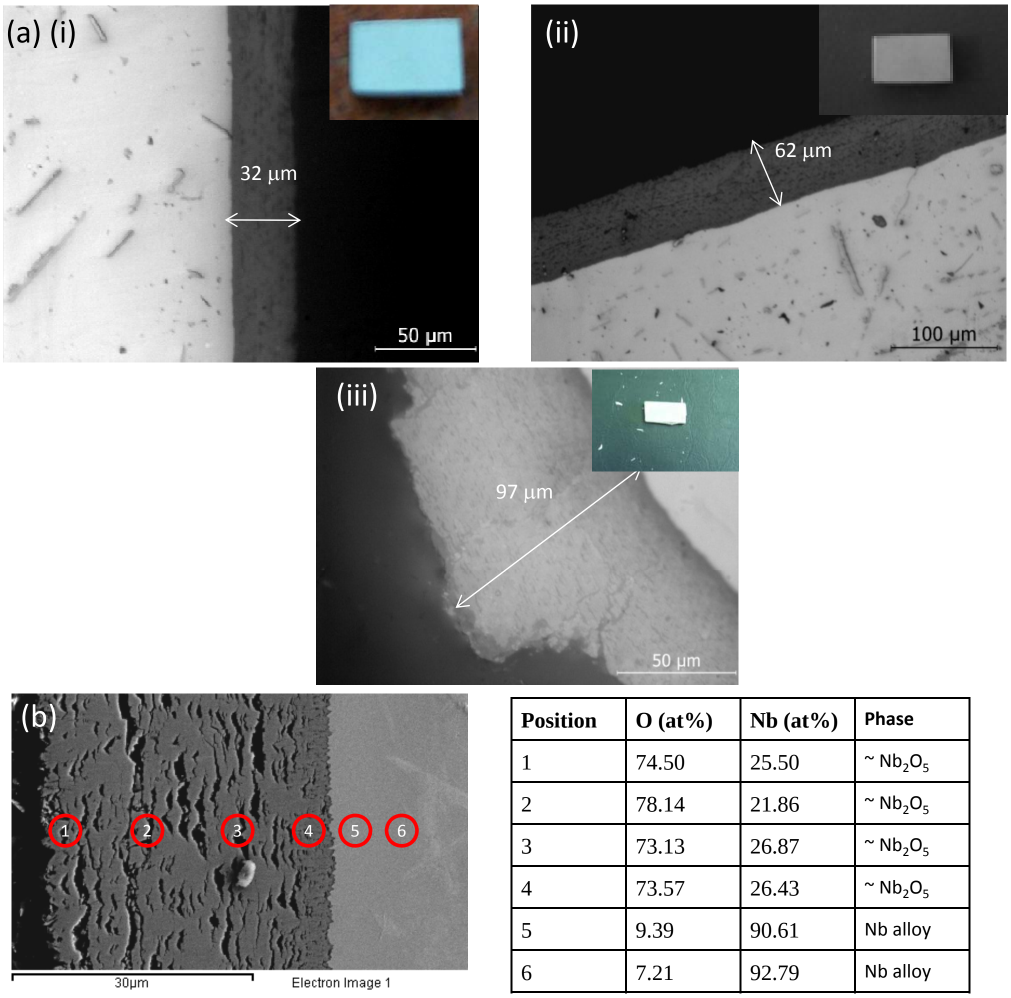

Position	O (at%)	Nb (at%)	Phase
1	74.50	25.50	~ Nb_2O_5
2	78.14	21.86	~ Nb_2O_5
3	73.13	26.87	~ Nb_2O_5
4	73.57	26.43	~ Nb_2O_5
5	9.39	90.61	Nb alloy
6	7.21	92.79	Nb alloy

Figure 7.12: Cross-sectional images of oxidized Nb alloy samples at 600 °C in air (a) optical micrographs of samples oxidized for (i) 0.1666 hrs, (ii) 0.333 hrs and (iii) 0.5 hrs, (b) BSE micrographs of oxidized sample for 0.1666 hrs and (c) EDS quantification at selected positions marked on (b).

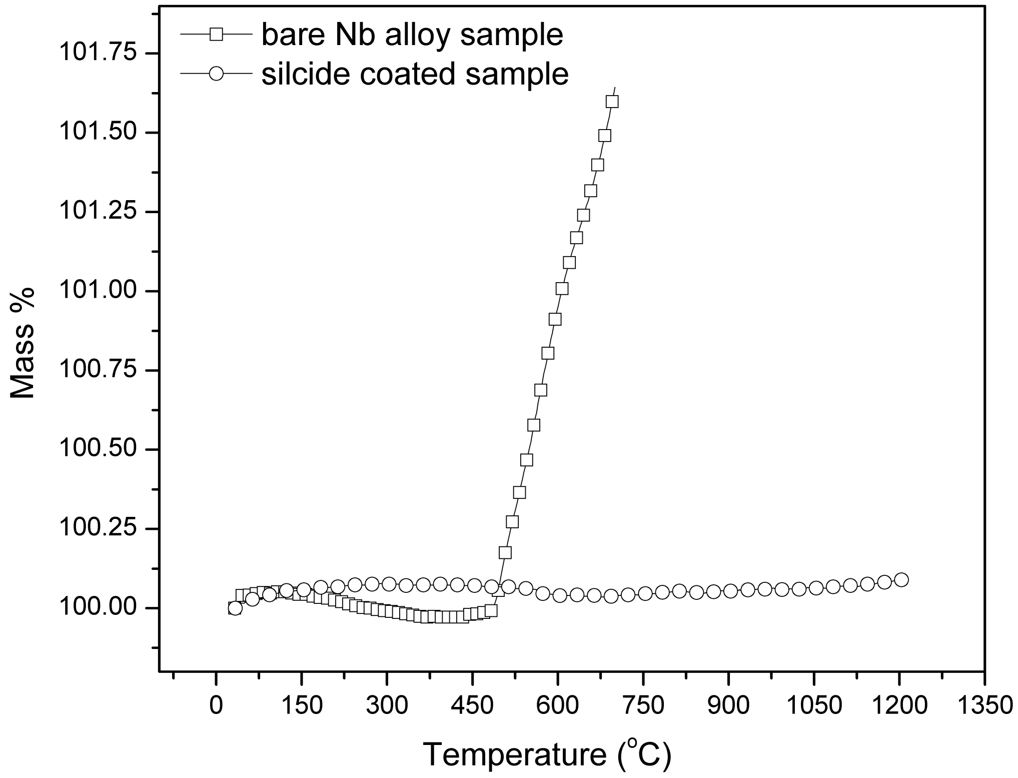

Figure 7.13: TGA analysis of silicide coated and bare Nb alloy heated in air atmosphere showing silicide coated sample has better oxidation resistance than bare Nb alloy at higher temperatures.

Table 7.7: Thickness of oxide layer, $NbSi_2$ and Nb_5Si_3 phases present in the isothermally oxidized silicide coated samples in air at 1000 °C shown in Fig.7.15.

	Thickness (μm)		
Time (hrs)	**Oxide layer**	**$NbSi_2$**	**Nb_5Si_3**
4	—	—	—
8	21±3	149±5	2.1±0.5
16	31±4	146±4	2.1±0.75
32	33±3	147±6	2.1±0.5
64	33±3	144±3	2.1±0.5

kg/m^2) initially. This gain in weight, increased linearly with time up to 8 hrs. Subsequently, weight gain of the sample reduced considerably indicating that initial weight gain was essentially due to the formation of a protective oxide phase on the surface of the sample, which prevented further oxidation of the sample. Cross-section of the oxide samples were examined by optical microscopy (Fig.7.15) and the thickness of the three layers within coating i.e. oxide layer, $NbSi_2$ and Nb_5Si_3 after oxidation at 1000 °C are tabulated in Table.7.7. It shows that the thickness of the oxide layer increased only up to 16 hrs and there after the thickness of oxide layer remained nearly constant. It indicates that the oxide layer formed on the silicide coated samples was protective. In order to find out the composition and phases in the oxide layer, EDS and XRD have been carried out. Fig.7.16 shows the SEM micrograph of the cross-section of oxidized silicide coated sample at 1000 °C for 64 hrs. On these micrographs, positions are marked from where EDS was obtained and the results are tabulated in Table.7.8. The oxide layer contained Nb-16.81±0.6 at.%, Si-27.83±0.7 at.% and O-55.35±1.3 at.%. Fig.7.17 shows the XRD patterns collected from all the oxidized samples. These results revealed that oxide layer contained a mixture of Nb_2O_5 and SiO_2 phases. Fig.7.18 shows the surface morphology of oxidized silicide coated Nb alloy. The oxide surface did not have any microcracks or voids. It confirms the protective nature of the oxide surface.

The isothermal oxidation results of weight gain data of silicide coated and bare samples showed that after oxidation for 8 hrs at 1000 °C, the weight gain in the silicide coated alloy was only 0.022 Kg/m^2, whereas the weight gain shown by the bare sample at temperature 600 °C for 4 hrs was only 0.657 kg/m^2. This comparison clearly shows that silicide coating has dramatically improved oxidation resistance in comparison to the bare Nb alloy. The reported literature on isothermal oxidation of silicide coated Nb alloys at 1000 °C shows that weight gain of the sample falls in the range of 0.02-0.03 kg/m^2 [95, 127]. The present results matched well

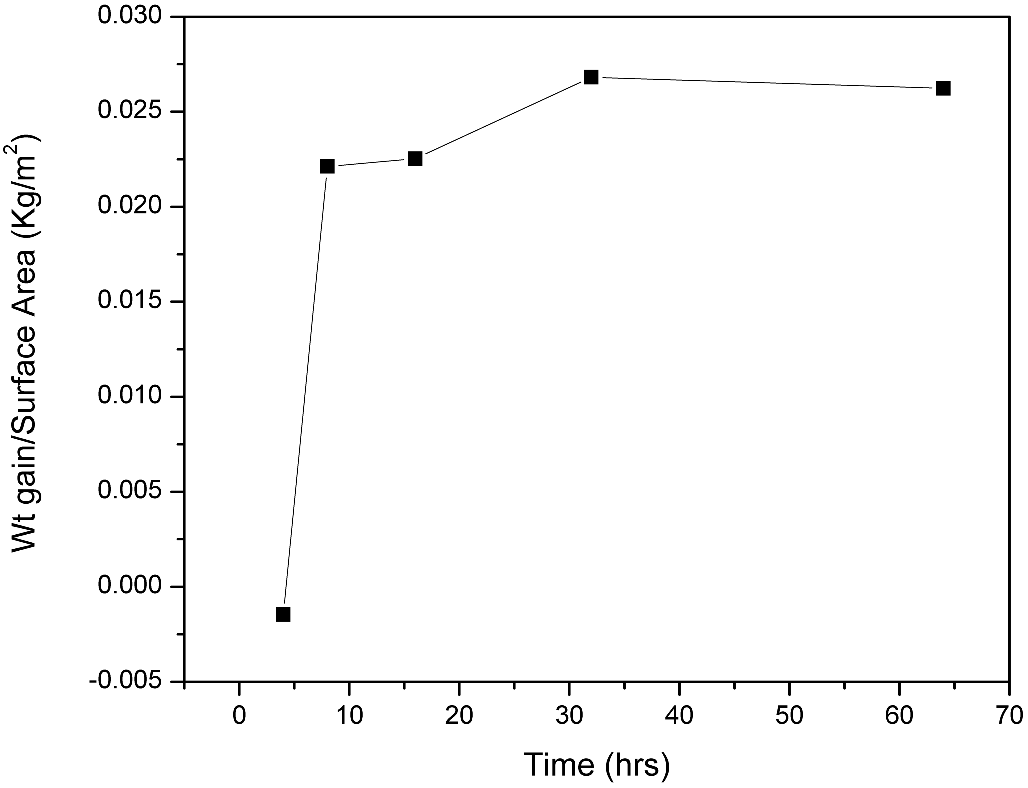

Figure 7.14: Weight gain curve as a function of time for oxidation of the silicide coated Nb alloy in air atmosphere at 1000 °C.

Table 7.8: Chemical composition determined by EDS at the positions marked on the cross-section of SEM micrograph of oxidized silicide coated sample at 1000 °C for 64 hrs shown in Fig.7.16.

	Elements (at%)			
Position	**Nb**	**Si**	**O**	**Phase**
1	65.34	34.66	0	~Nb_5Si_3
2	37.66	62.34	0	~$NbSi_2$
3	37.55	62.45	0	~$NbSi_2$
4	35.89	64.11	0	~$NbSi_2$
5	36.78	63.22	0	~$NbSi_2$
6	16.19	27.06	56.75	
7	17.38	28.51	54.11	
8	16.87	27.92	55.21	

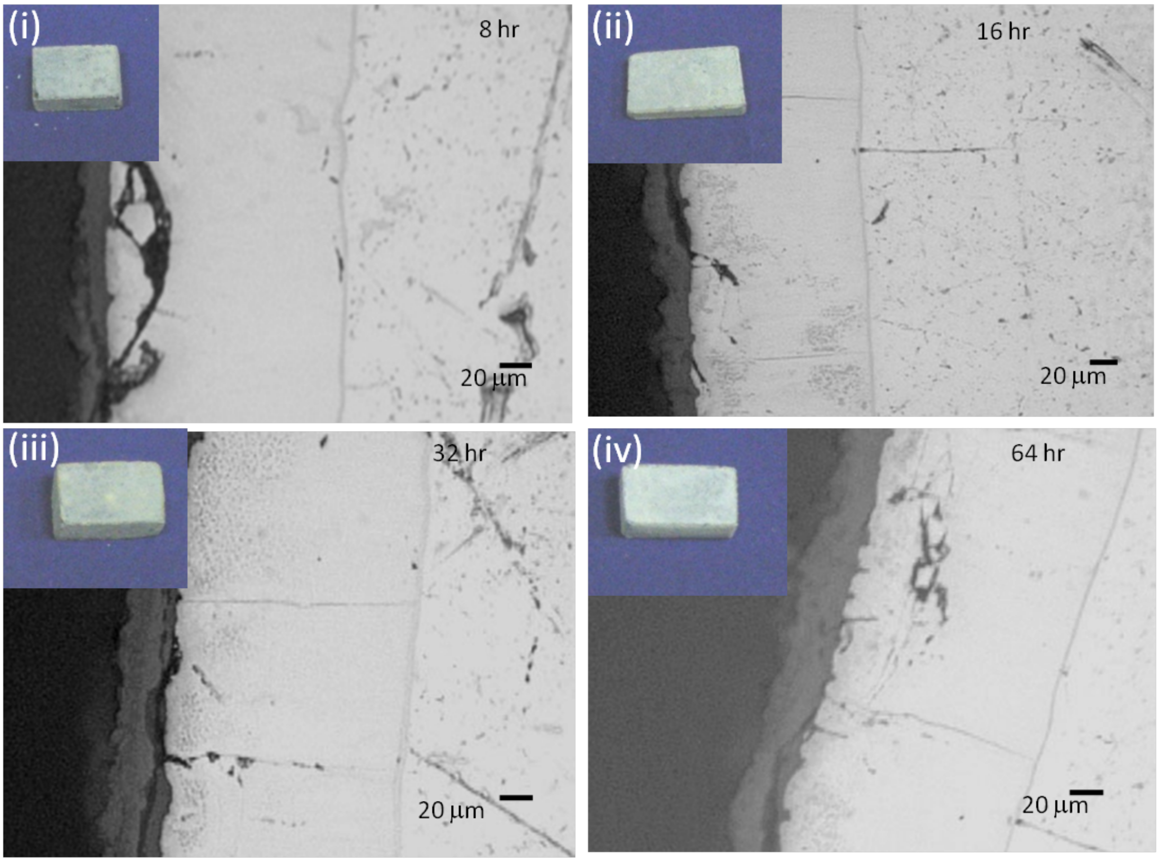

Figure 7.15: Optical micrographs of the cross-section of oxidized silicide coated Nb alloy samples after oxidizing at 1000 °C in air environment for (i) 8, (ii) 16, (iii) 32 and (iv) 64 hrs.

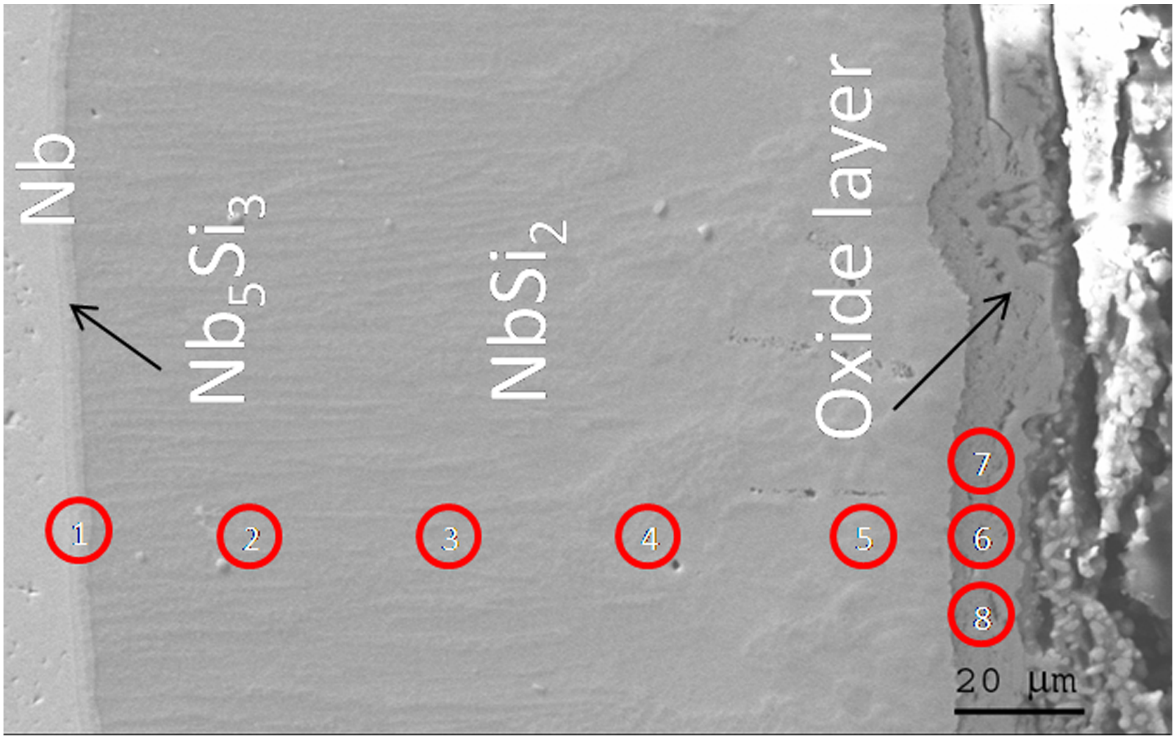

Figure 7.16: Secondary electron micrograph of the cross-section of oxidized silicide coated sample at 1000 °C for 64 hrs showing the presence of three layers Nb_5Si_3, $NbSi_2$ and oxide layer on the Nb alloy.

with the reported data, though the conditions of coating and composition of the Nb alloy were different from the literature. Isothermal oxidation data of silicide coated samples also show that after 8 hrs, there is no appreciable weight gain of the sample due to oxidation; it remained almost constant. It clearly shows that the oxide layer which formed during initial stages of oxidation on the silicide coated samples was protective against further oxidation of the sample.

The XRD and EDS results showed that the protective oxide layer contained a mixture of SiO_2 and Nb_2O_5 phases. Out of the two phases, SiO_2 phase acts as a protective layer [95, 127]. The other reason of showing higher oxidation resistance by silicide coated samples is the presence of Nb_5Si_3 layer between Nb and $NbSi_2$. The Nb_5Si_3 layer improves oxidation essentially because of two reasons: (i) Coefficient of thermal expansion of Nb_5Si_3 is in between $NbSi_2$ and Nb [137, 138]. Therefore, it provides a better adhesive strength to silicide coating and Nb. Due to this the silicide coated layer will not spall off during oxidation. (ii) It is well known fact that during formation of oxide layer because of the formation of a mixture of Nb_2O_5 and SiO_2 oxide phases in the oxide layer of silicide coated sample, the SiO_2 could not cover whole surface area of the Nb alloy. Therefore, the presence of Nb_5Si_3 in between Nb and $NbSi_2$ can provide a better oxidation resistance than a single $NbSi_2$ coating on Nb alloy [96]. Alam

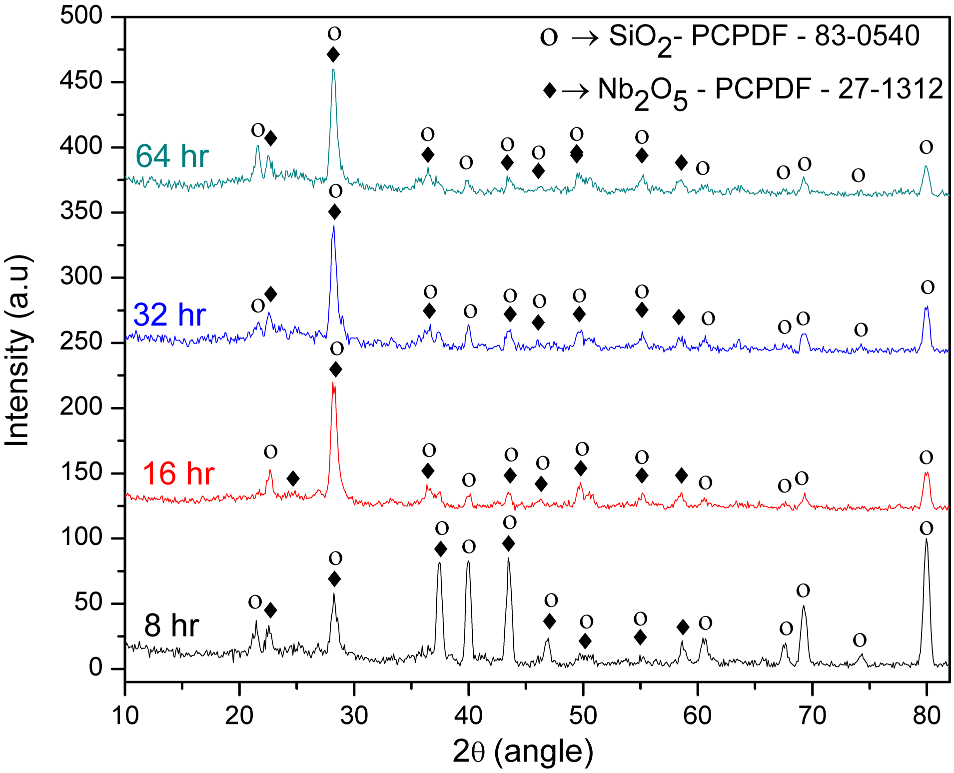

Figure 7.17: XRD pattern collected from the oxidized silicide coated samples showing the formation of Nb_2O_5 and SiO_2 phases in the oxide layer.

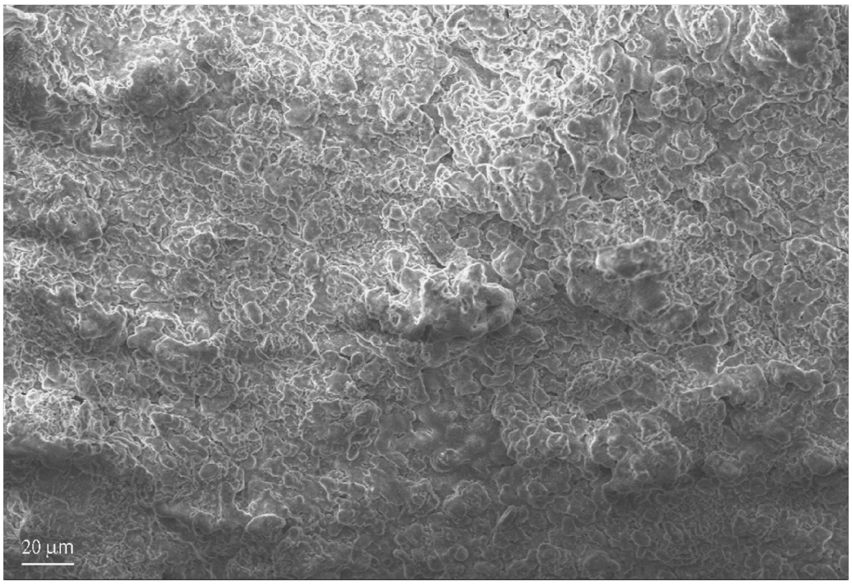

Figure 7.18: Secondary electron micrograph showing the surface morphology of oxidized silicide coated sample in air environment at 1000 °C for 64 hrs.

et al.[127] have reported the formation of plate shape morphology of Nb_2O_5 phase in the SiO_2 oxide layer. As shown by Stringer et al.[136], if the oxidation temperature is higher than 600 °C, Nb_2O_5 does not form in the form of plate shape morphology. In the present study also the Nb_2O_5 oxide did not form in the form of plate shape morphology on the both oxidized bare Nb alloy and silicide coated samples (Figs.7.12(b) and 7.18). The similar oxide morphology was reported by Li et al. [128]. The SEM micrographs clearly showed that wherever cracks presented in the coating layer, SiO_2 has formed during oxidation and prevented the growth of cracks and prevented further oxidation of the material.

7.5.3. Oxidation mechanism of silicide coated Nb alloy

There are two mechanisms by which the silicide phase undergoes oxidation at higher temperature >900 °C [127, 128].

According to first mechanism [128], during oxidation at high temperatures, initially, $NbSi_2$ decomposes into Nb_5Si_3 and Si (equation 7.7). The released Si reacts with oxygen and forms SiO_2, as well as O_2 reacts with Nb and forms Nb_2O_5 (equations 7.8, 7.9). According to this mechanism the oxidized layer will have a mixture of two phases Nb_2O_5 and SiO_2. The decomposed Si may undergo inward diffusion and forms Nb_5Si_3 between Nb and $NbSi_2$. If Nb_5Si_3 already exists, the thickness of Nb_5Si_3 should increase.

$$5NbSi_2 \rightarrow Nb_5Si_3 + 7Si \tag{7.7}$$

$$Si + O_2 \rightarrow SiO_2 \tag{7.8}$$

$$Nb + O_2 \rightarrow Nb_2O_5 \tag{7.9}$$

According to second mechanism [127], $NbSi_2$ undergoes oxidation and forms a mixture of Nb_2O_5 and SiO_2 (reaction 7.10). In comparison to first mechanism difference is that in this case it does not form Nb_5Si_3 phase.

$$4NbSi_2 + 13O_2 = 2Nb_2O_5 + 8SiO_2 \tag{7.10}$$

In the present study, increase in Nb_5Si_3 layer and formation of Nb_5Si_3 beneath the oxide layer was not observed. Therefore, the silicide coated samples have undergone oxidation according to the second mechanism (reaction 7.10).

7.6. Summary

In the present chapter, detailed microstructural characterization of the silicide coated samples and oxidized samples were carried out and oxidation performance of the bare Nb alloy and silicide coated Nb alloy had been evaluated at higher temperatures in atmospheric condition.The highlights of the work can be summarized in the following points:

- Silicide coatings produced by pack cementation technique at different temperatures (1200 - 1500 °C) showed uniform coating thickness on the Nb alloy samples.

- The silicide coating layer produced at 1200 °C had a single $NbSi_2$ phase, whereas, the coating layer produced at and higher temperature of 1300 °C had two silicide phases: $NbSi_2$ and Nb_5Si_3.

- SEM micrographs of all the coated samples showed that the thickness of the $NbSi_2$ is higher than the Nb_5Si_3. This shows that growth rate of $NbSi_2$ was higher than the Nb_5Si_3. This was attributed to higher diffusivity of Nb and Si in $NbSi_2$ than in Nb_5Si_3.

- Crystal structure of the $NbSi_2$ and Nb_5Si_3 were determined by TEM analysis of the cross-sectional silicide coated samples. It showed that the Nb_5Si_3 had tetragonal crystal structure with lattice parameters of a = 0.65 nm and c = 1.19 nm and the $NbSi_2$ had hexagonal crystal structure with lattice parameters of a = 0.48 nm and c = 0.66 nm.

- Microstructural characterization by TEM and EBSD have revealed the presence of small size ($\sim$ 0.6 μm) equiaxed grains in the Nb_5Si_3 phase and two morphologies (columnar and large equiaxed) of grains in the $NbSi_2$ phase. In $NbSi_2$, columnar grains have formed near to the $Nb_5Si_3/NbSi_2$ interface and large size equiaxed grains ($\sim$ 30 μm) have formed near to the surface of the coated samples. It also revealed that $NbSi_2$ had formed by inward diffusion of Si as well as by outward diffusion of Nb, whereas, Nb_5Si_3 had formed by only inward diffusion of Si.

- Microhardness results showed that Nb_5Si_3 had higher hardness than the $NbSi_2$.

- The oxidation studies of Nb alloy showed that Nb-1Zr-0.1C alloy undergoes severe oxidation at and above $\sim$ 600 °C. However, The Nb alloy exhibited higher oxidation resistance than pure Nb. It was attributed to the presence of Zr in the Nb matrix.
- The produced silicide coating at 1300 °C for 6 hrs on Nb alloy greatly improved the oxidation resistance of the Nb alloy.
- The oxide layer that formed on silicide coated surface consisted of a Nb_2O_5-SiO_2 mixed oxide layer. The SiO_2 phase was the main phase that increased the oxidation resistance of the silicide coated Nb alloy sample.

CHAPTER 8

Conclusions

In the present work, effect of thermomechanical treatments, microstructural characterization and structure property correlations of Nb-1Zr-0.1C (wt.%) alloy were studied. In this work, thermomechanical parameters were optimized to develop a flow sheet for fabrication of the Nb alloy at temperatures lower than 0.4 Tm. For this purpose, detailed dilatometry as well as laboratory scale warm rolling experiments were carried out. With these optimized deformation parameters, the as-solidified Nb alloy samples were successfully extruded at low temperatures (800 °C). To determine the recrystallization parameters, deformed samples were annealed at various temperatures and time. The optimized deformation and recrystallization parameters were latter used to develop a flow sheet for the fabrication of tubular products of Nb alloy at low temperatures. During thermomechanical processing of the alloy formation of various carbides was noticed. Detailed study on the carbide formation was carried out using optical microscopy, X-ray diffraction, orientation imaging microscopy and transmission electron microscopy techniques. Crystallographic details of each carbide phase was determined and their formation mechanisms have been studied in detail. The effect of thermomechanical treatments on the deformation and annealing textures were carried out using orientation imaging microscopy for microtexture analysis and X-ray diffraction for bulk texture analysis. In order to know the type of slip systems get activated during deformation, deformation textures were simulated using the Taylor type models. In addition, the effect of thermomechanical treatments on the mechanical properties of the Nb alloy were evaluated by carrying out tensile tests and hardness measurements. Keeping in view of the fact that one of the major application of the Nb alloy is for high temperature applications, study of silicide coatings on the Nb alloy by pack cementation technique has been carried out. Further, the oxidation behaviour of bare Nb alloy and silicide coated samples were investigated. These oxidized and silicide coated samples were characterized by scanning electron microscopy and also by aforementioned techniques. The important conclusions that have been drawn from the present investigation are listed below under the Chapters:

8.1. Thermomechanical processing of the alloy

1. Microstructural characterization of the electron beam melted Nb alloy revealed the presence of large grain size and needle morphology of precipitates. Tensile testing of the as-solidified samples at room temperature showed low ductility ($\sim$ 2%). Examination of Fracture surface of samples revealed that needle morphology of precipitates acted as stress concentration regions and led to crack initiator.

2. Flow stress for the as-solidified samples at different temperatures (600 - 1300 °C) was estimated by dilatometry. It showed three distinct temperature regions of flow stress: (1) decrease in flow stress up to 800 °C, (2) gradual increase in flow stress between 800 to 1000 °C and (3) decrease in flow stress beyond 1000 °C. Increase in the flow stress in the temperature range of 800 to 1000 °C was found due to the precipitation of the cuboidal precipitates. The reason for decrease in flow stress beyond 1000 °C was due to the softening of the matrix phase and precipitate dissolution.

3. The compression tests at 800 °C at different strain rates showed that the Nb alloy at 800 °C is low (negligible) strain rate sensitive. Therefore, to avoid cracking of the Nb alloy during extrusion experiments, hollow ingots were made and successful extrusion was carried out without cracking and oxidation at 800 °C.

4. Heat treatments of deformed samples at different temperatures and time showed that heat treating at 1200 °C up to 24 hrs did not produce recrystallized microstructure. The annealing treatment of 3 hrs at 1300 °C, on the other hand, produced a nearly full annealed microstructure (97% of the grains recrystallized, which was confirmed by analyzing the data of electron back scattering diffraction).

5. Recrystallized samples had 98 ± 3 MPa yield strength, 274 ± 5 MPa ultimate tensile strength and 21 ± 2 % total strain. It showed improvement in mechanical properties of the Nb alloy in comparison to as-solidified samples. These mechanical properties matched well with the mechanical properties of the Nb alloy fabricated at higher temperatures (deformed at 1600 °C and annealed at 1400 °C [9]).

6. The detailed study on the effect of thermomechanical processing on the Nb alloy had led to development of a flow sheet for the fabrication of tubes of the Nb alloy at low temperatures.

8.2. Formation of different carbide phases in the Nb alloy

1. For the identification of second phase precipitates present in the as-solidified, deformed and annealed microstructures, samples were characterized by synchrotron-XRD and TEM techniques. It showed that precipitates with needle morphology presented in the as-solidified samples corresponded to γ-Nb_2C type of carbide phase. Similarly in deformed sample, the needle morphology and cuboidal morphology precipitates corresponded to α-$(Nb,Zr)_2C$ and $(Nb,Zr)_3C_2$ carbide precipitates. Optical and EBSD micrographs of the recrystallized samples showed absence of second phase precipitates in the recrystallized samples. But TEM analysis had revealed the presence of fine scale ($\sim$ 100 nm) spherical morphology of (Nb,Zr)C carbide precipitates in the Nb matrix.

2. Detailed crystallographic analysis of the structures of the Nb and γ-Nb_2C had revealed that transformation of Nb to γ-Nb_2C had taken place by the occupation of carbon atoms at octahedral sites in bcc Nb lattice. This transformation involved small movement of Nb atoms. Similarly, crystallographic analysis revealed that for the transformation of Nb to (Nb,Zr)C, large movement of Nb and C atoms were required. The (Nb,Zr)C carbide phase in recrystallized samples had formed by diffusional phase transformation.

3. The high resolution electron microscopic analysis of the recrystallized sample showed the presence of Nb_3C_2 at the interface between Nb and (Nb,Zr)C carbide phase. It indicated the presence of carbon in solution due to the dissolution of Nb_3C_2 aided in the formation of (Nb,Zr)C carbide phase. It showed that the activation energy required for the formation of (Nb,Zr)C at the vicinity of $(Nb,Zr)_3C_2$ is low. Hence, the (Nb,Zr)C carbides were present at the regions of the $(Nb,Zr)_3C_2$ and not distributed uniformly within grains as well as at the grain boundaries.

4. Based on the detailed carbide phase formation study the phase formation sequence for the formation of stable (Nb,Zr)C carbide phase can be expressed as:
   γ-$Nb_2C \rightarrow \alpha$-$(Nb,Zr)_2C$ + $(Nb,Zr)_3C_2 \rightarrow (Nb,Zr)C$.

8.3. Textural and microstructural evolutions during deformation and annealing of the Nb alloy

1. The presence of texture in the deformed samples was analyzed by bulk and microtexture analysis. It showed that up to 40% deformation, the Nb alloy exhibited random texture. At and beyond 60% deformation, it showed strong presence of α and γ-fiber texture. Among both the fibers, volume fraction of γ-fiber was higher than the α-fiber. Within the α-fiber, the $\{111\}\langle 110\rangle$ texture component was dominant and in the γ-fiber, increase in texture gradient from $\{111\}\langle 112\rangle$ to $\{111\}\langle 110\rangle$ were found. The deformed texture simulated using pancake relaxed constraint Taylor type model using $\{110\}\langle 111\rangle$ slip systems were in good accordance with the experimentally observed deformed texture. It showed that during deformation, $\{110\}\langle 111\rangle$ type of slip systems get activated and it lead to the formation of α and γ-fiber textures in the deformed samples.

2. Annealing of deformed samples showed substantial decrease in the intensity of γ-fiber and marginal change in the intensity of α-fiber. After annealing, within α-fiber, $\{111\}\langle 110\rangle$ texture component which was dominant in the deformed sample got reduced and there was weak preference for $\{001\}\langle 110\rangle$ texture component. Similarly in the γ-fiber, intensities of all the texture components decreased and the trend observed in the deformed samples ($\{111\}\langle 110\rangle$ component intensity is slightly higher than the $\{111\}\langle 112\rangle$) remained similar. These changes lead to the development of a random texture in the annealed samples with a weak $\{001\}\langle 110\rangle$ texture.

3. The orientation imaging micrographs of the annealed samples showed that the deformed samples were fully recrystallized at 1300 °C with out any soaking time (0 hrs). In addition, with increasing soaking time negligible grain growth was observed. The chemical composition analysis had revealed that with increasing annealing soaking time, Nb/Zr ratio in the precipitate has decreased. It indicates that Zr present in the Nb alloy has preferentially partitioned into precipitates. Macrohardness of the annealed samples showed that due to decrease in Zr content in the matrix, the hardness of the annealed samples decreased.

8.4. Silicide coating on the Nb alloy and its oxidation behaviour

1. Thermogravimetric analyses have shown that the Nb alloy undergoes severe oxidation at and above 600 °C. In order to decrease oxidation of the Nb alloy at higher temperatures ($\sim$ 1000 °C), silicide coatings were produced by pack cementation coating technique. Coating experiments were carried out from 1200 to 1500 °C. The microstructure characterization revealed that coatings carried out at and below 1200 °C had a single $NbSi_2$ phase, whereas, at and above 1300 °C, the coating layer had two silicide phases: $NbSi_2$ and Nb_5Si_3 ($NbSi_2$ formed at the surface of the sample and Nb_5Si_3 formed in between substrate (Nb alloy) and $NbSi_2$ coating layer).

2. Cross-sectional microstructure of the silicide coating showed that $NbSi_2$ had hexagonal crystal structure with lattice parameters of a = 0.48 nm and c = 0.66 nm and Nb_5Si_3 had tetragonal crystal structure with lattice parameters of a = 0.65 nm and c = 1.19 nm. It also showed that Nb_5Si_3 had fine equiaxed grains, whereas, $NbSi_2$ had duplex grain morphology. $NbSi_2$ had formed with columnar grain morphology near to the Nb_5Si_3 layer and with large equiaxed grains at the surface of the coating sample. Columnar morphology of grains were attributed to outward diffusion of Nb and equiaxed grains were attributed to inward diffusion of Si.

3. Oxidation behaviour of the silicide coated samples studied in thermogravimetric analyzer up to 1200 °C in air showed marginal change in the weight of the sample. This shows that silicide coating had effectively provided the oxidation resistance for Nb alloy.

4. Detailed microstructural characterization of oxidized bare Nb alloy and silicide coated samples showed that due to the formation of Nb_2O_5 on the bare Nb alloy, it had undergone severe oxidation. Whereas, major constituents in oxidized layer of silicide coated sample was SiO_2 phase. Presence of SiO_2 phase in silicide coated samples provided high oxidation resistance for the silicide coated Nb alloy samples.

Scope of Further Research

Based on the work carried out in this dissertation, the following are a few suggestions for further work:

1. Since, Nb alloys are mainly applicable for high temperature reactors, hence, effect of irradiation on the microstructure, carbide phase stability and mechanical properties of the Nb alloys can be studied.
2. Investigation on the effect of temperature on the mechanical properties and microstructure of the Nb alloys.
3. To improve the mechanical properties of the Nb-Zr-C alloys, the addition of other refractory based alloying elements can be explored.
4. Development of low oxidation rate Nb alloys by studying the effect of alloying elements on the oxidation rate of Nb-Zr-C alloys can be carried out.

References

[1] P. Enghag, *Encyclopedia of the Elements: Technical Data - History - Processing - Applications*. Wiley, 2008.

[2] E. J. Delgrosso, C. E. Carlson, and J. J. Kaminsky, “Development of niobium-zirconium-carbon alloys,” *J Less Common Met*, vol. 12, no. 3, pp. 173 – 201, 1967.

[3] V. Fischer, H. Stormer, D. Gerthsen, M. Stenzel, H. Zillgen, and E. I. Tiffee, “Niobium as New Material for Electrolyte Capacitors with Nanoscale Dielectric Oxide Layers,” *Proceedings of the 7th international conference on properties and applications of dielectric materials*, vol. 3, pp. 1134–1137, 2003.

[4] L. Charles, “Niobium demand and superconductor applications: An overview,” *J Less Comm Met*, vol. 139, no. 1, pp. 107–122, 1988.

[5] W. S. Hazelton, *Potential Application of Niobium to Aviation Gas Turbines*. Society of Automotive Engineers, 1958.

[6] J. R. Davis, *Heat resistant Materials*. ASM International, 1997.

[7] E. M. Lyutyi, O. I. Eliseeva, and R. I. Bobyk, “Corrosion of refractory metals and alloys in liquid lithium (a review),” *Soviet materials science: a transl of Fiziko-khimicheskaya mekhanika materialov / Academy of Sciences of the Ukrainian SSR*, vol. 26, pp. 611–621, 1991.

[8] L. Lundberg, “Refractory Metals in Space Nuclear Power,” *J Met*, vol. 37, pp. 44–47, 1985.

[9] R. H. Titran and M. Uz, “Effect of themomechanical processing on the microstructure and mechanical properties of Nb-Zr-C alloys,” *NASA*, vol. TM-107207, 1996.

[10] I. V. Dulera and R. K. Sinha, “High temperature reactors,” *J Nucl Mater*, vol. 383, no. 1-2, pp. 183–188, 2008.

[11] S. L. Dickerson and J. C. Gibeling, “Low cycle fatigue of niobium-zirconium and niobium-zirconium-carbon alloys,” *Mater Sci Eng A*, vol. 278, no. 1-2, pp. 121–134, 2000.

[12] B. O. Brien, J. Stinson, and W. Carroll, “Development of a new niobium-based alloy for vascular stent applications,” *J Mech Behav Biomed*, vol. 1, pp. 303 – 312, 2008.

[13] L. D. Zardiackas, H. L. Freese, and M. J. Kraay, *Titanium, Niobium, Zirconium, and Tantalum for Medical and Surgical Applications*. ASTM International, 2006.

[14] X. Zheng, R. Bai, D. Wang, X. Cai, F. Wang, M. Xia, and J. Yu, “Research development of refractory metal materials used in the field of aerospace,” *Rare Metal Mat Eng*, vol. 40, pp. 1871–1875, 2011.

[15] M. S. El-Genk and J.-M. Tournier, “A review of refractory metal alloys and mechanically alloyed-oxide dispersion strengthened steels for space nuclear power systems,” *J Nucl Mater*, vol. 340, pp. 93 – 112, 2005.

[16] M. Uz and R. H. Titran, “Thermal stability of the microstructure of an aged Nb-Zr-C alloy,” *AIP Conf Proc*, vol. 217, no. 1, pp. 172–185, 1991.

[17] T. B. Massalski and H. Okamoto, *Binary alloy phase diagrams*. ASM International, Materials Park, Ohio), 1990.

[18] T. B. Massalski and H. Okamoto, *Binary alloy phase diagrams*. ASM International, Materials Park, Ohio), 1990.

[19] F. Ostermann, “Controlling carbide dispersions in niobium base alloys,” *J Less Common Met*, vol. 25, no. 3, pp. 243 – 256, 1971.

[20] J. F. Smith, O. N. Carlson, and R. R. D. Avillez, “The niobium carbon system,” *J Nucl Mater*, vol. 148, no. 1, pp. 1 – 16, 1987.

[21] K. Yvon and E. Parthe, “On the crystal chemistry of the close packed transition metal carbides I The crystal structure of the V, Nb and Ta carbides,” *Acta Crystallogr B*, vol. 26, pp. 149 – 153, 1970.

[22] E. Parthe and K. Yvon, “On the crystal chemistry of the close packed transition metal carbides II A proposal for the notation of the different crystal structures,” *Acta Crystallogra B*, vol. 26, pp. 153 – 163, 1970.

[23] R. L. Crane and F. Ostermann, “An X-ray diffraction analysis of the ϵ phase in dilute Nb-C alloys,” *Metall Trans*, vol. 2, pp. 3487 – 3488, 1971.

[24] H. Jiang, T. R. Bieler, C. Compton, and T. L. Grimm, “Cold rolling evolution in high purity niobium using a tapered wedge specimen,” *Physica C*, vol. 441, pp. 118–121, 2006.

[25] P. Kofstad, *High temperature oxidation of metals*. John Wiley & Son, New York, 1966.

[26] E. N. Sheftel and O. A. Bannykh, “Niobium base alloys,” *Int J Refract Met H*, vol. 12, pp. 303–314, 1993-1994.

[27] R. Smith, “The development of oxidation-resistant niobium alloys,” *J Less Common Met*, vol. 2, pp. 191–206, 1960.

[28] Y. Tan, H. Tanaka, C. L. Ma, A. Kasama, R. Tanaka, Y. Mishima, and S. Hanada, "Solid solution strengthening and high temperature compressive strength of Nb-X alloys (X = Ta, V, Mo and W)," *J Jpn I Met*, vol. 64, pp. 559–565, 2000.

[29] Y. Tan, H. Tanaka, C. L. Ma, A. Kasama, R. Tanaka, Y. Mishima, and S. Hanada, "Solid solution strengthening and high temperature compressive ductility of Nb-Mo-W ternary alloys," *J Jpn I Met*, vol. 64, pp. 566–570, 2000.

[30] S. Hanada, T. Tabaru, and R. Gnanamoorthy, "Processing and properties of Nb_3Al alloys," *Acta Metall Sin*, vol. 8, pp. 477–487, 1995.

[31] T. Tabaru and S. Hanada, "High temperature strength of Nb_3Al base alloys," *Intermetallics*, vol. 6, pp. 735 – 739, 1998.

[32] D. L. Anton, D. B. Snow, and A. F. Giamei, *Dispersion strengthening of high temperature niobium alloys", publisher = "TMS, ed J Stephens and Iqbal Ahmed, , Warrandale, PennsylvaniaASM International, Materials Park, Ohio*. 1991.

[33] E. N. Sheftel, V. K. Grigorovich, and G. S. Usmanova, *Research and use of refractory metal alloys*. Ed E M Savitskij, M A Tylkina and N K Kazanskaja, Nauka, Moscow, 1983.

[34] V. K. Grigorovich and E. N. Sheftel, *Dispersion strengthening of refractory metals*. Nauka, Moscow, 1980.

[35] S. R. Lampman and T. B. Zorc, *Refractory metals and alloys, Metals Handbook, 10th Ed ,vol 2*. American Society for Metals (ASM) International, Metals Park, OH, 1990.

[36] A. Taylor and N. J. Doyle, "The solid solubility of carbon in Nb and Nb-RICH Nb-Hf, Nb-Mo and Nb-W alloys," *J Less Common Met*, vol. 13, pp. 511 – 529, 1967.

[37] I. I. Druzhinin, A. M. Zakharov, and I. I. Novikov, "Phase equilibria in the niobium corner of the Nb-Zr-C and Nb-Ti-C systems," *Izvestija Vuzov Tsvetnaja Metallurgija*, vol. 1, pp. 118–21, 1972.

[38] A. D. Korotnev, A. N. Tumentsev, and V. F. Sukhovarov, *Dispersion strengthening of refractory metals*. Nauka, Moscow, 1989.

[39] V. Gennari *Proc 1st Europ Conf Adv Mater Processes, ed H E Exner and V Schumacher, DGM lnformationsgesellshaft, Verlag*, vol. 2, pp. 731–736, 1990.

[40] Y. R. He, R. A. Rapp, and P. P. Tortorelli, "Oxidation resistant Ge doped silicide coating on Cr-Cr_2Nb alloys by pack cementation," *Mat Sci Eng A*, vol. 222, no. 2, pp. 109 – 117, 1997.

[41] Y. Tan, C. L. Ma, H. Tanaka, A. Kasama, R. Tanaka, Y. Mishima, and S. Hanada, "Influence of boron addition on high temperature mechanical properties of Nb_3Ir intermetallic compounds," *Mater T JIM*, vol. 41, pp. 1605–1611, 2000.

[42] C. L. Ma, A. Kasama, Y. Tan, H. Tanaka, R. Tanaka, Y. Mishima, and S. Hanada, "Synthesis of Nb/Nb_5Si_3 in-situ composites by mechanical milling and reactive spark plasma sintering," *Mater Trans , JIM*, vol. 41, pp. 719–726, 2000.

[43] D. M. Shah, D. L. Anton, D. P. Pope, and S. Chin, "Insitu refractory intermetallic based composites," *Mater Sci Eng A*, vol. 192-193, pp. 658–672, 1995.

[44] C. L. Ma, Y. Tan, H. Tanaka, A. Kasama, R. Tanaka, S. Miura, Y. Mishima, and S. Hanada, "Phase equilibria in Nb-Mo rich zone of the Nb-Si-Mo ternary system," *Mater T JIM*, vol. 41, pp. 1329–1336, 2000.

[45] H. Tanaka, Y. Tan, C. L. Ma, A. Kasama, and R. Tanaka *Report of the 123rd committee on heat resisting materials and alloys*, vol. 41, pp. 223–227, 2000.

[46] N. Nomura, K. Yoshimi, and S. Hanada, "Mechanical properties of Mo-Nb-TiC in-situ composites synthesized by hot pressing," *Mater T JIM*, vol. 41, pp. 1599–1604, 2000.

[47] T. Suzuki, N. Nomura, K. Yoshimi, and S. Hanada, "Microstructure and creep of Mo-ZrC in-situ composite," *Mater T JIM*, vol. 41, pp. 1164–1167, 2000.

[48] Y. Tan, C. L. Ma, A. Kasama, R. Tanaka, Y. Mishima, S. Hanada, and J. Yang, "Effect of alloy composition on microstructure and high temperature properties of Nb-Zr-C ternary alloys," *Mat Sci Eng A*, vol. 341, pp. 282 – 288, 2003.

[49] F. Ostermann and E. E. Kibbey, "Molybdenum in Nb-C alloys," *Metall Mater Trans B*, vol. 1, no. 8, pp. 2257 – 2263, 1970.

[50] R. Lesser and G. Brauer, "Carbide phases of tantalum," *Z Metallk*, vol. 49, pp. 622 – 625, 1958.

[51] L. D. C. P Villars, *Pearson's handbook of crystallographic data for intermetallic phases*, vol. 1. American Society for Metals, Metals Park Ohio, 1986.

[52] A. N. Christensen, "Vacancy order in Nb_6C_5," *Acta Chem Scand A*, vol. 39, pp. 803–804, 1985.

[53] G. Brauer, H. Renner, and J. Wernet, "The carbides of niobium," *J Inorg Gen Chem*, vol. 277, no. 5, pp. 249 – 257, 1954.

[54] E. Rudy and C. E. Brukl, "Lower temperature modifications of Nb_2C and V_2C," *J Am Ceram Soc*, vol. 50, pp. 265 – 268, 1967.

[55] R. K. Viswanadham and C. A. Wert, "Electron microscopic study of precipitation in the niobium-carbon system," *J Less Common Met*, vol. 48, no. 1, pp. 135 – 150, 1976.

[56] E. Friederich and L. Sittig, "Production and qualities of carbides," *J Inorg Gen Chem*, vol. 144, no. 1, pp. 169 – 189, 1925.

[57] F. Ostermann and F. Bollenrath, *High temperature materials*. Springer Verlog, Wien-New York, 1969.

[58] A. J. Williams and D. C. Briggs, "Ageing in niobium-rich niobium-hafnium-carbon alloys," *J Less Common Met*, vol. 21, no. 3, pp. 255 – 273, 1970.

[59] O. A. Filipleva, E. M. Volin, G. S. Baeva, N. Y. Volina, and A. E. Lokshina, "Increasing the ductility of cast niobium alloys by heat treatment," *Met Sci Heat Treat*, vol. 14, no. 1, pp. 26–31, 1972.

[60] T. L. Grobstein and R. H. Titran, "Characterization of precipitates in a Niobium Zirconium Carbon alloy," *NASA TM 100848*, pp. 1–13, 1989.

[61] E. M. Lyutyi, G. G. Maksimovich, and O. S. Tsvikilevich, "Quantitative analysis on the distribution of hardening-phase particles in an Nb-Zr-C alloy," *Sov Mater Sci*, vol. 14, no. 3, pp. 284 – 288, 1978.

[62] M. Uz and R. H. Titran, "Characterization of the microstructure of Nb-1Zr-0 1C tubes as affected by thermomechancial processing," *AIP Conf Proc*, vol. 301, pp. 393–402, 1994.

[63] M. Uz and R. H. Titran, "Processing and microstructure of Nb-1Zr-0.1C alloy sheet," *AIP Con Proc*, vol. 271, no. 1, pp. 69 – 83, 1993.

[64] A. E. Kissil, P. A. Khandarov, A. D. Rapp, L. P. Onisenko, L. Z. Polyak, A. G. Arakelov, and I. I. Maksimov, "Study of the structure and morphology of the strengthening phase in an Nb-Zr-C alloy during the prolonged action of high temperature and pressure in vacuo," *Sov Mater Sci*, vol. 12, no. 6, pp. 640–643, 1977.

[65] G. G. Maksimovich, E. M. Lyutyi, A. E. Kissil, L. P. Onisenko, P. A. Khandarov, and O. S. Tsvikilevich, "Structure and morphology of the hardening phase in an Nb-Zr-C alloy after strain aging at 900 °C," *Sov Mater Sci*, vol. 13, no. 5, pp. 576–578, 1977.

[66] P. A. Khandarov, A. N. Lukyanov, A. G. Arakelov, O. S. Tsvikilevich, E. M. Lyutyi, and G. G. Maksimovich, "Kinetics of structural changes in an Nb-Zr-C alloy with prolonged holding under load at high temperatures," *Sov Mater Sci*, vol. 14, no. 4, pp. 431–435, 1978.

[67] D. Raabe and K. Lucke, "Texture of ferritic stainless steels," *Mater Sci Tech*, vol. 9, pp. 302–312, 1993.

[68] B. Verlinden, J. Driver, I. Samajdar, and R. D. Doherty, *Thermomechanical processing of metallic materials*. Elsevier, 2007.

[69] D. Raabe and K. Lucke, "Rolling and annealing textures of BCC metals," *Mater Sci Forum*, vol. 157-162, pp. 597–610, 1994.

[70] M. M. Borodkina, G. F. Chusova, Y. A. Gruznov, and L. N. Fedotov, "Texture of niobium bands," *Met Sci Heat Treat*, vol. 17, pp. 540–542, 1975.

[71] H. F. G. Abreu, S. S. M. Tavares, S. S. Carvalho, T. H. T. Eduardo, A. D. S. Bruno, and M. H. P. da Silva, "Texture and microstructure of cold rolled and recrystallized pure niobium," *Mater Sci Forum*, vol. 539-543, pp. 3436–3441, 2007.

[72] H. R. Z. Sandim, J. F. C. Lins, A. L. Pinto, and A. F. Padilha, "Recrystallization behavior of a cold rolled niobium bicrystal," *Mater Sci Eng A*, vol. 354, no. 1-2, pp. 217–228, 2003.

[73] J. Lepinoux, D. Maziere, V. Pontikis, and G. Saada, *Multiscale Phenomena in Plasticity: From Experiments to Phenomenology, Modeling and Materials Engineering*. Springer, 2000.

[74] R. A. Lebensohn and C. N. Tome, “A self-consistent anisotropic approach for the simulation of plastic deformation and texture development of polycrystals: Application to zirconium alloys,” *Acta Metall Mater*, vol. 41, no. 9, pp. 2611 – 2624, 1993.

[75] J. G. Sevillano, P. van Houtte, and E. Aernoudt, “Large strain work hardening and textures,” *Prog Mater Sci*, vol. 25, pp. 69–134, 1980.

[76] T. G. Tang, X. M. Zhang, Z. Y. Chen, and Y. L. Deng, “Simulation of rolling deformation texture of fcc metals with crystal plasticity finite element model,” *Mater Sci Tech*, vol. 22, pp. 1171–1176, 2006.

[77] S. Huang, S. Zhang, D. Li, and Y. Peng, “Simulation of texture evolution during plastic deformation of FCC, BCC and HCP structured crystals with crystal plasticity based finite element method,” *T Nonferr Metal Soc*, vol. 21, pp. 1817 – 1825, 2011.

[78] D. Raabe, G. Schlenkert, and K. Lucke, “Texture and microstructure of rolled and annealed tantalum,” *Mater Sci Tech*, vol. 10, pp. 299–305, 1994.

[79] D. Raabe, “Investigation of contribution of 123 slip planes to development of rolling textures in bcc metals by use of Taylor models,” *Mater Sci Tech*, vol. 11, pp. 455–460, 1995.

[80] P. Kofstad, *High temperature corrosion*. Elsevier Science, New York, 1988.

[81] N. Birks, G. H. Meier, and F. S. Pettit, *Introduction to the high temperature oxidation of metals*. Cambridge University Press, New york, 2006.

[82] A. S. Khanna, *Introduction to High Temperature Oxidation and Corrosion*. ASM International, 2002.

[83] P. Sarrazin, A. Galerie, J. Fouletier, and H. Evans, *Mechanisms of High Temperature Corrosion: A Kinetic Approach*. Materials science foundations, Trans tech publications limited, Switzerland, 2008.

[84] M. Levy, J. J. Falco, and R. B. Herring, “Oxidation of columbium (niobium) and coated columbium alloys,” *J Less Common Met*, vol. 34, pp. 321–343, 1974.

[85] T. Hurlen, “Oxidation of niobium,” *J I Met*, vol. 89, p. 273, 1960-61.

[86] I. Mckee and G. R. Wallwork, “Oxidation of tantalum and niobium in the temperature range of 400 to 600 °C,” *J Less Comm Met*, vol. 30, pp. 249–258, 1973.

[87] O. Kubaschewski and B. E. Hopkins, “Oxidation mechanisms of niobium, tantalum, molybdenum and tungsten,” *J Less Comm Met*, vol. 2, no. 2-4, pp. 172–180, 1960.

[88] N. Cabrera and N. F. Mott, “Theory of oxidation of metals,” *Rep Prog Phys*, vol. 12, pp. 163–184, 1949.

[89] M. P. Arbuzov and V. G. Chuprina, “The oxidation of niobium and the structure of niobium oxides,” *Sov Phys J*, vol. 8, pp. 87–89, 1965.

[90] W. D. Klopp, C. T. Sims, and R. I. Jaffee, “Effects of alloying on the kinetics of oxidation of niobium,” *proc 2nd intern conf on peaceful uses of atomic energy*, vol. 6, p. 293, 1958.

[91] S. Majumdar, A. Arya, I. G. Sharma, A. K. Sharma, and S. Banerjee, “Deposition of aluminide and silicide based protective coatings on niobium,” *Appl Surf Sci*, vol. 257, pp. 635–640, 2010.

[92] B. V. Cockeram, “Growth and oxidation resistance of boron modified and germanium doped silicide diffusion coatings formed by the halide activated pack cementation method,” *Surf Coat Tech*, vol. 76-77, pp. 20–27, 1995.

[93] S. R. J. Saunders and J. R. Nicholls, “Coatings and surface treatments for high temperature oxidation resistant,” *Mater Sci Tech*, vol. 5, no. 8, pp. 780–798, 1989.

[94] R. W. Chan, *Physical Metallurgy*, vol. 1. Elsevier, 1996.

[95] M. Levy and J. J. Falco, “Oxidation behaviour of a complex disilicide/tantalum-10tungsten alloy system at temperatures of 927 °C to 1482 °C,” *J Less Common Met*, vol. 27, pp. 143–162, 1972.

[96] R. O. Suzuki, M. Ishikawa, and K. Ono, “$NbSi_2$ coating on niobium using molten salt,” *J Alloy Compd*, vol. 336, pp. 280–285, 2002.

[97] H. J. Grabke and G. H. Meter, “Accelerated oxidation, internal oxidation, intergranular oxidation, and pesting of intermetallic compounds,” *Oxid Met*, vol. 44, pp. 147–176, 1995.

[98] E. Strom, Y. Cao, and Y. M. Yao, “Low temperature oxidation of Cr-alloyed $MoSi_2$,” *T Nonferr Metal Soc*, vol. 17, pp. 1282–1286, 2007.

[99] R. Streiff, J. M. N. G. Muamba, and D. H. Boone, “Surface morphology of diffusion aluminide coatings,” *Thin Solid Films*, vol. 119, no. 3, pp. 291 – 300, 1984.

[100] D. K. Das, V. singh, and S. V. Joshi, “Evolution of aluminide coating microstructure on Nickel base cast superalloy CM-247 in a single step high activity aluminizing process,” *Metall Mater Trans A*, vol. 29, pp. 2173–2188, 1998.

[101] D. C. Goldberg, G. Dicker, and S. A. Worcester, “Niobium and niobium alloys in nuclear power,” *Nucl Eng Des*, vol. 22, no. 1, pp. 124–137, 1972.

[102] Myneni and G. Rao, “Physical and Mechanical Properties of Niobium for SRF Science and Technology,” *AIP Conf Proc*, vol. 927, pp. 41–47, 2007.

[103] H. Jiang, D. Baars, A. Zamiri, C. Antonie, P. Bauer, T. R. Bieler, F. Pourboghrat, C. Compton, and T. L. Grimm, “Mechanical Properties of High RRR Niobium With Different Texture,” *IEEE T Appl Supercon*, vol. 17, pp. 1291–1294, 2007.

[104] O. R. M L Grossbeck, R L Heestand, “Effect of irradiation on the tensile properties of niobium base alloys,” *Symposium on Space Nuclear Power Systems Albuquerque, NM, USA*, pp. 5–11, 1970.

[105] R. W. Kelcher and A. Carter, *High temperature materials*. Newyork, Springer Verlag, 1969.

[106] E. M. Lyutyi, “Influence of intertitial atoms on the heat resistance of refractory metals,” *Sov Mater Sci*, vol. 16, pp. 170 – 174, 1980.

[107] D. M. Farkas, J. R. Groza, and A. K. Mukherjee, "Thermodynamic analysis of carbide precipitates in a niobium-zirconium-carbon alloy," *Scripta Mater*, vol. 34, no. 1, pp. 103–110, 1996.

[108] S. Banerjee, S. J. Vijayakar, and R. Krishnan, "Precipitation in zirconium niobium martensites," *J Nucl Mater*, vol. 62, pp. 229 – 239, 1976.

[109] F. Ernst, Y. Cao, and G. M. Michal, "Carbides in low-temperature-carburized stainless steels," *Acta Mater*, vol. 52, no. 6, pp. 1469 – 1477, 2004.

[110] U. Mehmet and R. H. Titran, "Effects of Processing and Prolonged High Temperature Exposure on the Microstructure of Nb-1Zr-C Sheet," *MRS Proc*, vol. 322, 1 1993.

[111] X. Zou, A. Hovmoller, and S. Hovmoller, "TRICE - A program for reconstructing 3D reciprocal space and determining unit cell parameters," *Ultramicroscopy*, vol. 98, no. 2-4, pp. 187–193, 2004.

[112] A. S. Kurlov, S. V. Rempel, and A. I. Gusev, "Symmetry analysis of ordered phases of the lower tungsten carbide W_2C," *Phys Solid State*, vol. 53, pp. 175–181, 2011.

[113] K. W. Andrews, D. J. Dyson, and S. R. Keown, *Interpretation of electron diffraction patterns*. London, Adam Hilger, 1971.

[114] M. I. Luppo, A. Politi, and G. Vigna, "Hydrides in α-Ti Characterization and effect of applied external stresses," *Acta Mater*, vol. 53, no. 19, pp. 4987 – 4996, 2005.

[115] S. A. David, A. T. Santhanam, and H. D. Brody, "Growth crystallography and lamellar to rod transition in directionally solidified Nb-Nb2C eutectic composites," *Metall Trans A*, vol. 7, pp. 1051–1055, 1976.

[116] F. Raghavan, *Physical Metallurgy: Principles and Practice*, vol. 2. PHI Learning Pvt Ltd, 2006.

[117] Z. Nishiyama *Sci Repts Tohoku Imp Univ*, vol. 23, pp. 637–664, 1934.

[118] G. Wasserman *Arch Eisenhuettenwes*, vol. 16, p. 647, 1933.

[119] F. Smith and J. Milewski, "Electron beam welding comes through in exacting job," *Weld J*, vol. 80, no. 6, pp. 43–47, 2001.

[120] S. N. Nasser and W. Guo, "Flow stress of commercially pure niobium over a broad range of temperatures and strain rates," *Mater Sci Eng A*, vol. 284, pp. 202–210, 2000.

[121] I. L. Dillamore and W. T. Roberts, "Rolling textures in FCC and BCC metals," *Acta Metall*, vol. 12, no. 3, pp. 281–293, 1964.

[122] G. Simmond and H. Wang, *Single crystal elastic constants and calculated aggregate properties: A Handbook*, vol. Cambridge, MA, Second edition. The MIT Press, 1971.

[123] N. Norman, P. Kofstad, and O. J. Krudtaa, "Metallic oxide phases of niobium and tantalum metallographic studies," *J Less Comm Met*, vol. 4, pp. 124–137, 1962.

[124] G. Brauer, H. Muller, and G. Kuhner, "High temperature oxidation of the niobium and tantalum," *J Less Comm Met*, vol. 4, no. 6, pp. 533–546, 1962.

[125] E. J. Delgrosso, R. C. Krutenat, C. E. Carlson, and J. S. Carta, "The oxidation characteristics of niobium-1zirconium alloy," *J Less Comm Met*, vol. 5, pp. 57–77, 1963.

[126] C. Milanese, V. Buscagila, F. Maglia, and U. A. Tamburini, "Reactive growth of niobium silicides in bulk diffusion couples," *Acta Mater*, vol. 51, pp. 4837–4846, 2003.

[127] M. Z. Alam, A. S. Rao, and D. K. Das, "Microstructure and high temperature oxidation performance of silicide coating on Nb-based alloy C-103," *Oxid Met*, vol. 73, pp. 513–530, 2010.

[128] M. Li, L. Song, J. Le, X. Zhang, B. Pei, and X. Hu, "Formation and oxidation resistance of $NbSi_2$ coatings on niobium by pack cementation," *Key Eng Mat*, vol. 280-283, pp. 907–910, 2005.

[129] J. M. Hampikian, M. Saqib, and D. I. Potter, "Improved oxidation resistance of group VB refractory metals by Al+ ion implantation," *Metall Mat Trans B*, vol. 27, no. 3, pp. 491–500, 1996.

[130] S. Majumdar, P. Sengupta, G. B. Kale, and I. G. Sharma, "Deposition of aluminide and silicide based protective coatings on niobium," *Surf Coat Tech*, vol. 200, pp. 3713–3718, 2006.

[131] S. Prasad and A. Paul, "Growth mechanism of phases by interdiffusion and diffusion of species in the niobium silicon system," *Acta Mater*, vol. 59, no. 4, pp. 1577–1585, 2011.

[132] D. L. Douglass, "The thermal expansion of niobium pentaoxide and its effect on the spalling of niobium oxide films," *J Less Comm Met*, vol. 5, pp. 151–157, 1963.

[133] K. Wang and R. R. Reeber, "The role of defects on thermophysical properties: thermal expansion of V, Nb, Ta, Mo and W," *Mater Sci Eng R*, vol. 23, pp. 101–137, 1998.

[134] D. W. Aylmore, S. J. Gregg, and W. B. Jepson, "Oxidation of niobium in the temperature range 350 - 750 C," *J Electrochem Soc*, vol. 107, pp. 495–501, 1960.

[135] M. del Pilar Moricca and S. K. Varma, "High temperature oxidation characteristics of Nb-10W-XCr alloys," *J Alloys Compd*, vol. 489, no. 1, pp. 195–201, 2010.

[136] J. Stringer, "Oxidation of niobium single crystals," *Acta Metall*, vol. 17, pp. 1227–1246, 1969.

[137] Y. S. Touloukian, *Thermal Expansion Metals and Alloys, Thermophysical Properties of Matter*, vol. 12. Plenum Press, New York, 1970.

[138] Y. S. Touloukian, *Thermal Expansion Nonmetals, Thermophysical Properties of Matter*, vol. 13. Plenum Press, New York, 1970.